Over recent years there has been a marked growth in interest in the study and techniques of cosmic ray physics by astrophysicists and particle physicists. Cosmic radiation is important for the astrophysicist because of the information it can yield about energetic astrophysical processes in the further reaches of the galaxy and beyond. For particle physicists, it provides the opportunity to study neutrinos and very high energy particles of cosmic origin. In addition, cosmic rays constitute the background, but also the calibration source, for searches for exotic hypothesized particles and processes such as monopoles, sparticles and proton decay.

Concentrating on the highest energy cosmic rays, this book describes where they may originate, acquire energy, and interact, in large-scale shock waves, in supernova remnants and in accreting neutron stars. It also describes their interactions in the atmosphere and in the earth, how they are studied in surface and very large underground detectors, and what they tell us.

The cover design is derived from a photograph of a shower of particles in the atmosphere. Each track is a spark along the path of a charged particle in the cascade. This snapshot of an air shower was made with an array of discharge chambers operated at the University of Leeds by a group headed by Leslie Hodson and Wayne Hazen. It shows a rather unusual, nearly horizontal shower. (Photograph courtesy of Leslie Hodson.)

Cambridge
University
Press

ISBN 0-521-33931-6

GAISSER

Ca

Cosmic Rays and Particle Physics

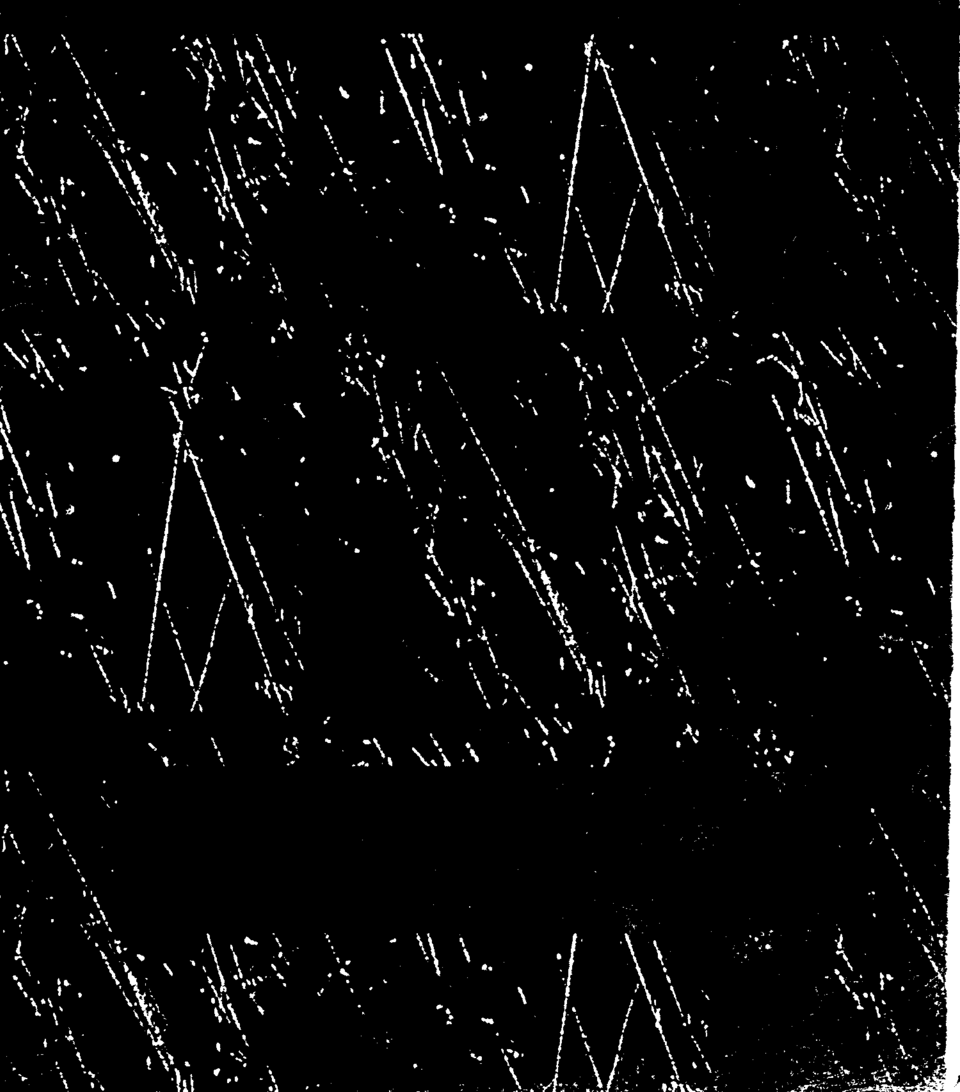

В.И. Зацепин

Over recent years there has been a marked growth in interest in the study and techniques of cosmic ray physics by astrophysicists and particle physicists. Cosmic radiation is important for the astrophysicist because of the information it can yield about energetic astrophysical processes in the further reaches of the galaxy and beyond. For particle physicists, it provides the opportunity to study neutrinos and very high energy particles of cosmic origin. In addition, cosmic rays constitute the background, but also the calibration source, for searches for exotic hypothesized particles and processes such as monopoles, sparticles and proton decay.

Concentrating on the highest energy cosmic rays, this book describes where they may originate, acquire energy and interact, in large-scale shock waves, in supernova remnants and in accreting neutron stars. It also describes their interactions in the atmosphere and in the earth, how they are studied in surface and very large underground detectors, and what they tell us.

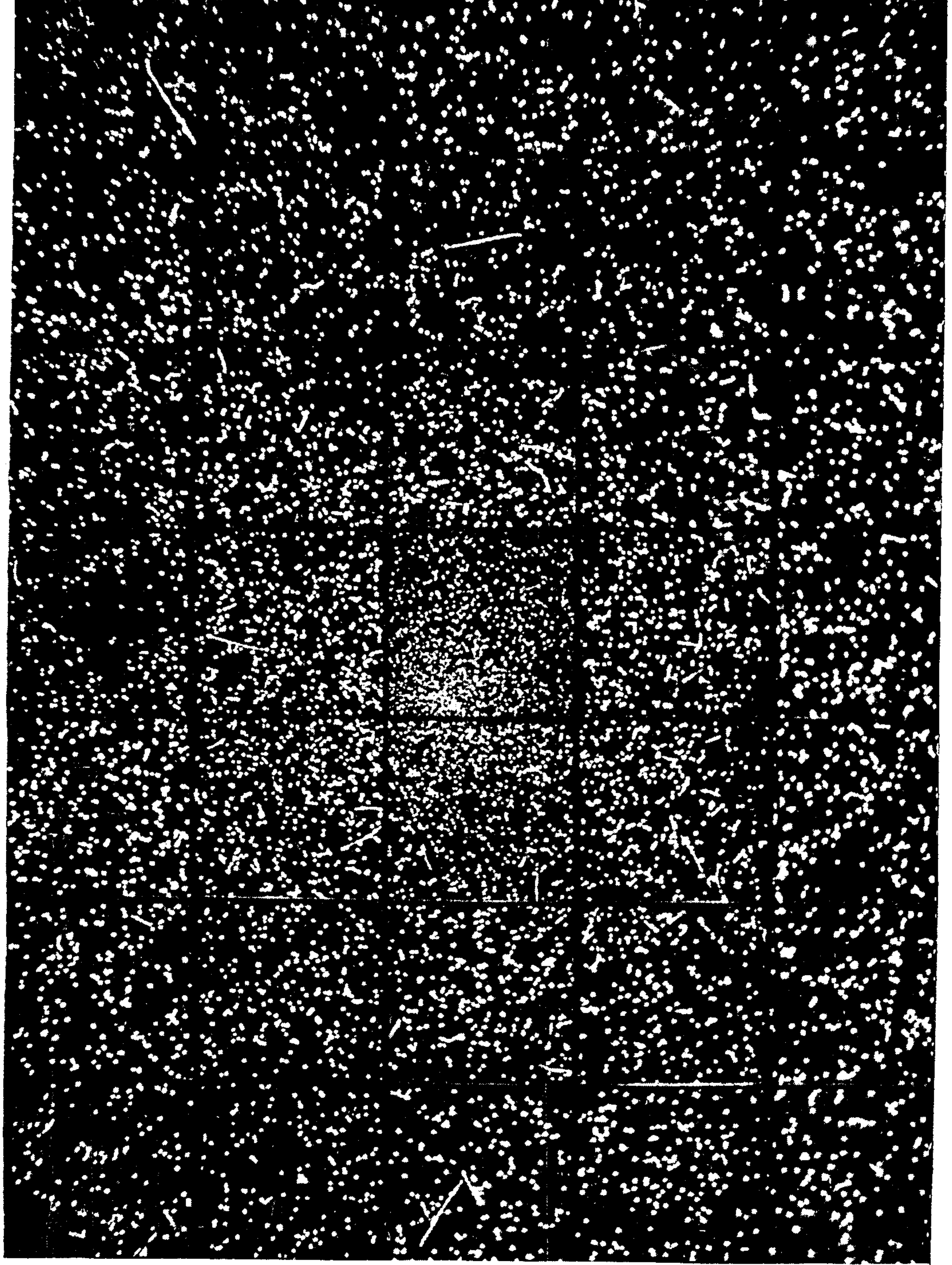

Frontispiece. Photograph of the central region of a small air shower as seen by the University of Leeds horizontal, close packed array of discharge chambers. The core of the shower is clearly visible, as well as the outlines o each of 35 one square meter chambers. Unlike the cover photo, this picture shows a typical shower with its axis (core) nearly perpendicular to the

Cosmic Rays and Particle Physics

Cosmic Rays and Particle Physics

Thomas K. Gaisser
Bartol Research Institute, University of Delaware

The right of the University of Cambridge to print and sell all manner of books was granted by Henry VIII in 1534. The University has printed and published continuously since 1584.

CAMBRIDGE UNIVERSITY PRESS
Cambridge
New York   Port Chester   Melbourne   Sydney

Published by the Press Syndicate of the University of Cambridge
The Pitt Building, Trumpington Street, Cambridge CB2 1RP
40 West 20th Street, New York, NY 10011, USA
10 Stamford Road, Oakleigh, Melbourne 3166, Australia

First published 1990

Printed in Great Britain by the University Press, Cambridge

British Library cataloguing in publication data

Gaisser, Thomas K.
Cosmic rays and particle physics.
1. Cosmic rays
I. Title
539.7223

Library of Congress cataloguing in publication data available

ISBN 0 521 32667 2 hardback
ISBN 0 521 33931 6 paperback

Contents

Tables

Preface

The connection between cosmic rays and particle physics has experienced a renewal of interest in the past decade. Large detectors, deep underground, sample groups of coincident cosmic ray muons and study atmospheric neutrinos while searching for nucleon decay, monopoles, neutrino oscillations, etc. Detector arrays at the surface measure atmospheric cascades in the effort to identify sources of the most energetic naturally occurring particles. This book is an introduction to the phenomenology and theoretical background of this field of particle astrophysics. The book is directed to graduate students and researchers, both experimentalists and theorists, with an interest in this growing interdisciplinary field.

The book is divided into an introductory section and three main parts. The two introductory chapters give a brief background of cosmic ray physics and particle physics. Chapters 3 through 8 concern cosmic rays in the atmosphere – hadrons, photons, muons and neutrinos. The second major part (chapters 9–13) is about propagation, acceleration and origin of cosmic rays in the galaxy. Air showers and related topics are the subject of the last four chapters.

I am grateful to many colleagues at Bartol and elsewhere for discussions which have helped me learn about aspects of the field. I thank Alan Watson, Raymond Protheroe, Paolo Lipari, Francis Halzen, David Seckel, Todor Stanev, Floyd Stecker and Carl Fichtel for reading various chapters and offering helpful suggestions.

I thank Leslie Hodson, Jack van der Velde, Jay Perrett and Sergio Petrera for providing me with photographs to illustrate the book.

Chapter 1

Cosmic rays

1.1 What are cosmic rays?

Cosmic ray particles hit the Earth's atmosphere at the rate of about 1000 per square meter per second. They are ionized nuclei - about 90% protons, 9% alpha particles and the rest heavier nuclei - and they are distinguished by their high energies. Most cosmic rays are relativistic, having energies comparable to or somewhat greater than their masses. A very few of them have ultrarelativistic energies extending up to 10^{20} eV (about 20 joules), eleven orders of magnitude greater than the equivalent rest mass energy of a proton. The fundamental question of cosmic ray physics is, "Where do they come from?" and in particular, "How are they accelerated to such high energies?"

The answer to the question of the origin of cosmic rays is not yet fully known. It is clear, however, that nearly all of them come from outside the solar system, but from within the galaxy. The relatively few particles of solar origin are characterized by temporal association with violent events on the sun and consequently by a rapid variability. In contrast, the bulk of cosmic rays show an anticorrelation with solar activity, being more effectively excluded from the solar neighborhood during periods when the expanding, magnetized plasma from the sun - the solar wind - is most intense. The very highest energy cosmic rays have gyroradii in typical galactic magnetic fields that are larger than the size of the galaxy. These may be of extragalactic origin.

1.2 Objective of this book

The focus of this book is the interface between particle physics and cosmic rays. Until the advent of accelerators, cosmic rays and their interactions were the main source of information about elementary particles. Although the highest energy cosmic rays can still offer clues about particle physics above accelerator energies, this is no longer the dominant aspect of the field. There are now, however, a number of important areas in which a knowledge of particle interactions is necessary to understand the astrophysical implications of cosmic ray data. Examples include:

> Production of **secondary cosmic rays** such as antiprotons by primary cosmic rays when they collide with atomic nuclei in the interstellar medium. From the relative amounts of such secondaries we learn about how cosmic rays propagate through the interstellar medium and hence about the nature of the matter and fields that make up the medium.
>
> Production of **photons, neutrinos** and other particles in collisions of cosmic rays with material near a site of cosmic ray acceleration. Seeing point sources of such particles is a way of identifying specific sources of cosmic ray acceleration and studying how they work.
>
> Penetration of **cosmic rays underground** and the detection of muons and neutrinos in large, deep detectors. Such particles can be both signal (for example, neutrinos from the point sources just mentioned) and background (for example, for the search for proton decay or magnetic monopoles).
>
> The relation between **atmospheric cascades** and the incoming cosmic rays that produce them. The highest energy cosmic rays are so rare that they cannot be directly observed with small detectors above the atmosphere, but they must be studied indirectly by large air shower arrays exposed for long periods at the surface. Then one has to infer the nature of the primary from its secondary cascade.
>
> Searches for **exotic particles and new interactions** in the cosmic radiation.

These topics clearly have a great deal in common: The same equations that govern particle cascades in the atmosphere of the Earth also describe particle production by cosmic rays accelerated by a collapsed star which then collide in a surrounding supernova envelope or in the atmosphere of a nearby companion star. The same cross sections that determine the neutrino-induced signal in an underground detector also determine how much energy is absorbed by a companion star due to interactions of neutrinos produced by cosmic rays accelerated in the system. The purpose of this book is to discuss the relevant particle physics and illustrate the application to cosmic ray astrophysics with examples of current interest. At the same time I will try to provide a sufficient overview of cosmic ray physics so the importance of these examples can be appreciated.

1.3 Types of cosmic ray experiment

The principal data about the cosmic rays themselves, from which one can hope to learn about their origin, are the relative abundances of the different nuclei (composition) and the distribution in energy (energy spectrum) of each component. Comparison with the chemical composition of various astrophysical objects, such as the Sun, the interstellar medium, supernovae or neutron stars, can give clues about the site at which cosmic rays are injected into the acceleration process. The energy spectra may be characteristic of certain acceleration mechanisms.

Figure 1.1 gives a global view of the total cosmic ray energy spectrum. Because of the enormous range of fluxes, it is useful to plot the flux per logarthmic interval of energy ($E\mathrm{d}N/\mathrm{d}E = \mathrm{d}N/\mathrm{d}\ln E$). Even so the vertical axis is extremely compressed. A moment's thought about the range of rates in fig. 1.1 will convince you that several quite different kinds of detectors are necessary to study cosmic rays over this whole energy range. In the interval around one GeV, about 10 particles per second cross a telescope consisting of two planes of area 100 cm^2 separated by 20 cm (see fig. 1.2). A small detector flown at the top of the atmosphere in a balloon or spacecraft is therefore sufficient to study details of cosmic ray composition in the GeV energy region down to the level of one part in a hundred thousand.

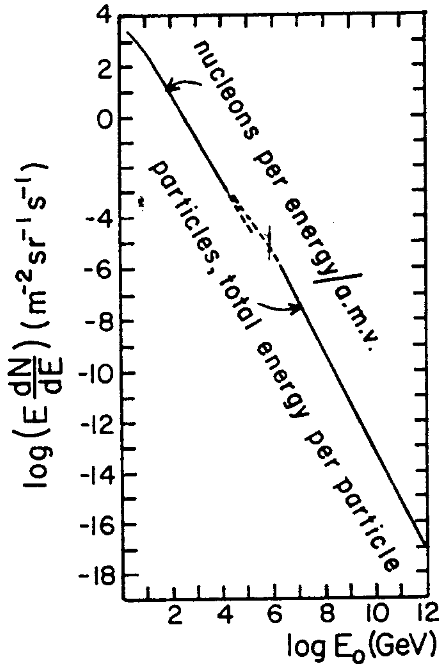

Figure 1.1: The cosmic ray energy spectrum. For the high energy part of the spectrum the curve represents the number of particles at a given total energy per nucleus. The low-energy part of the spectrum shows the number of nucleons as a function of energy per nucleon.

In contrast, the University of Chicago detector on Spacelab (fig. 1.3) is one of the largest ever flown, so it is sensitive to cosmic rays of much higher energy. It was carried on board the Challenger spacecraft from July 29 to August 6, 1985, during which time it had an effective exposure of 94 hours. It has an aperture of approximately 2 m^2sr. From fig. 1.1 we can therefore estimate that during this exposure nearly 100 000 particles with energies within a factor of two of 1 TeV passed through the detector. The spectrum is so steep, however, that only about 50 particles above 100 TeV would have passed through the detector during the flight, and most of these would likely have had charge below the charge threshold of the detector, which was designed for heavy nuclei. An earlier Soviet spacecraft experiment (Grigorov et al., 1970), as well as the Japanese-American balloon experiment (Burnett et al., 1983) also probed similar energies. For the time be-

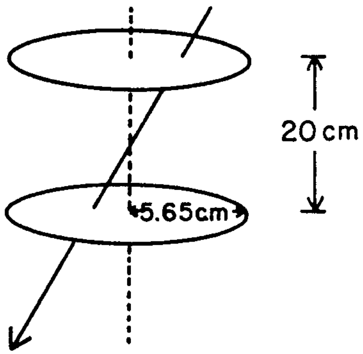

Figure 1.2: Schematic diagram of a small cosmic ray telescope.

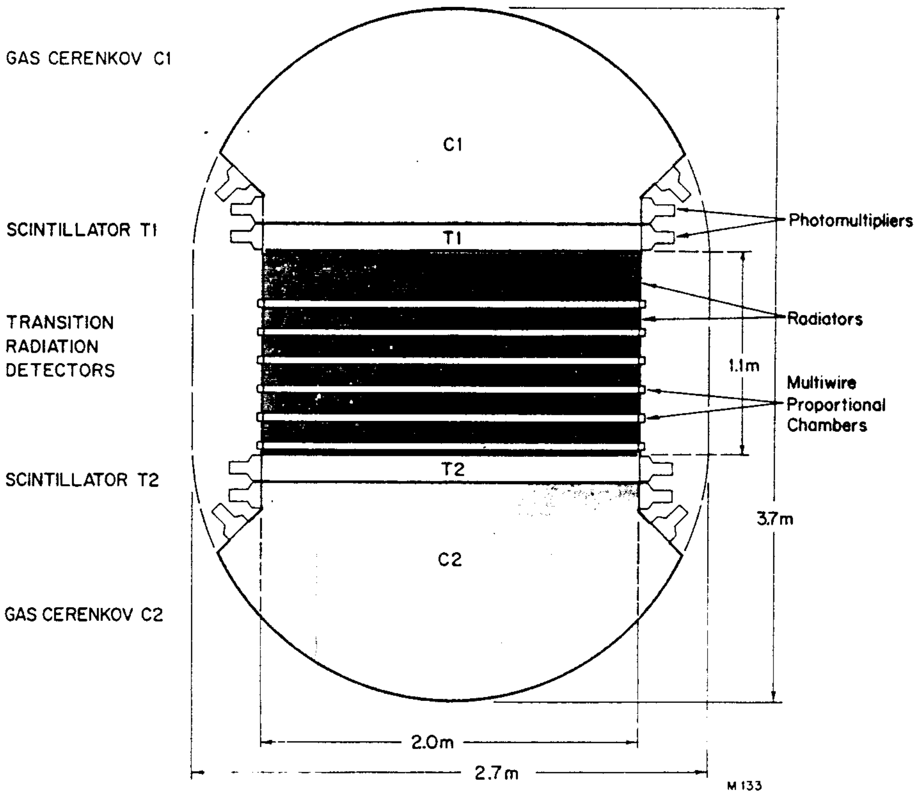

Figure 1.3: Cross sectional view of the University of Chicago Cosmic Ray Nucleus Experiment on Spacelab (Grunsfeld et al., 1988). (Reprinted with permission from *The Astophysical Journal.*)

ing, because of the limited exposure available, 100 TeV is about the highest energy at which cosmic rays can be studied directly with detectors at the top of the atmosphere.

> **Problem:** The instrument in fig. 1.2 consists of two circular detectors in coincidence, each with 100 cm^2 area and separated by 20 cm. The maximum angle that will trigger the detector depends on the point of intersection of the trajectory with the first detector as well as its direction. Show that the acceptance of this detector is $\approx 22\,\text{cm}^2$ sr for downward-going particles.

To study cosmic rays with higher energies requires detectors with larger areas exposed for longer periods of time. At present the only way to overcome the problem of low flux at high energy is to build a detector on the surface of the Earth. Such detectors, called air shower arrays, can have areas measured in square kilometers and exposure times limited only by the patience of the experimenters and the generosity of the funding agencies. Ground-based detectors cannot detect the primary cosmic rays directly, but only the remnants of the atmospheric cascades of particles initiated by the incident particle. They therefore give only limited, indirect information about the nature of the primaries. Despite the obvious difficulty of the subject, the ultra-high energies involved continue to stimulate interest in it. A knowledge of particle physics is essential in order to interpret the cascades and infer something about the primaries. We will return to this subject in the final section of the book. For the remainder of this chapter we focus on the bulk of the cosmic rays at lower energies.

1.4 Composition

The relative abundances of cosmic rays are compared with abundances of elements in the solar system in fig. 1.4. The symbols in fig. 1.4 have the following meanings: Solid circles: low energy data, 70 - 280 MeV/A; open circles: high energy data, 1000 - 2000 MeV/A. Solar system abundances are shown by open diamonds. Both solar system and cosmic ray abundances show the odd even effect, with the more tightly bound, even Z nuclei being more abundant. There are, however, two striking differences between the two compositions.

First, nuclei with $Z > 1$ are much more abundant relative to protons in the cosmic rays than they are in solar system material. This is not really understood, but it could have something to do with the fact that hydrogen is relatively hard to ionize for injection into the acceleration process, or it could reflect a genuine difference in composition at the source.

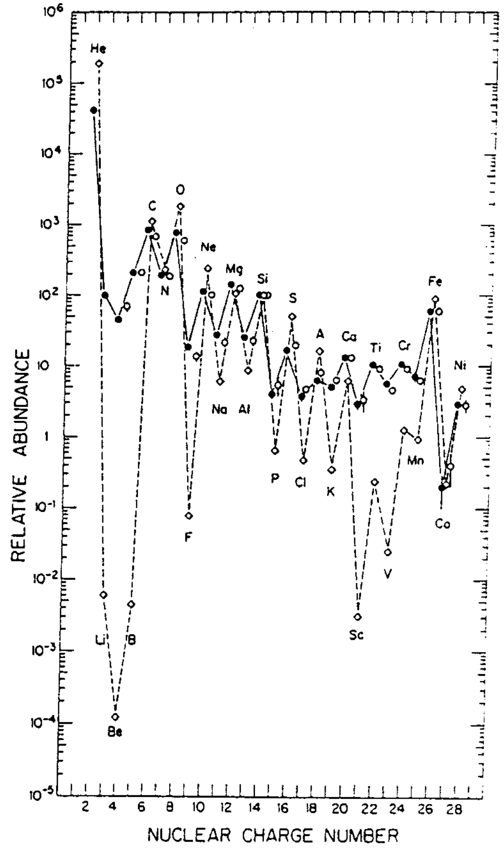

Figure 1.4: The cosmic ray elemental abundances (He-Ni) measured at Earth compared to the solar system abundances, all relative to silicon (from Simpson, 1983). (Reproduced with permission, from the *Annual Review of Nuclear and Particle Science,* Vol. 33, © 1983 by Annual Reviews Inc.)

The second difference *is* well understood and is an important tool for understanding propagation and confinement of cosmic rays in the galaxy. The two groups of elements Li, Be, B and Sc, Ti, V, Cr, Mn are many orders of magnitude more abundant in the cosmic radiation than in solar system material. These elements are essentially absent as end products of stellar nucleosynthesis. They are nevertheless present in the cosmic radiation as spallation products of the abundant nuclei of carbon and oxygen (Li,Be,B) and of iron (Sc,Ti,V,Cr,Mn). They are produced by collisions of cosmic rays in the interstellar medium (ISM). From a knowledge of the cross sections for spallation, one can learn something about the amount of matter traversed by cosmic rays between production and observation. (Note the implication that secondaries such as photons, neutrinos and antiprotons should also be produced at a certain rate as cosmic rays propagate through the ISM. We shall return to this subject in chapter 10.) For the bulk of the cosmic rays the mean amount of matter traversed is of order $X = 5$ to 10 g/cm^2. The density ρ_N in the disk of the galaxy is of order one proton per cm^3, so this thickness of material corresponds to a distance of

$$l = X/(m_p \rho_N) = 3 \times 10^{24}\,\mathrm{cm} \approx 1000\,\mathrm{kpc}.$$

Since the cosmic rays may spend some time in the more diffuse galactic halo, this is a lower limit to the distance travelled. In any case, $l \gg d \approx 0.1$ kpc, the half-thickness of the disk of the galaxy. This implies that cosmic ray confinement is a diffusive process in which the particles rattle around for a long time before escaping into intergalactic space.

1.5 Energy spectra

The spectra for several elements of the cosmic rays are shown in fig. 1.5. The proportions of the major components (with the exception of iron) are relatively constant with energy (see table 1.1). They are well described by an inverse power law in energy, with differential flux given by

$$\frac{\mathrm{d}N}{\mathrm{d}E} \propto E^{-(\gamma+1)}.$$

The spectrum continues up to $E \sim 10^6$ GeV with $\gamma \approx 1.7$ Above this energy the spectrum steepens to $\gamma \sim 2.0$.

An important point to note, however, is that the boron spectrum is steeper than the spectra of its parent oxygen and carbon nuclei. In fact, all secondary nuclei (i.e. those produced as spallation products of abundant species) have significantly steeper spectra than the primary nuclei. The secondary to primary ratios decrease as energy increases. This tells us that the higher energy cosmic rays diffuse out of the galaxy faster.

Cosmic ray composition relative to protons in the 10 - 100 GeV range is shown in table 1.1. The table shows the fraction of nuclei relative to protons in four different ways. Fluxes are normally quoted as in column (1): particles per GeV per nucleon. If we define the fractions in column (1) as F_A (e.g. $F_4 = 0.036$ for helium nuclei), then the fractions in the other columns are related to those in column (1) by $2^\gamma F_A$ for column (2); $A\,F_A$ for column (3) and $A^\gamma F_A$ for column (4). These relations hold for a power law spectrum with $N_A(> E) \propto E^{-\gamma}$. Note that these relations are for *integral* fluxes, i.e., for the number of particles above the threshold energy E. The designations

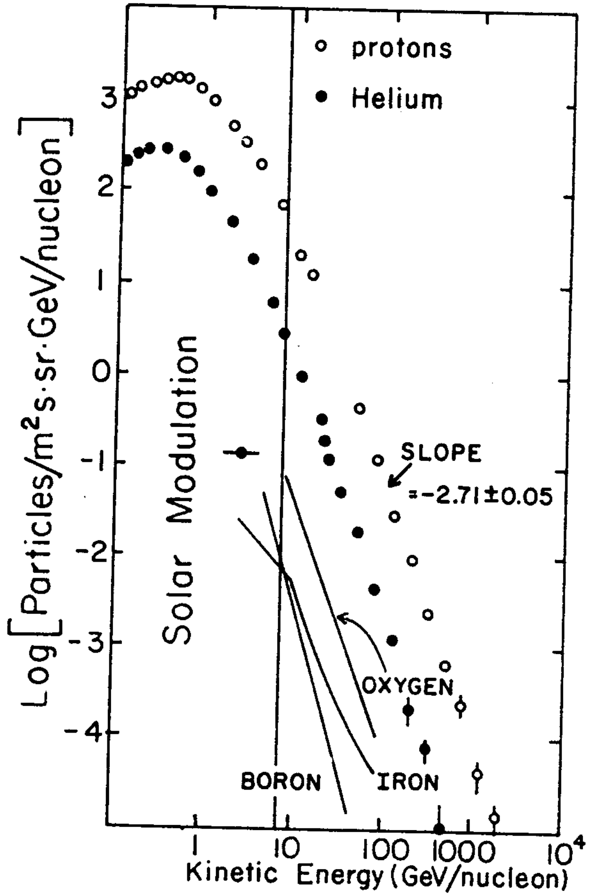

Figure 1.5: Energy spectra of several components of the cosmic rays, compiled from the review of Ormes and Freier (1978). For energies to the left of the vertical line the flux varies significantly during the solar cycle, an effect called "solar modulation".

M (medium), H (heavy) and VH (very heavy) are standard cosmic ray nomenclature for these groups of nuclei. Light nuclei (denoted L for $Z = 3$ to 5) are omitted from the table because of their extremely low abundance.

Table 1.1: Fraction of nuclei relative to protons.

Mass group	$< A >$	(1) Particles ($> E/A$)	(2) Particles ($> R$)	(3) Nucleons ($> E/A$)	(4) Particles ($> E$/nucleus)
p	1	1	1	1	1
α	4	0.036	0.12	0.14	0.38
M ($Z = 6$ to 9)	14	0.0025	0.0083	0.035	0.22
H ($Z = 10$ to 20)	24	0.0007	0.0023	0.017	0.15
VH ($Z = 21$ to 30)	56	0.0004	0.0013	0.022	0.40

Each of the columns is relevant for certain situations. Column (1) (nuclei per energy per nucleon) is appropriate for propagation calculations because energy per nucleon remains essentially unchanged in spallation processes. Rigidity, $R \equiv pc/Ze$, is appropriate whenever the gyroradius is the relevant consideration, as for acceleration or for propagation through the geomagnetic field. From column (2), for example, it follows that at a given location, for every 1000 protons that get through the geomagnetic field to reach a detector at the top of the atmosphere, there will be 120 alpha-particles, 8 M-group nuclei, 2 H-group nuclei and one VH nucleus. Rigidity has the dimensions of energy over charge. Units of GeV per charge are denoted GV. The number of nucleons per GeV per nucleon (column (3)) is the relevant quantity in calculating secondary fluxes of particles such as muons, antiprotons, pions, etc., because these are essentially produced in nucleon nucleon encounters, even when the nucleons are bound in nuclei (though there may be some nuclear effects). Finally, total energy per nucleus is relevant for air showers because the size of the shower reflects the total energy of the incident particle. Note that when the cosmic rays are classified by total energy per nucleus, less than half are protons!

1.6 Energy density of cosmic rays

The mechanism for cosmic ray confinement is coupling between the charged particles and the tangled magnetic field lines that thread the interstellar medium. That this is plausible can be seen by comparing the energy density of cosmic rays to the energy in magnetic fields. The relation between the energy spectrum and energy density follows from the relation between flux and number density of cosmic rays, $\rho_{\rm CR}$:

$$\mathrm{Flux}\left(\frac{\text{particles}}{\text{cm}^2\,\text{s}\,\text{sr}}\right) = \frac{\rho_{\rm CR}\beta c}{4\pi}. \qquad (1.1)$$

The energy density, ρ_E, is therefore

$$\rho_E = 4\pi \int E \frac{\mathrm{d}N}{\mathrm{d}E}\frac{\mathrm{d}E}{\beta c} = \int \frac{4\pi E^2}{\beta c}\frac{\mathrm{d}N}{\mathrm{d}E}\,\mathrm{d}\ln E. \qquad (1.2)$$

The purpose of rewriting the integral as I have done in the second step of (1.2) is to make the area under a semilogarithmic plot of the integrand proportional to the integral. This is a device that is useful in the presence of a steeply falling spectrum that spans several decades of energy. It also reflects the correct way to do an integral in this situation.

Note that we are interested here in the cosmic ray spectrum in the galaxy, which, because of the sun's influence, is not the same as that observed at the top of the atmosphere. The sun emits a plasma wind with an embedded magnetic field that tends to exclude low energy galactic cosmic rays from the heliosphere. The heliosphere is the region in which the background plasma is dominated by this solar wind. Its extent is not well known but is much farther out than the orbit of Earth. The solar wind intensity varies with the 11 year solar cycle, and the observed cosmic ray flux at Earth is inversely correlated with solar activity. The open circles in fig. 1.5 show the measured flux of protons at Earth at a time of minimum solar activity (for example, *circa* 1977). At a period of high solar activity (for example in 1982), the flux below a GeV can be suppressed by as much as an order of magnitude. The spectrum in the local interstellar (LIS) medium can be inferred (with rather large uncertainties) from the theory of solar modulation fitted to the observations at different epochs of the solar cycle (Evenson, 1988).

Figure 6 shows the integrand of the energy density integral (1.2) for proton spectra at periods of minimum and maximum solar activity

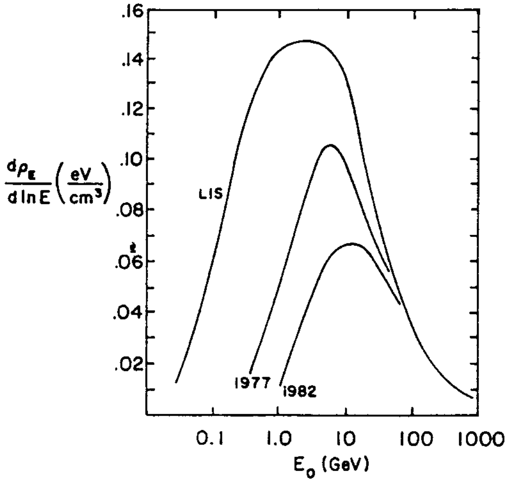

Figure 1.6: Distribution of the energy density in cosmic rays (integrand of equation (1.2)).

as measured at Earth, as well as that inferred for the local interstellar medium. Note that half or more of the energy carried by the cosmic rays is not directly measurable at Earth. The area under the LIS proton curve is 0.83 eV/cm^3. Helium and heavier nuclei together contribute another $\sim$ 0.27 eV/cm^3. This is to be compared with a magnetic field energy density $\epsilon \approx$ 0.25 eV/cm^3 in a typical galactic field of $B \approx 3\ \mu$Gauss. The two energy densities are comparable. Consequently it is not surprising that the interaction between cosmic rays and magnetic fields in the galaxy is mutual, with field configurations being influenced by cosmic rays and *vice versa*.

Chapter 2

Particle physics

2.1 Beta-decay, a helpful example

A short history of β-decay makes an efficient introduction to the modern understanding of particle physics at a level that is appropriate as background for this book. In nuclear β-decay a nucleus of mass number $A = Z + N$ with Z protons and N neutrons undergoes the transition

$$A(Z,N) \rightarrow A'(Z+1, N-1) + e^- + \overline{\nu}_e. \qquad (2.1)$$

At a more elementary level, we understand this as a transition of a single nucleon inside the nucleus:

$$n \rightarrow p + e^- + \overline{\nu}_e, \qquad (2.2)$$

together with an appropriate rearrangement of the residual nucleus.

Protons and neutrons themselves have structure, so that a still more fundamental description of β-decay is possible. In the quark model a proton consists of three valence quarks - two up quarks, u, and one down quark, d - together with an indeterminate sea of gluons and quark-antiquark pairs. A list of quark flavors and other properties is given in table 2.1. Quark "flavors" come in pairs known as generations, though the top quark has yet to be discovered experimentally. Since quarks apparently do not exist as free particles, their masses are ill-defined. They can be taken roughly as half the mass of the corresponding $q\overline{q}$ ("quarkonium") state, e.g. the ϕ-meson for $s\overline{s}$ and the J/ψ-meson for $c\overline{c}$. Quarks have a baryon-number of one-third, so that baryons have the valence quark structure qqq and mesons $q\overline{q}$. At the quark level, therefore, the β-decay process (2.2) is really an

Table 2.1: Quark properties and nomenclature

	Charge	Mass(GeV)
u (up)	+2/3	light
d (down)	-1/3	light
c (charm)	+2/3	1.6
s (strange)	-1/3	0.5
[t (top)]	+2/3	?
b (bottom)	-1/3	5

elementary transition

$$d \rightarrow u + e^- + \overline{\nu}_e \tag{2.3}$$

together with the implied change of state of the nucleon that contains the quarks. Prevailing opinion is that, in a profound way, this is the most fundamental level at which a description of β-decay is possible: Fractionally charged quarks apparently cannot exist as free particles, but only as constituents of hadrons, so it is not necessary to postulate another level of structure. Experimentally, quarks are structureless at least to the level of 10^{-15} cm, two orders of magnitude smaller than the characteristic size of hadrons. In the Standard Model they are truly pointlike and elementary in the same sense as leptons such as electrons and muons.

In fact, the Feynman diagram that describes β-decay of a quark is the same as that for β-decay of a muon (fig. 2.1). Of course there are substantial differences in decay rates and distribution of the energies of the secondary particles because the quarks are bound in the nucleon - just as there are differences between nuclear β-decay and decay of a free neutron due to nuclear binding. Nevertheless, in particular cases of hadrons containing heavy quarks such as charm or bottom (so that the quark mass dominates the mass of the hadron that contains it), even these differences are minor. The decay of the D^+ charmed meson, for example, can be understood in the spectator quark model as shown in fig. 2.2. Here the formulas for decay rate and energy distributions (Cabibbo, Corbo and Maiani, 1979) are essentially the same

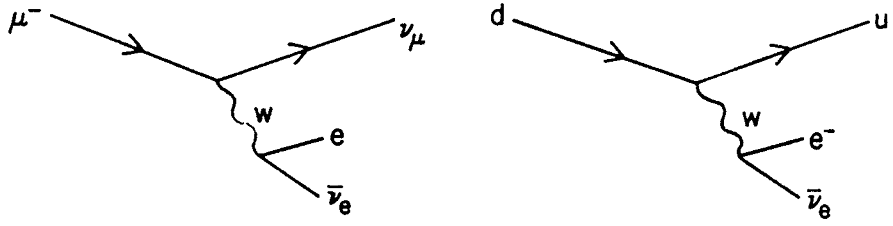

Figure 2.1: (a) Muon decay. (b) β-decay of d-quark.

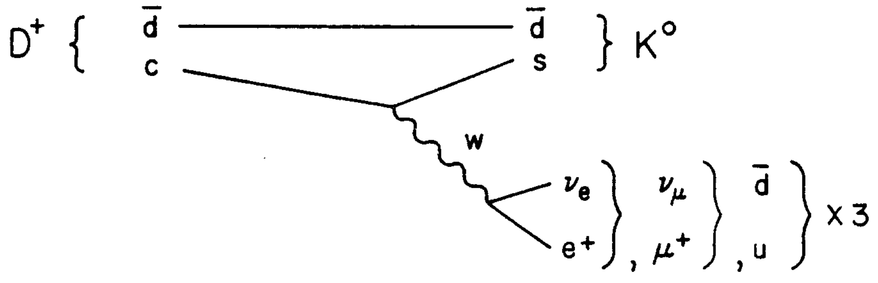

Figure 2.2: Decay of the charged D^+-meson in the spectator quark model (the $\overline{d}$ is the "spectator").

as for muon decay provided the muon mass is replaced by the mass of the charmed quark, which is approximately equal to the mass of the charmed meson. The possible leptonic decay products are grouped into pairs called "weak isodoublets," which are related to the quark generations (e to u and d and μ to c and s). Because quarks come in three colors, a decay to $u\overline{d}$ is three times as probable as a decay to one of the leptonic channels. Decays to heavier flavors (e.g. to $\nu_\tau + \tau^+$) are forbidden by energy conservation since the mass of the D is too small.

2.2 Unity of forces among elementary particles

We shall have occasion later to use the formulas for the distribution of energies of the decay products in the β-decay of a pointlike particle, for example, to calculate the flux of electron neutrinos in the atmosphere, which come in large part from decay of muons (fig 2.1a). In the meantime, these examples of β-decay serve to illustrate the paradigm of modern particle physics, which is: to explain processes in terms of elementary transitions among fermions together with production or exchange of vector bosons. In the case of β-decay, the vector particle is (a very virtual) massive W-particle - the famous intermediate weak vector boson that was discovered with the $\overline{p}p$-collider at CERN in 1983. Within the standard unified theory of weak and electromagnetic interactions, it is a close relative of the most familiar vector gauge boson of all, the photon. Within this unified theory, weak processes like those shown in figs. 2.1 and 2.2 are related to electromagnetic processes, some of which are illustrated in fig. 2.3.

The weak and electromagnetic forces are now understood in a unified way within the "standard" theory of Weinberg, Salam and Glashow. The phenomenology of cosmic ray cascades also reflects in an essential way processes governed by the strong force. We cannot begin to understand cosmic ray processes without taking account of the production of pions and other hadrons (i.e. strongly interacting particles) in high energy collisions of protons, pions, etc. with target particles such as nitrogen nuclei in the atmosphere or hydrogen nuclei in the ISM.

The fundamental theory of strong interactions is quantum chromodynamics (QCD). QCD is a nonabelian analog of quantum electrodynamics (QED) in which quarks couple to 8 massless vector "gluons" via a generalized charge called color. The theory is nonabelian because the gluons carry the color charge (unlike the electrically neutral photon of QED). Quarks are fermions that come in three colors, and all hadrons are colorless bound states of quarks. Mesons are $q\overline{q}$ pairs and baryons are color-neutral bound states of three quarks antisymmetrized in the color indices. (This solves the spin-statistics problem for baryons that would exist in the quark model without color. For example, the Ω^- is a state of three identical strange quarks that would be symmetric were it not for the antisymmetry of the color quantum numbers.) The valence-quark content of some familiar hadrons is shown in table 2.2. A difficulty with QCD is that at low momentum transfer the coupling constant is large, and perturbation theory does not give adequate results except for particular configurations that make up only a small part of the cross section. For calculation of total hadronic cross sections and distributions of produced particles it is necessary to rely on accelerator data together with phenomenological models that are motivated by the quark model described above, but which are not derived from the underlying theory of QCD.

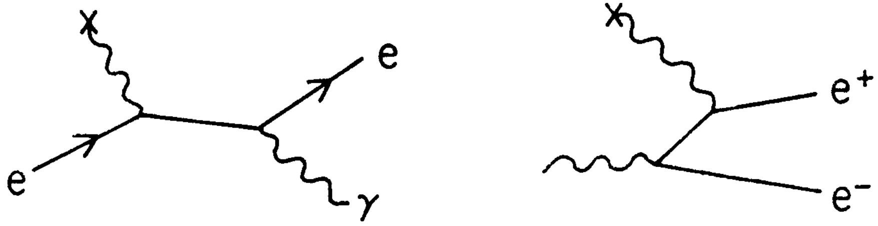

Figure 2.3: Some Quantum Electro-Dynamical (QED) processes important for cascade theory: bremsstrahlung and pair production. In each case the "X" indicates the action of the nuclear field that causes the transition.

2.3 Dynamical evidence for pointlike quarks

Before discussing models of particle production via the strong interaction, it will be useful to go back and say a word about the experiments

Table 2.2: Valence quark content of some hadrons.

Particles	Quark content
p	uud
$\overline{p}$	$\overline{u}\overline{u}\overline{d}$
n	udd
Λ	uds
Ω^-	sss
π^+	$u\overline{d}$
π^-	$\overline{u}d$
π^0	$\frac{1}{\sqrt{2}}(u\overline{u}+d\overline{d})$
K^+	$u\overline{s}$
K^0	$d\overline{s}$
$\overline{K}^0$	$\overline{d}s$
K^-	$\overline{u}s$
D^-	$\overline{c}d$
ϕ	$\approx s\overline{s}$
ψ	$c\overline{c}$

that indicated that hadrons are made of pointlike constituent quarks. They are essentially a relativistic generalization of Rutherford's discovery of the atomic nucleus (see fig. 2.4). Rutherford irradiated gold foil with α-particles and studied the angular distribution of the scattered particles. The distribution had a characteristic tail at large scattering angles indicating that the positive charge is concentrated in a pointlike nucleus rather than spread out over the full dimensions of the atom. The angular distribution of scattered particles was described by Coulomb scattering in the electric field of a point charge even though the classical distance of closest approach was several orders of magnitude smaller than the size of the atom. In other words, the α-particles penetrated deep inside the atom and still saw all the positive charge concentrated in a small volume. A measure of the size of the nucleus is then given by noting the projectile energy at which deviation from Coulomb scattering from a point charge first occurs.

A relativistic analog of Rutherford's experiment is the scattering of energetic electrons from protons, as carried out at the Stanford Linear Accelerator Center in the late 1960's. The angular distribution of the electrons was characteristic of scattering from pointlike concentrations of charge within the proton rather than from a charge distribution spread over the 10^{-13} cm scale of the proton. (An intermediate analog is electron-nucleus scattering.)

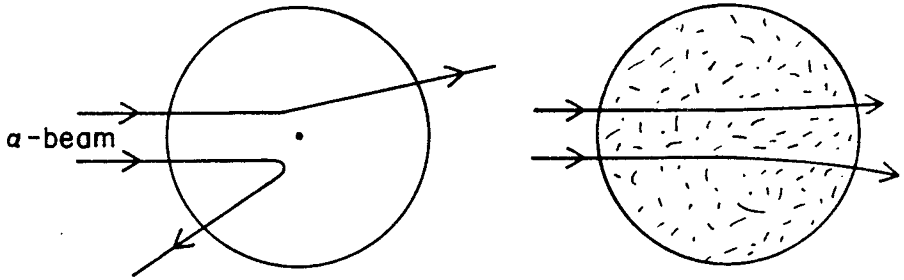

Figure 2.4: The Rutherford experiment. The first view shows α-particle scattering from an atom with a pointlike nucleus; the second shows the process as it would be if the positive charge were distributed throughout the atom.

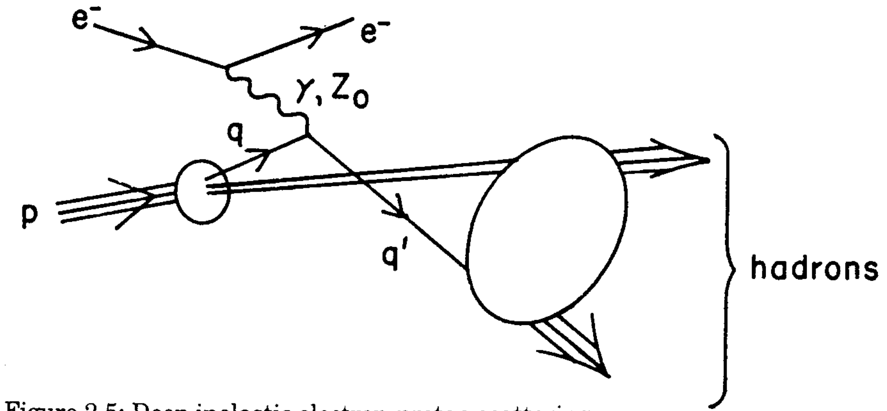

Figure 2.5: Deep inelastic electron-proton scattering.

Subsequent experiments have verified the quark picture in considerable detail, as indicated in figs. 2.5 - 2.7. The examples of deep inelastic lepton nucleon scattering shown in figs. 2.5 and 2.6 are structurally identical. The charged current neutrino process, which involves exchange of a virtual charged W to create a muon, can only proceed by the weak interaction. The amplitude contains a factor α/M_W^2 (for neutrino energy small compared to the mass of the W), so the process is suppressed by some 8 orders of magnitude relative to

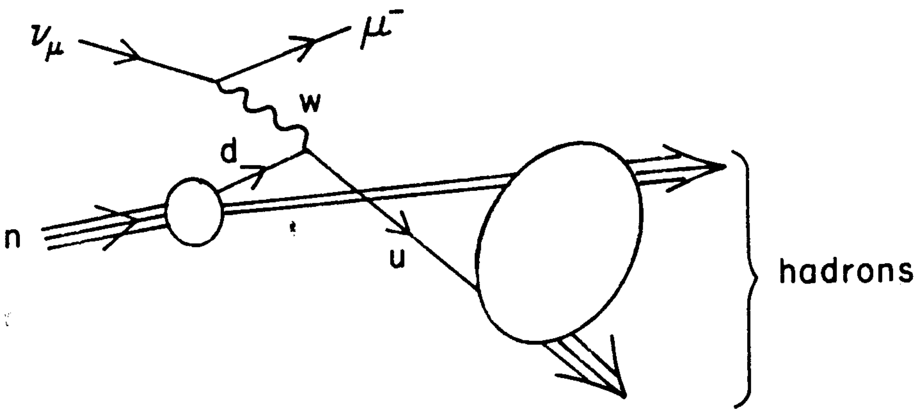

Figure 2.6: Deep inelastic, charged current neutrino-neutron scattering.

electron scattering. For the same reason, the dominant contribution to the electron scattering process shown in fig. 2.5 is exchange of the massless photon. The amplitude for exchange of the Z_0 is suppressed by $\approx 1/M_Z^2$.

A particularly clean illustration of the dynamical quark picture is the measurement of the ratio $R = (e^+e^- \rightarrow \text{hadrons})/(e^+e^- \rightarrow \mu^+\mu^-)$ (fig. 2.7). Here everything cancels out except the number and charges of the quarks relative to the muons. There is a factor $\alpha \equiv e^2/\hbar c$ in the cross section for annihilation to muons due to the coupling of the photon to the $\mu^+\mu^-$ pair. The corresponding coupling in the annihilation to hadrons is $(\frac{2}{3})^2/\hbar c = \frac{4}{9}\alpha$ for a quark with charge $\frac{2}{3}e$ and $\frac{1}{9}\alpha$ for a quark with charge $\frac{1}{3}e$. Thus for

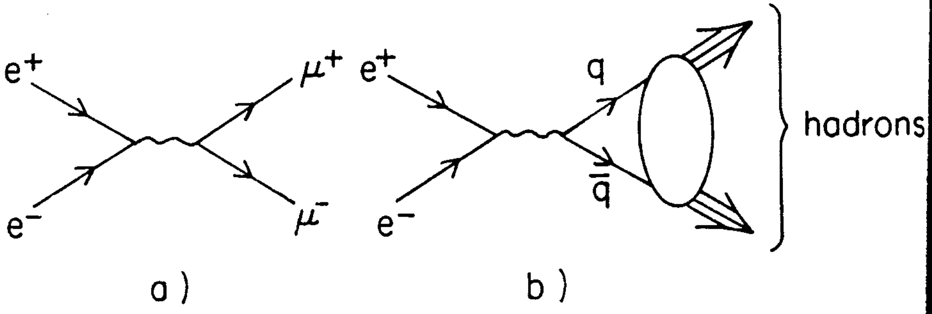

Figure 2.7: Electron-positron annihilation.

$$1 \text{ GeV} \leq E_{\text{CM}} \leq 3.6 \text{ GeV}, \quad R \approx 3\left(\tfrac{4}{9} + \tfrac{1}{9} + \tfrac{1}{9}\right) = 2,$$

and for

$$3.7 \text{ GeV} \leq E_{\text{CM}} \leq 10 \text{ GeV}, \quad R \approx 3\left(\tfrac{4}{9} + \tfrac{1}{9} + \tfrac{1}{9} + \tfrac{4}{9}\right) = \tfrac{10}{3}.$$

In the first energy region u, d, and s are active and in the second u, d, s and c. The factor 3 comes from the sum over three quark colors.

2.4 Phenomenology of strong interactions

The feature that makes deep inelastic lepton scattering and e^+e^- annihilation tractable is that these processes proceed via the electromagnetic and weak interactions. These are characterized by coupling strengths α and α/M_W^2 that are small, so that perturbation theory makes sense and the lowest order perturbation calculation gives a good estimate of the cross section. Even so it is necessary to resort to phenomenology to describe the "hadronization" of the final state quarks as indicated by the blobs in figs. 2.5 - 2.7.

When the initial particles are both hadrons, so that the whole process is governed by the strong force, the situation becomes still more complicated, as illustrated in fig. 2.8. The diagram of fig. 2.8, complicated as it is, applies only to that relatively small part of the proton-proton cross section for which transverse momentum $(p_T) \gg 1$ GeV. Then scattered quarks get separated by more than a fermi before multiple interactions with the spectator quarks can occur. This is the regime in which the "impulse approximation" applies. In this approximation the cross section can be written as a convolution of structure functions, elementary parton-parton cross sections and fragmentation functions. The structure functions, $F_{ij}(x)$, give the probability of finding a particular kind of constituent, i with a certain fraction, x, of the momentum of the incident hadron, j. Fragmentation functions, conversely, give the probabilities for a hadron to emerge from a parton as a function of the fraction of the parton momentum carried by the hadron. Structure functions are represented by the initial blobs in figs. 2.5 - 2.6 and 2.8. The pictures also indicate how the structure functions and fragmentation functions can be measured.

The elementary cross sections here are essentially the same as for Rutherford scattering because they involve exchange of a massless vector boson, the gluon. The elementary processes illustrated in fig. 2.8

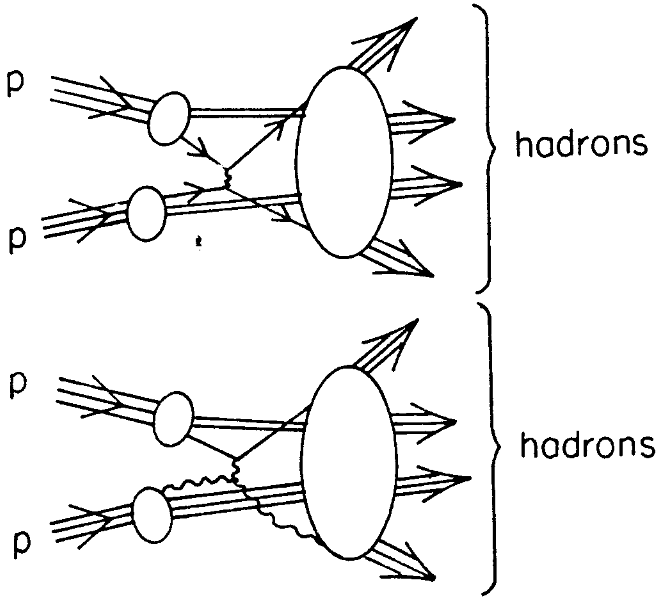

Figure 2.8: Examples of 'hard scattering' between protons. Wavy lines indicate vector bosons (e.g. gluons, photons or *W*-particles) and the single straight lines represent elementary fermions (e.g. quarks, electrons, etc.). Gluons and quarks dominate hadronic interactions.

are $q\,q \rightarrow q\,q$ and $q\,g \rightarrow q\,g$ (where $q =$ quark and $g =$ gluon). Gluon-gluon scattering is also an important elementary process. All should have the basic Rutherford form at small angle,

$$\frac{\mathrm{d}\hat{\sigma}}{\mathrm{d}\cos\theta} \propto \frac{1}{\sin^4 \frac{1}{2}\theta}.$$

This has actually been measured directly at the CERN $\bar{p}p$-collider in calorimeter experiments (Arnison et al., 1984; Bagnaia et al., 1984) that measure whole jets of particles. These experiments have verified the underlying Rutherford form for the elementary cross section, $\hat{\sigma}$. At the same time they have measured the structure functions, $F(x)$, and find values consistent with those determined in a more straightforward way from deep inelastic lepton scattering (figs. 2.5 and 2.6).

As mentioned earlier, jet experiments have a simple interpretation only at relatively large transverse momentum. Up to fairly high energies (hundreds of TeV) the bulk of the proton-proton inelastic cross section is due instead to processes with small transverse momentum. In this case multiple scatterings among the constituents are important as illustrated in fig. 2.9. Here QCD calculations become impractical because of the large coupling constants, which prevent the use of perturbation theory. Then one is forced to fall back on purely phenomenological models, albeit motivated by the ideas of the constituent quark model.

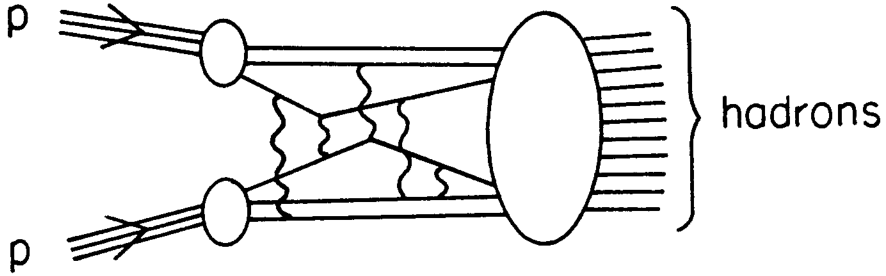

Figure 2.9: Example of a QCD contribution to the ordinary *pp* inelastic collisions at high energy. All such diagrams contribute comparably.

For these typical hadronic processes, the produced particles reflect the motions of the constituents. Since multiple interactions are occurring during a collision, it is not surprising that the transverse momentum distribution of the emerging particles is approximately a Gaussian, characteristic of a two-dimensional transverse random walk. The characteristic transverse momentum is related by the uncertainty principle to the size of the hadron within which the quarks are confined: one fermi corresponds to a few hundred MeV.

The distributions of longitudinal momentum of the produced particles reflect the momentum distributions of the constituents inside the incident particles. They tend to scale with the incident energy. This is known as the hypothesis of limiting fragmentation (HLF) - see Yen (1974).

Particle production can be completely characterized by a series of n-particle inclusive cross sections, σ_0, σ_1, σ_2, $\ldots$, σ_n. The first in the series, labelled here by σ_0, is the total cross section. In general,

$$\sigma_n = E_1 E_2 \cdots E_n \frac{\mathrm{d}\sigma}{\mathrm{d}^3p_1 \mathrm{d}^3p_2 \cdots \mathrm{d}^3p_n} \tag{2.4}$$

is the multiply differential, invariant cross section for finding one produced particle in the invariant phase space d^3p_1/E_1, another in

d^3p_2/E_2, and so on up to n, regardless of what else is produced. In practice σ_0 and σ_1 are generally sufficient for cosmic ray cascade calculations except in particular cases where two-particle correlations are important. An example of this is the process $p\,p \to \Lambda\,K\,N$ +anything. In this case, conservation of strangeness requires production of a K^+ (or other particle with strangeness +1) in conjunction with the Λ, which has strangeness -1. The momenta of these two particles will be correlated as well.

The cross sections are of course different for different particle types. The single particle inclusive cross section for $a + b \to c$ + anything is labelled

$$\sigma_1 = E_c \frac{d^3\sigma_{ab}}{d^3p_c}(\sqrt{s}, p_\parallel^*, p_T) \equiv f_{ac}^{(b)}(\sqrt{s}, p_\parallel^*, p_T), \tag{2.5}$$

where $\sqrt{s}$ is the total center of mass energy of the initial system $a+b$:

$$s_{ab} = (p_a^\mu + p_b^\mu)^2 = (E_a^* + E_b^*)^2 = m_a^2 + m_b^2 + 2m_bE_a. \tag{2.6}$$

Here E_a is the total energy (including rest mass energy) of particle a in the coordinate system in which the target particle b is at rest. The asterisk denotes the center of momentum system (CM) in which $\vec{p}_a^* + \vec{p}_b^* = 0$. In (2.6) I have taken advantage of the Lorentz invariance of the scalar product of two 4-vectors (p_μ) to obtain the relation between CM and laboratory energy. Note that at high energy $\sqrt{s} \propto \sqrt{E_{Lab}}$. Recall also that d^3p/E is a Lorentz invariant so that $E_c^* d\sigma/d^3p_c^* = E_c d\sigma/d^3p_c$.

The mathematical expression of HLF is

$$f_{ac}^{(b)}(\sqrt{s}, p_\parallel^*, p_T) \xrightarrow{\sqrt{s}\to\infty} f_{ac}^{(b)}(x^*, p_T), \tag{2.7}$$

where $x^* \equiv 2\,p_\parallel^*/\sqrt{s}$. The variable x^* is limited to $-1 < x^* < 1$. The condition that x^* remain fixed as $s \to \infty$ ensures that particle c is a fragment of the beam particle or of the target particle (depending on the sign of $p_\parallel^*$.) These are called respectively the beam and target fragmentation regions. For $p_\parallel^* > 0$ there is no dependence on the target b in the scaling limit, and the distribution is similarly independent of the nature of the projectile when $p_\parallel^* < 0$. The kinematic region $x \sim 0$ as $s \to \infty$ is called the central region. A stronger version of the scaling hypothesis, due to Feynman (1969), is (2.7) with x^* fixed at any value *including* 0. It implies $f_{ac}^{(b)}(0, p_T)$ = constant and $< n_{ac}^{(b)} > \propto A \ln s + B$, both of which are violated at high energy.

Table 2.3 shows the definition of x^* and some other scaling variables in use in the literature. By using a Lorentz transformation from the laboratory to the CM system, one finds the relation between x^* and x_L. For high energy interactions it is

$$x^* \cong x_L - \frac{\mu_T^2}{2\,m\,E} + O\left[\left(\frac{\mu_T}{E}\right)^2\right]. \tag{2.8}$$

Table 2.3: Scaling variables and definitions

Variable	Definition	Description
x^*	$\frac{p_\parallel^*}{p_\parallel^*(max)} \cong \frac{2p_\parallel^*}{\sqrt{s}}$	Feynman x
x_R	$\frac{E^*}{E_{max}^*} \cong 2\frac{E^*}{\sqrt{s}}$	radial x
μ_T	$\sqrt{p_T^2 + m_c^2}$	transverse mass
$x_{Lab} \equiv x_L$	$E_{Lab}/E_{Lab}(max)$	$\cong E_{Lab}/E_{beam}$
y	$E^* = \mu_T \cosh y$	rapidity
η	$-\ln\tan\frac{1}{2}\theta$	pseudorapidity[a]

[a] Used as a substitute for rapidity when only angle (but not momentum) can be measured.

A typical experiment to measure a single particle inclusive cross section is illustrated in fig. 2.10. It consists of a spectrometer with acceptance d^3p to count the rate of particles of type c that scatter into this momentum bin. For a stationary thin target experiment (as opposed to a colliding beam experiment)

$$d\sigma_{ac}^{(b)} = \frac{\text{rate of } c\text{-particles into } d^3p}{(\text{beam current of } a\text{-particles}) \times (\text{no. targets/cm}^2)}. \tag{2.9}$$

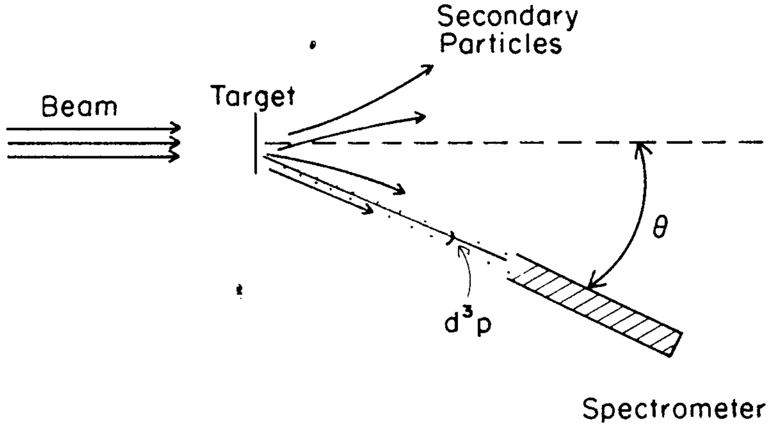

Figure 2.10: Schematic illustration of a spectrometer to measure the single particle inclusive cross section.

By moving the spectrometer around all angles and tuning it to all momenta, all produced particles will be counted. Thus

$$\int d\sigma_1 = \sigma_a^{(b)} < n_{ac}^{(b)} > . \tag{2.10}$$

The total cross section for scattering of a on b is $\sigma_a^{(b)}$, and $< n_{ac}^{(b)} >$ is the mean multiplicity of c-particles produced per a - b interaction.

As a preview of the application of these ideas to cosmic ray cascades, it is interesting to consider the classic problem of the ratio of positive to negative muons in the atmosphere. The measured value of ≈ 1.25 is nearly independent of energy. It reflects the excess of protons over neutrons in the incident cosmic rays. But if this were all, the charge ratio would go to zero at high energy because the multiplicity per collision of produced pions (the parents of the muons) becomes very large so that one extra charge becomes negligible. But this is not the whole story. Because of the steepness of the cosmic ray energy spectrum, muons of a given energy come from relatively fast secondaries; i.e. they reflect the projectile fragmentation region. Since the fragmentation region of the proton reflects the momentum distribution of its quarks, and since it has two u-quarks of charge $+2/3$ each and only one d-quark (charge $-1/3$) positive pions are favored in the fragmentation region. This causes an excess of positive over negative muons at all energies. The energy independence of the ratio also reflects the invariance with energy of the inclusive distributions, i.e., scaling in the fragmentation region or HLF.

Chapter 3

Cascade equations

The next six chapters are mostly about cosmic ray cascades in the atmosphere of the Earth. The basic ideas and results apply also to other settings and problems of interest that will be discussed later. These include particle production in stellar atmospheres, decay and interaction in the interior of the Sun, propagation in the interstellar medium, etc. Much of the specific material on particle production and cascades in the atmosphere has been discussed in previous monographs (e.g. Hayakawa, 1969). It is included here for completeness and to provide the basis for a self-contained discussion of many current topics in cosmic rays.

3.1 Transport equation for nucleons

Propagation of particles through the atmosphere is described by transport or cascade equations that depend on the properties of the particles and their interactions and on the structure of the atmosphere. Because nucleons are stable compared to their transit time through the atmosphere, they obey a particularly simple cascade equation. The one-dimensional version is

$$\frac{\mathrm{d}N(E,X)}{\mathrm{d}X} = -\frac{N(E,X)}{\lambda_N(E)} + \int_E^\infty \frac{N(E',X)}{\lambda_N(E')} F_{NN}(E,E') \frac{\mathrm{d}E'}{E}. \tag{3.1}$$

Here $N(E,X)\mathrm{d}E$ is the flux of nucleons (neutrons plus protons) at depth X in the atmosphere with energies in the interval E to $E+\mathrm{d}E$. (Note that X - called the *slant depth* - is measured from the top of the atmosphere downward along the direction of the incident nucleon - see fig. 3.1.) The probability that a nucleon interacts in traversing

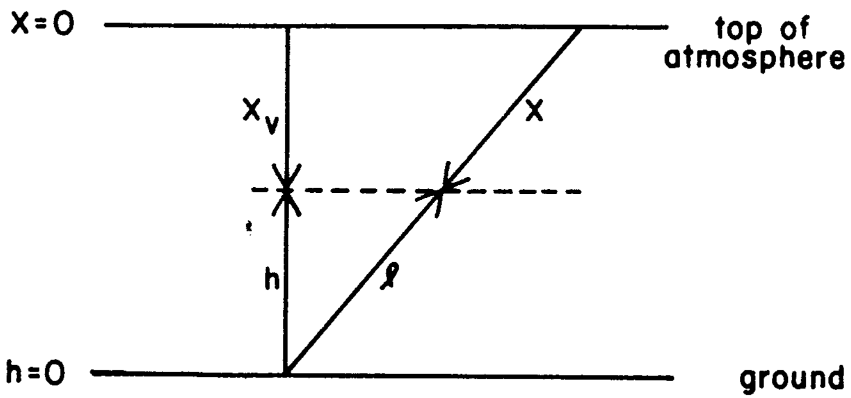

Figure 3.1: Definition of variables to describe the atmosphere.

an infinitesimal element of the atmosphere is $\mathrm{d}X/\lambda_N(E)$, where λ_N is the nucleon interaction length in air.[1] Both $X$and λ_N are measured in g/cm^2. The vertical atmospheric depth, X_v, is related to the density profile of the atmosphere by

$$X_v \;=\; \int_h^\infty \rho(h')\mathrm{d}h'. \tag{3.2}$$

The nucleon interaction length in air is

$$\lambda_N \;=\; \frac{\rho}{\rho_N \sigma_N^{\mathrm{air}}} \;=\; \frac{A\,m_p}{\sigma_N^{\mathrm{air}}}, \tag{3.3}$$

where $\rho(h)$ is the density of the atmosphere at altitude h and ρ_N is the corresponding number density of nuclei. For a calculation of the atmospheric cascade we can take the target nucleus to be an average "air" nucleus with $A \approx 14.5$ and omit the target designation from the notation. For $\sigma_N \approx 300$ mb (appropriate for nucleons interacting with air in the TeV range) $\lambda_N \approx 80$ g/cm^2.

Finally in (3.1), the function $F_{NN}(E, E')$ is the dimensionless inclusive cross section (integrated over transverse momentum) for an incident nucleon of energy E' to collide with an air nucleus and produce an outgoing nucleon with energy E. In general we define

$$F_{ac}(E_c, E_a) \equiv E_c \frac{\mathrm{d}n_c(E_c, E_a)}{\mathrm{d}E_c}, \tag{3.4}$$

where $\mathrm{d}n_c$ is the number of particles of type c produced on average in the energy bin $\mathrm{d}E_c$ around E_c per collision of an incident particle of type a. The precise relation between the quantities in (3.4), all of which are defined in the laboratory system, and the CM quantities of chapter 2 will be discussed in chapter 5. We note, however, from (2.8) that for energetic secondaries, i.e. those with $E_c \gg (\mu_T)_c$,

$$E_c/E_a = x_L \approx x^*. \tag{3.5}$$

(We always define CM as a projectile on a target *nucleon* even when that nucleon is bound in a nucleus, because nuclear binding energies will usually be much lower than energies of interest in cosmic ray problems we consider.)

3.2 Boundary conditions

The transport equation (3.1) for nucleons is only valid to the extent that production of nucleons by other types of particles (e.g. pions) can be neglected. In general, fluxes of particles in the atmosphere are governed by a set of coupled cascade equations, which will be discussed in the next chapter. We will need solutions of these equations subject to two physically important boundary conditions that correspond to two quite different types of experiments. The boundary conditions are

$$N(E,0) = N_0(E) = \frac{\mathrm{d}N}{\mathrm{d}E} \approx 1.8\,E^{-2.7}\,\frac{\text{nucleons}}{\mathrm{cm^2\,sr\,s\,GeV}/A} \tag{3.6}$$

and

$$N(E,0) \;=\; A\,\delta(E \;-\; E_0/A), \tag{3.7}$$

where A is the mass number of an incident nucleus. Equation (3.6) is relevant for a single detector that simply measures the rate at which particles of a given type are detected. The explicit power law approximation is valid for primary energy < 1000 TeV. Equation (3.7) is the boundary condition for an air shower experiment. This is an array of detectors with a fast–timing capability that can be triggered to measure the coincident, extended shower front initiated at the top of the atmosphere by a single particle. The primary particle has to have sufficient energy to give a measurable cascade at the surface of the Earth. Both boundary conditions have been written in a way that

---

[1] Upper case X denotes atmospheric depth and lower case x denotes fractional energy or momentum, as in table 2.3.

assumes that incident nuclei of mass A and total energy E_0 can be treated as A independent nucleons each of energy $E = E_0/A$. This is called the superposition approximation, the validity of which must be considered for each application.

3.2.1 Elementary solutions

The general treatment of transport equations subject to these boundary conditions is contained in the classic paper of Rossi and Greisen in 1941 about electron–photon cascades. We illustrate the general method and define some of the terminology by considering (3.1). It is possible to find *elementary solutions* in which the dependence on energy and depth factorizes: $N(E,X) = G(E)\,g(X)$. Substitution of the factorized form into (3.1), together with a change of variable from E' to $x_L = E/E'$, gives

$$G\,g' = -\frac{G\,g}{\lambda_N} + g\int_0^1 \frac{G(E/x_L)\,F_{NN}(x_L,E)}{\lambda_N(E/x_L)}\,\frac{\mathrm{d}x_L}{x_L^2}. \tag{3.8}$$

This separates to

$$\frac{g'}{g} = -\frac{1}{\lambda_N(E)} + \frac{1}{G(E)}\int_0^1 \frac{g(E/x_L)\,F_{NN}(x_L,E)}{\lambda_N(E/x_L)}\,\frac{\mathrm{d}x_L}{x_L^2}. \tag{3.9}$$

If we define a separation constant $-1/\Lambda$, the solution of the differential equation for $g(X)$ is written

$$g(X) = g(0)\,\exp(-x/\Lambda). \tag{3.10}$$

This elementary solution has the property that the flux attenuates exponentially through the atmosphere with attenuation length Λ while preserving an energy spectrum $G(E)$ that is independent of depth. In general, because of the complicated constraint placed on $G(E)$ by (3.9), the elementary solution does not correspond to either of the physically significant boundary conditions, (3.6) or (3.7). We show next, however, that it is approximately valid for the power law boundary condition (3.6).

3.2.2 Approximation A

In electromagnetic cascade theory *Approximation A* denotes the following three assumptions: i) energy loss by ionization is neglected; ii)

the radiation length is independent of energy; iii) the inclusive cross sections for pair production and bremsstrahlung scale. The approximation is valid for large energy. The analogous approximations for nucleonic cascades are

$$\lambda_N(E) \to \lambda_N = \text{constant} \tag{3.11}$$

and

$$F_{NN}(x_L,E) \to F_{NN}(x_L). \tag{3.12}$$

In fact the interaction cross section (and hence λ_N) varies slowly with energy, and the assumption of hadronic scaling (3.12) is also violated. These energy dependences are mild enough in practice, however, that the solutions in approximation A are useful over limited energy ranges, at least as a guide to more detailed results.

This is nice because in approximation A (i.e. when (3.11)–(3.12) hold) the cascade equations have elementary solutions that satisfy the power law boundary conditions. For nucleons, as approximated by (3.1), the solution is

$$N(E,X) = g(0)\,e^{-X/\Lambda}\,E^{-(\gamma+1)}, \tag{3.13}$$

where the attenuation length is given by

$$\frac{1}{\Lambda} = \frac{1}{\lambda_N}\left[1 - \int_0^1 (x_L)^{\gamma-1} F_{NN}(x_L)\,\mathrm{d}x_L\right] \tag{3.14}$$

and $-\gamma \cong -1.7$ is the power of the integral energy spectrum. Thus, to the extent that scaling is valid, nucleon fluxes in the atmosphere have the same energy spectrum as the primary cosmic rays. This connection between scaling for hadronic cross sections and the spectrum of hadrons in the atmosphere was recognized by Heitler & Janossy (1949). They motivated the scaling form for pion production by nucleons by analogy with bremsstrahlung of photons by electrons, anticipating Feynman (1969).

The spectrum-weighted moments of the inclusive cross sections,

$$Z_{ac} \equiv \int_0^1 (x_L)^{\gamma-1} F_{ac}(x_L)\,\mathrm{d}x_L, \tag{3.15}$$

determine the uncorrelated fluxes of energetic particles in the atmosphere (Frazer et al., 1972; Garraffo et al., 1973). For $\gamma = 1$, it follows from (3.4) that $Z_{ac}(1)$ is simply the average fraction of the interaction energy that goes into particles of type c. For $\gamma > 1$ the contribution to the moment from $x_L \to 0$ vanishes. Thus, for a steep primary spectrum, the uncorrelated fluxes depend on the behavior of the inclusive cross sections only in the forward fragmentation region, i.e., $x^* > 0$ in (2.8) and (3.5). This is why the μ^+/μ^- ratio remains large and greater than one. It is also why approximation A remains useful for uncorrelated fluxes of energetic particles, because hadronic scaling (3.12) is more nearly valid in the fragmentation regions than elsewhere.

3.3 Fluxes of neutrons and protons

Equation (3.13) gives the total flux of neutrons plus protons. The corresponding solutions for n and p separately depend on the four moments

$$Z_{pp} = Z_{nn} \text{ and } Z_{pn} = Z_{np}.$$

These two independent parameters can be expressed in terms of two independent interaction lengths:

$$\Lambda_+ = \Lambda_N \equiv \lambda_N(1 - Z_{NN})^{-1} \text{ and } \Lambda_- \equiv \lambda_N(1 - Z_{pp} + Z_{pn})^{-1},$$

where $Z_{NN} = Z_{pp} + Z_{pn}$. In approximation A, the ratio of neutrons to protons is

$$\frac{n(X)}{p(X)} = \frac{1 - \delta_0 \exp(-x/\Lambda^*)}{1 + \delta_0 \exp(-x/\Lambda^*)}. \tag{3.16}$$

Here $\delta_0 \equiv (p_0 - n_0)/(p_0 + n_0)$ is the relative proton excess at the top of the atmosphere and $\Lambda^* \equiv (\Lambda_+ - \Lambda_-)/(\Lambda_+\Lambda_-)$.

From column (3) of table 1.1 we find $\delta_0 \approx 0.82$, so the neutron to proton ratio is approximately 0.099 at the top of the atmosphere. It increases gradually, approaching one at large slant depths. The numerical value of the ratio deep in the atmosphere is very sensitive to the value of $Z_{pp} - Z_{pn}$, which occurs in the exponent. In addition, antinucleon production must be included in the calculation before a detailed comparison with experiment can be made. One must also consider whether a given experiment discriminates against long-lived neutral hadrons other than than neutrons, such as K_L^0.

> **Problem:** Write the separate cascade equations for neutrons and protons and find the explicit solutions for $n(E,X)$ and $p(E,X)$ in approximation A, neglecting production of $N\overline{N}$ pairs. Hence derive (3.16).

3.4 Coupled cascade equations

Since all types of hadrons can be produced when an energetic hadron of any flavor interacts, a set of coupled transport equations is needed to describe hadron fluxes in the atmosphere in full detail. In matrix notation one has

$$\frac{\mathrm{d}N_i(E,X)}{\mathrm{d}X} = -\left(\frac{1}{\lambda_i} + \frac{1}{d_i}\right)N_i(E,X) + \sum_j \int \frac{F_{ji}(E_i,E_j)}{E_i}\frac{N_j(E_j)}{\lambda_j}\,\mathrm{d}E_j, \tag{3.17}$$

where d_i is the decay length (in g/cm^2) for particles of type i. Other quantities are defined as in (3.1).

In practice, the simplest way to handle a detailed treatment of particle fluxes is with a Monte Carlo simulation or a numerical integration of the transport equations. A study of analytic solutions is useful for qualitative understanding and to check numerical results. For this purpose it is sufficient to look at (3.17) in the pion–nucleon sector, neglecting nucleon–antinucleon production as well as the coupling to other channels. Then we have to consider only (3.1) together with a simplified equation for the pion flux, $\Pi(E,X)$:

$$\begin{aligned}\frac{\mathrm{d}\Pi}{\mathrm{d}X} = -\left(\frac{1}{\lambda_\pi} + \frac{1}{d_\pi}\right)\Pi \;+\; &\int_0^1 \frac{\Pi(E/x_L)\,F_{\pi\pi}(E_\pi,E_\pi/x_L)}{\lambda_\pi(E/x_L)}\frac{\mathrm{d}x_L}{x_L^2} \qquad (3.18)\\ +\; &\int_0^1 \frac{N(E/x_L)\,F_{N\pi}(E_\pi,E_\pi/x_L)}{\lambda_N(E/x_L)}\frac{\mathrm{d}x_L}{x_L^2}.\end{aligned}$$

The loss due to decay in (3.18) is

$$\Delta\Pi = -\Pi\frac{\Delta\ell}{\gamma\,c\,\tau_\pi} = -\Pi\frac{\Delta X}{\rho\,\gamma\,c\,\tau_\pi} \equiv -\frac{\Pi}{d_\pi}\Delta X, \tag{3.19}$$

where γ is the Lorentz factor[2] and of the pion and ρ is the local atmospheric density. In (3.19) ΔX and $\Delta\ell$ are both measured along the direction of the trajectory of the cascade, and X is the corresponding slant depth.

---

[2] Note the ambiguity in the use of γ. It is conventional to use it both as the integral index of the cosmic ray energy spectrum, as in (3.13), and as the Lorentz factor.

3.5 The atmosphere

The relation between altitude and depth is shown in fig. 3.1. The pressure at vertical depth X_v in the atmosphere is $p = X_v$, and the density is $\rho = -\mathrm{d}X_v/\mathrm{d}h$. Since specific volume is inversely proportional to density,

$$\frac{p}{\rho} = \frac{X_v}{-\mathrm{d}X_v/\mathrm{d}h} \propto T. \tag{3.20}$$

So for an isothermal atmosphere, the ratio in (3.20) is equal to a constant scale height, h_0. Then

$$X_v = X_0\,\mathrm{e}^{-h/h_0}, \tag{3.21}$$

where $X_0 \cong 1030\ \mathrm{g/cm^2}$.

In reality the temperature and hence the scale height decrease with increasing altitude until the tropopause (12–16 km). At sea level $h_0 \cong 8.4$ km, and for $X_v < 200\,\mathrm{g/cm^2}$ $h_0 \cong 6.4$ km. A useful parametrization[3] of the relation between altitude and vertical depth (due to M. Shibata) is

$$h_v(\mathrm{km}) = \begin{cases} 47.05 + 6.9 \ln X_v + 0.299 \ln^2\left(\frac{1}{10}X_v\right), & X_v < 25\,\mathrm{g/cm^2} \\ 45.5 - 6.34 \ln X_v, & 25 < X_v < 230 \\ 44.34 - 11.861 (X_v)^{0.19}, & X_v > 230\,\mathrm{g/cm^2}. \end{cases} \tag{3.22}$$

In general, the relation between vertical altitude (h_v) and distance up the trajectory (ℓ) is (for $\ell/R_\oplus \ll 1$)

$$h_v \cong \ell\cos\theta + \frac{1}{2}\frac{\ell^2}{R_\oplus}\sin^2\theta \tag{3.23}$$

for zenith angle θ where $R_\oplus$ is the radius of the Earth. The corresponding slant depth is

$$X = \int_\ell^\infty \rho\left[h_v = \ell\cos\theta + \frac{1}{2}\frac{\ell^2}{R_\oplus}\sin^2\theta\right]\mathrm{d}\ell. \tag{3.24}$$

---

[3] Warning: when a parametrization like this is used in a Monte Carlo simulation, care must be taken to avoid the program getting hung up (due to round-off errors) when converting back and forth between h and X in the vicinity of one of the boundaries in (3.22). Such conversion between altitude and depth is necessary in an atmosphere of varying density because decay lengths are in terms of distance and interaction lengths in terms of column density.

Problem: Derive (3.23) and (3.24).

For $\theta \leq 60°$ the second term in (3.23) can be neglected, and

$$\rho \equiv X_v/h_0 \cong \frac{X\cos\theta}{h_0},$$

with h_0 evaluated at the appropriate atmospheric depth. Then from (3.19),

$$\frac{1}{d_\pi} = \frac{m_\pi c^2 h_0}{E\,c\,\tau_\pi X\,\cos\theta} \equiv \frac{\epsilon_\pi}{E\,X\,\cos\theta}.$$

Decay or interaction dominates depending on whether $1/d_\pi$ or $1/\lambda_\pi$ is larger in (3.18). This in turn depends on the relative size of ϵ_π and E, and similarly for other particles. Since most particle interactions occur in the first few interaction lengths, we summarize the decay constants for various particles in table 3.1, using the high altitude value of $h_0 \cong 6.4$ km.

Table 3.1: Decay constants.

Particle	$c\tau_0$(cm)	ϵ (GeV)
$\mu^\pm$	6.59×10^4	1.0
$\pi^\pm$	780	115
π^0	2.5×10^{-6}	3.5×10^{10}
$K^\pm$	371	850
K_S	2.68	1.2×10^5
K_L	1554	205
$D^\pm$	0.028	4.3×10^7
D^0	0.013	9.2×10^7
n	2.69×10^{13}	–

3.6 Meson fluxes

In the limit that $E \gg \epsilon_\pi$, decay can be neglected. Then the scaling limit solution of (3.18), with boundary condition $\Pi(E,0) = 0$, is

$$\Pi(E,X) = N(E,0)\,\frac{Z_{N\pi}}{1 - Z_{NN}}\,\frac{\Lambda_\pi}{\Lambda_\pi - \Lambda_N}\left(\mathrm{e}^{-X/\Lambda_\pi} - \mathrm{e}^{-X/\Lambda_N}\right). \tag{3.25}$$

The moments Z_{ac} are defined in (3.15) and the attenuation lengths are related to the interaction lengths by

$$\Lambda_i \equiv \lambda_i (1 - Z_{ii})^{-1} \tag{3.26}$$

The solution for charged kaons is the same as for charged pions with subscript π replaced by subscript K. Attenuation lengths in the 100 GeV range are tabulated in table 3.2, based on the values of Z_{ij} and interactions lengths given in chapter 5.The pion flux given by (3.25) rises from zero at the top of the atmosphere to a maximum at

$$X = \ln(\Lambda_\pi/\Lambda_N) \times (\Lambda_N \Lambda_\pi)/(\Lambda_\pi - \Lambda_N) \sim 140 \text{ g/cm}^2.$$

It then declines, eventually with attenuation length Λ_π. This behavior is characteristic of secondary fluxes in the atmosphere when decay can be neglected.

Table 3.2: Atmospheric attenuation lengths (g/cm^2).

Λ_N (nucleons)	Λ_π (pions)	Λ_K (kaons)
120	160	180

Before going on to consider the solutions at lower energy, where decay is important, it is instructive to consider the sum of all hadrons at high energy. Within the simplified coupling scheme we are using, the total flux of hadrons is

$$\Sigma = N(E,0)\Big[e^{-X/\Lambda_N} + \frac{Z_{N\pi}}{1 - Z_{NN}}\,\frac{\Lambda_\pi}{\Lambda_\pi - \Lambda_N}\left(e^{-X/\Lambda_\pi} - e^{-X/\Lambda_N}\right) + \frac{Z_{NK}}{1 - Z_{NN}}\,\frac{\Lambda_K}{\Lambda_K - \Lambda_N}\left(e^{-X/\Lambda_K} - e^{-X/\Lambda_N}\right)\Big]. \tag{3.27}$$

Let us now consider (3.27) for a very flat spectrum, $\gamma = 1$. This corresponds to the *normal solution* in electromagnetic cascade theory. Let us further artificially treat the π^0 as stable instead of feeding the electromagnetic component *via* $\pi^0 \rightarrow \gamma\gamma$. Then by energy conservation $Z_{\pi\pi}(\gamma = 1) = 1$. Also, since in this artificial example we neglect $K \rightarrow \pi$ and $K \rightarrow N$, $Z_{KK} = 1$ and $Z_{NN} + Z_{N\pi} + Z_{NK} = 1$. Thus the expression in square brackets in (3.27) is one, so an incident spectrum with $\gamma = 1$ preserves itself without attenuation. Note, however, that this requires infinite energy: the energy contained in a spectrum is

$$\int E\left[\frac{\mathrm{d}N}{\mathrm{d}E}\right]\mathrm{d}E \propto \int E\left[E^{-(\gamma+1)}\right]\mathrm{d}E,$$

which is logarithmically divergent for $\gamma = 1$.

Returning now to the real world, we consider the transport equation for charged pions at lower energy, where pion decay cannot be neglected. Then the scaling version of (3.18) is

$$\begin{aligned} \mathrm{d}\Pi/\mathrm{d}X = & -\left(\frac{1}{\lambda_\pi} + \frac{\epsilon_\pi}{E\,X\cos\theta}\right)\Pi(E,X) \\ & + \frac{1}{\lambda_\pi}\int_0^1 \Pi(E/x_L, X)\,F_{\pi\pi}(x_L)\frac{\mathrm{d}x_L}{x_L^2} \\ & + \frac{Z_{N\pi}}{\lambda_N} N(E,0)e^{-X/\Lambda_N}. \end{aligned} \tag{3.28}$$

An explicit approximate expression for the solution can be found if $\Pi(E,X)$ is replaced under the integral in (3.28) by a factorized form which is a product of $E^{-(\gamma+1)}$ and a function of depth. The motivation for this trial form is that the driving source term in (3.28) is proportional to the nucleon flux, which has the $E^{-(\gamma+1)}$ dependence on energy.

With this *ansatz*, (3.28) becomes

$$\frac{\mathrm{d}\Pi}{\mathrm{d}X} = -\Pi(E,X)\left(\frac{1}{\Lambda_\pi} + \frac{\epsilon_\pi}{E\,X\cos\theta}\right) + \frac{Z_{N\pi}}{\lambda_N} N_0(E)\,e^{-X/\Lambda_N}. \tag{3.29}$$

The effect of this approximation is to represent the pion interaction and regeneration in (3.28) by a single attenuation term with attenuation length Λ_π. The last term in (3.29) is the production spectrum of pions by nucleons. The exact solution of (3.29) is

$$\Pi(E,X) = e^{-(X/\Lambda_\pi)}\frac{Z_{N\pi}}{\lambda_N} N_0(E)\int_0^X \left(\frac{X'}{X}\right)^{\epsilon_\pi/E\cos\theta} \exp\left(\frac{X'}{\Lambda_\pi} - \frac{X'}{\Lambda_N}\right)\mathrm{d}X'. \tag{3.30}$$

In the high energy limit $(X'/X)^{\epsilon_\pi/E\cos\theta} \to 1$ and (3.30) reduces to (3.25). In the low energy limit $E\cos\theta \ll \epsilon_\pi$, so $(X'/X)^{\epsilon_\pi/E\cos\theta}$ is small except for X' near X. In this low energy limit therefore one can set $X' = X$ in the exponential and (3.30) becomes

$$\Pi(E,X) \xrightarrow{E\ll\epsilon_\pi} \frac{Z_{N\pi}}{\lambda_N} N(E,0)\, \mathrm{e}^{-X/\Lambda_N}\, \frac{X\,E\,\cos\theta}{\epsilon_\pi}. \tag{3.31}$$

Problem: Show that the expression (3.31) is the correct low energy solution of (3.28) by calculating

$$\Pi(E,X) = \int_0^X \frac{\mathrm{d}n_\pi(E,X')}{\mathrm{d}X'}\, P_s(X-X')\,\mathrm{d}X',$$

where $\mathrm{d}n_\pi(E,X)/\mathrm{d}X$ is the pion production spectrum and $P_s(X-X')$ is the probability that a pion produced at X' survives to depth $X > X'$. Hint: First show that

$$P_s(X-X') = (X'/X)^{\epsilon_\pi/E\cos\theta}\exp[-(X-X')/\lambda_\pi].$$

The expression (3.30) is thus an approximate solution to (3.28) that interpolates between the correct low energy and high energy limiting solutions. Analogous results may be obtained for kaons.

Chapter 4

Hadrons and photons

Because of their short lifetime, neutral pions up to the highest cosmic ray energies decay before they interact in the atmosphere. The electromagnetic cascades they generate (through $\pi^0 \to 2\,\gamma$) are therefore very closely related to fluxes of hadrons in the atmosphere. Fluxes of high energy hadrons and photons in the atmosphere are discussed in this chapter as an introduction to some of the cosmic ray data. The chapter begins with a general discussion of the kinematics of meson decay. This will be needed for later chapters on muons and neutrinos, as well for the calculation of photon fluxes in this chapter.

4.1 Meson decay

The production spectrum of secondaries of type i (differential in depth and energy) is given by

$$\mathcal{P}_i(E,X) = \sum_j \int_{E_{\min}}^{E_{\max}} \frac{\mathrm{d}n_{ij}(E,E')}{\mathrm{d}E}\,\mathcal{D}_j(E',X)\,\mathrm{d}E', \tag{4.1}$$

where $\mathrm{d}n_{ij}(E,E')/\mathrm{d}E$ is the inclusive spectrum of secondaries i from decay of particles j with energy E'. In (4.1), $E_{\min} \geq E$ and $E_{\max}$ are the minimum and maximum energies of the parent that can give rise to the secondary i. The function $\mathcal{D}_j(E',X)$ is the spectrum (differential in energy and depth) of the decaying parent particles j. For charged pions

$$\mathcal{D}_\pi(E,X) = \frac{\epsilon_\pi}{E X\cos\theta}\Pi(E,X). \tag{4.2}$$

The most important channels and their branching ratios are

$$\pi^{\pm} \to \mu^{\pm} + \nu_{\mu}(\overline{\nu}_{\mu}) \qquad (\sim 100\%) \tag{4.3}$$

$$\pi^{0} \to 2\gamma \qquad (\sim 98.8\%) \tag{4.4}$$

$$K^{\pm} \to \mu^{\pm} + \nu_{\mu}(\overline{\nu}_{\mu}) \qquad (\sim 63.5\%) \tag{4.5}$$

In a detailed calculation the $K \to n \times (\pi)$ and $K_{\ell 3}$ channels need to be considered also. A particularly important example of a $K_{\ell 3}$ decay ($\ell 3$ means three-body, semileptonic final state) is

$$K_L \to \pi^{\pm} e^{\pm} \nu_e(\overline{\nu}_e) \quad (38.7\%), \tag{4.6}$$

which is the dominant source of ν_e for energies $E_\nu \gg \epsilon_\mu \cong 1$ GeV when muon decay is unimportant. At lower energies, muon decay is important, so we will also need to consider

$$\mu^{\pm} \to e^{\pm} + \nu_e(\overline{\nu}_e) + \overline{\nu}_{\mu}(\nu_{\mu}). \tag{4.7}$$

At high energy, where its production becomes large, it may also be necessary to consider production and decay of the eta meson (which predominantly feeds the electron–photon cascade) separately from neutral pions. The channel $\pi^0 \to \gamma e^+ e^-$ (1.2%) can, however, always be included with the dominant channel by assigning an effective 100% branching ratio to (4.4). Production of heavier flavors, especially charm, eventually becomes important for muon and neutrino fluxes at very high energy. Because of their short lifetimes, their decay is not inhibited by interaction until nearly 10^8 GeV (see table 3.1). At sufficiently high energy they actually become the dominant source of muons and neutrinos through their semileptonic decay channels. We will discuss these *prompt leptons* in chapter 6.

For two-body decay, $M \to m_1 + m_2$, the magnitude of the momenta of the secondaries in the rest frame of M is

$$p_1^* = p_2^* = p^* = \frac{\sqrt{M^4 - 2M^2(m_1^2 + m_2^2) + (m_1^2 - m_2^2)^2}}{2M}.$$

In the laboratory system the energy of the decay product is

$$E_i = \gamma E_i^* + \beta\gamma p^* \cos\theta^*, \tag{4.8}$$

where β and γ are the velocity and Lorentz factor of the parent in the laboratory system. In the absence of polarization

$$\frac{\mathrm{d}n}{\mathrm{d}\Omega^*} = \frac{\mathrm{d}n}{2\pi \mathrm{d}\cos\theta^*} \propto \frac{\mathrm{d}n}{\mathrm{d}E_i} = \text{constant}. \tag{4.9}$$

From (4.8) the limits on the laboratory energy of the secondary i are

$$\gamma(E_i^* - \beta p^*) \le E_i \le \gamma(E_i^* + \beta p^*).$$

The distribution in laboratory energy for a product of 2-body decay of an unpolarized particle is therefore flat between these limits, as illustrated in fig. 4.1. Normalization requires

$$\frac{\mathrm{d}n_{ij}}{\mathrm{d}E_i} = \frac{B_{ij}}{2\gamma\beta p^*} = \frac{B_{ij}M}{2p^* P_L}, \tag{4.10}$$

where B_{ij} is the branching ratio for $j \to i$ and P_L is the laboratory momentum of the parent. For the process (4.5), for example,

$$\frac{\mathrm{d}n}{\mathrm{d}E_\nu} = \frac{\mathrm{d}n}{\mathrm{d}E_\mu} = \frac{0.635}{(1 - \mu^2/K^2)P_K}, \tag{4.11}$$

where μ and K in the denominator represent the respective particle masses.

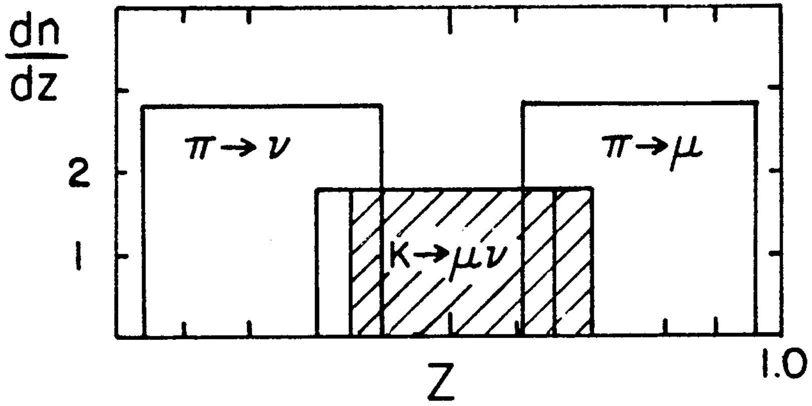

Figure 4.1: Decay distributions of π-decay and K-decay into $\mu\nu_\mu$ for 200 MeV/c parent mesons. z is the ratio of the total laboratory energy of the decay product to that of the parent.

Often we will deal with decays of relativistic particles, in which case $\beta \to 1$ in these kinematic formulas. For $M \to \mu\,\nu$ the kinematic limits on the laboratory energies of the secondaries are

$$E(\mu^2/M^2) \le E_\mu \le E$$

and

$$0 \le E_\nu \le (1 - \mu^2/M^2)E,$$

where E is the laboratory energy of the decaying meson. Numerically

$$< E_\mu > / E \;=\; 0.79 \;\text{ and }\; < E_\nu > / E_\pi \;=\; 0.21$$

for $\pi \to \mu\nu$. The corresponding numbers for decay of charged kaons are 0.52 and 0.48. Note that, as a consequence of kinematics, when one of the decay products has a mass comparable to the parent, it will carry most of the energy.

> **Problem:** Show that a neutrino or antineutrino produced *via* (4.3) with energy $E_\nu > p^* \cong 30$ MeV must have a trajectory within 90° of the direction of that of the parent pion. Show that the maximum angle of such a neutrino relative to the parent is $\theta = \sin^{-1}[p^*/E_\nu]$.

4.2 Fluxes of hadrons and photons

We have already obtained the fluxes of nucleons and charged pions in the high energy limit (3.13) and (3.25). The production spectrum of photons from $\pi^0 \to 2\gamma$ is obtained from (4.1). Because the lifetime of neutral pions is so short, the spectrum of decaying π^0's is just their production spectrum:

$$\mathcal{D}_{\pi^0}(E,X) = \frac{1}{\lambda_N} N(E,X) Z_{N\pi^0} + \frac{1}{\lambda_\pi}\Pi(E,X) Z_{\pi\pi^0} + \cdots . \qquad (4.12)$$

For the decay channel (4.4), $\mathrm{d}n_\gamma/\mathrm{d}E_\gamma = 2/E_{\pi^0}$, so the production spectrum of photons is

$$\frac{\mathrm{d}n_\gamma(E,X)}{\mathrm{d}X} = 2\int_E^\infty \{N(E',X)\frac{Z_{N\pi^0}}{\lambda_N} + \Pi(E',X)\frac{Z_{\pi\pi^0}}{\lambda_\pi}\}\frac{\mathrm{d}E'}{E'}. \qquad (4.13)$$

If the energy spectra of both nucleons and charged pions are proportional to $E^{-(\gamma+1)}$, then

$$\frac{\mathrm{d}n_\gamma(E,X)}{\mathrm{d}X} = \frac{2}{\gamma+1}\left(\frac{Z_{N\pi^0}}{\lambda_N}N(E,X) + \frac{Z_{\pi\pi^0}}{\lambda_\pi}\Pi(E,X)\right). \qquad (4.14)$$

To calculate the photon flux at a particular level in the atmosphere we need to fold the photon production spectrum (4.14) with the electromagnetic cascade equations to account for the pair production and bremsstrahlung processes that subdivide an initial high energy photon into many photons and electrons of lower energy. The equations

of electromagnetic cascade theory are analogous to (3.17) with F_{ji} the distribution functions for bremsstrahlung and pair production. These functions scale, and the solution for power law boundary conditions is

$$\frac{\mathrm{d}N_{\gamma+e^\pm}(E,X)}{\mathrm{d}E} = C\,K_\gamma\,E^{-(\gamma+1)}\,\mathrm{e}^{-X/\Lambda_{\mathrm{e.m.}}}, \qquad (4.15)$$

where $K_\gamma\,E^{-(\gamma+1)}$ is the initial photon flux at $X = 0$. The electromagnetic attenuation length $\Lambda_{\mathrm{e.m.}}$ is related to the radiation length of electromagnetic cascade theory. Both $\Lambda_{\mathrm{e.m.}}$ and $C \equiv 1 + N_{e^\pm}/N_\gamma$ depend on the spectral index γ. We defer a discussion of electromagnetic cascade theory to chapter 15, but simply use the values for $\gamma = 1.7$ here. They are $C = 1.18$ and $\Lambda_{\mathrm{e.m.}} = 85$ g/cm^2.

In the high energy limit, both terms in (4.14) have an $E^{-(\gamma+1)}$ energy dependence. The resulting vertical differential flux of photons plus electrons and positrons at depth X is given by the convolution of (4.14) and (4.15):

$$\begin{aligned}
\phi_{\mathrm{e.m.}}(E,X) \;&=\; C\int_0^X \mathrm{d}X'\,\exp\left(-\frac{X-X'}{\Lambda_{\mathrm{e.m.}}}\right) \qquad (4.16)\\
&\quad\times\frac{2}{\gamma+1}\left(\frac{Z_{N\pi^0}}{\lambda_N}N(E,X') + \frac{Z_{\pi\pi^0}}{\lambda_\pi}\Pi(E,X')\right)\\
&=\; \frac{2}{\gamma+1}\,C\,N(E,0)\,\exp\left(-\frac{X}{\Lambda_{\mathrm{e.m.}}}\right)\times\\
&\quad\left[\frac{Z_{N\pi^0}\Lambda_N^*}{\lambda_N}\left(\mathrm{e}^{X/\Lambda_N^*}-1\right) + \frac{Z_{N\pi}}{1-Z_{NN}}\frac{Z_{\pi\pi^0}\Lambda_\pi}{\lambda_\pi(\Lambda_\pi-\Lambda_N)}\{\cdots\}\right],
\end{aligned}$$

where

$$\{\cdots\} = \left\{\Lambda_\pi^*\left(\mathrm{e}^{X/\Lambda_\pi^*}-1\right) \;-\; \Lambda_N^*\left(\mathrm{e}^{X/\Lambda_N^*}-1\right)\right\}.$$

Combinations of attenuation lengths in (4.16) are defined as

$$\Lambda_N^* \;\equiv\; \left(\frac{1}{\Lambda_{\mathrm{e.m.}}} - \frac{1}{\Lambda_N}\right)^{-1} \;\sim\; 290\ \mathrm{g/cm^2}$$

and

$$\Lambda_\pi^* \;\equiv\; \left(\frac{1}{\Lambda_{\mathrm{e.m.}}} - \frac{1}{\Lambda_\pi}\right)^{-1} \;\sim\; 180\ \mathrm{g/cm^2}.$$

If we use the low energy values of attenuation lengths (table 3.2) and moments (table 5.2) to evaluate (4.16), we get the result shown by the solid curve in fig. 4.2 for the flux of the uncorrelated electromagnetic component at high energy. The all nucleon flux at the top

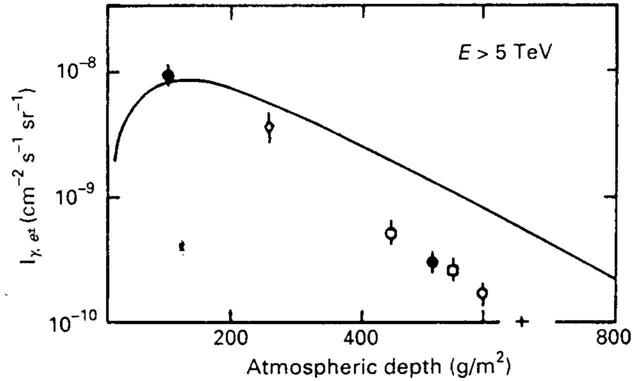

Figure 4.2: Vertical flux of $\gamma + e^{\pm}$ with $E > 5$ TeV. References to the original data may be found in Navia et al., 1989.

of the atmosphere given by (3.6) has been used. About 75% of the signal is from $N \rightarrow \pi^0$ (the first term on the right hand side of (4.16)) and 25% from $N \rightarrow \pi^{\pm} \rightarrow \pi^0$ (the second term). The curve rises rapidly to a maximum[1]around 100 g/cm^2, then attenuates - but not as fast as the data at these high energies.

The shape of the energy spectrum of electrons and photons predicted by (4.16) also differs from the data. Under the assumptions of scaling and constant cross section, the spectral index for the secondary spectrum is the same as that of the primaries. here assumed to be $\gamma = 1.7$. Fig. 4.3 shows the comparison with data, which is characterized by a spectral index $\gamma \approx 2.00 \pm 0.08$. The solid line is calculated from (4.16). The other calculations are those of Ren et al. (1987). The areas enclosed by dashed lines have $\sigma^{\mathrm{inel}}_{\mathrm{p-air}} \propto E^{0.04}$, and the shaded areas $\propto E^{0.06}$. The letters P and M stand for different assumptions about the primary composition: P= predominantly protons and M= predominantly heavy nuclei. Evidently, some of the assumptions made in deriving (4.16) must be wrong. In fact, it turns out that all are - none is badly wrong by itself, but all err in the same direction! The cross section increases with energy, the primary spectrum steepens above $\sim 10^{15}$ eV, and the spectrum-weighted moments decrease slightly as energy increases. Each of these effects both steepens the secondary spectrum and makes it attenuate faster. For a detailed comparison with the data, it may also be necessary to treat interactions of nuclei separately (Navia et al., 1989).

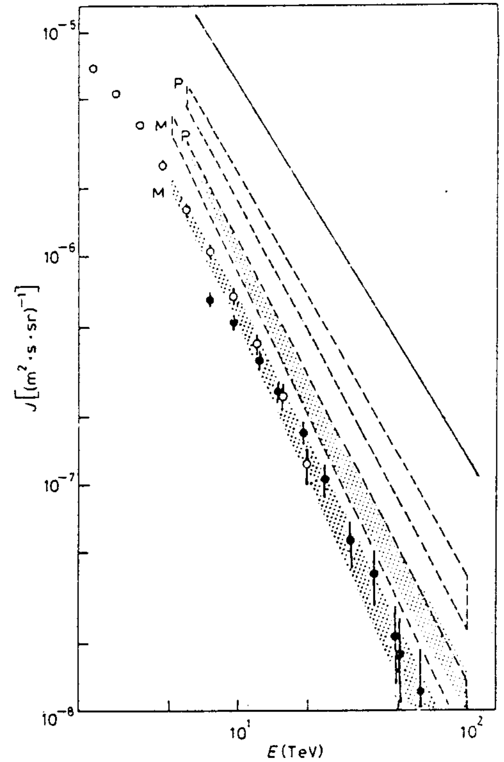

Figure 4.3: Integral spectrum of $\gamma + e^{\pm}$ from the measurement of Ren et al. (1987) at Mt. Kanbala, altitude 5500 m., in Tibet. (© Società Italiana di Fisica.)

4.3 Emulsion chambers

The detectors used to make the measurements shown in figs. 4.2 and 4.3 are known as *emulsion chambers*. They are direct descendants of the classic photographic emulsion technique used to discover the pion (Lattes, Occhialini and Powell, 1947) and to study hadronic interactions before the advent of accelerators (Powell, Fowler & Perkins, 1959). For current applications at the highest possible energy, a calorimeter is made that consists of layers of various materials interleaved with x-ray film or more sensitive photographic emulsion.

---

[1] The maximum in the flux of $e^{\pm}$ is known as the Pfotzer maximum, discovered in balloon flights in the 1930's. (Pfotzer, 1936.)

The exact arrangement depends on the application, but the idea is to use lead, iron, plastic or plates made of other non-photographic materials in various combinations to develop electromagnetic and hadronic cascades, which are sampled by the layers of photographic material. After calibration, the shower curves can be reconstructed by measurements in the photosensitive layers. This allows an estimate of the energy of the cascade and hence of the particle that made it. These devices are currently used to measure the primary cosmic ray composition and the hadronic and electromagnetic components of the cosmic radiation in the atmosphere as well as to study high energy nucleus–nucleus interactions.

4.3.1 Direct measurements

Typical of small emulsion chambers used for direct measurements of the primary cosmic rays and their interactions at the top of the atmosphere are those of the JACEE collaboration, one of which is shown schematically in fig. 4.4. This chamber was designed to measure primary composition (Burnett et al., 1983) during balloon exposures above 99.5% of the atmosphere. The upper portion of the chamber consists of layers of sensitive emulsion separated by layers of plastic, so the charge of an incident primary nucleus can be measured before it begins to interact. The charge is inferred from the darkness of the track in the emulsion. The middle part of the chamber is designed to follow tracks with minimal probability of interaction. This allows tracks to diverge sufficiently so that cascades generated by interactions in the calorimeter part of the chamber can be individually measured. The essential elements of the calorimeter are x-ray films and lead plates. Electromagnetic cascades initiated either directly by electrons and photons or by photons from π^0 decay develop rapidly in lead, and their energy can be determined by summing up the measurements of darkening of the x-ray file along each cascade. Other configurations have been used by this group to study individual nucleus–nucleus collisions (Burnett et al., 1987).

Small emulsion chambers with good spatial resolution ($\sim 10\,\mu$) have been used to search for short-lived ($\tau = 10^{-14}$ to 10^{-12} second) particles produced by interactions of cosmic rays. Since the discovery of charm, they have been used to study production and decay of charmed particles at accelerators as well. Indeed, it is likely that the first example of charm was seen with an emulsion chamber experiment

looking at cosmic rays (Niu, Mikumo & Maeda, 1971). An interesting aspect of the early history of charm is that the Niu event was immediately interpreted by Hayashi et al. (1972) as production of a new hadron containing a fourth quark *á la* Glashow-Iliopoulos-Maiani (1970). This was several years in advance of the rapid development of the field stimulated by the discovery of the $J(\Psi)$ particle (Aubert et al., 1974 and Augustin et al., 1974).[2]

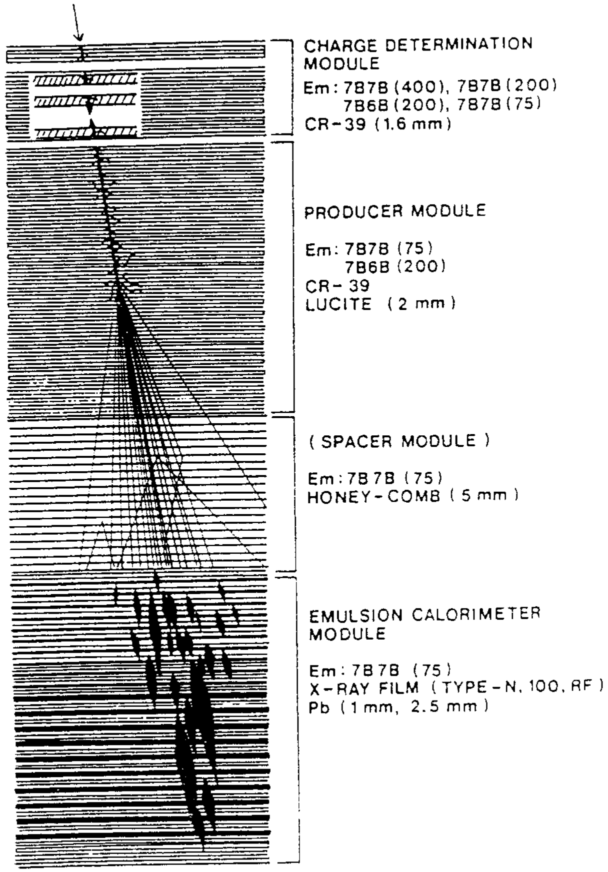

Figure 4.4: A JACEE emulsion chamber designed to measure the primary spectrum of cosmic rays. (From Burnett et al. (1990) *Ap. J.* to be published: reprinted with permission from *The Astrophysical Journal.*)

---

[2] Further details of this early history and its relation to studies of charm at accelerators may be found in a paper by Gaisser & Halzen (1976) and in the book by Cahn & Goldhaber (1989).

4.3.2 Large emulsion chambers

At the other extreme, the emulsion chamber technique has long been used to study air shower cores, as well as to measure fluxes of energetic photons and hadrons, with very large devices exposed at the highest possible mountain altitude. Table 4.1 gives the vertical depth and total accumulated exposures up to 1987 (Shibuya, 1987) for the four large emulsion chamber experiments. Typically, the chambers are reassembled with new film each summer, and left to collect events through the rest of the year. The values quoted here for total exposure are somewhat ambiguous because the detector changes from year to year so that the exposure differs depending on the type of measurement that is referred to. It is clear, however, that with detector areas of order 100 m^2 and total exposures of order 1000 m^2 yr, it is possible to reach into the 10^{15} to 10^{16} eV energy range. The integral flux above 10^{15} eV is of order 10^{-10}cm^{-2}sr^{-1}s^{-1}. If we use an attenuation length for hadrons of 100 g/cm^2 (smaller than in table 3.2 because we anticipate that the cross section increases with energy) then the counting rate at 550 g/cm^2 would be ~ 10 events per 100 m^2 per year.

Table 4.1: Large emulsion chambers.

Experiment	Depth (g/cm^2)	Exposure (m^{2}yr)
Mt. Kanbala (Ren et al., 1988)	520	420
Mt. Fuji (Ren et al., 1987)	650	1000
Pamir Mountains (Bayburina et al., 1981)	596	6000
Mt. Chacaltaya (Lattes et al., 1980)	540	690

To achieve the highest possible energies, the experiments study families of parallel, energetic cascades in the chambers. These are cores of air showers that have been initiated in the last one or two interaction lengths above the detector - not quite single interactions, but close to it. The counting rate for such events corresponds to the flux of hadrons higher in the atmosphere - say at 400 g/cm^2, which gives a factor ~ 5 increase in rate. The actual calculation of the rate is a much more complicated procedure than indicated by these crude estimates. It depends crucially on the details of each experiment - sensitivity of the film, rules for scanning, assembly of the detector, etc. Some of the complexity can be inferred by looking at a schematic diagram of one of the detectors. Fig. 4.5 shows how different kinds of particles and events look in the Chacaltaya detector.

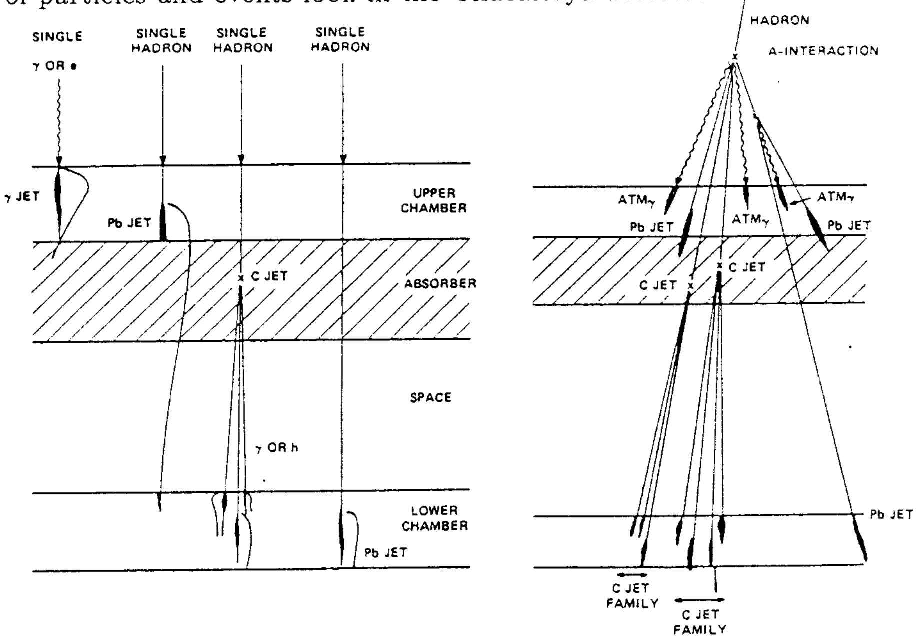

Figure 4.5: Schematic diagrams of the Chacalataya emulsion chamber (Lattes et al., 1971 and Gaisser & Yodh, 1980). (Reproduced with permission, from the *Annual Review of Nuclear and Particle Science,* Vol. 30, © 1980 by Annual Reviews Inc.)

The Chacaltaya emulsion chamber consists of two lead–x-ray film sandwich chambers separated by a layer of carbon and some space. The radiation length in lead is very short (6.37 g/cm^2) compared to a nuclear interaction length (~ 190 g/cm^2), so photons and electrons initiate cascades very soon after entering the upper chamber. (A photon produced in the atmosphere above the chamber is denoted ATM$_\gamma$ in fig. 4.5.) Hadrons, on the other hand, interact deep in the upper chamber, in the carbon layer or in the lower chamber (or not at all).

Interactions of hadrons above the detector would be expected to produce both hadrons ($\pi^\pm$ kaons and nucleons) and photons (from π^0 decay) at the chamber, as indicated in the figure. A pure electromagetic cascade in the atmosphere would manifest itself at the chamber as a group of cascades all starting near the top of the upper chamber. One of the curiosities of the emulsion chamber work is that a few events have been reported in which there are almost no cascades starting at the top of the chamber. These are known as *Centauro* events (Lattes et al., 1980). Events like this would result if a group of parallel hadrons hit the chamber without any accompanying photons. Simulations show, however, that this is exceedingly unlikely given what we know about hadronic interactions, even allowing for a large fraction of heavy nuclei in the incident cosmic radiation (Ellsworth et al., 1981). These few anomalous events are not understood even now.

The relative probabilities of interaction for different types of particles in different parts of the chamber, and the fluctuations in energy deposition are crucial ingredients in interpreting the events and extracting their implications for primary composition and for hadronic interactions. A full Monte Carlo of the cascades in and above the detector is required. A complete treatment of data from the Mt Kanbala and Mt Fuji experiments is contained in the series of papers by Ren et al., 1988). Further references may be found there and in the two review papers listed in table 4.1 as well as in the reviews by Stanev & Yodh (1988) and by Gaisser & Yodh (1980). The analysis of gamma and hadron families by Ren et al., leads to the conclusions hinted at in connection with their analysis (Ren et al., 1987) of uncorrelated fluxes of photons that was discussed in §3.5. In particular, they find that the cross section for hadrons in air increases with energy,

$$\sigma^{\text{inel}}_{\text{p-air}} \approx 290\ \text{mb} \times \left(\frac{E_p}{1\ \text{TeV}}\right)^{0.06}. \tag{4.17}$$

They also find that the Z_{ij} decrease slightly with energy, and that the primary composition becomes relatively rich in heavy nuclei above 10^{14} eV. Qualitatively, the first two are in accord with what is expected from accelerator experiments, although the cross section of (4.17) is perhaps 10% larger than one would expect at 10^{15} eV. These questions are the subject of the next chapter. The question of composition is much disputed and is of great current interest in high energy cosmic ray physics.

Chapter 5

Accelerator data

The purpose of this chapter is to review data on strong interactions of particles and to collect tables of interaction lengths and other parameters for use in cosmic ray calculations.

Below 100 GeV most pions and kaons produced in the atmosphere decay before they interact. In this case, the flux of hadrons at depth X is simply given by the flux of nucleons from (3.13),

$$\mathrm{d}N/\mathrm{d}E \;=\; N_0 E^{(-\gamma+1)} \exp(-X/\Lambda_N),$$

where γ is the same spectral index as measured at the top of the atmosphere. We have seen that this factorized form - a power law energy dependence attenuating through the atmosphere with a characteristic length Λ - follows from scaling for the inclusive cross section, F_{ij}, and constancy of the interaction length λ. As noted in chapter 3, the fact that measurements of attenuation of the "nuclear active" component of cosmic rays approximately agree with (3.13) was used very soon after discovery of the pion to justify a scaling form for the inclusive cross section for pion production by nucleons.

Later Pal and Peters (1964) in a classic paper made a model based on the physics of nucleon resonances called the "isobar-pionization" model. In this picture an inelastic nucleon interaction has two components: The projectile nucleon is excited to an isobar state,[1] which decays strongly ($\tau \approx 10^{-23}$ s) to give a few fast secondaries, including the "leading nucleon." Excitation of an isobar may also be accompanied by emission of slower pions - the "pionization" component.

---

[1] An isobar is an excited state (resonance) with the same quark content as the ground state of the baryon.

Figure 5.1 illustrates the basic idea of the model and shows its contemporary interpretation in terms of quarks and gluons. In both terms (i.e. with or without pionization) the projectile fragments reflect the quantum numbers of the incident projectile, e.g. charge, strangeness, baryon number, etc. Pal and Peters normalized their model to accelerator data available at the time ($E^{\mathrm{Lab}} \leq 30$ GeV) and calculated the fluxes of hadrons, muons and neutrinos along the lines outlined in the previous chapters. Their paper remains an excellent guide to the subject.

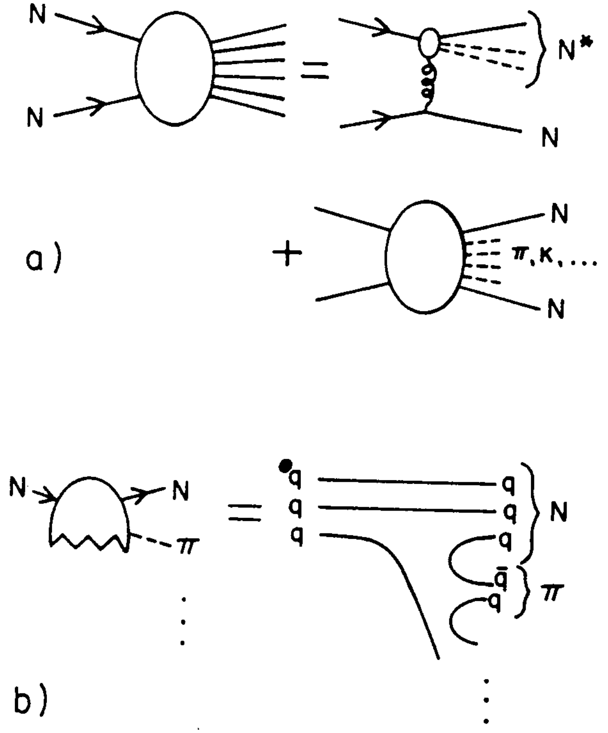

Figure 5.1: (a) Isobar-pionization picture of a nucleon–nucleon collision. (b) Fragmentation of a projectile nucleon.

5.1 Hadronic cross sections

The fundamental theory underlying high energy collisions of hadrons is generally accepted to be QCD. But because of the large coupling constant (which precludes use of perturbation theory), rigorous calculations of soft processes are not possible - at least not at present.

Nevertheless, certain gross features of the data are consistent with one's intuition on the basis of a simple-minded parton picture, in which the quarks and gluons in a hadron are treated by analogy with nucleons in a nucleus. One of these features is the relative size of the pion–nucleon and nucleon–nucleon cross sections. Since the valence quark content of the pion is a quark–antiquark pair and that of a nucleon three quarks, the most naive expectation for the ratio of the cross sections would be

$$\frac{\sigma_{\pi p}}{\sigma_{pp}} = \frac{2 \times 3 \times \sigma_{qq}}{3 \times 3 \times \sigma_{qq}} = \frac{2}{3}.$$

The experimental number is ≈ 0.6, remarkably close to two-thirds.

Figure 5.2 shows the proton–proton cross section. For calculation of cascade processes we will mainly be interested in the inelastic cross section, because elastic scattering generally only leads to a small deflection of the projectile with no loss of energy. From threshold, $\sigma_{pp}^{\mathrm{inel}}$ rises rapidly to about 28–30 mb in the region 1.26 GeV/$c \leq p_{beam} \leq 2 - 3$ GeV, where the nucleon–nucleon cross section is largely (but not entirely) given by

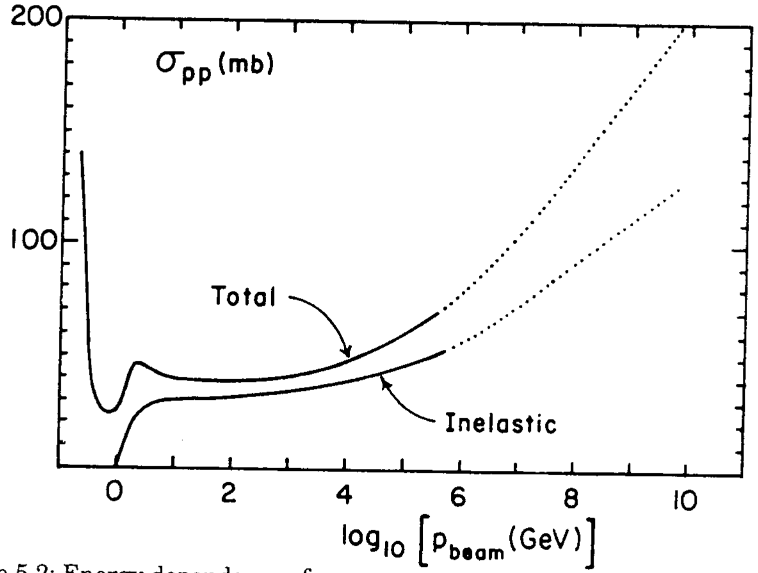

Figure 5.2: Energy dependence of σ_{pp}.

$$N + N \to \Delta(1.232) + N.$$

It then increases slowly to about 35 mb at 1.5 TeV, after which the increase becomes more rapid. Thus for three decades of energy the inelastic cross section changes by less than 25%, justifying use of the constant cross section approximation for atmospheric cosmic rays in this energy regime.

Cross sections for scattering of pions and kaons on protons also vary rather slowly with energy from several GeV to several hundred GeV. At low energies (in the GeV range), the total and elastic cross sections are dominated by the role of individual resonances, the classic case being π^+p scattering, which goes almost entirely through the $\Delta^{++}(1232\,\mathrm{MeV})$ baryon resonance for pion beam momenta of 300 ± 200 MeV. In the threshold region, there are rapid variations in some of the cross sections, especially for $\pi^- p$. In contrast, the inelastic cross sections rise smoothly from threshold (apart from the quasi-elastic charge exchange processes, $\pi^- p \rightarrow \pi^0 n$ and $K^- p \rightarrow K^0 n$, which dominate inelastic scattering below pion production threshold).

Direct measurements of hadron–hadron cross sections at present extend up to equivalent beam momenta of ≤ 400 GeV/c for mesons and ≤ 2000 GeV/c for nucleons. Data and references on cross sections are summarized in detail in a series of CERN-HERA reports (Flaminio et al., 1983, 1984). Measurements made at $\bar{p}p$ colliders (e.g. Bozzo et al., 1984; Alner et al., 1986a) can be used to extend the proton–proton cross section plots up to a laboratory energy equivalent to ~ 1000 TeV on the conventional assumption that $\sigma_{pp} - \sigma_{\bar{p}p}$ vanishes at high energy. The extrapolations to higher energy (Durand & Pi (1989) - denoted by the dotted lines in fig. 5.2) are based on a QCD model of hadronic interactions to be discussed further in §5.4.

5.2 Nuclear cross sections

The relation between hadron–nucleon and hadron–nucleus cross sections is given by the multiple scattering theory of Glauber (Glauber & Matthiae, 1970). A simplified version of the full theory[2] is represented by the formula

$$\sigma_{\mathrm{abs}} = \int \mathrm{d}^2 b \{1 - \exp[-\sigma T(b)]\}. \tag{5.1}$$

Here $\sigma_{\mathrm{abs}} = \sigma_{\mathrm{tot}} - \sigma_{\mathrm{el}}$ for hadron–nucleus scattering and σ is the corresponding hadron–nucleon cross section. The function $T(b)$ is the number of target nucleons/cm^2 in the nucleus at impact parameter b:

$$T(b) = \int \rho_N(b)\mathrm{d}z, \tag{5.2}$$

where ρ_N is the number density of nucleons at distance $r = \sqrt{b^2 + z^2}$ from the center of the nucleus.

Two limits follow directly from (5.1). If σ is very small, then there is no "shadowing," and

$$\sigma_{\mathrm{abs}} \approx \int \sigma T(b)\mathrm{d}^2 b = A\sigma. \tag{5.3}$$

In the opposite limit of complete screening (σ very large) the integrand of (5.1) is approximately unity out to an effective nuclear radius R_A, so

$$\sigma_{\mathrm{abs}} \approx \pi R_A^2 \propto A^{2/3}. \tag{5.4}$$

In the range of beam momentum 20–50 GeV/c, the A-dependence of $\sigma_{\mathrm{p-nucleus}}$ for $A > 1$ can be approximated (Denisov et al., 1973) by

$$\sigma_{pA}^{\mathrm{inel}} \cong 45 \text{ mb } A^{0.691}. \tag{5.5}$$

This A dependence is closer to the black disk limit of (5.4) in which $\sigma_{hA} \propto A^{2/3}$, than to the transparent limit (5.3) in which the nuclear cross section is proportional to the nuclear mass number, A. In contrast

$$\sigma_{\pi A} \cong 28 \text{ mb } A^{0.75}. \tag{5.6}$$

The larger exponent in (5.6) is a consequence of the fact that $\sigma_{\pi p}^{\mathrm{inel}} < \sigma_{pp}$, so that π-nucleus scattering is farther from the black disk limit. Thus

$$\sigma_{\pi A}/\sigma_{pA} > \sigma_{\pi p}/\sigma_{pp}.$$

For the same reason, σ_{pA} increases more slowly with energy than σ_{pp}. We will also sometimes need values for inelastic cross sections between two nuclei. A standard parametrization, used originally to describe emulsion data at tens of GeV, is

$$\sigma_{A_1 A_2} = \pi R_0^2 (A_1^{1/3} + A_2^{1/3} - \delta)^2, \tag{5.7}$$

with $\delta = 1.12$ and $R_0 = 1.47$ fm (Westfall et al., 1979).

---

[2] See Gaisser, Sukhatme and Yodh (1987) for a brief summary, with references, of the relevant multiple scattering formalism.

The full multiple scattering theory must take account of the angular dependence of hadron–nucleon scattering, which affects the degree of screening. This angular dependence is characterized by the "slope" parameter, B, in the elastic scattering amplitude. The conventional form used to fit the elastic amplitude at small angles is

$$f(q) \;=\; \frac{k\,\sigma^{\rm tot}}{4\pi}\,(\rho + i)\,\mathrm{e}^{-Bq^2/2},$$

where ρ here is the ratio of the real to the imaginary part of the scattering amplitude, and $\mathbf{q} = \mathbf{k} - \mathbf{k}'$ is the momentum transfer. The value of the hadron–nucleus cross section depends both on $\sigma_{pp}^{\rm tot}$ and on the slope parameter, B. For a given value of $\sigma_{pp}^{\rm tot}$, the nuclear cross section is larger for larger B. Contour plots relating the proton–proton and proton–nucleus cross section for various values of slope parameter are given in the paper by Gaisser, Sukhatme and Yodh (1987).[3] These may also be used to estimate nuclear cross sections of other hadrons.

Hadron–nucleus cross sections have been measured up to several hundred GeV. Over this energy range it is therefore possible to check the multiple scattering relation between σ_{hN} and $\sigma_{h-\rm nucleus}$. This has been studied by Yodh et al. (1983) with good results, so the multiple scattering relation can be used at higher energy with confidence. Thus, we can use the total pp cross section from fig. 5.2, together with a parametrization of the slope parameter (Durand & Pi, 1989), to construct $\sigma_{p-\rm air}^{\rm inel}$ from the appropriate contour plots. The result is shown in fig. 5.3. The measured values of π–air and K–air cross sections around 100 GeV are indicated by the corresponding symbols on the figure, and an extrapolation analogous to that for p–air is also shown for π–air. Corresponding values of hadron interaction lengths in hydrogen and in air ($A \cong 14.5$) are summarized in Table 5.1. They are related to the inelastic cross sections by (3.3).

The relation between $\sigma_{pp}^{\rm inel}$ and $\sigma_{p-\rm air}^{\rm inel}$ is rather well-determined in a class of models in which nucleon–nucleon scattering is related to the charge distribution in the nucleons as measured by electron scattering (Block & Cahn 1985). Kopeliovich et al. (1989) give the following numerical formula valid at high energy ($E_{\rm Lab} > 2$ TeV)

$$\sigma_{p--\rm air}^{\rm inel} \;\approx\; 507\ {\rm mb}\left(\frac{\sigma_{pp}^{\rm inel}}{100\ {\rm mb}}\right)^{0.529}.$$

The predicted increase in the cross section is large enough so that it can have important effects for very energetic showers. For example, the p–air cross section from fig. 5.3 at 10^{19} eV is slightly larger than

---

[3] The contour plots in this reference give values of $\sigma_{p-\rm air}^{\rm inel}$ in which diffractive excitation of the target nucleon to an "isobar" state has been subtracted. In this book, I use the more usual definition of the p-air inelastic cross section, which includes all pion production, even if only a target nucleon is excited. The difference is about 20 mb out of 300–400 mb. Processes in which only the target nucleus breaks apart, but no pions are produced, are excluded from the inelastic hadron–nucleus cross section because they make no contribution to high energy cascades.

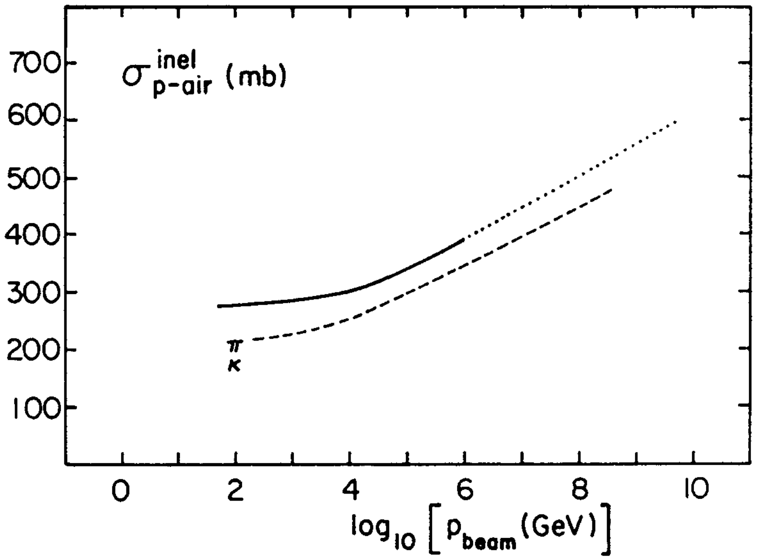

Figure 5.3: The inelastic p–air cross section predicted from a QCD minijet model.

Table 5.1: Interaction lengths of hadrons (g/cm^2).

$E_{\rm Lab}$(TeV)	$p-p$	p-air	$\pi-p$	π-air	$K-p$	K-air
0.1	53	86	82	116	96	138
1.0	49	83	[74]	[107]	-	-
1000	30	60	[41]	[70]	-	-
10^6	[15]	[43]	[26]	[50]	-	-

the α–air cross section from (5.7). In fact, reported values of the p–air cross section from air shower experiments in the 10^{17} to 10^{18} eV range (Hara et al., 1983; Baltrusaitis et al., 1984) are consistent with the extrapolation of the p–air cross section in fig. 5.3 (see §17.3). Unfortunately, interpretation of the air shower measurements is very difficult for two reasons. First, at these high energies the primary composition is not known, so an unknown fraction of the showers may be due to nuclei heavier than protons. Second, fluctuations in the response of the detectors add to the intrinsic fluctuations in shower development. This obscures the intrinsic fluctuations that must be isolated and measured to determine the cross section from air shower experiments in which the primary itself is not detected. (See e.g. Ellsworth et al., 1982 and the book by Sokolsky (1988) for further discussion.)

Various observations suggest that air showers indeed develop rather more rapidly than expected, so qualitatively this argues in favor of large cross sections at high energy - and perhaps also a larger fraction of heavy primaries. This would be consistent with a continuation to $\sim 10^{18}$ eV of trends suggested by the emulsion chamber measurements up to $\sim 10^{15}$ eV, as discussed in chapter 4. As a historical point, it is interesting to note that cosmic ray experiments of a different sort were successfully used to point out the increase in σ_{pp} from 1–30 TeV before it was measured at accelerators (Yodh, Pal & Trefil, 1972, 1973).

5.3 Inclusive cross sections

Development of quark models for inclusive cross sections in hadronic interactions is currently an active field of research, and a systematic treatment is beyond the scope of this book. The current state of the field is admirably described in the book by Anisovich et al. (1985). Briefly, one expects the momentum distributions of the secondaries to reflect the momentum distributions of the partons inside the incident hadrons. This leads to the expectation of hadronic scaling as alluded to in chapter 2. The scaling is modified, however, by QCD processes, as discussed in the next section.

Quark distributions inside hadrons (structure functions) are divided into two components, valence quarks and sea quarks. Explicit forms for the structure functions may be found in the review of Eichten

et al. (1984). The quark distributions are normalized to obtain the correct number of valence quarks. For a proton, for example,

$$\int_0^1 [u(x) - \overline{u}(x)]\,dx = 2$$

and

$$\int_0^1 [d(x) - \overline{d}(x)]\,dx = 1. \tag{5.8}$$

Here $u_v(x) = u(x) - \overline{u}(x)$ is the distribution of valence up quarks in the proton, and $d_v(x)$ is similarly defined for down quarks. The "sea" consists of an equal mixture of quarks and antiquarks. The sea quark distribution, $S(x)$, is customarily defined to include up, down and strange flavors in equal numbers, so that for example $\overline{u}(x) = \frac{1}{6}S(x)$. Charm and heavier flavors are treated separately.

The momentum carried by the quarks in a proton, expressed as a fraction of the proton momentum, is

$$f_q \equiv \int_0^1 \{x u_v(x) + x d_v(x) + x S(x)\}\,dx \cong 0.5. \tag{5.9}$$

The rest of the proton's momentum (roughly half) is presumed to be carried by gluons. Their momentum distributions inide a proton can also be characterized by a structure function, $G(x)$. Gluons and quarks are referred to collectively as *partons.* All structure functions have a behavior at small x that can be characterized by x^{-p} (where the power p may be a function of momentum transfer, etc). For valence quarks, the normalization conditions (5.8) require $p < 1$. For sea quarks and gluons, however, $p > 1$. The number of sea quarks and gluons is therefore divergent at $x = 0$. In practice the divergence is avoided because there is always a threshold mass parameter. Thus for pion production, $x > 2m_\pi/\sqrt{s}$. For production of a jet with transverse momentum greater than some threshold value, $x > 2p_T^{\min}/\sqrt{s}$. Therefore, because of the divergence of $S(x)$ and $G(x)$ at small x, processes with high transverse momentum will become more important as $\sqrt{s}$ increases.

Because the valence quarks have much flatter distributions than the sea quarks and the gluons, the inclusive distributions of secondaries in the fragmentation regions reflect mainly the valence quark distributions. In contrast, the central region, especially at high energy, reflects the structure functions for sea quarks and gluons. Since the behavior of the gluon and sea quark distributions is uncertain at very small values of x, the behavior of inclusive cross sections is less certain in the central region than in the fragmentation regions.

An essential feature of the structure functions is that they depend on the momentum transfer to the lepton used to measure them (see figs. 2.5 and 2.6). This "QCD evolution" of the structure functions is predicted by the theory. It arises essentially from the increased probability for emission of soft gluons at large momentum transfer, which increases the number of partons at small x. There is a similar evolution of the fragmentation functions that describe partons $\rightarrow$ hadrons.

In summary, we expect the momentum distributions of secondary hadrons to reflect the momentum distributions of their parent partons. Because the quark and gluon distributions depend on the momentum transfer scale, we expect the inclusive hadron cross sections to show a scaling violation if, as expected, high transverse momentum processes become relatively more important at high energy. The fastest hadrons (fragmention region) will be descended primarily from "spectator" valence quarks, which will not have scattered through large angles. We therefore expect these particles to come closest to showing scaling behavior. Slow particles in the "central region" are associated primarily with gluons and sea quarks, which become more numerous at high energy where smaller values of x are probed in the structure functions. This leads to a marked increase in the inclusive cross section near $x_F = 0$.

Data taken with the UA5 detector at CERN over an energy range from $\sqrt{s}$ = 53 GeV to 900 GeV illustrate these points. The upper graph in fig. 5.4 shows the energy dependence of the inclusive cross sections for charged particles. The pseudorapidity variable ($\eta \equiv -\ln\tan\frac{1}{2}\theta$) is used because the detector only measures the directions of tracks, not momenta. To the extent that the transverse momentum distribution is known, the distribution in pseudorapidity can be related to a distribution in x_F or rapidity, y. The dip in the pseudorapidity distribution near zero is a kinematic effect due to the Jacobian of the transformation between η and y. Because of the logarithmic relation between pseudorapidity (or rapidity) and momentum, the region near $x_f = 0$ in the CM is stretched out in a pseudorapidity distribution; however, $\eta = 0$ corresponds to x_F=0. The inclusive cross section at η = 0 rises by somewhat less than a factor of two with slightly more than an order of magnitude increase in center of

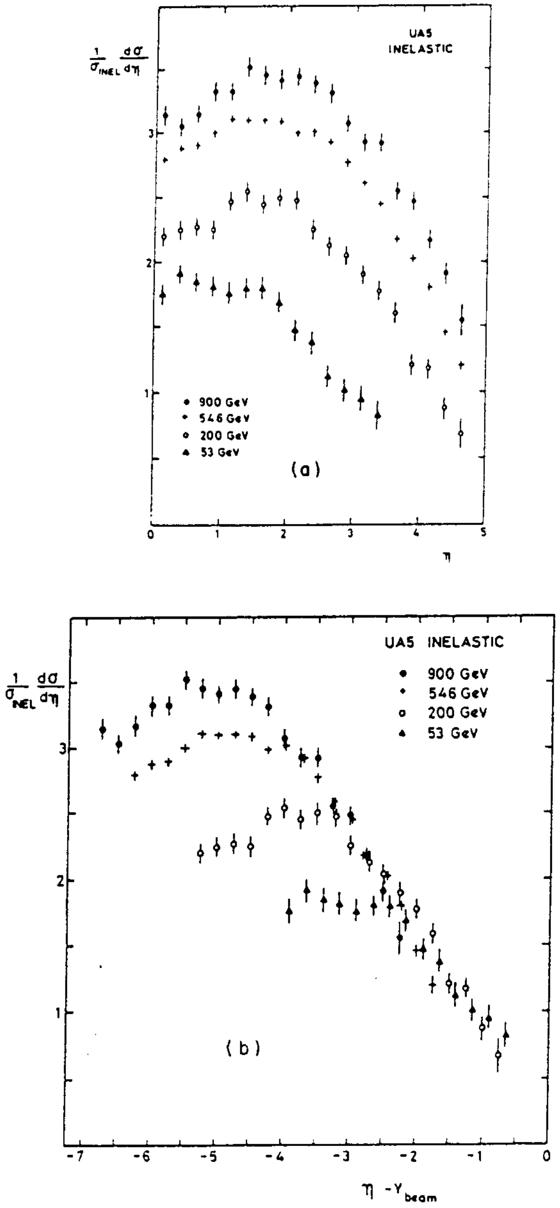

Figure 5.4: Pseudorapidity distributions of charged particles (Alner et al. 1986b).

mass energy, which corresponds to more than two orders of magnitude in laboratory energy ($\sim$ 1.5 TeV to $\sim$ 430 TeV). Thus, even in the central region, scaling violation is relatively slow.

Problem: Show from the definitions in table 2.3 that

$$y = \ln\frac{E+p_{\parallel}}{\mu_T} \quad \text{and} \quad \eta = \ln\frac{p+p_{\parallel}}{p}$$

Hence show that, for fixed transverse momentum,

$$\frac{dn}{d\eta} \to \frac{dn}{dy}, \quad \text{for } p \gg m$$

and

$$\frac{dn}{d\eta} \to \frac{p}{E}\frac{dn}{dy}, \quad \text{for } p_{\parallel} = 0.$$

In the lower graph in fig. 5.4, the distributions have been shifted by $y_{\text{beam}} \approx \ln(2E_{\text{beam}}/m_p)$ so that the fragmentation regions overlap. This is equivalent to a Lorentz transformation of each distribution to the rest frame of one of the projectile nucleons. A Lorentz boost with velocity $\beta = \beta_{\text{beam}}$ transforms the rapidity variable according to

$$y' = y + \frac{1}{2}\ln\frac{(1-\beta)}{(1+\beta)} = y - y_{\text{beam}}.$$

Apart from possible x-dependence of the transverse momentum distribution, the shifted pseudorapidity distributions will overlap in the fragmentation region if scaling is valid there It is clear from fig. 5.4 that scaling holds at least approximately in the fragmentation region, though there appears to be a slight tendency for the distributions to soften as energy increases.

Inclusive cross sections on nuclear targets are surprisingly similar to those on protons. There is an excess of slow particles that is larger for heavier nuclei. Also, the fragmentation region is somewhat depleted as compared to the case of a nucleon target. These effects are far less, however, than would be expected if every particle created in the first hadron–nucleon encounter within the nucleus were available for reinteraction inside the same nucleus. One explanation is that the excited projectile acts as a single object inside the nucleus and only materializes after it emerges. In addition, slow particles with p_T/E large enough to become separated from the projectile jet by more than one fermi while they are still inside the nucleus may reinteract.

As far as possible, it is best to use nuclear target data directly for atmospheric cascade calculations to minimize dependence on models of nuclear cascading. In any case, cascading is relatively unimportant in light nuclei.

5.4 Minijet model

It is tempting to try to extend perturbative QCD to low transverse momentum and make a model for inclusive cross sections that accommodates, or even "predicts," the scaling violation implicit in fig. 5.4. There is an observed correlation between transverse momentum and multiplicity that suggests that the rise with energy of the central plateau may be associated with the increasing importance of QCD jets that have p_T^{jet} of a few GeV. There is experimental support for this idea from the UA1 experiment (Albajar et al. 1989), which sees evidence for production of small "minijets" at the level of 10% of the inelastic cross section. If there is a threshold around $p_T^{\text{min}} \sim$1–2 GeV above which the QCD coupling is weak enough to justify use of perturbation theory, then contributions from processes like those shown in fig. 2.8 should make a calculable contribution to the cross section.

If we call this contribution σ_{jet}, it can be calculated by integrating a sum of terms like

$$\frac{d\sigma_{\text{jet}}}{dx_1 dx_2 d\cos\hat{\theta}} = F(x_1)\,F(x_2)\,\frac{d\hat{\sigma}}{d\cos\hat{\theta}}, \tag{5.10}$$

where $F(x)$ denotes a quark or gluon structure function and $\hat{\sigma}$ represents the corresponding elementary cross section for scattering of the partons. To ensure that the QCD calculation makes sense, the region of integration of (5.10) must be restricted to

$$\sim 1.5 \text{ GeV} \sim p_T^{\text{min}} < p_T^{\text{jet}} \sim \frac{\sqrt{x_1 x_2 s}}{2}\sin\hat{\theta}. \tag{5.11}$$

Long ago Cline, Halzen and Luthe (1973) noted that the integral of (5.10) gives an increasing contribution to the cross section. This is because of the growth of the structure functions (especially the gluon content) at small x, a region which becomes increasingly important as s increases - see (5.11). In fact, the σ_{jet}, defined by the integral of (5.10), becomes *larger* than the total cross section around $\sqrt{s}$ of several TeV. This is a symptom of the fact that σ_{jet} is an inclusive cross section. This follows from the nature of the structure functions, $F(x)$, which simply count the number of partons in the given x-range that are available for scattering. Thus the mean number of pairs of minijets is

$$< N(s) >= \frac{\sigma_{\rm jet}}{\sigma_{\rm inel}}. \qquad (5.12)$$

When multiple scattering becomes important, $N > 1$ in (5.12), and the calculation of the total cross section becomes nontrivial. It is then necessary to treat the multiple scattering in a quantum mechanical framework that accounts for interference and cancellation between various terms (Durand & Pi, 1987). The formalism is similar to the treatment of scattering on nuclei in terms of multiple scattering of constituent nucleons. The relevant equation is similar to (5.1) with $T(b)$ replaced by the density profile of the nucleon, and $\sigma \to \sigma_{\rm jet}$. The extrapolation of the total cross section shown in fig. 5.2 is based on an equation like (5.1) due to Durand and Pi (1989).

The minijet model also has interesting consequences for the extrapolation of the inclusive cross sections. By energy conservation, it relates the central region to the fragmentation region in a physically reasonable way. Production of minijets increases with energy; as more are produced there is less energy left for the beam jets. This leads to a small violation of scaling in the fragmentation region—the Z_{ij} become slightly smaller at high energy. It is possible to build a quantitative interaction model of this type for use in cosmic ray cascade calculations (Gaisser & Stanev, 1989). Such a model has two main applications, both of which require extrapolation beyond the kinematic regions explored by accelerator experiments:

Coincident energetic muons. The central region is measured at hadron colliders up to energies equivalent to 1000 TeV lab energy, but the fragmentation region is only measured directly at fixed target experiments, up to a TeV. The energy range around 1000 TeV is relevant for measurements of coincident multiple muons in large, deep detectors. Because the detectors are of finite extent, not all muons in a shower front will intersect the detector. It is therefore crucial to know the transverse structure of the events, as well as the correlation between the central and fragmentation regions, in order to interpret the events correctly.

Giant air showers. Interpretation of giant air shower experiments, such as Fly's Eye (§14.2.4), that work with showers of energies of millions of TeV, requires extrapolation well beyond the energy range of current collider experiments. Extrapolation of the model over three orders of magnitude in center of mass energy (from 1 TeV to 10^6 TeV in laboratory energy) leads to nearly a threefold increase in central rapidity density, and also to a shift of energy from the fragmentation region to the central region (see §5.6 below). Both the types of air shower experiment mentioned here will be the subject of later chapters.

5.5 Spectrum weighted moments

The fluxes of uncorrelated particles in the atmosphere depend primarily on the fragmentation region because of the steep energy spectrum of the cosmic rays. Mathematically, the factor $x^{\gamma-1}$ in the integrand of Z_{ij} in (3.15) suppresses the dependence on $F(x, E)$ near $x = 0$. We can therefore reliably use fixed target accelerator data with beam energy ≤ 1 TeV for estimates of uncorrelated fluxes even beyond 1 TeV. We have used the data of Brenner et al.(1982) on proton targets and of Barton et al. (1983) and Braune et al. (1983) on nuclear targets to obtain values of Z_{ij}. We will later have occasion to use Z_{ij} for values of γ different from that of cosmic rays at Earth. An example is the calculation of secondaries produced by cosmic rays near an astrophysical source where the spectrum may be less steep than in the terrestrial atmosphere. We therefore show in fig. 5.5 the values of Z_{ij} for a proton beam on a proton target as a function of spectral index γ. Recall that for $\gamma = 1$ Z_{ij} is the fraction of the beam energy carried off by particles of type j. Table 5.2 gives Z_{ij} for protons, pions and kaons on a nucleus of mass $A = 14.5$ to be used for calculations in the atmosphere. Here the numbers are evaluated at $\gamma = 1.7$.

Some relations among the moments follow from isospin symmetry:

$$Z_{p\pi^\pm} = Z_{n\pi^\mp} \;\text{ and }\; Z_{pK^{+,0}} = Z_{nK^{0,+}}. \qquad (5.13)$$

Note that $Z_{pK^+} \neq Z_{nK^-}$ because K^+ and K^- are not in the same isospin multiplet. In fact

$$Z_{pK^+} \approx Z_{pK^0} \gg Z_{NK^-} = Z_{N\overline{K}^0}$$

because the K^+ and ^{0} can be produced in association with a leading Λ or Σ baryon, whereas production of $\overline{K}$ requires production of

Table 5.2: Spectrum-weighted moments for hadrons on air nuclei.

projectile	p	π^+	K^+
p	0.263	-	-
n	0.035	-	-
π^+	0.046	0.243	0.030
π^-	0.033	0.028	0.022
π^0	0.039	0.098	0.026
K^+	0.0090	0.0067	0.211
K^-	0.0028	0.0067	0.012

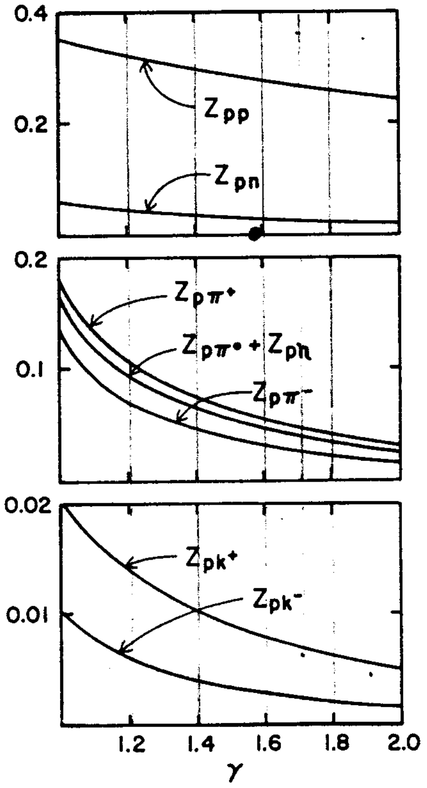

Figure 5.5: Spectrum-weighted moments for protons on hydrogen as a function of integral spectral index of the protons.

a strange–antistrange pair in addition to the leading nucleon. Integrated inclusive cross sections of the type needed to compute the moments have especially large uncertainties for π^0 and η production because of the difficulty of reconstructing the parent meson distribution from an observed distribution of photons from decay of the mesons. In table 5.2 η production has been neglected. In fig. 5.5 the assumption for the η is $Z_{p\eta} = (m_\pi^2/m_\eta^2)Z_{p\pi^0}$. Production of the η-meson may be even more important than this at high energy.

There is an important disclaimer that must accompany the numerical values of Z_{ij} in fig. 5.5 and table 5.2. These are global numbers that depend on extrapolations and interpolations into regions where data do not exist. Any independent treatment of the data (which the reader is urged to undertake for himself for any serious calculation) will therefore lead to somewhat different values of the Z_{ij}. The values here should be treated as indicative rather than definitive.

5.6 Inelasticity

The inelasticity, like the cross section, is a global parameter of hadronic interactions that is of fundamental importance for cosmic ray cascades. It is defined as the fraction of energy given up by the leading nucleon[4] in a collision induced by a proton or neutron incident on a target nucleon or nucleus. An analogous definition of inelasticity can be made for collisions with pions and kaons as projectiles. Formally, the inelasticity, K, in a proton-induced collision is related to the spectrum-weighted moments evaluated at $\gamma = 1$ as

$$1 - K = Z_{pp}(\gamma = 1) + Z_{pn}(\gamma = 1) = Z_{NN}(1)$$

(neglecting $N\bar{N}$ production). At low energy the inelasticity is slightly less than 0.5 in *pp* collisions and roughly 0.4 in *p*–air interactions.

The discussion of §5.4 shows that the inelasticity increases with energy in a minijet model, as a consequence of the increased energy that goes into production of minijets in the central region. Kopeliovich et al. (1989) have shown that in a naive multiple scattering model, the leading particle distribution in proton-proton and in

---

[4] "Leading nucleon" as defined here is a theoretical concept. Correction must be made for baryon-antibaryon production before inelasticity can be determined experimentally. Inelasticity here is defined in the laboratory system, as appropriate for cascade calculations.

proton-nucleus collisions is determined at high energy by $\sigma_{pp}^{\mathrm{inel}}$. They give explicit parametrizations of the leading particle distributions and the inelasticity at high energy. For example, for the p–air cross section shown in fig. 5.3, they predict an average inelasticity of about 0.7 at $E_{\mathrm{Lab}} \sim 10^6$ GeV and 0.8 at $\sim 10^9$ GeV for proton collisions on hydrogen, assuming an average inelasticity of 0.5 at $E_{\mathrm{Lab}} = 100$ GeV. The corresponding numbers with an atmospheric nucleus as target are 0.8 and 0.9.

Such large inelasticity values would have significant effect on cascade development because they imply rapid deposition of energy by a high energy proton as it penetrates into the atmosphere. Not all models predict such a rapidly increasing inelasticity. In the minijet model, for example, the inelasticity increases more slowly, reaching ~ 0.63 at $E_{\mathrm{Lab}} \sim 10^6$ GeV and ~ 0.69 at $E_{\mathrm{Lab}} \sim 10^9$ GeV for p-nucleus interactions. At the other extreme, some models predict that the inelasticity *decreases* as energy increases. For example, a statistical model of particle production (Fowler et al., 1987) gives $K \sim 0.26$ and ~ 0.1 for $E_{\mathrm{Lab}} \sim 10^6$ and $\sim 10^9$ GeV, respectively. It is difficult to discriminate between even such drastically different models with collider experiments because the important high energy fragments are too near the beam to be readily detected. It may be possible to rule out the extreme of low inelasticity by comparison with observations of individual cascades with the Fly's Eye experiment, because a very low inelasticity would tend to produce very deeply penetrating showers. This question is currently under investigation.

Chapter 6

Muons

Muons are nearly stable and have a small cross section for interactions, so they are very penetrating. Indeed, muons are traditionally called the "penetrating component" of cosmic rays. Yet, because they are charged, they are relatively easy to detect. Thus muons give the dominant signal deep in the atmosphere and underground. The classic discussion of high energy muon fluxes and their measurement deep underground is the review of Barrett, Bollinger, Cocconi, Eisenberg and Greisen in 1952, which remains a very useful reference.

6.1 Muons in the atmosphere

The production spectrum of muons is calculated from (4.2) by folding the kinematics for $\pi \to \mu\,\nu$ and $K \to \mu\,\nu$ (4.10) with the spectrum of decaying parents. For the two body decay, $M \to \mu\,\nu$, it follows from the discussion of §4.1 that, for decay of relativistic mesons,

$$\frac{\mathrm{d}n}{\mathrm{d}E_\mu} = \frac{\mathrm{d}n}{\mathrm{d}E_\nu} = \frac{1}{1-r_M}\,\frac{1}{E_M}. \tag{6.1}$$

Here M is the mass of a parent meson of total energy E_M, and $r_M \equiv \mu^2/M^2$. From (4.2) and a similar equation for charged kaons we have

$$\begin{aligned} \mathcal{P}_\mu(E,X) \;=\; & \frac{\epsilon_\pi}{X\cos\theta(1-r_\pi)}\int_{E_\mu}^{E_\mu/r_\pi}\frac{\Pi(E,X)}{E}\frac{\mathrm{d}E}{E} \\ & + \frac{0.635\,\epsilon_K}{X\cos\theta(1-r_K)}\int_{E_\mu}^{E_\mu/r_K}\frac{K(E,X)}{E}\frac{\mathrm{d}E}{E}. \end{aligned} \tag{6.2}$$

Equation (6.2) applies for angles small enough ($< 60°$) so the curvature of the Earth can be neglected. The limits on the integrals in (6.2) give the range of parent energies that can produce a muon of energy E_μ. The limits are obtained by inverting the limits on muon energy for fixed parent energy.

The full expression for the muon production spectrum follows by substituting (3.30) and the corresponding expression for kaons into (6.2). When $E_\mu \gg \epsilon_\mu$, both muon decay and energy loss in the atmosphere can be neglected. Then the differential muon energy spectrum at depth X is

$$\mu(E_\mu, X) = \int_0^X \mathcal{P}_\mu(E_\mu, X)\mathrm{d}X. \tag{6.3}$$

For $X \gg \Lambda_i$, the upper limit can be taken to infinity. Then

$$\begin{aligned}\frac{\mathrm{d}N_\mu}{\mathrm{d}E_\mu} = \; & N_0(E_\mu) \; \left\{\frac{Z_{N\pi}}{1-r_\pi}\xi_\pi(E_\mu)I_\pi(E_\mu)\right. \\ & \left. +0.635\frac{Z_{NK}}{1-r_K}\xi_K(E_\mu)I_K(E_\mu)\right\},\end{aligned} \tag{6.4}$$

where $\xi_i(E_\mu) \equiv \epsilon_i \times (E_\mu \cos\theta)^{-1}$ and

$$\begin{aligned}I_i(E_\mu) \; = \; & \frac{\Lambda_i}{\lambda_N}\int_1^{1/r_\pi}\frac{\mathrm{d}z}{z^{\gamma+2}} \\ & \times \left[\frac{1}{z+\xi_i(E_\mu)} - \frac{\Lambda_i/\Lambda_N - 1}{2z+\xi_i(E_\mu)} + \frac{(\Lambda_i/\Lambda_N-1)^2}{3z+\xi_i(E_\mu)} - \cdots\right].\end{aligned} \tag{6.5}$$

In the limiting cases respectively of high and low energy,

$$\begin{aligned}I_i(E_\mu) \; & \rightarrow \; \frac{1}{(\gamma+2)}\frac{\Lambda_N}{\lambda_N}\left[1-(r_i)^{\gamma+2}\right]\frac{\Lambda_i}{\Lambda_i-\Lambda_N}\ln\frac{\Lambda_i}{\Lambda_N} \\ & \rightarrow \; \frac{1}{(\gamma+1)}\frac{\Lambda_N}{\lambda_N}\left[1-(r_i)^{\gamma+1}\right]\frac{1}{\xi_i(E_\mu)}.\end{aligned} \tag{6.6}$$

An approximate expression that combines the high and low energy forms is

$$\begin{aligned}\frac{\mathrm{d}N_\mu}{\mathrm{d}E_\mu} \simeq \; & \frac{N_0(E_\mu)}{1-Z_{NN}} \\ & \left\{ \mathcal{A}_{\pi\mu}\frac{1}{1+\mathcal{B}_{\pi\mu}\cos\theta E_\mu/\epsilon_\pi} \right. \\ & \left. +0.635\,\mathcal{A}_{K\mu}\frac{1}{1+\mathcal{B}_{K\mu}\cos\theta E_\mu/\epsilon_K}\right\}.\end{aligned} \tag{6.7}$$

Here

$$\mathcal{A}_{\pi\mu} \equiv Z_{N\pi}\left[1-(r_\pi)^{\gamma+1}\right](1-r_\pi)^{-1}(\gamma+1)^{-1}$$

and

$$\mathcal{B}_{\pi\mu} \equiv \frac{(\gamma+2)}{(\gamma+1)}\frac{1-(r_\pi)^{\gamma+1}}{1-(r_\pi)^{\gamma+2}}\frac{\Lambda_\pi-\Lambda_N}{\Lambda_\pi\ln(\Lambda_\pi/\Lambda_N)}.$$

$\mathcal{A}_{K\mu}$ and $\mathcal{B}_{K\mu}$ are defined similarly with the pion mass replaced by the kaon mass. We can use the results of chapter 5 to get numerical values for the various quantities in (6.7):

$$\frac{\mathrm{d}N_\mu}{\mathrm{d}E_\mu} \approx \frac{0.14\,E^{-2.7}}{\mathrm{cm^2\,s\,sr\,GeV}}\left\{\frac{1}{1+\frac{1.1\,E_\mu\cos\theta}{115\ \mathrm{GeV}}} + \frac{0.054}{1+\frac{1.1E_\mu\cos\theta}{850\ \mathrm{GeV}}}\right\}.$$

Comparison of this expression with the measured vertical muon flux at sea level is shown in fig. 6.1. Below 10 GeV muon decay and muon energy loss become important, and (6.7) then overestimates the flux. (See §7.1.2 for a discussion of the effect of energy loss by muons.) Note that the relative contribution from kaons increases substantially with energy even in this approximation in which Z_{NK} is assumed constant. At low energy, about 5% of vertical muons come from kaons. This increases to 8% at E_μ = 100 GeV, 19% at 1000 GeV and 27% asymptotically.

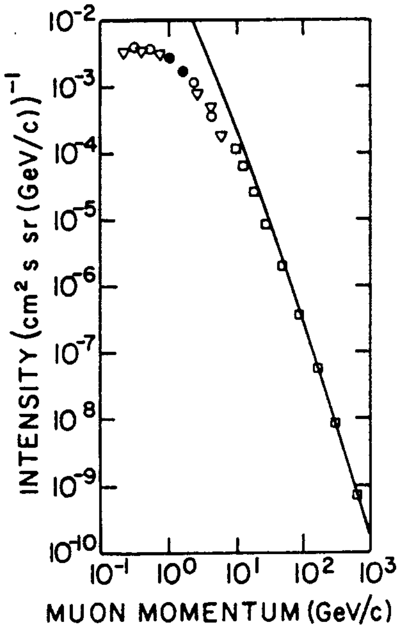

Figure 6.1: Comparison between measured muon flux and that calculated from (6.7). ⊙ Data is from a summary of Allkofer & Grieder (1984).

6.2 Relation to primary energy

It is often of interest to estimate the range of primary energies to which a given measured flux in the atmosphere corresponds. This information is contained in a "response curve" that shows the distribution of primary energies responsible for a certain measured quantity. Figure 6.2 is an example of an integral response curve. It gives the distribution of primary energies that produce vertical muons with $E_\mu > 14$ GeV at sea level. The corresponding differential response is

$$\frac{\mathrm{d}R_\mu}{\mathrm{d}E_\mu \mathrm{d}E_0} = \frac{\mathrm{d}n_\mu(E_\mu, E_0)}{\mathrm{d}E_\mu} N_0(E_0), \tag{6.8}$$

where $\mathrm{d}n_\mu/\mathrm{d}E_\mu$ is the differential yield of muons from a primary nucleon of energy E_0.

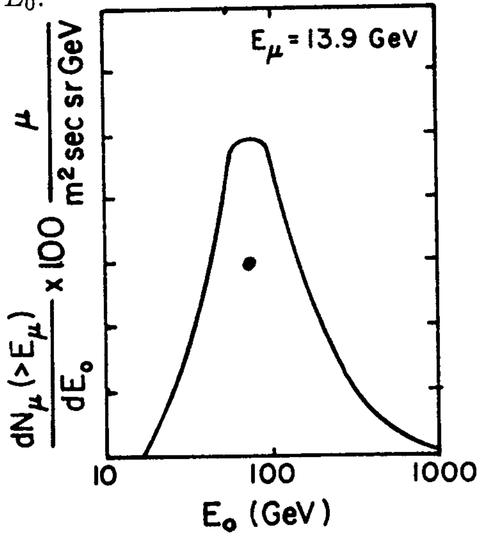

Figure 6.2: The muon response, $\mathrm{d}N_\mu(> E_\mu)/\mathrm{d}E_0$, as a function of primary energy E_0 for $E_\mu \geq 14$ GeV (from Gaisser, 1974).

The response curve shown in fig. 6.2 was obtained by multiplying the results of a numerical calculation of the muon yield by the primary spectrum. It is possible to write down a simple expression for the mean primary energy responsible for any secondary quantity, i:

$$< E_0 >_i = \left(\int_{E_i}^{\infty} E_0 \frac{\mathrm{d}R_i}{\mathrm{d}E_0} \mathrm{d}E_0\right) \left(\int_{E_i}^{\infty} \frac{\mathrm{d}R_i}{\mathrm{d}E_0} \mathrm{d}E_0\right)^{-1}.$$

The denominator of this expression is $n_i(E_i, X)$, so

$$\frac{< E_0 >}{E} = \frac{n_i'(E_i, X)}{n_i(E_i, X)}.$$

The interpretation of n_i' is that it is the flux of type i that would be measured if the primary spectrum were $N_0'(E_0) = [E_0/E] N_0(E_0)$. For the differential muon flux deep in the atmosphere

$$n_i' \rightarrow \frac{\mathrm{d}N_\mu'}{\mathrm{d}E_\mu} = N_0(E_\mu) \times \left\{ \frac{Z_{N\pi}'}{1 - r_\pi} \xi_\pi(E_\mu) I_\pi'(E_\mu) \right.$$
$$\left. + 0.635 \frac{Z_{NK}'}{1 - r_K} \xi_K(E_\mu) I_K'(E_\mu) \right\}.$$

Here the primed quantities are calculated with $\gamma' = \gamma - 1 \approx 0.7$.

As an illustration, consider the example shown in fig. 6.2. The energy 14 GeV is high enough for energy loss by muons to be neglected, but low enough for the low energy approximation for I_π to apply. If we also neglect the 5% contribution from kaons, then

$$\frac{< E_0 >}{E} \approx \frac{\gamma}{\gamma - 1} \left(\frac{1 - Z_{NN}}{1 - Z_{NN}'}\right) \frac{Z_{N\pi}'}{Z_{N\pi}} \left(\frac{1 - (r_\pi)^\gamma}{1 - (r_\pi)^{\gamma+1}}\right) \frac{\gamma + 1}{\gamma}$$

for the integral flux of muons with $E_\mu > E$. The corresponding expression for the differential muon flux is identical except for the omission of the initial factor $\gamma/(\gamma - 1) \approx 2.4$. With $Z_{NN} \approx 0.3$, $Z_{N\pi} \approx 0.08$, $Z_{NN}' \approx 0.5$ and $Z_{N\pi}' \approx 0.7$, we find $< E_0 > /E \approx 37$ for the integral spectrum. The mean primary energy for $E_\mu > 14$ GeV is thus ~ 500 GeV/nucleon, in agreement with the result of the numerical calculation in fig. 6.2. Note, however, that the distribution has a long tail, so the mean is significantly bigger than the median.

In the high energy limit, $E_\mu \gg \epsilon_\pi$, the parent nucleon energy is closer to the muon energy because of the suppression of the decay probability of pions and kaons with increasing energy. High energy mesons tend to interact before they decay. As in the low energy limit, the distribution of parent energies has a tail so that the mean parent energy is greater than the median. The ratio of median energy of parent nucleons to minimum muon energy is ≈ 10 for $E_\mu > 1$ TeV, decreasing to ≈ 8 for $E_\mu > 6$ TeV (Elbert et al., 1975). This is a range of muon energies relevant for deep underground detectors.

6.3 Muon charge ratio

We can use the results of the preceding chapters to make an analytic estimate of the muon charge ratio. To do so we need first to solve the analog of (3.28) for $\Delta_\pi \equiv \Pi^+(E,X) - \Pi^-(E,X)$,

$$\begin{aligned}\frac{\mathrm{d}\Delta_\pi}{\mathrm{d}X} &= -\left(\frac{1}{\lambda_\pi} + \frac{\epsilon_\pi}{E\,X\cos\theta}\right)\Delta_\pi \\ &+ \frac{\Delta_\pi}{\lambda_\pi}\left(Z_{\pi^+\pi^+} - Z_{\pi^+\pi^-}\right) + \frac{\Delta_N}{\lambda_N}\left(Z_{p\pi^+} - Z_{p\pi^-}\right). \qquad (6.9)\end{aligned}$$

Here, $\Delta_N = p(E,X) - n(E,X)$, and we have made use of the following isospin symmetries valid for isoscalar targets:

$$\begin{aligned} Z_{\pi^+\pi^+} &= Z_{\pi^-\pi^-} \qquad & Z_{p\pi^+} &= Z_{n\pi^-} \\ Z_{\pi^+\pi^-} &= Z_{\pi^-\pi^+} \qquad & Z_{p\pi^-} &= Z_{n\pi^+}. \end{aligned}$$

We now follow exactly the same sequence of steps used in §4.1 to find the total muon flux. In the low energy limit, accounting only for muons from decay of pions, the result for the muon charge ratio is (Frazer et al., 1972)

$$K_\mu \equiv \frac{\mu^+}{\mu^-} = \frac{1+\delta_0\mathcal{A}\mathcal{B}}{1-\delta_0\mathcal{A}\mathcal{B}}, \qquad (6.10)$$

where δ_0 is the relative proton excess at the top of the atmosphere (see chapter 3),

$$\mathcal{A} \equiv (Z_{p\pi^+} - Z_{p\pi^-})/(Z_{p\pi^+} + Z_{p\pi^-})$$

and

$$\mathcal{B} \equiv (1 - Z_{pp} - Z_{pn})/(1 - Z_{pp} + Z_{pn}).$$

The numerical value of K_μ is very sensitive to the factor $\mathcal{A}$. It is therefore crucial to use nuclear target data to get the correct value of the charge ratio. For the values of $Z_{p\pi^\pm}$ for nuclei with mass number $A = 14.5$, $K_\mu \approx 1.22$, but if we use the values of $Z_{p\pi^\pm}$ for single nucleon targets we find $K_\mu \approx 1.46$. The experimental value is approximately 1.25 in the low energy range ($E_\mu < 100$ GeV). At higher energies the contribution from kaon decay becomes important and the analysis is more complicated. In particular, unlike the case for pions, one cannot take $Z_{pK^+} = Z_{nK^-}$. As explained in §5.5, $Z_{pK^+} \gg Z_{nK^-} \approx Z_{pK^-}$ and the K^+/K^- ratio is larger than the π^+/π^- ratio. For this reason the muon charge ratio increases somewhat at high energy as muons from K-decay become increasingly important.

6.4 Passage of muons through matter

In preparation for a discussion of muons underground I review muon propagation through matter. Energy loss processes for muons can be divided into two categories - continuous and discrete. In the former, which is due to ionization of the medium through which the muon passes, the energy loss rate $\mathrm{d}E/\mathrm{d}X$ is nearly constant for relativistic particles. The magnitude depends somewhat on the medium. The energy loss rate for relativistic muons has a broad minimum (~ 1.8 MeV/(g/cm^2) in rock) below 1 GeV and rises slowly at higher energy. An approximate numerical formula for ionization loss of muons in rock, good to better than 5% for $E_\mu > 10$ GeV, is

$$\frac{\mathrm{d}E}{\mathrm{d}X} \approx -\left[\,1.9 + 0.08\ln(E_\mu/\mu)\,\right] \qquad (6.11)$$

(Rosental, 1968).[1] For numerical estimates of ionization loss here I use $\mathrm{d}E/\mathrm{d}X = -\alpha$ with $\alpha \sim 2$ MeV/(g cm^{-2}).

Muons also lose energy by bremsstrahlung, by electromagnetic interactions with nuclei and by direct production of e^+e^- pairs. For muons these processes are only important at high energy, and they are characterized by discrete bursts along the muon trajectory. On average, however, the energy loss rate for these processes is proportional to E. To see this, consider the inclusive cross section $F_{\ell\ell'}$ for the process

$$\ell(E) + \text{target} \rightarrow \ell(E') + \text{anything}, \qquad (6.12)$$

where E and E' are initial and final energies of a charged lepton ℓ. The mean energy loss per collision is

$$<\Delta E> = E\,(1 - \int_0^1 F_{\ell\ell'}(x)\mathrm{d}x), \qquad (6.13)$$

where $F_{\ell\ell'}$ is defined as in (3.4). Therefore, in traversing $\mathrm{d}X$ g/cm^2 of material the mean energy loss is

$$\mathrm{d}E = -E\left[1 - \int_0^1 F_{\ell\ell'}(x)\mathrm{d}x\right]\sigma\frac{N_A}{A}\,\mathrm{d}X \equiv \frac{E}{\xi(\ell)}\,\mathrm{d}X. \qquad (6.14)$$

---

[1] A compilation of the formulas and parameters for muon energy loss at high energy in a variety of materials is contained in the report of W. Lohrmann, R. Kopp and R. Voss, CERN Report 85-03. A Monte Carlo program for propagation of high energy muons through rock is that of T. Stanev, Bartol Technical Report BA-83-41.

As is well known, the cross section for bremsstrahlung is logarithmically divergent in the limit $E_{\ell'} \to E_{\ell}$, but the energy loss per collision (6.13) also vanishes in such a way that $\sigma \times (1 - \int F\mathrm{d}x)$ is finite. Thus the energy loss rate due to bremsstrahlung is well defined, and

$$\frac{\mathrm{d}E}{\mathrm{d}X} = -\frac{E}{\xi_B(\ell)}. \tag{6.15}$$

For electrons $\xi_B(e) \approx 61$ g/cm^2 in hydrogen, 37 g/cm^2 in air, 22 g/cm^2 in silicon and 13.8 g/cm^2 in iron.

The power radiated in each bremsstrahlung encounter with a nucleus is proportional to the square of the acceleration given to the radiating particle. For a given momentum impulse, the bremsstrahlung energy loss is therefore inversely proportional to the square of the mass of the radiating particle. Thus the radiation length for muons is approximately $(m_\mu/m_e)^2$ larger than that for electrons. Since the atmosphere is only 1030 g/cm^2 thick, bremsstrahlung in the atmosphere is crucial for electrons but completely negligible for muons. Discrete energy loss processes do, however, become important for propagation of muons deep underground.

For electrons, bremsstrahlung is by far the dominant mechanism for discrete energy loss. For muons, for which bremsstrahlung is suppressed by the mass-squared factor, direct pair production ($\mu + Z \to \mu\, e^+e^-\, Z'$) and muon hadroproduction (μ + nucleus $\to \mu$ + hadrons) are also important. (Direct pair production is comparable to but slightly more important than bremsstrahlung. Hadroproduction is about a factor of three less important.) In general then, we can write the energy loss rate for muons as

$$\frac{\mathrm{d}E}{\mathrm{d}X} = -\alpha - E/\xi, \tag{6.16}$$

where

$$\xi^{-1} = \xi_B^{-1} + \xi_{\text{pair}}^{-1} + \xi_{\text{hadronic}}^{-1},$$

and $\xi \approx 2.5 \times 10^5$ g/cm^2 in rock. Equating the two energy loss terms defines a critical energy, $\epsilon \equiv \alpha\xi$, above which discrete, radiative processes are more important than continuous energy loss. For electrons in air, the critical energy is $E_c \sim 80$ MeV. For muons in rock, $\epsilon \sim 500$ GeV.

The general solution of (6.16) is

$$< E(X) > = (E_0 + \epsilon)\mathrm{e}^{-X/\xi} - \epsilon. \tag{6.17}$$

The left side of (6.17) is to be interpreted as the mean energy of a beam of muons of initial energy E_0 after penetrating a depth X of material. A measure of the minimum energy required of a muon at the surface to reach slant depth X is the solution of (6.17) with residual energy $E(X) = 0$:

$$E_0^{\text{min}} = \epsilon\,(\mathrm{e}^{X/\xi} - 1). \tag{6.18}$$

6.5 Muons underground

For precise calculations of the flux of muons underground one needs to take account of fluctuations in range, which give rise to a distribution of energies at depth X even for a monoenergetic beam incident at the surface (see the footnote after (6.11) above). Fluctuations in energy due to the large range of energies in the spectrum are, however, much larger than fluctuations in propagation. It is therefore possible to obtain a semiquantitative understanding of the gross features of underground muons from (6.17) and (6.18), which neglect range straggling.

6.5.1 Depth–intensity relation

In this approximation, the vertical flux at depth X underground (measured from the surface) is

$$I_v(X) = N_\mu(> E_0^{\text{min}}(X)), \tag{6.19}$$

where $N_\mu(> E_\mu)$ is the vertical flux of muons at the surface. The deepest underground experiment currently in operation is at the Kolar Gold Fields (KGF) in India, with a vertical depth of 2.3 km, roughly equivalent to 7000 hg/cm^2.[2] The South African experiment (Crouch et al. 1978) was deeper, at 8.89 km.w.e. The vertical intensities at still deeper equivalent depths must be obtained from measurements made in other directions, with larger slant depths, corrected for the angular dependence of muon production in the atmosphere. For zenith angles less than ~ 60° the correction to the vertical can be made with (6.7). At larger angles, the curvature of the Earth must be accounted for,

---

[2] The notation hg stands for hectograms, and one hg/cm^2 is equivalent to one meter of water. The unit kilometers of water equivalent, km.w.e., is also used to represent slant depths to deep underground detectors. One km.w.e.= 10^5 g/cm^2.

as described in §3.5. At a mountain site such as Mont Blanc, the maximum flux will not be from overhead but from the direction that minimizes slant depth while maximizing zenith angle. When comparing measurements made at various locations, it is necessary to correct for differences in density of rock. For example, "Kolar rock" is characterized by $\rho = 3.04\,\mathrm{gm/cm^2}$, $Z/A = 0.495$, and $Z^2/A = 6.4$. The corresponding numbers for "standard rock" are 2.55, 0.5 and 5.5. The higher value of Z^2/A means that ξ_B and ξ_{pair} are about 8% shorter for Kolar rock than for standard rock. Table 6.1 is a summary of sites of current large underground experiments.

Table 6.1: Sites of some large subsurface experiments.

Location	Depth (km.w.e.)	E_0^{min} (TeV)
KGF	≤ 7 (many levels)	10 (deepest level)
Homestake	4.4	2.4
Mont Blanc	~ 5	~ 3
Frejus	~ 4.5	~ 2.5
Gran Sasso	~ 4	~ 2
IMB	1.57	0.44
Kamiokande	2.7	~ 1
Soudan	1.8	0.53

The relation between intensity underground and vertical depth is shown in fig. 6.3. The line shows the fluxes calculated from (6.7) with $\epsilon = 550$ GeV used to convert depth to energy with the relation (6.18). The muons at very large depths are produced by interactions in the rock of atmospheric neutrinos, a subject that is discussed in detail in the next two chapters.

6.5.2 Energy spectrum underground

At depth X the muon energy spectrum is

$$\frac{\mathrm{d}N_\mu(X)}{\mathrm{d}E_\mu} = \frac{\mathrm{d}N_\mu}{\mathrm{d}E_0}\,\frac{\mathrm{d}E_0}{\mathrm{d}E_\mu} = \frac{\mathrm{d}N_\mu}{\mathrm{d}E_0}\exp(X/\xi)\bigg|_{E_0=E_0^*}, \qquad (6.20)$$

which follows from (6.17) with $E_0^* = \mathrm{e}^{X/\xi}(E_\mu + \epsilon) - \epsilon$. For

$$X \ll \xi \approx 2.5 \text{ km.w.e.}, \qquad E_0 \approx E_\mu(X) + \alpha X.$$

Thus the muon energy spectrum at depth $X \ll \xi$ is approximately constant for $E_\mu(X) \ll \alpha X$ and steepens to reflect the surface muon spectrum for $E_\mu(X) > \alpha X$. For $X > \xi$, the underground differential spectrum is again constant for small muon energies but steepens to reflect the surface muon spectrum for $E_\mu(X) > \epsilon \approx 500$ GeV, independent of depth. Thus for $X \gg \xi$ the *shape* of the underground energy spectrum of muons becomes independent of depth. This behavior is illustrated in fig. 6.4 on the next page.

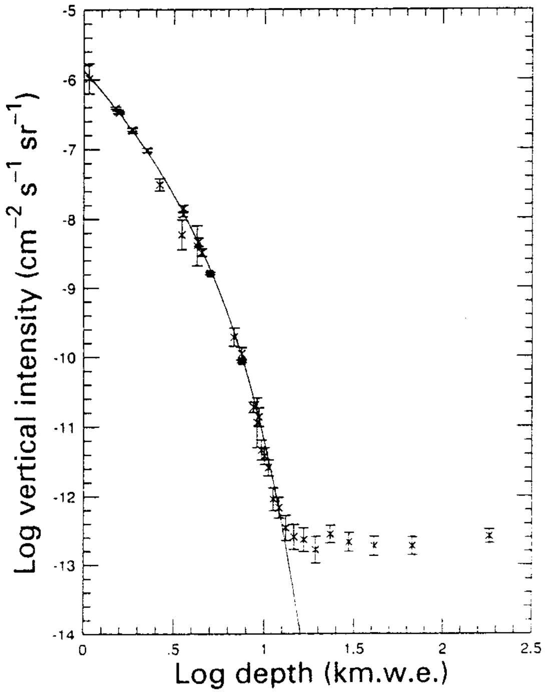

Figure 6.3: Relation between muon intensity and depth underground. The data are taken from a summary by Crouch (1987) with the addition of recent data from the Frejus experiment (Berger et al., 1989 – filled squares).

Another quantity of interest is the ratio, $R(X)$, of stopping to throughgoing muons in a detector of thickness ΔX at depth $X \gg \Delta X$. If we parametrize the integral muon flux at the surface by

$$N_\mu(> E_0) \sim K E_0^{-\gamma_\mu}, \qquad (6.21)$$

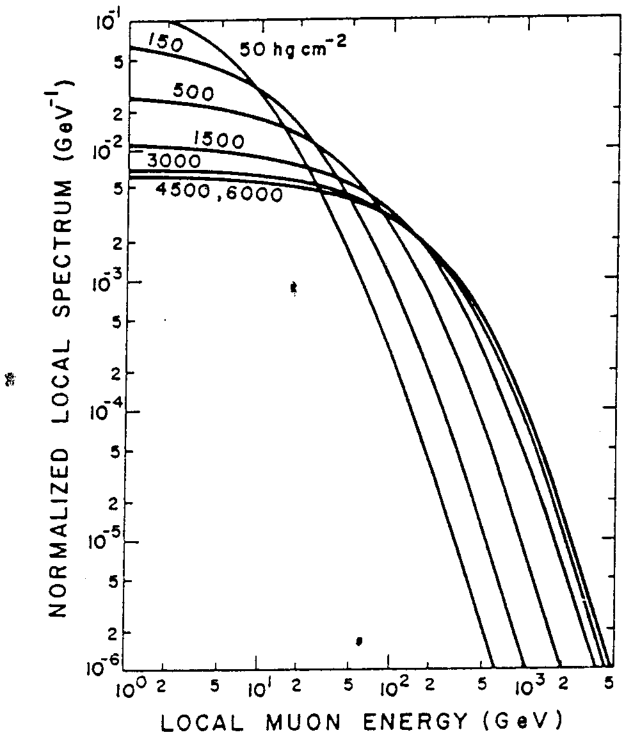

Figure 6.4: Local differential energy spectrum of muons underground, normalized to the vertical muon intensity at each underground depth shown. From Cassidy, Keuffel & Thompson (1973).

then

$$R(X) = \frac{\Delta N_\mu}{N_\mu} = \gamma_\mu \frac{\Delta E_0}{E_0} \approx \frac{\gamma_\mu \Delta E\, e^{X/\xi}}{(e^{X/\xi} - 1)\,\epsilon_\mu}. \tag{6.22}$$

Here $\Delta E \approx \alpha \Delta X$ is the minimum energy needed to traverse the detector. Typically ΔE is in the range of several GeV, $\ll \epsilon_\mu$. For shallow depths ($X < \xi$), $R(X) \propto 1/X$, while for depths $X > \xi$

$$R(X) \to \text{constant} \approx \gamma_\mu \frac{\Delta E}{\epsilon_\mu}. \tag{6.23}$$

Recall that γ_μ increases slowly with energy in the range $\gamma \le \gamma_\mu \le \gamma+1$. In (6.22) γ_μ is to be evaluated at the energy given by (6.18). In fact, the numerical value of $R(X)$ at deep detectors is somewhat larger than given in 6.22. This is due to extra low energy muons produced locally by the muon beam itself *via* muon hadroproduction. These nuclear interactions of muons give rise to pions in or very near the detector cavity which can decay to give low energy muons. In addition, detector geometry needs to be taken into account in defining "throughgoing" muons. At very large slant depths (~ 10 km.w.e.) neutrino-induced muons dominate and a different calculation is required.

6.5.3 Prompt muons

Charmed particles have lifetimes so short that they almost always decay before interacting. This is why muons from decays of charm (and heavier flavors) are called *prompt* muons. For $E_\mu < \epsilon_{\text{charm}} \approx 4 \times 10^7$ GeV the flux of prompt muons, $I_X(> E_\mu)$, is to be calculated in the low energy limit of (6.4) and (6.6) in which

$$I_X(> E_\mu) \propto \frac{B_\mu Z_{N\,\text{charm}} Z_{\text{charm}\,\mu}}{(1 - Z_{NN})} \times \frac{1.8}{\gamma} E_\mu^{-\gamma}\ \text{cm}^{-2}\text{s}^{-1}\text{sr}^{-1}, \tag{6.24}$$

where B_μ is the branching ratio for charm decays including a muon and $Z_{\text{charm}\,\mu}$ is the spectrum weighted moment of the distribution of a muon from charm decay.[3] In contrast, for $E_\mu \gg \epsilon_\pi \approx 115$ GeV (~ 850 GeV for charged kaons), parents of ordinary muons prefer to interact rather than decay. For ordinary muons, therefore, the high energy solution is relevant deep underground ($X > 2.5$ km.w.e.). From (6.7), for $\theta < 60°$, we have

$$I(> E_\mu) = \sec\theta\, \frac{0.37\ \text{TeV}}{E_\mu} \frac{Z_{N\pi}}{(1 - Z_{NN})(\gamma + 2)} \times \frac{1.8}{(\gamma + 1)} E_\mu^{-\gamma}\ \text{cm}^{-2}\text{s}^{-1}\text{sr}^{-1}. \tag{6.25}$$

The flux of prompt muons differs qualitatively in two ways from ordinary muons. First, the energy spectrum is as flat as the primary spectrum up to $E_\mu \approx \epsilon_{\text{charm}} \approx 4 \times 10^7$ GeV. Second, the angular distribution is isotropic. The flux of ordinary muons, in contrast, contains the factor $\sec\theta / E_\mu$ relative to the primary spectrum at high energy, characteristic of the competition between decay and interaction. Because of their flatter energy spectrum, prompt muons will eventually dominate the muon flux despite the much lower production of their exotic parents as compared to pions and kaons.

The total integral flux of muons is

$$I(> E_\mu) = I_X + I_\nu \sec\theta. \tag{6.26}$$

---

[3] In this case—see fig. 2.2— we have a three-body decay, instead of the two-body decay characteristic of $\pi \to \mu\nu$. For $\gamma = 1.7$, $Z_{\text{charm}\,\mu} \sim 0.2$.

From (6.24-25) (including the contribution from kaons)

$$\frac{I_X}{I_v} \approx \frac{(\gamma+2)(\gamma+1)}{\gamma}\,\frac{E_\mu}{0.37\ \mathrm{TeV}}\,R_\mu, \qquad (6.27)$$

where $R_\mu \equiv B_\mu Z_{\mathrm{N\,charm}} Z_{\mathrm{charm}\mu}/Z_{\mathrm{N}\pi}$. If $R_\mu \approx 10^{-4}$, as at ~ 200 GeV, then $I_X/I_v > 1$ for $E_\mu > 1000$ TeV. If charm production in the fragmentation region increases with energy as suggested by some colliding beam experiments, then this crossover energy may occur as low as 100 TeV.

> **Problem:** Show that the crossover energy at which $I_X/I_v = 1$ is of order 100 TeV if the main source of prompt muons is production of $\Lambda_c^+ D^0$ in the forward fragmentation region with cross section for charm production on air $\mathrm{d}\sigma/\mathrm{d}x \sim 20\,\mathrm{mb}\,(1-x)^2$. Assume $B_\mu \approx 0.06$ as the average branching ratio for Λ_c^+ or D^0 to give a muon.

In practice, looking for a prompt component with underground muons is a tricky business. The procedure is to fit the data to an equation of the form of (6.26) using (6.18) to relate minimum muon energy at the surface to slant depth and allowing the ratio $I_X/(I_v E_\mu)$ to vary as a free parameter. Because the location of the detector is fixed, one needs to know the density profile of the overburden very well in order to cover a range of slant depths by varying zenith and azimuth. Clearly, accuracy in determining the muon's direction is also crucial: because of the steep energy spectrum, a small error in the zenith angle can lead to a relatively large overestimate of the muon energy at the surface. These difficulties are particularly severe when the experiment is under a mountain, although in that case it is possible to find different directions for which slant depth is the same but zenith angle differs considerably. Then in principle one can look directly for a dilution of the $\sec\theta$ effect as a signal of prompt muon production.

For a detector with a flat overburden, the angular dependence of the flux underground is obtained simply by substituting a minimum E_μ from (6.18) into (6.26) with slant depth X independent of azimuth. Fig. 6.5 shows data from KGF at 7 km.w.e. (Krishnaswamy et al. 1982). The solid curve shows the angular distribution calculated from (6.26) with $R_\mu = 0$. The quantity plotted is

$$\frac{\mathrm{d}I_\mu}{\mathrm{d}\theta} = 2\pi \sin\theta\,\frac{\mathrm{d}I_\mu}{\mathrm{d}\Omega}.$$

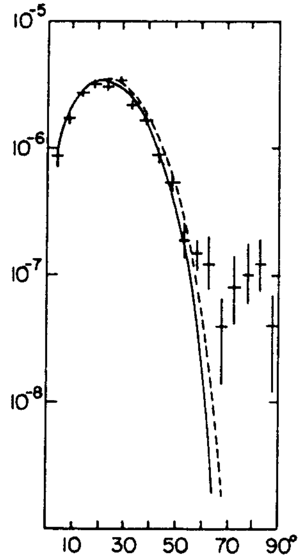

Figure 6.5: Angular distribution of muons at KGF under 7000 m.w.e.

The phase space factor, $\sin\theta$, suppresses the distribution at small angle. The dashed curve shows the shape for $R_\mu = 10^{-2}$. It exceeds the $R_\mu = 0$ curve at large angle because the slant depth is large enough so the flux of ordinary muons falls below the flux of prompt muons because the $1/E_\mu$ suppression more than compensates for the $\sec\theta$ enhancement of ordinary muons. The calculated curve with $R_\mu = 0$ fits the data out to 50° quite well, but the shape alone is very insensitive to R_μ. Even the very large ratio of $R_\mu = 10^{-2}$ assumed for the dashed curve is difficult to see. In addition, the excess muons at large angles produced by atmospheric neutrinos must be subtracted before the measured fluxes in the angular range between 50 and 60° can be used for the prompt muon analysis. The KGF (Adarkar, 1990) and Baksan (Andreyev et al., 1990) groups have reported analyses of their data that suggest the possibility of prompt muons at the level of $R_\mu \sim 10^{-3}$ for $E_\mu > 10$ TeV.

> **Problem:** The depth-intensity relation can be parameterized locally by $I_v(> E_\mu(X_v)) \propto X_v^{-n}$. The angular distribution at vertical depth X_v under a flat overburden can be written $I(\cos\theta)/I_v = \cos^m\theta$ for small θ ($\leq 30°$). Show that for $E_\mu(X_v) \gg \epsilon_\pi$, $n = m+1$, where $n \approx \gamma+1$ for $X_v < \xi$, and $n \to (\gamma+1)X_v/\xi$ for $X_v \gg \xi$.

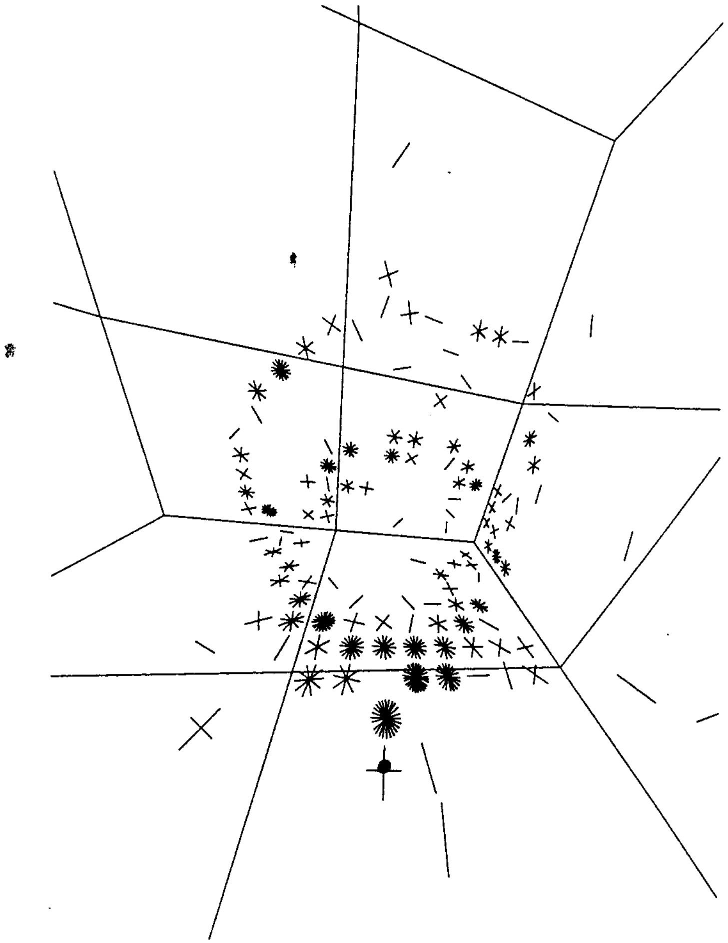

This photograph shows a reconstructed neutrino interaction inside the IMB detector. In this event, the neutrino produced a muon and an energetic proton which generated the two overlapping circles of phototube hits as they travelled through the detector. The IMB detector is a large rectangular volume (60 × 65 × 80 ft.) filled with ultra-pure water and located 2000 ft. below the surface in a salt mine near Cleveland, Ohio. Relativistic charged particles emit Cherenkov light as they pass through the water. The light patterns are recorded by 2048 phototubes arrayed on the six surfaces of the volume. Computer reproductions of the phototube hits are represented by symbols consisting of a number of slashes proportional to the intensity of each hit. Each trapezoidal area delineates one-sixth or one-fourth of a face of the detector. The detector faces and phototube hits are drawn from a "fisheye" perspective taken along the direction of the particles that produced the pattern. (Photo courtesy of the IMB Collaboration.)

Chapter 7

Neutrinos

Though neutrinos are the most abundant cosmic rays at sea level, their interactions have only recently been measured, with the advent of large underground detectors. This is a consequence of the small neutrino–nucleon cross section. The cross section for producing a charged lepton (averaged over ν and $\overline{\nu}$) in the energy region 1–3000 GeV is

$$\sigma \simeq 0.5\times10^{-38}\,\mathrm{cm}^2\times E_\nu\,(\mathrm{GeV}). \tag{7.1}$$

The neutrino flux around 1 GeV (where the product of flux and cross section is a maximum) is $\sim 1\,\mathrm{cm}^{-2}\mathrm{s}^{-1}$ from all directions. The interaction rate of atmospheric neutrinos is thus of order

$$1\,\frac{\nu}{\mathrm{cm}^2\,\mathrm{s}}\times\frac{0.5\times10^{-38}\,\mathrm{cm}^2}{\mathrm{nucleon}}\times\frac{6\times10^{32}\,\mathrm{nucleons}}{\mathrm{kT}}\times\frac{3.15\times10^{7}\mathrm{s}}{\mathrm{yr}}$$

$$\sim 100\,\frac{\nu-\mathrm{interactions}}{\mathrm{kT\ yr}}.$$

Therefore, as pointed out many years ago by Reines (1960) and by Greisen (1960), detectors with a kiloton or more of sensitive volume are required to study interactions of cosmic ray neutrinos.

A knowledge of the flux of cosmic ray neutrinos produced in the atmosphere is important because their interactions constitute the background for the search for nucleon decay. In addition, cosmic ray neutrinos of local origin are also the background for neutrino astronomy. This chapter is devoted to describing how to calculate the secondary neutrinos produced by a cosmic ray beam. We emphasize the neutrinos from interactions in the Earth's atmosphere. The methods and results are, however, very similar for production of neutrinos by particles interacting with astrophysical targets, such as the interstellar medium, supernova remnants and binary stellar systems, all of which will be discussed later in the book.

7.1 Fluxes

The principal sources of secondary neutrinos in diffuse targets are the decays of pions, kaons and muons. The decay chain from pions is

$$\begin{array}{lll} \pi^{\pm} \to & \mu^{\pm} & + \nu_\mu(\overline{\nu}_\mu) \\ & \searrow & \\ & & e^{\pm} + \nu_e(\overline{\nu}_e) + \overline{\nu}_\mu(\nu_\mu), \end{array} \tag{7.2}$$

with a similar chain for charged kaons. When conditions are such that all particles decay, we therefore expect

$$\nu_\mu \sim \overline{\nu}_\mu \sim 2\,\nu_e \tag{7.3}$$

and

$$\nu_e/\overline{\nu}_e \sim \mu^+/\mu^-. \tag{7.4}$$

Moreover, the kinematics of π and μ decay is such that roughly equal energy is carried on average by each neutrino in the chain.

In the Earth's atmosphere the muon decay length becomes larger than its typical production height ($\sim$ 15 km) for E_μ more than $\sim$2.5 GeV. The ν_e/ν_μ ratio therefore quickly decreases with energy above a GeV or so, until at high energy the only source of ν_e is a small contribution from $K^0_L \to \pi\, e\, \nu_e$. In astrophysical targets the density is generally much less, and the simple situation described by (7.3) and (7.4) persists to much higher energies. Figure 7.1 shows the neutrino ratios in the range 0.2–3 GeV. Note that the $\nu_e/\overline{\nu}_e$ ratio falls below μ^+/μ^- at very low energy. This is because the μ^+/μ^- ratio for muons of $\simeq$ 1 GeV *at production* is near one, reflecting the contribution of pions from the target fragmentation region, which is charge symmetric. Because of energy loss in the atmosphere, however, muons of energy around a GeV *at sea level* were produced with about three GeV, so their charge ratio still reflects the forward fragmentation region. Most ν_e's originate from muon decays high in the atmosphere before the parent muons have lost much energy, so the $\nu_e/\overline{\nu}_e$ ratio approaches unity below 1 GeV.

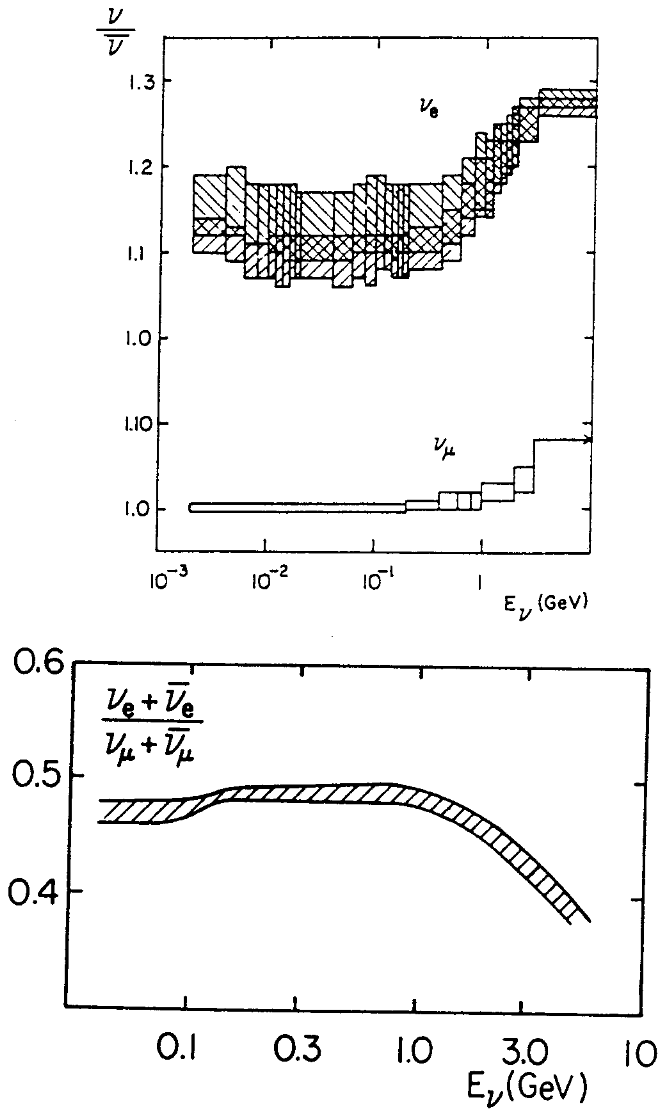

Figure 7.1: Ratios of atmospheric neutrinos. The bands indicate the range of variation for different sites and for different epochs of solar modulation. ($\nu/\overline{\nu}$ ratios from Gaisser, Stanev & Barr, 1988; ν_e/ν_μ from Barr, Gaisser & Stanev, 1989.)

7.1.1 Neutrinos from pions and kaons

As emphasized in the preceding discussion, neutrinos and muons are very closely related. Indeed, when muon energy loss and decay can be neglected ($E_\mu > 10$ GeV), it is straightforward to derive the neutrino flux from the measured flux of muons (§4.1 in Hayakawa, 1969). But this requires an assumption about the relative contribution of kaons and pions to the muon flux. In any case, it is simpler just to calculate the neutrino flux directly from the incident cosmic ray spectrum, following the pattern of the calculation of muon fluxes in chapter 6.

For ν_μ from the decay of charged pions and kaons, the production spectrum is given by (6.2) with only the limits on the integrals changed. For neutrinos the upper limit for the parent energy is infinity and the lower limit $E_\nu(1-\mu^2/M^2)^{-1}$. The same series of steps used for muons leads to a result analogous to (6.7). For $E_\nu >$ several GeV, when neutrinos from decay of muons can be neglected, this procedure gives a good estimate of the total flux of ν_μ. The result for the sum of neutrinos plus antineutrinos has the same form as (6.7) with $E_\mu \to E_\nu$ and different expressions for the quantities $\mathcal{A}$ and $\mathcal{B}$:

$$\mathcal{A}_{\pi\nu} \equiv Z_{N\pi}\frac{(1-r_\pi)^\gamma}{\gamma+1}$$

and

$$\mathcal{B}_{\pi\nu} \equiv \left(\frac{\gamma+2}{\gamma+1}\right)\left(\frac{1}{1-r_\pi}\right)\left(\frac{\Lambda_\pi-\Lambda_N}{\Lambda_\pi \ln\left(\Lambda_\pi/\Lambda_N\right)}\right).$$

$\mathcal{A}_{K\nu}$ and $\mathcal{B}_{K\nu}$ are again obtained by replacing the pion mass by the mass of the kaon. The flux of $\nu_\mu + \bar\nu_\mu$ from the decay of pions and kaons is thus

$$\frac{\mathrm{d}N_\nu}{\mathrm{d}E_\nu} \simeq \frac{N_0(E_\nu)}{1-Z_{NN}}\left\{\frac{\mathcal{A}_{\pi\nu}}{1+\mathcal{B}_{\pi\nu}\cos\theta\, E_\nu/\epsilon_\pi} + 0.635\,\frac{\mathcal{A}_{K\nu}}{1+\mathcal{B}_{K\nu}\cos\theta\, E_\nu/\epsilon_K}\right\} \qquad (7.5)$$

Because of the difference in kinematics, the contribution from kaons is somewhat more important here than in the case of muons. As a consequence, the ratio of $\nu_\mu/\overline{\nu}_\mu$ at high energy is somewhat larger than the μ^+/μ^- ratio since the bias towards $\mu^+\,\nu_\mu$ is greater for kaons than for pions.

7.1.2 Neutrinos from decay of muons

As a consequence of parity nonconservation, muons from pion decay are produced fully polarized, left-handed for π^+ decay and right-handed for π^- decay (see Fig. 7.2). In the muon rest frame, the distribution of the neutrinos from the decay $\mu^\pm \to e^\pm + \nu_e(\bar\nu_e) + \bar\nu_\mu(\nu_\mu)$ is given by

$$\frac{\mathrm{d}n}{\mathrm{d}x\,\mathrm{d}\Omega} = \frac{1}{4\pi}\left[f_0(x) \mp f_1(x)\cos\theta\right], \qquad (7.6)$$

where $x \equiv 2\,E'_\ell/\mu$ is the scaled energy of the final state lepton in the muon rest frame ($0 \le x \le 1$) and θ is the angle between the lepton and the spin of the muon. Equation 7.6 is valid also for the electron in the approximation that m_e is neglected. (The subscript ℓ here represents any of the leptons from muon decay.) The functions $f_0(x)$ and $f_1(x)$ are calculated from the matrix elements for muon decay with the results given in Table 7.1. For muons that stop and then decay, these distributions give the neutrino energy spectra directly. The mean energies of the ν_μ and ν_e (averaged over all θ) are 37 MeV and 32 MeV respectively.

For muon decay in flight the distributions must be transformed to the laboratory system. There are two ways to proceed. One can transform the distribution first to the pion rest frame and then from the pion rest frame to the laboratory frame, integrating over all muon energies and angles consistent with kinematics (S. Barr et al., 1988). This leads to an expression for the lepton distribution as a function of energy of the parent pion. Alternatively, one can project the polarization along the laboratory direction of the muon then transform the distribution from the muon rest frame to the laboratory. We describe the latter procedure here, which is more useful for calculation

Table 7.1: Functions for muon decay

	$f_0(x)$	$f_1(x)$
ν_μ, e:	$2x^2(3-2x)$	$2x^2(1-2x)$
ν_e:	$12x^2(1-x)$	$12x^2(1-x)$

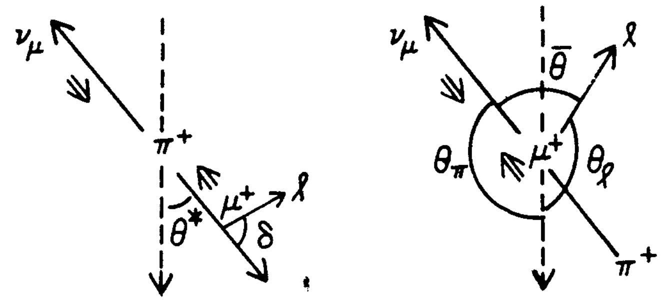

a) pion rest frame b) muon rest frame

Figure 7.2: The $\pi \to \mu \to \nu$ decay chain.

of atmospheric neutrinos where the muons must be followed as they lose energy by ionization between production and decay (G. Barr et al, 1989).

We start by expressing the lepton solid angle in the muon rest frame in terms of the polar angles of the lepton relative to the fixed z-axis defined by the direction of the muon. Thus $d\Omega = d\cos\theta_\ell d\phi_\ell$, where ϕ_ℓ is the azimuthal angle of the lepton relative to the π–μ plane. Then

$$\cos\bar\theta \;=\; \cos\theta_\pi\,\cos\theta_\ell \;+\; \sin\theta_\pi\,\sin\theta_\ell\,\cos\phi_\ell, \qquad (7.7)$$

where θ_π is the angle between the pion and the fixed z-axis, and $\bar\theta$ is the angle between the lepton and the pion. All the angles in (7.7) are defined in the rest frame of the muon (see fig. 7.2*b*). Because of the opposite helicity of ν_μ and $\bar\nu_\mu$, $\cos\bar\theta = \pm\cos\theta$. Substituting (7.7) into (7.6), one therefore has

$$\frac{dn}{dx\,d\cos\theta_\ell} \;=\; \frac{1}{2}\left[f_0(x) \;-\; f_1(x)\,\cos\theta_\ell\,\cos\theta_\pi\right], \qquad (7.8)$$

after integrating over the azimuthal angle, ϕ_ℓ. Thus, because of the opposite relation between spin and kinematics for μ^+ and μ^-, the effect of polarization is the same for neutrinos and antineutrinos. The quantity $\cos\theta_\pi$ is determined solely by the direction in which the pion decays. It is given by

$$\cos\theta_\pi \;=\; \frac{1}{\beta_\mu}\left(\frac{2\,E_\pi\,r_\pi}{E_\mu\,(1-r_\pi)} \;-\; \frac{1+r_\pi}{1-r_\pi}\right) \;\equiv\; P_\mu, \qquad (7.9)$$

where E_π and E_μ are the total energy of the pion and the muon in the laboratory frame, β_μ is the muon velocity in the laboratory and

$r_\pi = (m_\mu/m_\pi)^2$. For a $\mu^\pm$, $\pm P_\mu$ is the projection of the muon spin in its rest frame along the direction of motion of the muon in the laboratory.

> **Problem:** (Due to Stephen Barr.) Derive (7.9) by evaluating the 4-vector scalar product $p_\pi \cdot u_{\rm lab}$ in the laboratory frame and in the muon rest frame. Here $u_{\rm lab}$ is the 4-velocity of the laboratory frame, which, in the muon rest frame, is given by $(E_\mu, -\mathbf{p}_\mu)/m_\mu$.

The distribution in the laboratory is obtained from (7.8) and the Lorentz transformation between the muon rest frame and the laboratory,

$$y \;\equiv\; \frac{E_\ell}{E_\mu} \;=\; x\,(1 \;+\; \beta_\mu\,\cos\theta_\ell). \qquad (7.10)$$

A Monte Carlo calculation of the neutrino spectrum proceeds by calculating $P_\mu = P_\mu(E_\pi, E_\mu)$, where E_μ is chosen randomly from the step-function distribution (4.25). Then the muon decays randomly in its rest frame with x and $\cos\theta_\ell$ chosen from the distribution (7.8) with the appropriate $f_i(x)$. Finally, the resulting neutrino is boosted to the laboratory frame. This procedure also works when the muon loses energy due to ionization between production and decay. In that case, P_μ is calculated from (7.9) with β_μ and E_μ at production, but the Lorentz transformation (7.10) must be evaluated with β_μ and E_μ after energy loss has occurred. Physical depolarization by the energy loss processes is unimportant for relativistic muons. In general, however, the second term in (7.8) must also be reduced by any physical depolarization that has occurred.

It is instructive to neglect energy loss by the muons and then to use the Lorentz transformation (7.10) to transform the distribution (7.8) to the laboratory frame. From (7.8) and (7.10) one has

$$\frac{dn}{dy\,dx\,d\cos\theta_\ell} \;=\; \frac{1}{2}\,\left[f_0(x) \;-\; P_\mu\,f_1(x)\,\cos\theta_\ell\right]\,\delta[y - \frac{1}{2}x\,(1+\beta_\mu\cos\theta_\ell)]. \qquad (7.11)$$

The integral over $\cos\theta_\ell$ can be done with the help of the δ-function. It is non-zero for

$$\frac{1}{2}x\,(1 \;-\; \beta_\mu) \;\le\; y \;\le \frac{1}{2}x\,(1 + \beta_\mu),$$

or equivalently for

$$x_{\rm min} \;\equiv\; \frac{2\,y}{1\,+\,\beta_\mu} \;\le\; x \;\le\; \min[1, \frac{2\,y}{1\,-\,\beta_\mu}] \;\equiv\; x_{\rm max}.$$

Thus for $y > \frac{1}{2}(1 - \beta_\mu)$,

$$\frac{dn}{dy} = \frac{1}{\beta_\mu}\int_{x_{\min}}^{x_{\max}}\left[f_0(x) - P_\mu f_1(x)\,\frac{2y/x - 1}{\beta_\mu}\right]\frac{dx}{x} \equiv \frac{1}{\beta_\mu}[g_0(y,\beta_\mu) - P_\mu\, g_1(y,\beta_\mu)]. \qquad (7.12)$$

Note that the expressions will differ depending on whether or not $y > \frac{1}{2}(1 - \beta_\mu)$. Explicit forms for g_0 and g_1 are given in table 7.2 in the limit $\beta_\mu \to 1$.

Table 7.2: Laboratory system distributions of ν's from μ-decay in the limit $\beta_\mu \to 1$ (courtesy of Paolo Lipari).

	$g_0(y)$	$g_1(y)$
ν_μ,(e):	$\frac{5}{3} - 3y^2 + \frac{4}{3}y^3$	$\frac{1}{3} - 3y^2 + \frac{8}{3}y^3$
ν_e:	$2 - 6y^2 + 4y^3$	$-2 + 12y - 18y^2 + 8y^3$

7.1.3 Flux of neutrinos from $\pi \to \mu \to \nu$

For the Earth's atmosphere, (7.12) is of somewhat academic interest, because at energies low enough so that muon decay is important, energy loss in the atmosphere is also important. The muon decay length is shorter than the typical altitude of production only for $E_\mu <$ several GeV, but a muon loses 2 GeV or more in traversing the atmosphere. In this situation, a Monte Carlo calculation that accounts for muon energy loss is desirable.

The simple analysis represented by (7.12) is, however, directly applicable in a low density environment with long pathlengths in which muons with a large range of energies decay without energy loss. Examples include the interstellar medium, stellar atmospheres, young supernova remnants and accretion disks around compact objects such as neutron stars and black holes. To prepare for our discussion in chapter 13 of some of these astrophysical beam dumps, it is useful to assemble the formulas for neutrino spectra from decay in flight of muons which in turn come from a power spectrum of pions such as might be produced near a cosmic accelerator.

The differential neutrino spectrum from $\pi \to \mu \to \nu$ is

$$\phi_\nu(E_\nu) = \int_{E_\nu}^{\infty} dE_\pi \int_{E_{\min}}^{E_\pi} dE_\mu\, \phi_\pi(E_\pi)\,\frac{dn}{dE_\mu}\,\frac{1}{E_\mu}\frac{dn}{dy}, \qquad (7.13)$$

where $\phi_\pi = K\,E_\pi^{-\alpha}$ is the differential pion spectrum. The distribution of muons from pion decay is given by (6.1) as $E_\pi^{-1}\,(1-r)^{-1}$, and dn/dy is the distribution of (7.12). (In this subsection the subscript on r_π has been dropped.) The lower limit of the integral over muon energy in (7.13) is

$$E_{\min} = \min[r\,E_\pi, E_\ell].$$

It is straightforward to evaluate (7.13) by changing the order of integration,

$$\int_{E_\nu}^{\infty} dE_\pi \int_{E_{\min}}^{E_\pi} dE_\mu \to \int_{E_\nu}^{\infty} dE_\mu \int_{E_\mu}^{E_\mu/r} dE_\pi,$$

and carrying out the integral over E_π. One is then left with the integral,

$$\int_{E_\nu}^{\infty}\frac{dE_\mu}{E_\mu} = \int_0^1 \frac{dy}{y}.$$

The result is

$$\phi_\nu(E_\nu) = \phi_\pi(E_\nu)\,\frac{1 - r^\alpha}{\alpha\,(1 - r)} \times \left\{\langle y^{\alpha-1}\rangle_0 + \frac{1}{1-r}\left[1 + r - \left(\frac{2\alpha\, r}{\alpha - 1}\right)\left(\frac{1 - r^{\alpha-1}}{1 - r^\alpha}\right)\right]\langle y^{\alpha-1}\rangle_1\right\}, \qquad (7.14)$$

where the moments,

$$\langle y^{\alpha-1}\rangle_i \equiv \int_0^1 y^{\alpha-1}\, g_i(y)\, dy,$$

are given in table 7.3.

The moments in table 7.3 at $\alpha = 2$ are related to the mean fraction of the muon's momentum that is carried by the neutrinos. From (7.12), at high energy,

$$\langle y\rangle_{\nu_\mu} = \langle y\rangle_e = \frac{7}{20} + \left(\frac{1}{20} \times P_\mu\right)$$

and

$$\langle y\rangle_{\nu_e} = \frac{3}{10} - \left(\frac{1}{10} \times P_\mu\right).$$

For decay of relativistic pions, when the muon goes along the direction of the pion, $E_\mu = E_\pi$, and it then follows from (7.9) that $P_\mu \to -1$. When the muon is produced backward in the pion rest frame, $E_\mu = r_\pi \times E_\pi$, and $P_\mu \to +1$. For a given muon energy and a steep parent pion spectrum, forward decay is weighted more heavily than backward decay, because there are more low energy than high energy pions. Thus negative P_μ is favored, and the effect of polarization on atmospheric neutrinos is to boost the ν_e and $\bar{\nu}_e$ somewhat relative to the ν_μ and $\bar{\nu}_\mu$ from muon decay in flight.

Table 7.3: Moments for the $\pi \to \mu \to \nu$ decay chain.

	$\langle y^{\alpha-1}\rangle_0$	$\langle y^{\alpha-1}\rangle_1$
ν_μ,(e):	$\frac{2\,(\alpha+5)}{\alpha\,(\alpha+2)\,(\alpha+3)}$	$\frac{2\,(1-\alpha)}{\alpha\,(\alpha+2)\,(\alpha+3)}$
ν_e:	$\frac{12}{\alpha\,(\alpha+2)\,(\alpha+3)}$	$\frac{12\,(\alpha-1)}{\alpha\,(\alpha+1)\,(\alpha+2)\,(\alpha+3)}$

7.2 Atmospheric neutrinos

A numerical or Monte Carlo calculation is required to calculate the spectrum of atmospheric neutrinos in the detail required for comparison with results from the large underground detectors, particularly the multikiloton water detectors, which have accumulated some thousand neutrino interactions. The geomagnetic field tends to prevent low energy cosmic rays from penetrating through the magnetosphere down to the Earth's atmosphere. Thus, for each location on the Earth and for each direction, there is a geomagnetic cutoff rigidity, below which primary nucleons do not contribute to production of secondaries in the atmosphere. The value ranges from less than a GeV for protons near the geomagnetic poles to ~ 15 GeV for vertical protons near the equator. In addition, the flux of cosmic rays in the heliosphere varies with the eleven year solar cycle as the strength of the solar wind varies. For these reasons, one needs to evaluate the neutrino spectrum produced by a non-power law primary spectrum that is different for each direction at each location. A Monte Carlo calculation is a natural way to do this and at the same time to include many details, such as energy loss by charged particles and all production and decay channels leading to neutrinos.

7.2.1 Calculated fluxes

Some results of one Monte Carlo calculation of the atmospheric neutrino flux at low energy (G. Barr, Gaisser & Stanev, 1989) are shown in fig. 7.3. The fluxes obtained in this calculation are expected to be somewhat higher than the true fluxes below 100 MeV because they are based on a one-dimensional, "straight ahead" calculation. In fact, for neutrino energies less than the masses of the parent mesons, the three-dimensional nature of decay and interaction is important. Some (less than half) of these very low energy neutrinos are projected away from the surface. A three-dimensional calculation of the neutrino flux has been carried out by Lee and Bludman (1988).

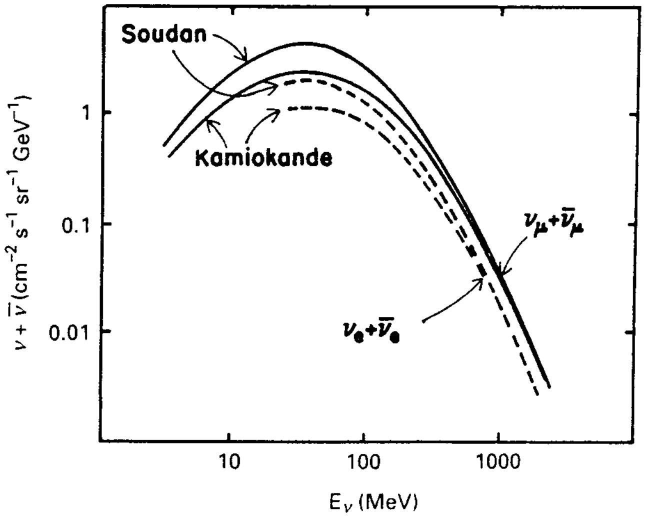

Figure 7.3: Neutrino fluxes ($\nu + \bar{\nu}$) at solar maximum for two locations averaged over all directions.

The neutrino fluxes in fig. 7.3 have broad maximums around 30–40 MeV. These reflect the sharply peaked distributions of neutrinos from decay of stopped pions and muons after they have been smeared out by Lorentz transformations to the frame of the decaying parent pion or muon. A maximum is a characteristic feature of a secondary spectrum when a mass scale is involved (here the mass of the parent meson). This important kinematic signature of secondary cosmic rays will be discussed in more detail in chapter 10.

The Monte Carlo calculation referred to in fig. 7.3 consists of a series of cascades simulated with a detailed hadronic interaction model for a range of energies and zenith angles (Gaisser, Stanev & G. Barr, 1988). Muon energy loss and neutrino production from decay of muons, pions and kaons, as described in section 7.1 above, are incorporated in the Monte Carlo. The neutrino yields per primary nucleon are then weighted according to the primary spectrum for each location and direction to produce the resulting neutrino spectra.

The angular distributions show some interesting features, characteristic of different locations and of different neutrino energies. The upward neutrino fluxes are about the same for any detector location because these neutrinos are produced over a large portion of the opposite side of the Earth, thus averaging over geomagnetic cutoffs. At low energy (several hundred MeV) the downward flux is much higher near the geomagnetic pole (e.g. in the Northern U.S.) than nearer the equator (e.g. in Japan) because of the local geomagnetic cutoff. These differences are reflected in the angular averaged fluxes in fig. 7.3.

Fluxes of $\nu_\mu + \bar{\nu}_\mu$ above several GeV can be estimated from (7.5) for angles out to about 70°. At larger angles it is necessary to take account of the curvature of the atmosphere, as discussed in §3.5. Volkova (1980) has calculated both ν_μ and ν_e fluxes at all angles for energies from 3 to 10^7 GeV, including prompt neutrinos from charm decay, which dominate above $\sim$ 100 TeV. The vertical fluxes calculated from (7.5) are within ~10% of the results of Volkova from 10 GeV to 10 TeV.[1] This is less than the overall uncertainty in the normalization, which is $\sim$ 20%. For the high energy fluxes where geomagnetic effects become unimportant (> 3 GeV), the distribution becomes up-down symmetric, with a maximum near the horizontal that reflects the increased probability of meson decay at large zenith angles. Fig. 7.4 shows the angular dependence of the high energy neutrino flux calculated by Volkova.

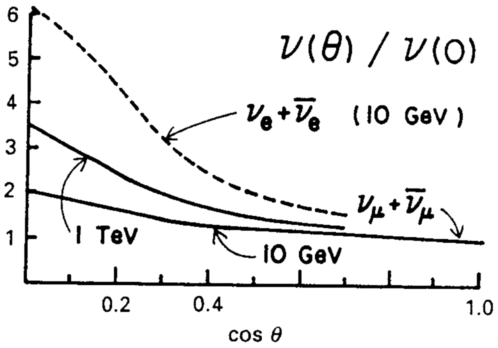

Figure 7.4: Angular dependence of ν-flux (from Volkova, 1980).

7.2.2 Contained events

Cosmic ray neutrinos are detected in two ways in underground detectors, events in which the neutrino interaction occurs inside the detector and events in which the interaction of a ν_μ or its antineutrino in the rock outside the detector projects a muon upward through the detector. The former are referred to as "contained" interactions. Strictly speaking, this definition applies only to neutrino interactions whose products are fully contained inside the fiducial volume of the detector. The strict definition is used particularly in the search for nucleon decay where maximal information about each event is required. For some purposes (e.g. a search for neutrinos from point sources) the definition can be relaxed.

The rate of contained events induced by the neutrino flux is

$$\text{Rate} = N_A\, M_f \sum_i \int \left[\int \frac{\mathrm{d}\sigma_i}{\mathrm{d}E_{\text{vis}}} \frac{\mathrm{d}N_\nu^i}{\mathrm{d}E_\nu}\, \mathrm{d}E_\nu\, \mathrm{d}\Omega \right] \epsilon_i(E_{\text{vis}})\, \mathrm{d}E_{\text{vis}} \qquad (7.15)$$

where $\mathrm{d}N_\nu^i/\mathrm{d}E_i$ is the flux of neutrinos of the ith flavor, $\mathrm{d}\sigma_i/\mathrm{d}E_{\text{vis}}$ is the cross section per nucleon for interaction of ν_i to produce visible energy E_{vis} in a detector of fiducial mass M_f. The experimental efficiency for containing and detecting a particular type of event i with its vertex inside the fiducial volume is ϵ_i. A complete quantitative comparison requires use of the Monte Carlo event generator for each detector to account correctly for the detection efficiency. A summary of comparisons made by various groups is shown in fig. 7.5.

The peak of the integrand in (7.15) occurs for neutrino energies in the neighborhood of 1 GeV – an unpleasant fact since this is just the

---

[1] Equation 7.5 is only for neutrinos produced by decay of pions and kaons. The contribution from muon decay is less than 10% for vertical neutrinos above 10 GeV.

energy range for nucleon decay. The median energy of the primary nucleons that produce such neutrinos is about 20 GeV. Above energies of several GeV, the atmospheric neutrino flux falls below the level of detectability in present detectors. To go to higher energies requires detection of neutrino interactions outside the fiducial volume of the detector.

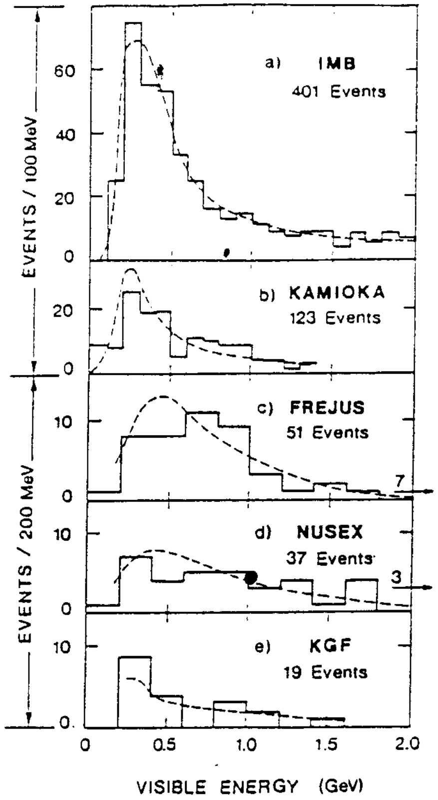

Figure 7.5: Comparison of calculated and measured ν-interactions. (From Ayres, et al., 1986.)

7.2.3 Neutrino ratios and oscillations

Comparison between expected and observed spectra of atmospheric neutrinos can be used to search for neutrino oscillations in a range of parameter space not entirely covered by accelerator experiments. The subject of neutrino oscillations, and especially the effects of propagation of astrophysical neutrinos in matter, have been studied very intensively in the past few years.[2] The purpose here is to describe very briefly several aspects of the calculations of atmospheric neutrinos relevant to neutrino oscillations.

Vacuum oscillations

If neutrinos have masses, the eigenstates, ν_e and ν_μ, of the weak Hamiltonian are related to mass eigenstates by

$$\begin{aligned} \nu_e &= \cos\theta\,\nu_1 + \sin\theta\,\nu_2 \\ \nu_\mu &= -\sin\theta\,\nu_1 + \cos\theta\,\nu_2 \end{aligned} \qquad (7.16)$$

(considering only two flavors for simplicity). The wave equation for the neutrino states may be written in matrix form as ($\hbar = c = 1$)

$$i\frac{\mathrm{d}}{\mathrm{d}t}\nu(t) = \mathcal{E}\,\nu(t) \approx \left(E_\nu + \frac{\mathcal{M}}{2E_\nu}\right)\nu(t). \qquad (7.17)$$

The approximation on the right side of (7.17) is obtained by expanding the relation between momentum and energy assuming that neutrinos propagate with a well-defined momentum and that $E_\nu \gg m_\nu$. In the mass eigenstate representation, $\mathcal{E}$ is diagonal with

$$\mathcal{E}_{ii} = \sqrt{p^2 + m_i^2} \approx E_\nu + \frac{m_i^2}{2E_\nu}.$$

The solution of (7.17) is of the form $\nu_i(t) = e^{-i\omega t}\nu(0)$. A phase difference, $(m_2^2 - m_1^2)t/(2E_\nu)$, develops between the two mass eigenstates as they propagate, which corresponds to an oscillation length

$$L_{\rm osc} = \frac{4\pi E_\nu}{\Delta} \approx 2.48\ \mathrm{km}\,\frac{E_\nu(\mathrm{GeV})}{\Delta(\mathrm{eV}^2)}, \qquad (7.18)$$

where $\Delta \equiv \Delta m^2 = m_2^2 - m_1^2$.

From (7.16) one can calculate the probability that a ν_μ is observed as a ν_e after propagating a distance $L = ct$. It is

$$P_{\nu_e\nu_\mu} = |\langle\nu_e|\nu_\mu\rangle|^2 = \sin^2 2\theta\,\sin^2\pi\frac{L}{L_{\rm osc}}. \qquad (7.19)$$

---

[2] For an excellent general treatment of neutrino oscillation theory with emphasis on reactor and accelerator experiments, see the book by Boehm and Vogel, 1987. Bahcall (1989) gives a nice account that emphasizes solar neutrinos and matter effects. The subject of neutrino oscillations in matter has been reviewed recently by Kuo & Pantaleone (1989).

For upward neutrinos, $L \sim 10^4$ km and there can be some effect for Δm^2 as small as 10^{-5} eV^2 if the experiment can detect neutrinos with energies of $\sim$ 200 MeV. At the other extreme, for downward neutrinos, $L \sim 20$ km, so Δm^2 as large as ~ 0.1 eV^2 could in principle give measurable effects for neutrinos of several GeV. In contrast, the region spanned by reactor and accelerator experiments together is roughly $10^{-2} \leq \Delta m^2 \leq 10^2$ eV^2.

As an example, an early result of the IMB experiment was a limit (LoSecco et al., 1985) on neutrino oscillations obtained by comparing the energy spectrum of upward and downward neutrinos. (Upward and downward were each defined to be $\frac{1}{5}$ of the total solid angle around the vertical, i.e. $\theta < 53°$.) They excluded a region of parameter space for oscillation into "sterile" neutrinos (i.e. ν_τ) of $\sim 3 \times 10^{-5} \leq \Delta m^2 \leq\sim 10^{-4}$ eV^2, but only for $\sin^2 2\alpha >\sim 0.3$. The limit obtained in this way did not extend to larger Δm^2 because of the requirement that the upward energy spectrum must be significantly different from the downward energy spectrum *as measured* to avoid dependence on a calculation of the absolute flux. In order to give such a difference, the onset of the effect would have to occur for E_ν in the range of sensitivity of the detector, which was $\sim 0.2 - 2$ GeV. For $L \sim 10^4$ km in (7.19), this energy range corresponds to the quoted range of Δm^2.

This experiment illustrates several difficulties inherent in neutrino oscillation searches with atmospheric neutrinos. Foremost is the problem of low statistics, which is always made worse by any attempt to cut the data to minimize systematic effects. In addition, the neutrino itself is not detected, but only some portion of the secondaries it produces when it interacts. There must always be some correction (which can only be made in an average sense) from the visible energy and direction of the event to E_ν and L_ν. In addition, the energy spectrum of upward neutrinos observed at a high geomagnetic latitude is expected to be different from the downward flux, even in the absence of oscillations, as a consequence of the geomagnetic effect. At IMB, for example, the upward flux should be about 40% lower than the downward flux in the 200 – 400 MeV bin, but nearly equal above a GeV. Finally, because of low statistics and systematic effects, any atmospheric neutrino experiment can only detect a vacuum oscillation effect if the mixing angle is large so that $1 - P_{\nu\to\nu_X}$ is significantly less than one.

Some of the systematic effects (such as that due to the geomagnetic cutoff) can be removed by studying the angular dependence of the ν_e/ν_μ ratio (Ayres et al., 1984). The Kamiokande group have developed a criterion for distinguishing electron (showering) events from muon (non-showering) events in their water Cherenkov detector. They find (Hirata et al., 1988) a ratio $(\nu_e + \bar{\nu}_e)/(\nu_\mu + \bar{\nu}_\mu)$ larger than expected by somewhat more than two standard deviations.[3] Results from other experiments are still inconclusive, and the existence and possible meaning of this result are at present unclear. A point worth noting is that there is no evidence of an angular dependence of the ratio such as might be expected if an oscillation effect were involved.

The fact that the muon mass is much larger than that of the electron gives rise to an experimental difficulty that must be overcome to make an accurate measurement of the ν_e/ν_μ ratio. One would like to compare the fluxes of ν_e and ν_μ at the same energy. The two kinds of neutrinos are distinguished by their charged current interactions,

$$\nu_\mu + \text{nucleon} \;\rightarrow\; \mu + \ldots$$

and

$$\nu_e + \text{nucleon} \;\rightarrow\; e + \ldots .$$

A larger fraction of the neutrino energy goes into rest mass of the produced lepton for ν_μ than for ν_e. The response of the detector must therefore be very well understood to make a statement about the ν_e/ν_μ ratio.

Matter oscillations

In the flavor representation, $\nu(t) = \begin{pmatrix} \nu_e \\ \nu_\mu \end{pmatrix}$, the squared mass matrix is given by

$$\begin{aligned} \mathcal{M} &= U \begin{pmatrix} m_1^2 & 0 \\ 0 & m_2^2 \end{pmatrix} U^{-1} \qquad (7.20) \\ &= \frac{1}{2} \begin{pmatrix} m_1^2 + m_2^2 - \Delta\cos 2\theta & \Delta\sin 2\theta \\ \Delta\sin 2\theta & m_1^2 + m_2^2 + \Delta\cos 2\theta \end{pmatrix}, \end{aligned}$$

---

[3] The discrepancy in the ratio was originally reported as a $\sim 3\,\sigma$ effect. Volkova (1988) pointed out that muon polarization had not been accounted for in the flux calculation (Gaisser et al., 1988) on which the result was based. When this is accounted for (S. Barr et al., 1989 and G. Barr et al., 1989) and the fluxes calculated as descibed in §7.1.2, the discrepancy reduces to a $2.2\,\sigma$ effect

where U is the mixing angle rotation matrix in (7.16). In matter the mass matrix must be modified to account for the fact that electron neutrinos have an extra interaction not present for ν_μ and ν_τ (Wolfenstein, 1978). Elastic scattering of ν_e on electrons can occur via exchange of a charged W-boson as well as by exchange of the neutral Z-boson. Neutrinos of other flavors only scatter elastically on electrons via neutral Z exchange. The potential energy for the extra interaction of electron neutrinos in matter is $V = \sqrt{2}G_F N_e$, where $G_F \approx 1.17 \times 10^{-5}$ GeV^{-2} and N_e is the electron density. In this potential the relation between momentum and energy is (Bethe, 1986),

$$p^2 + m^2 = (E_\nu - V)^2 \approx E_\nu^2 - 2E_\nu V. \tag{7.21}$$

This is equivalent to incrementing $\langle \nu_e | \mathcal{M} | \nu_e \rangle$ by $2EV$, so in matter (7.20) becomes

$$\mathcal{M}_m = \frac{1}{2}\begin{pmatrix} m_1^2 + m_2^2 + 2A - \Delta\cos 2\theta & \Delta \sin 2\theta \\ \Delta \sin 2\theta & m_1^2 + m_2^2 + \Delta \cos 2\theta \end{pmatrix}, \tag{7.22}$$

where $A = 2\sqrt{2}E_\nu G_F N_e$.

The next step is to find the rotation matrix, U_m, that diagonalizes (7.22) and relates flavor eigenstates to mass eigenstates in matter (just as (7.16) does in vacuum). The eigenvalues of the mass matrix in matter (7.22) are

$$\lambda_\pm = \frac{1}{2}(m_1^2 + m_2^2 + A) \pm \frac{1}{2}\sqrt{(A - \Delta\cos 2\theta)^2 + \Delta^2 \sin^2 2\theta}. \tag{7.23}$$

The mixing angle in matter that characterizes the rotation matrix, U_m, is related to the vacuum parameters by

$$\tan 2\theta_m = \tan 2\theta \left(1 - \frac{L_{\rm osc}}{L_0 \cos 2\theta}\right), \tag{7.24}$$

where $L_0 \equiv 2\pi(\sqrt{2}G_F N_e)^{-1}$ is a characteristic length that sets the scale for the matter effects.

A phase difference $(\lambda_+ - \lambda_-)t/(2E_\nu)$ develops between the two mass eigenstates as they propagate in matter. As in vacuum, this leads to a transition probability

$$P_{\nu_e\nu_\mu} = \sin^2 2\theta_m \sin^2 \pi\frac{L}{L_m}, \tag{7.25}$$

where,

$$L_m = L_{\rm osc}\left(\frac{\sin 2\theta_m}{\sin 2\theta}\right) \tag{7.26}$$

is the effective oscillation length in matter.

The crucial point is that – even if the vacuum mixing angle is small – full mixing can occur for a narrow range of energies for which

$$L_{\rm osc} \approx L_0 \cos 2\theta. \tag{7.27}$$

This resonant enhancement of neutrino oscillations in matter (Mikheyev & Smirnov, 1985) appears explicitly in (7.24). Numerically, (assuming small vacuum mixing angle) it occurs for

$$E_\nu \approx 4 \text{ GeV} \times \frac{\Delta m^2}{10^{-3}\text{ eV}^2}. \tag{7.28}$$

If the neutrino masses are ordered in the same way as the corresponding lepton masses (so that the mass eigenstate closest to the electron neutrino is smallest), then $\Delta = m_2^2 - m_1^2$ is positive (Langacker et al., 1983), and there can be a resonant oscillation effect for neutrinos propagating in the Earth if the vacuum oscillation parameters happen to have the right values. (If the sign of Δm^2 is reversed, the effect occurs for antineutrinos.) It is significant (Carlson, 1986) that the density of the Earth is such that L_0 is comparable to the radius of the Earth. L_0 varies from ~ 3000 km in the core (where $\rho \sim 10$ g/cm^3) to $\sim 10^4$ km in the mantle ($\rho \sim 3$ g/cm^3). In this situation the mass matrix (7.22) varies as the neutrino propagates, and (7.17) must be integrated numerically to take account of this variation.

Auriemma et al. (1988) have pointed out that there could be an interesting signature of matter oscillation effects in the flux of neutrino-induced muons in underground detectors. This is because an effect would appear for

$$\nu_\mu + \text{nucleon} \rightarrow \mu^- + \ldots$$

but not for

$$\bar{\nu}_\mu + \text{nucleon} \rightarrow \mu^+ + \ldots.$$

Figure 7.6 shows the expected rates of upward μ^- for various values of Δ assuming $\sin^2 2\alpha = 0.04$ (that is, assuming that the neutrino mixing angle is the same as the Cabibbo angle that relates the electron and

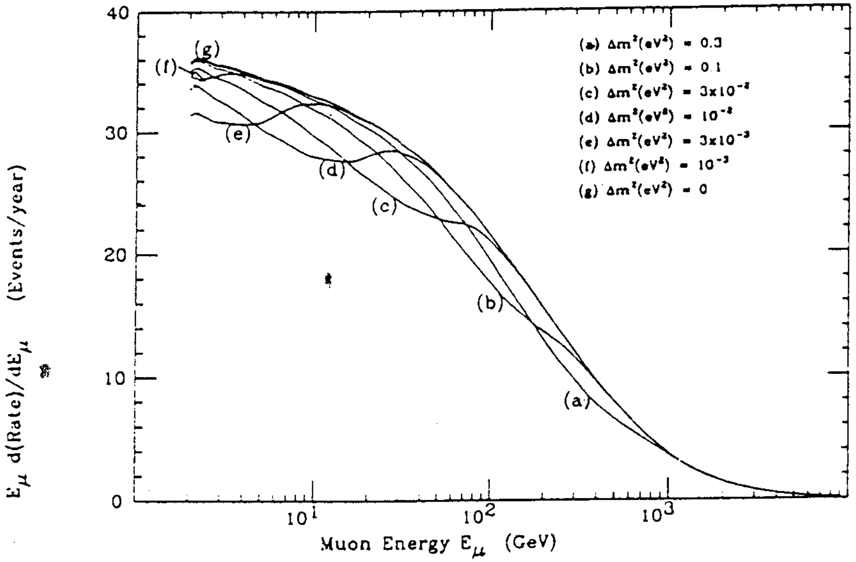

Figure 7.6: Rates of upward, ν_μ-induced μ^- in the MACRO detector for various assumed oscillation parameters (from Auriemma et al., 1988).

muon families). The location of the feature in the energy spectrum of the neutrino–induced muons for a given value of Δm^2 can be obtained from (7.28). It is smeared out because there is a broad distribution of muon energies from interactions of ν_μ of a fixed energy, as will be discussed in more detail in the next chapter.

Chapter 8

Neutrino-induced muons

Cosmic ray neutrinos were in fact first detected with very deep underground detectors of relatively small sensitive volume by observation of muons produced by interactions of neutrinos outside the actual detector. As mentioned in chapter 6, the characteristic signal of a neutrino-induced muon is one that emerges from the rock at such a large angle that it could not be a muon generated in the atmosphere that penetrates through the overburden to the detector. This technique for measuring neutrinos is made possible by the fact that energetic muons produced in the reaction

$$\nu_\mu + \text{nucleon} \rightarrow \mu + \ldots \tag{8.1}$$

have a relatively long range in rock, so the volume of a detector is effectively expanded by accepting events that originate outside its sensitive volume. A muon that emerges from the rock from below the detector must be produced by a ν_μ that happens to interact within a kilometer or so of the detector. The neutrino itself could have been produced 10^4 km away by a cosmic ray incident on the atmosphere on the other side of the globe – or it could come from an energetic astrophysical source 10^4 light years away. So far, only atmospheric neutrinos have been measured in this way. Figure 8.1 illustrates the concept.

The detectors that were used for the first observations of neutrino-induced muons (Crouch et al, 1978 and Krishnaswamy et al., 1982) did not have the power to discriminate upward from downward muons, and so had to restrict themselves to muons near the horizontal as a signal of neutrino interactions in the surrounding rock. (This excess of muons induced by atmospheric neutrinos shows up, for example,

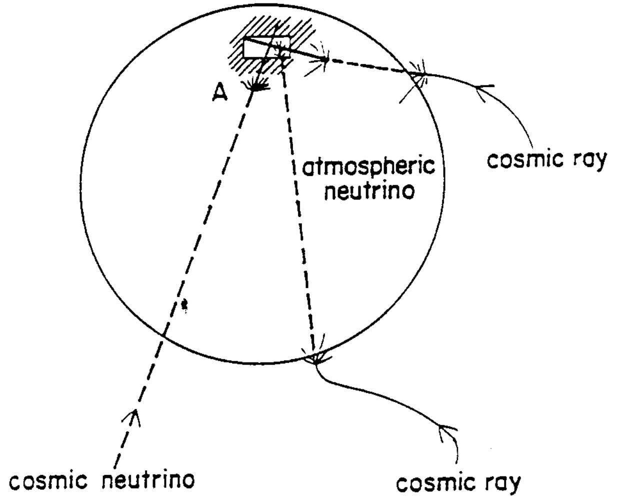

Figure 8.1: A diagram illustrating (clockwise) (i) a horizontal muon induced by an atmospheric neutrino; (ii) an upward atmospheric neutrino interacting inside the sensitive volume of a detector; and (iii) an upward muon induced by a high energy neutrino of extraterrestrial origin. (From Gaisser: *Science* 247, 1049–56, © 1990 by AAAS.)

at zenith angles greater than 60° in the experiment shown in fig. 6.5.) With the large water detectors, as well as with some other large underground detectors, it is now possible by fast timing to find upward, neutrino-induced muons among a large background of downward muons of local atmospheric origin. Among other things, this allows somewhat shallower detectors to be used to look for neutrino-induced muons.

There are several reasons for measuring the neutrino-induced muons. The first is to extend the range of neutrino energies that can be explored by effectively expanding the detector volume. In addition to extending the flux measurement to higher energies, the ability to search for extraterrestrial, point sources of neutrinos improves because of the improved angular resolution possible at higher energy. A range of neutrino energies is also useful for geophysical neutrino oscillation searches since the oscillation length grows with energy.

8.1 Calculation of rates

Three elements are needed to calculate a rate of neutrino-induced muons: (i) the flux of ν_μ and $\bar{\nu}_\mu$; (ii) the cross section for the muon production process (8.1) and (iii) the muon range–energy relation. It is convenient to separate the calculation into two parts by writing

$$\frac{\mathrm{d}N_\mu}{\mathrm{d}E_\mu} = \int_{E_\mu}^{\infty} \mathrm{d}E_\nu \left(\frac{\mathrm{d}N_\nu}{\mathrm{d}E_\nu}\right)\left(\frac{\mathrm{d}P(E_\nu)}{\mathrm{d}E_\mu}\right). \tag{8.2}$$

The first factor in the integrand represents the neutrino spectrum, which could be either of terrestrial or of extraterrestrial origin. The second depends on the physics of neutrino interaction and muon propagation but is independent of the neutrino spectrum. It is the probability that a neutrino on a trajectory that passes through the detector produces a muon at the detector in the interval $[E_\mu, E_\mu + \mathrm{d}E_\mu]$,

$$\frac{\mathrm{d}P(E_\nu)}{\mathrm{d}E_\mu} = \int_{E_\mu}^{E_\nu}\int_0^\infty \mathrm{d}X\, N_A \frac{\mathrm{d}\sigma}{\mathrm{d}E'_\mu}\, g(X, E_\mu, E'_\mu)\mathrm{d}E'_\mu. \tag{8.3}$$

Here $g(X, E_\mu, E'_\mu)$ is the probability (differential in E_μ) that a muon produced with energy E'_μ finds itself in the energy interval $[E_\mu, E_\mu + \mathrm{d}E_\mu]$ after losing energy for a thickness X(g/cm^2).

To obtain the neutrino cross section in the integrand of (8.3), we start with the expression (Okun, 1982) for the doubly differential charged current cross section for $\nu_\mu \rightarrow \mu^-$:

$$\begin{aligned}\frac{\mathrm{d}\sigma_\nu}{\mathrm{d}x\,\mathrm{d}y} = {} & \frac{G^2 m_p E_\nu}{\pi}\frac{M_W^4}{(2m_p x y E_\nu + M_W^2)^2} \\ & \times\{q(x,Q^2) + s(x,Q^2) + [\bar{q}(x,Q^2) - \bar{s}(x,Q^2)](1-y)^2\}.\end{aligned} \tag{8.4}$$

Here $y = 1 - E_\mu/E_\nu$, and $2m_p x y E_\nu = |Q^2|$, the square of the four-momentum transfer. The corresponding cross section for antineutrinos is obtained by $q \leftrightarrow \bar{q}$ and $s \leftrightarrow \bar{s}$ in (8.4). Here $q \equiv u + d + s$ is the quark structure function of the nucleon defined so that

$$\int_0^1 u(x, Q^2)\mathrm{d}x$$

is the fraction of the nucleon momentum (in an infinite momentum frame) carried by up quarks, etc. The structure functions also depend on Q^2. The other constants in (8.4) are the mass, $M_W \approx 81$ GeV, of the W-boson and the Fermi coupling constant, G. The cross section in (8.3) is the integral of (8.4),

$$\frac{\mathrm{d}\sigma}{\mathrm{d}E_\mu} = \frac{1}{E_\nu}\int_0^1 \frac{\mathrm{d}\sigma}{\mathrm{d}x\,\mathrm{d}y}\mathrm{d}x,$$

evaluated at $y = 1 - E_\mu/E_\nu$.

Problem: Use the expression for charged current interactions of neutrinos given above (8.4) to show that for 10 GeV $< E_\nu <$ 3000 GeV the root mean square angle between a ν_μ and a μ^- that it produces is approximately given by

$$\sqrt{<\theta^2>} \sim \sqrt{m_p/E_\nu} \text{ (radians).}$$

"External" events are dominated by high energy neutrinos because of the long range of the high energy muons they produce. The approximate form for the range–energy relation discussed in §6.4 (neglecting straggling) gives sufficiently accurate results for quantitative estimates of rates of neutrinos-induced muons. Thus we can use

$$g(X, E_\mu, E'_\mu) = \delta(E_\mu - <E(X)>), \tag{8.5}$$

with $<E(X)>$ given by (6.17).

Problem: Show that the δ-function in (8.5) can be rewritten as

$$\frac{\delta(X - X_0)}{\alpha(1 + E_\mu/\epsilon)}, \text{ where } X_0 = \xi \ln \frac{E'_\mu + \epsilon}{E_\mu + \epsilon}.$$

With this approximation, (8.3) becomes

$$\epsilon \frac{\mathrm{d}P(E_\nu)}{\mathrm{d}E_\mu} = \frac{\epsilon N_A}{\alpha(1 + E_\mu/\epsilon)} \int_0^{1-E_\mu/E_\nu} \mathrm{d}y' \int_0^1 \mathrm{d}x \frac{\mathrm{d}\sigma}{\mathrm{d}x\,\mathrm{d}y'} \tag{8.6}$$

Equation 8.6 is written in dimensionless form to make its physical interpretation clear. The factor $\xi = \epsilon/\alpha \sim 2.5 \times 10^5$ g/cm^2 is the limiting range of high energy muons, as discussed in §6.5. Multiplied by Avogadro's number, it gives the effective number of target nucleons/cm^2 in the path of a high energy ($E_\nu > \epsilon \sim 500$ GeV) neutrino as

$$N_A\,\xi \approx 1.5 \times 10^{33}\,\frac{\text{nucleons}}{\text{m}^2}. \tag{8.7}$$

Thus the probability in Eq. 8.6 is the product of a cross section and a number of target nucleons per unit area. We can also note from (8.7) that, for a detector of cross sectional area $A \sim V^{\frac{2}{3}}$ normal to a high energy neutrino beam, the number of potential target nucleons is $\sim V^{\frac{2}{3}} N_A \xi$. The number of target nucleons available inside a detector of volume V and density ρ is $N_A \rho V$. Comparison of the two shows that for detectors with $V < (\xi/\rho)^3$ the event rate will be higher for external events generated by ν_μ with $E_\nu > \sim 1$ TeV. For water the critical volume is 10^{10} m^3!

For a muon threshold energy $E_{\rm th}$, the integral of (8.2) over all $E_\mu > E_{\rm th}$ gives the signal (upward muons cm^{-2}s^{-1}sr^{-1}). Changing the order of integration, we write

$$S(> E_{\rm th}) = \int_{E_{\rm th}}^\infty \mathrm{d}E_\nu \frac{\mathrm{d}N_\nu}{\mathrm{d}E_\nu} P_\nu(E_\nu, > E_{\rm th}), \tag{8.8}$$

where

$$P_\nu(E_\nu, > E_{\rm th}) = \int_{E_{\rm th}}^{E_\nu} \mathrm{d}E_\mu \frac{\xi N_A}{(\epsilon + E_\mu)} \int_0^{1-E_\mu/E_\nu} \mathrm{d}y' \int_0^1 \mathrm{d}x \frac{\mathrm{d}\sigma}{\mathrm{d}x\mathrm{d}y'}. \tag{8.9}$$

Calculations of $P_\nu(E_\nu)$ for various assumptions about the quark structure functions are shown in fig. 8.2 for $E_{\rm th} = 2$ GeV. The corresponding neutrino-nucleon charged current cross sections are shown in fig. 8.3.

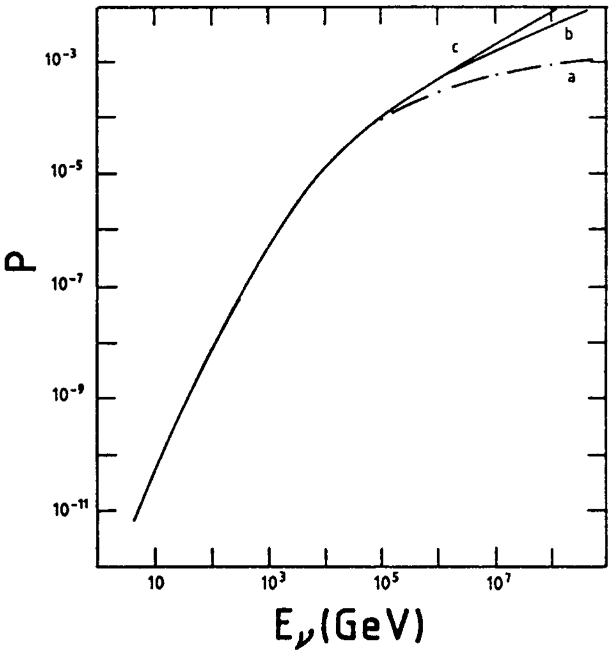

Figure 8.2: P_ν for $E_{\rm th} = 2$ GeV (from Gaisser & Grillo, 1987).

For $E_\nu \gg M_W^2/2m_p \approx 3600$ GeV the growth of σ_ν changes from linear to a slower, logarithmic-like growth, because the W-propagator factor (denominator) in (8.4) cuts off the cross section at large Q^2. In this high energy region the cross section is dominated by the small x behaviour of the structure functions, which is the same for quarks and antiquarks, so $\sigma_{\bar\nu} \to \sigma_\nu$. The small xy region of the numerical integration must be carried out with special care because of the divergence in the integrand for $E_\nu \to \infty$. The curves labelled (a) in figs. 8.2 and 8.3 are for "scaling" structure functions (i.e., no Q^2 dependence).

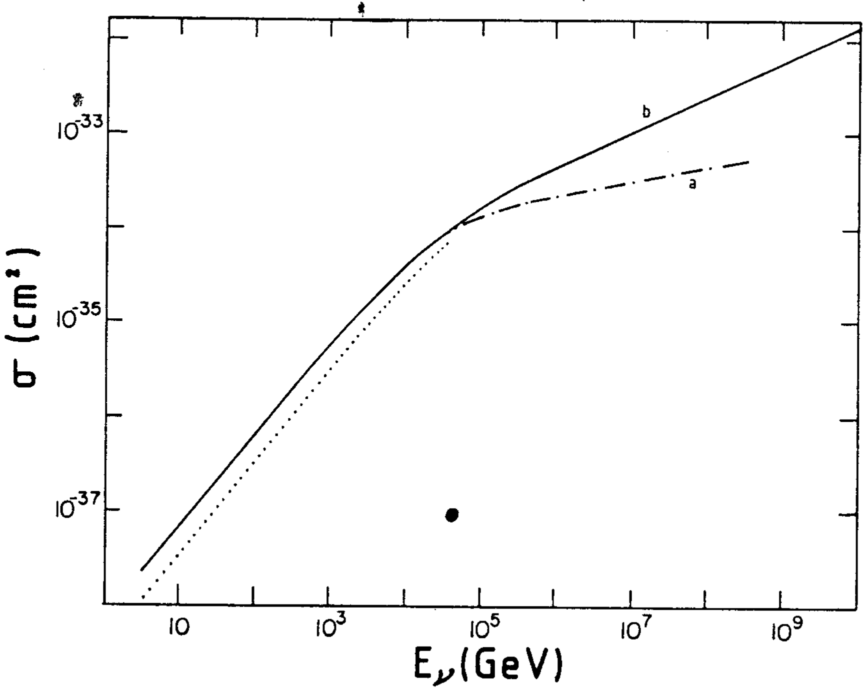

Figure 8.3: Neutrino–nucleon charged current cross sections. Solid: σ_ν. Dotted: $\sigma_{\bar\nu}$.

Those labelled (b) and (c) are for different forms of Q^2 and small x behaviour of the structure functions. It is clear that, for $E_\nu > 10^4$ GeV, it is important to take account of the non-scaling behavior of the structure functions (Reno & Quigg, 1988 and references therein), but the specific form used is not crucial in this application.

At low energy ($E_\nu < M_W^2/2m_p$), the calculation simplifies greatly because the W-propagator factor can be set to unity over the whole integration range of x and y. In this energy range, since small x-behaviour of the structure functions is not emphasized, one can obtain a rather good approximation both for σ_ν and for P_ν by neglecting the contributions of antiquarks to (8.4). Then

$$\frac{d\sigma_\nu}{dy} \sim f_q \frac{G^2 m_p E_\nu}{\pi} \tag{8.10}$$

and

$$\frac{d\sigma_{\bar\nu}}{dy} \sim f_q \frac{G^2 m_p E_\nu}{\pi} (1-y)^2. \tag{8.11}$$

The factor $f_q \approx \frac{1}{2}$ is the momentum fraction of a nucleon that is carried by quarks, (see 5.9). Integration over y gives the estimate (7.1) for $\sigma \equiv 0.5\,(\sigma_\nu + \sigma_{\bar\nu})$. Substitution of (8.10) into (8.9) gives, for $E_{\rm th} \ll E_\nu < 3600$ GeV,

$$P_\nu \approx \xi N_A \sigma_\nu(\epsilon) \left\{ \left(\frac{E_\nu}{\epsilon} + 1\right) \ln\left(1 + \frac{E_\nu}{\epsilon}\right) - \frac{E_\nu}{\epsilon} \right\}, \tag{8.12}$$

with a similar, somewhat more complicated expression for $P_{\bar\nu}$. For $E_{\rm th} \ll E_\nu \ll \epsilon$, one can expand the logarithm to show that

$$P_\nu \to \frac{1}{2}\xi N_A \sigma_\nu(\epsilon) \left(\frac{E_\nu}{\epsilon}\right)^2 \sim 3 \times 10^{-7} (\frac{E_\nu}{\epsilon})^2. \tag{8.13}$$

Problem: Show that, for $E_\nu < 3600$ GeV,

$$\sigma_\nu \sim 0.8 \times 10^{-38}\,\mathrm{cm}^2 \times E_\nu(\mathrm{GeV}).$$

Find the explicit form for $P_{\bar\nu}$ in this energy region and show that, for $E_\nu \ll \epsilon$, $P_{\bar\nu} \to P_\nu/2$.

8.2 Muons from atmospheric neutrinos

Because the atmospheric neutrino spectrum steepens for

$$E_\nu > \epsilon_\pi / B_{\pi\nu} \cos\theta \sim \frac{115\ \mathrm{GeV}}{2.9 \times \cos\theta}, \tag{8.14}$$

the low energy form of P_ν can be used to make a rough estimate of the upward flux of neutrino-induced muons near the vertical. The products of muon decay can be neglected since these ν_μ and $\bar\nu_\mu$ are too low in energy to produce muons with a significant range. Combining the nucleon flux (3.6), the spectrum of $\nu_\mu + \bar\nu_\mu$ (7.5) and the expression for $(P_\nu + P_{\bar\nu})/2$, we can evaluate (8.8). Cutting off the integral at $E_\nu = \epsilon$ gives

$$S \sim 1.4 \times 10^{-13} \frac{\text{upward events}}{\mathrm{cm}^2\,\mathrm{s\,sr}}.$$

The measured value of $\sim 2 \times 10^{-13}$ near the vertical (Svoboda et al., 1987) is less than a factor of two higher than this crude estimate. The complete calculation, using P_ν from fig. 8.2 and taking account of the angular dependence of the neutrino flux and of the muon energy threshold for each detector, gives numbers in reasonably good agreement with the measured rates in various detectors, as shown in fig. 8.4.[1]

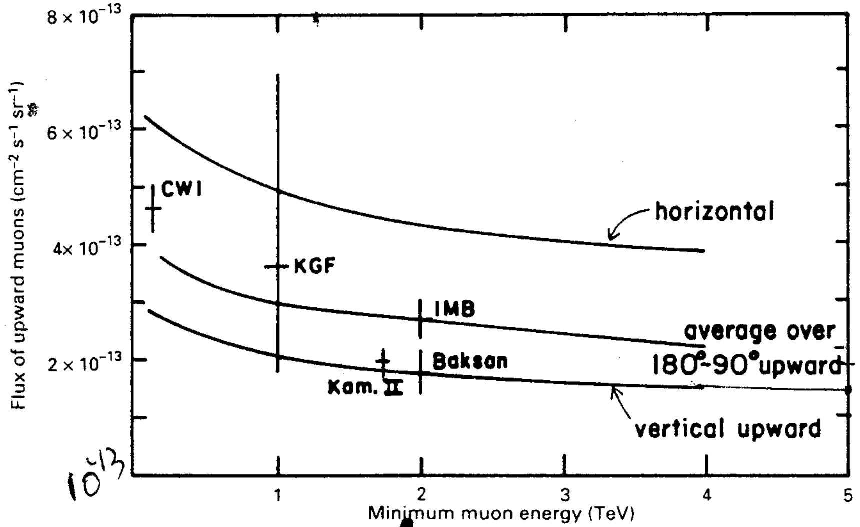

Figure 8.4: Comparison to data on upward muons, updated from Gaisser & Stanev, 1985.

8.3 Astrophysical neutrinos

The successful measurement of high energy atmospheric neutrinos by detection of upward muons demonstrates that the technique can be applied to high energy neutrino astronomy, provided a detector big enough to detect the low rate of events can be constructed. This subject is discussed in detail in chapter 13, but one comment concerning the shape of the neutrino energy spectrum is appropriate for this chapter.

The basic quantity that is measured for external events is the total rate of upward muons with sufficient energy to go through the

detector. In addition, it may be possible to get a crude measurement of the energy of the neutrino-induced muons by measuring the bursts of energy due to radiative processes, which dominate the energy loss when $E_\mu > 1$ TeV. It has been suggested that it might be possible in this way to enhance a signal of neutrinos from an astrophysical source, which is expected to have a flatter energy spectrum than the background of atmospheric neutrinos. There are two reasons to expect that the spectrum of an astrophysical source might be different from the spectrum of atmospheric neutrinos. First, in a diffuse astrophysical environment the pion decay constant, ϵ_π, is likely to be much greater than in the Earth's atmosphere. The associated steepening of the spectrum will therefore occur at much higher energy, if at all. (See the discussion of (8.14) above.) Second, the spectrum of accelerated protons that produces the astrophysical neutrinos at the source may be harder than the local spectrum of galactic cosmic rays.

Figure 8.5 shows the distributions of neutrino energies that give rise to neutrino-induced muons for various assumed neutrino spectra.

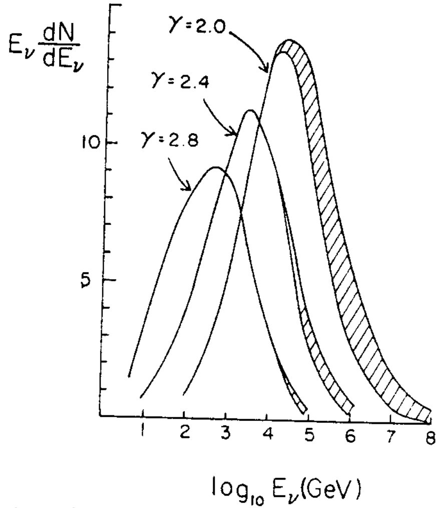

Figure 8.5: Distribution of primary neutrino energies that give rise to upward muons with $E_\mu > 2$ GeV at the detector for power spectra with differential index from 2.0 to 2.8. From Gaisser & Grillo (1987).

The atmospheric neutrino spectrum at high energy is steep enough (differential index 2.7 to 3.7) so that the contribution from neutrinos with $E_\nu > M_W^2/2m_p \approx 3600$ GeV is unimportant. There are reasons

---

[1] Data in fig. 8.4 are from Crouch et al. 1978 (CWI), Krishnaswamy et al., 1982 (KGF), Svoboda et al, 1987 (IMB), Oyama et al. 1989 (Kamiokande II) and Boliev et al. 1981 (Baksan). Data of KGF and CWI are horizontal and Baksan vertically upward. Kamioka and IMB are averaged over all directions below the horizontal.

(to be discussed in the next chapter) to expect that the spectrum of protons or nuclei produced by a cosmic accelerator might have a differential energy spectrum as flat as E^{-2}. In such a case, neutrinos with energies of 100 TeV and greater would contribute substantially to any neutrino-induced signal. For this reason, use of the correct high energy behavior of P_ν (as shown by the outer envelopes of the curves in fig. 8.2) is essential for calculating muons induced by astrophysical neutrinos, whereas it gives only a small correction for atmospheric neutrinos.

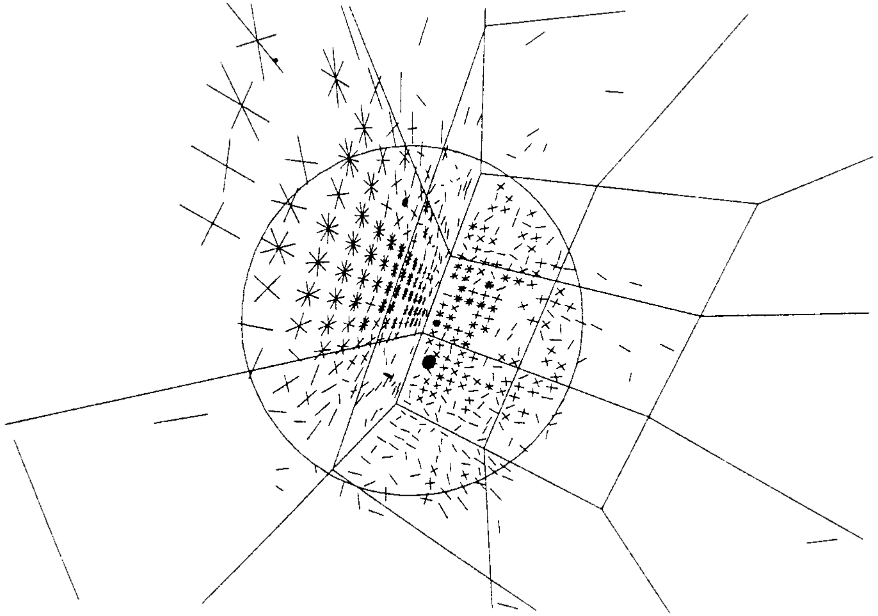

This photograph shows the intense light pattern made by an energetic muon entering the IMB detector from the bottom and exiting near the top. The view is straight upwards. The muon was made by a neutrino (presumed to be of atmospheric origin) that passed through the entire earth and interacted in the rock below the detector. (Photo courtesy of the IMB Collaboration.)

Chapter 9

Propagation

Many aspects of the origin of most cosmic ray nuclei – those with energies from ~ 1 to ~ 10^5 GeV/nucleon – can be understood in terms of shock acceleration at supernova blast waves and diffusive propagation in turbulent magnetic fields in the Galaxy. Some of the main aspects of diffusive propagation and shock acceleration are summarized in the next three chapters. The reader is referred to Longair's book and to reviews of acceleration by Blandford and Eichler (1987) and of propagation by Cesarsky (1980, 1987) for detailed treatments of these subjects. The goal here is to set the stage for a discussion in later chapters of possible point sources of high energy cosmic rays and the related subjects of high energy gamma ray astronomy and neutrino astronomy.

9.1 Transport equation

Two of the most important facts with implications for origin of cosmic rays were already mentioned in the chapter 1. Both relate to the presence in the cosmic radiation of a much greater proportion of "secondary" nuclei, such as lithium, beryllium and boron, than is found generally in the universe. These nuclei are almost absent as end products of stellar nucleosynthesis. They are readily produced in the cosmic radiation, however, as spallation products of the abundant "primary" nuclei such as carbon and oxygen. Measurements of the secondary to primary ratios lead to the following conclusions:

(1) On average, cosmic rays in the GeV range traverse 5 – 10 g/cm^2 equivalent of hydrogen between injection and observation.

(2) This effective grammage decreases as energy increases, at least as far as observations extend, as illustrated in fig. 9.1.

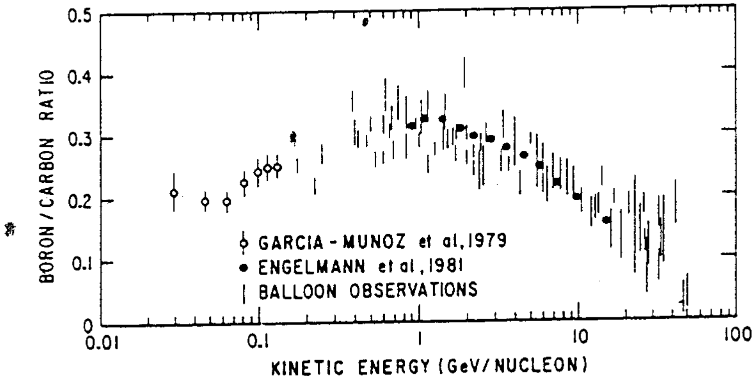

Figure 9.1: Summary of measurements of the ratio of boron to carbon from Ormes & Protheroe (1983). (Reprinted with permission from *The Astophysical Journal.*)

Since the amount of matter along a line of sight through the disk of the Galaxy is about 10^{-3} g/cm^2, (1) implies that cosmic rays travel distances thousands of times greater than the thickness of the disk during their lifetimes. This suggests diffusion in a containment volume that includes some or all of the disk of the Galaxy. The fact that the amount of matter traversed decreases as energy increases suggests that higher energy cosmic rays spend less time in the Galaxy than lower energy ones. It also suggests that cosmic rays are accelerated before most propagation occurs. If, on the contrary, acceleration and propagation occurred together, one would expect a constant ratio of secondary/primary cosmic rays – or even an increasing ratio for some stochastic mechanisms in which it takes longer to accelerate particles to higher energy.

Acceleration and transport of cosmic rays are nevertheless very closely related. In the theory of shock acceleration by supernova blast waves, in particular, diffusive scattering of particles by irregularities in the magnetic field plays a crucial role for acceleration as well as for propagation. Moreover, since acceleration occurs as the supernova remnants (SNR's) expand into the interstellar medium, there is no sharp division between acceleration and propagation. For our purposes, the transport equation as written by Ginzburg and Syrovatskii is sufficiently general to treat both acceleration and propagation of cosmic rays. It is,

В модели Leaky box этот член заменяется на $-N/\tau_{esc}$.

$$\frac{\partial \mathcal{N}}{\partial t} = \nabla\cdot(D_i\nabla\mathcal{N}_i) - \frac{\partial}{\partial E}[b_i(E)\mathcal{N}_i(E)] - \nabla\cdot\mathbf{u}\,\mathcal{N}_i(E) \tag{9.1}$$
$$+\; Q_i(E,t) - p_i\mathcal{N}_i + \frac{v\rho}{m}\sum_{k\geq i}\int \frac{d\sigma_{i,k}(E,E')}{dE}\mathcal{N}_k(E')dE',$$

where $\mathcal{N}_i(E,\mathbf{x},t)dE$ is the density of particles of type i at position $\mathbf{x}$ with energy between E and $E+dE$.

The six terms on the right side of (9.1) have the following physical interpretations. The first represents diffusion, and the diffusion coefficient can be interpreted as

$$D = \frac{1}{3}\lambda_D v, \tag{9.2}$$

where v is the particle velocity and λ_D the diffusion mean free path. With

$$b_i(E) \equiv \frac{dE}{dt} \tag{9.3}$$

the mean rate at which a particle gains energy, the second term in (9.1) can represent either energy loss (e.g. by ionization) or acceleration, depending on the application. The third term represents convection with velocity $\mathbf{u}$. The source term is $Q_i(E,\mathbf{x},t)$ particles of type i per cubic centimeter at position $\mathbf{x}$ and time t per energy interval dE. The fifth term represents losses of nuclei of type i by collisions and decay, with

$$p_i = \frac{v\rho\sigma_i}{m} + \frac{1}{\gamma\tau_i} = \frac{v\rho}{\lambda_i} + \frac{1}{\gamma\tau_i}, \tag{9.4}$$

where $\gamma\tau_i$ is the Lorentz dilated lifetime of the nucleus. Equation (9.4) has been written as if all interstellar gas were hydrogen (mass m). In quantitative work it is necessary to take account separately of $\sim$ 10% helium in the interstellar medium. Finally, the last term is the cascade term, written here to include both feed-down from higher energy as in a nucleonic cascade, and nuclear fragmentation processes.

9.2 The Galaxy

For convenience, various properties of the Galaxy and the interstellar medium (ISM) that we will need for the discussion of galactic cosmic rays are summarized in this section. The basic structure of the galaxy is illustrated in fig. 9.2. Longair (1981) has summarized the measurements on which the following estimates are based.[1] The disk of the Galaxy has a radius of about 15 kpc (1 parsec = 3×10^{18} cm) and a thickness of $2\,h = 200 - 300$ pc at the radius of Earth, which is ~ 8.5 kpc. The mean gas density is nominally 1 hydrogen atom per cm^3 (Gordon & Burton, 1976). The density of diffuse neutral hydrogen is ~ 0.5 cm^{-3}. There is a diffuse component of ionized hydrogen of density ~ 0.03 cm^{-3} and half thickness ~ 700 pc. In addition, there are molecular clouds with densities thousands of times above average on scales of 1 to 10 pc. The central region of the Galaxy (inside $\sim$4 kpc) is more dense than the local disk and mostly molecular. There may be a halo of ionized gas and cosmic rays.

The galactic magnetic field is $\sim 3\,\mu$Gauss and is roughly parallel to the local spiral arm, but with large fluctuations. The magnetic field is "frozen in" to the ionized part of the gas. Together the ionized gas and the magnetic field form a magnetohydrodynamic (MHD) fluid, which supports waves that travel with a characteristic Alfvén velocity, v_A, where

$$\frac{1}{2}\rho v_A^2 \;=\; \frac{B^2}{8\pi}. \tag{9.5}$$

As mentioned in chapter 1, the energy density in the galactic magnetic field, $B^2/8\pi \sim 0.4 \times 10^{-12}$ erg/cm^3 is comparable to that in cosmic rays, which is about 1.5×10^{-12} erg/cm^3. The two are strongly coupled. Streaming of the cosmic rays can generate Alfvén waves, which can in turn be a source of scattering for the cosmic rays.

9.3 Models of propagation

This is a rather complex subject with a long history and an extensive literature (see Cesarsky, 1980, 1987, for reviews). For orientation it is helpful to consider several standard, simplified models, each of which can be expressed by some form of (9.1) with appropriate boundary conditions.

---

[1] The standard reference on the interstellar medium is the book by Spitzer (1978). A classic paper on the interaction of cosmic rays with the galactic medium is that of Parker (1966).

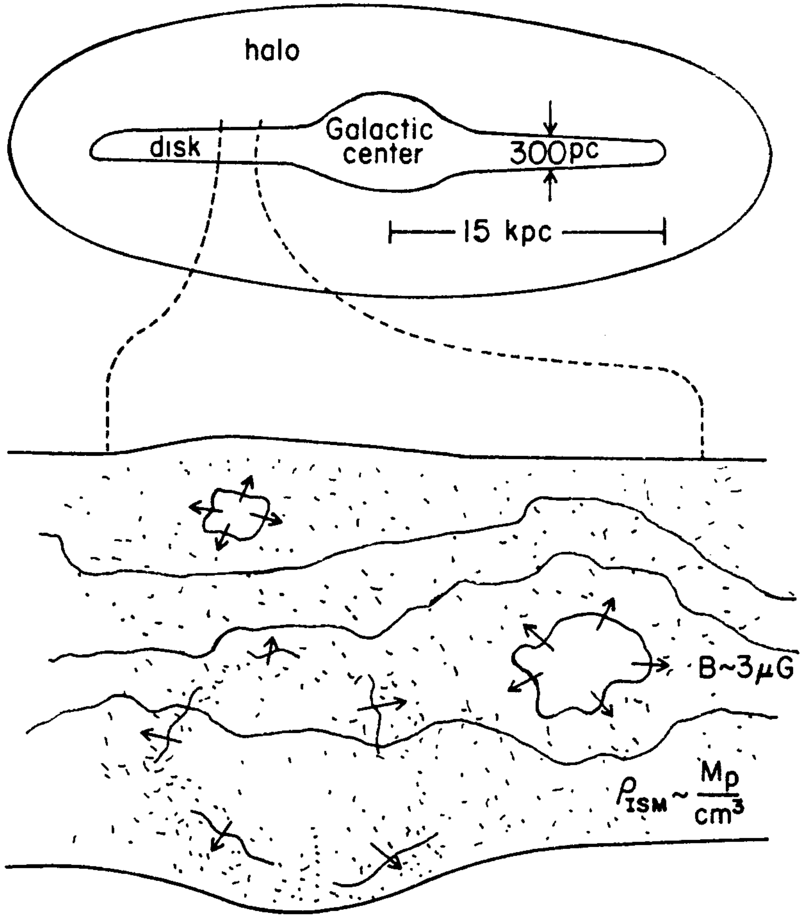

Figure 9.2: Schematic view of the galaxy seen edge on. In the exploded section of the disk, arrows indicate possible regions of cosmic ray acceleration as supernova remnants expand into the interstellar medium.

9.3.1 Leaky box model

The cosmic rays propagate freely in a containment volume, with a constant probability per unit time of escape, $\tau_{\rm esc}^{-1} \ll c/h$. In this model, the diffusion term is replaced in (9.1) by $-\mathcal{N}/\tau_{\rm esc}$. In the absence of collisions and other energy changing processes (and without convection), the solution for a delta function source, $Q(E,t) = \mathcal{N}_0(E)\delta(t)$, is

$$\mathcal{N}(E,t) \;=\; \mathcal{N}_0(E)\,\exp[-t/\tau_{\rm esc}]. \tag{9.6}$$

Thus $\tau_{\rm esc}$ is interpreted as the mean time spent by the cosmic rays in the containment volume and $\lambda_{\rm esc} \equiv \rho\beta c\tau_{\rm esc}$ as the mean amount of matter traversed by a particle of velocity βc.

In equilibrium, the left hand side of (9.1) vanishes. If the picture is further simplified by neglecting energy gains and losses and convection, then (9.1) simplifies to

$$\frac{\mathcal{N}_i(E)}{\tau_{\rm esc}(E)} = Q_i(E) - \left(\frac{\beta c\rho}{\lambda_i} + \frac{1}{\gamma\tau_i}\right)\mathcal{N}_i(E) + \frac{\beta c\rho}{m}\sum_{k\geq i}\sigma_{i,k}\mathcal{N}_k(E), \quad (9.7)$$

E - per nucleon

where $\sigma_{i,k}$ is a spallation cross section. This form of the equation is appropriate for treating primary and secondary cosmic ray nuclei, which retain the same energy per nucleon during fragmentation processes. A great deal of data on elemental composition of low energy galactic cosmic rays has been treated within the framework of this set of equations (Shapiro & Silberberg, 1970; Simpson, 1983; Silberberg, Tsao & Letaw, 1983). The important result is that, starting from measured fragmentation cross sections, data on carbon and oxygen and their stable secondaries, as well as data on iron and its secondaries, can be approximately understood under the assumption that all the nuclei have the same propagation history (i.e. by (9.7) with a single parameter $\lambda_{\rm esc}$). Relatively small discrepancies are the subject of current investigations, which take into account modifications of the pathlength distribution from the exponential distribution that follows from (9.6), the energy dependence of the fragmentation cross sections and the possibility of some degree of "re-acceleration" during propagation.

Within this model, the energy dependence of the secondary to primary ratios is attributed to an energy dependence of $\lambda_{\rm esc}$. One recent fit (Gupta & Webber 1989) gives

$$\lambda_{\rm esc} = \beta c\rho\tau_R = 10.8\,\frac{\rm g}{\rm cm^2}\,\beta\left(\frac{4}{R}\right)^{\delta}, \quad R > 4\ {\rm GV}, \quad (9.8)$$

with $\delta \approx 0.6$, and $\lambda_{\rm esc} = 10.8\,\beta$ for $R < 4$ GV. This has an important implication for the source spectrum, $Q_i(E)$. For a primary nucleus (P) for which feed-down from fragmentation of heavier nuclei can be neglected, the solution of (9.7) has the form

$$\mathcal{N}_P(E) = \frac{Q_P(E)\tau_{\rm esc}(R)}{1 + \lambda_{\rm esc}(R)/\lambda_P}. \quad (9.9)$$

For protons, for which the interaction length $\lambda_{\rm proton} \sim 55$ g/cm^2, $\lambda_{\rm esc} \ll \lambda_P$ for all energies. In this case, only the numerator in (9.9) is important. Thus, if the observed spectrum is $\mathcal{N} \propto E^{-(\gamma+1)}$ at high energy, the source spectrum must be

$$Q(E) \propto E^{-\alpha}, \quad (9.10)$$

with $\alpha = (\gamma + 1 - \delta) \approx 2.1$. At the other extreme, for iron the interaction length is, from (5.5), about 2.3 g/cm^2. In this case, at low energies losses are due primarily to interactions rather than to escape, and the spectrum should reflect the source spectrum directly. There should then be a gradual steepening of the spectrum in the energy range where the escape length falls below the interaction length. From (9.8), this should occur around 18 GeV/nucleon for iron. The spectrum of iron is indeed flatter than that of protons and light nuclei such as carbon, and there is some evidence that it steepens at high energy (Esposito et al., 1990). It remains somewhat flatter than the proton spectrum up to ~ 1 TeV/nucleon (Grunsfeld et al., 1988).

The other major constraint on models of propagation comes from the ratios of unstable to stable isotopes of secondary nuclei. Unstable nuclei with lifetimes comparable to $\tau_{\rm esc}$, such as ^{10}Be and ^{26}Al, can be used as "cosmic ray clocks." For a stable secondary, the solution of (9.7) depends only on $\lambda_{\rm esc}$ and not on $\tau_{\rm esc}$ and ρ separately. A measurement of the ratio of an unstable to a stable isotope allows separation of escape time and density.

> **Problem:** Show that for a secondary nucleus (S) with rest lifetime τ_S
>
> $$\frac{\mathcal{N}_S}{\mathcal{N}_P} = \frac{\sigma_{P\to S}}{\sigma_P}\,\frac{\lambda_{\rm esc}}{\lambda_P\left[1 + \lambda_{\rm esc}/\lambda_S + \tau_{\rm esc}/(\gamma\tau_S)\right]}.$$

The most well studied example is beryllium. The isotope ^{10}Be is unstable to β-decay with $\tau_S \approx 3.9 \times 10^6$ yrs. This is in just the right range to be of interest. If the confinement volume for the cosmic rays were the galactic disk, then the escape time would be identical to the residence time in the disk, τ_R. For a nominal disk density of one hydrogen atom per cubic centimenter and a value of $\lambda_{\rm esc} \sim 10$ g/cm^2, we have

$$\tau_R = \frac{\lambda_{\rm esc}}{\rho\beta c} \sim 6 \times 10^6\ {\rm yrs}. \quad (9.11)$$

If $\tau_{esc} < \tau_{^{10}Be}$, then the measured ratio of unstable to stable beryllium should be not much less than the ratio expected at production from the ratio of the fragmentation cross sections of the parent nuclei. On the contrary, however, the measured ratio is much less than its value at production. The implication is that $\tau_{esc} > \tau_{^{10}Be}$. From analysis of their measurement, Garcia-Munoz, Mason & Simpson (1977) find $\tau_{esc} \sim 2\times10^7$ yrs, with rather large uncertainties. This implies that the cosmic rays propagate in a volume of mean density ~ 0.3 g/cm^2 and suggests therefore that the containment volume in the leaky box model is considerably wider than the disk of the galaxy, perhaps extending into a galactic halo.

9.3.2 Nested leaky box model

In this model (Cowsik and Wilson, 1973, Meneguzzi, 1973) there are assumed to be small confinement regions near the sources with relatively high density in which particles diffuse for a short, but energy dependent time. A physical realization might be supernovas inside dense clouds. The energy dependence of the secondary to primary nuclei is attributed to energy dependent leakage from the source regions, characterized by $\lambda_1(E)$. The Galaxy is considered as an outer volume in which the nuclei from the shrouded sources may traverse a further small, constant amount of matter, λ_2. Clearly all the data on secondary to primary ratios that can be explained in the leaky box model can be explained here also, with differences perhaps occurring at energies where the escape length in the simple leaky box model would be lower than λ_2 =constant. The outer containment volume will have to be larger than in the simple leaky box model to allow the ^{10}Be/Be ratio to fall to its observed value while still keeping λ_2 small.

An observer *inside* a source region would measure a differential spectrum $\propto E^{-(\alpha+\delta)}$ due to energy dependent leakage out of the source, as in the simple leaky box model. The Earth is, however, not inside a source region, so we observe the source spectrum. In this model therefore, the cosmic accelerators will need to produce a differential spectrum $\alpha = \gamma + 1 \approx 2.7$.

9.3.3 Closed galaxy model

This can be considered a variation of the nested leaky box model in which the inner volume is the local spiral arm of the Galaxy (Peters and Westergaard, 1977), so that Earth is again *inside* the region from which energy-dependent escape gives the observed decrease with energy of the ratio of secondary to primary nuclei. The large outer volume may be completely closed so that nuclei are completely destroyed, and the "old" component of cosmic rays consists only of stable particles with a lifetime determined by their lifetime against energy loss, which in turn is determined by the ratio of the total interstellar gas in the Galaxy to the gas in the spiral arm.

9.3.4 Diffusion models

Models in which the diffusion equation (9.1) is solved without treating the diffusion operator as a constant are more realistic in a physical sense than the various "leaky box" models. For many purposes they are equivalent; hence the persistence of the use of leaky box models. The main difference is that in a leaky box model, in steady state the distribution of cosmic rays is uniform inside the containment volume. When there is diffusion, there are density gradients and consequently also anisotropy.

The diffusion coefficient, D, relates the current of particles to a spatial gradient in the density of the particles,

$$\mathbf{J}(\mathbf{r},t) = -D\,\nabla\mathcal{N}. \tag{9.12}$$

Since

$$\dot{\mathcal{N}} = -\nabla\cdot\mathbf{J} + Q(\mathbf{r},t), \tag{9.13}$$

where Q is an explicit source of particles, we can write

$$\dot{\mathcal{N}} = \nabla\cdot(D\,\nabla N) + Q. \tag{9.14}$$

This is recognizable as the transport equation (9.1) with acceleration, convection and collision losses and gains omitted.

The Green's function for the diffusion equation (9.14) is

$$G(\mathbf{r},t) = \frac{1}{8(\pi\,D\,t)^{3/2}}\exp\{-r^2/(4\,D\,t)\}. \tag{9.15}$$

This gives the probability for finding a particle that was injected at the origin at position $\mathbf{r}$ after time t. If we consider diffusion away from a plane source (the galactic plane), we want to consider the mean value of the distance from the plane, $< |z| >$, as a function of time:

$$< |z| > = 2\sqrt{D t/\pi}. \tag{9.16}$$

In a delightfully polemical paper, Ginzburg, Khazan & Ptuskin (1980) have argued forcefully that the correct picture of cosmic ray propagation is a diffusion model. In the simplest version, which serves to illustrate the main points, the galaxy has a halo of scale height $H \gg h \sim 100$ pc, the scale height of the gaseous disk. From the fact that the scale height of the ionized component of the interstellar medium is ~ 700 pc, we might guess that H is at least this large. From (9.16) the characteristic time to reach a height H is

$$t_H \sim H^2/D, \tag{9.17}$$

neglecting a numerical constant of order one, and assuming $D \sim$ constant throughout the volume of the halo and the disk. Cosmic rays are assumed to escape freely at H, where the cosmic ray density approaches zero. The quantity

$$v_D \sim H/t_H \sim D/H \tag{9.18}$$

is a characteristic average velocity for escape from the galaxy.

At this point it is helpful to compare this model with the leaky box model so that the parameters determined there can be translated into values for parameters of the diffusion model. The method is to find an equivalent homogeneous leaky box model. The mean density of gas in the total volume, including the halo, is

$$\rho_H = \rho_g \frac{h}{H}, \tag{9.19}$$

where ρ_g is the density in the gaseous disk (~ 1 proton/cm^3). If this matter were distributed homogeneously throughout the halo and disk, then cosmic rays travelling with velocity βc for a time t_H would pass through an amount of matter

$$\lambda_{\rm esc} = \rho_g \beta c \frac{h\,H}{D}. \tag{9.20}$$

To get the observed ratios of secondary to primary stable nuclei, $\lambda_{\rm esc} \sim 10\,{\rm g/cm^2}$, so $D/H \sim 1.5 \times 10^6$ cm/s.

The energy dependence of $\lambda_{\rm esc}$ (9.8), which follows from the observed energy-dependence of $\mathcal{N}_S/\mathcal{N}_P$, then implies $D \propto E^\delta$ at high energy if H is assumed fixed. In the diffusion model, the density of cosmic rays is not homogeneous; it decreases as a function of distance from the galactic plane. Associated with the flow away from the plane is an anisotropy, A, of order v_D/(particle velocity). At low energy we therefore expect $A \sim 10^{-4}$, with $A \propto E^\delta$ above 5 GeV or so. Apparently the value $\delta \sim 0.6$ can only hold for energies below about a TeV because the observed anisotropy is only $\sim 10^{-3}$ in the 1–100 TeV range. This will be discussed further in Chapter 12 in connection with propagation of very high energy cosmic rays.

For stable secondaries, the diffusion model and the leaky box model are equivalent in their treatment of the average pathlength for production of secondaries, although the pathlength distribution is in general different. (A.J. Owens (1976) gives some nice illustrations of cosmic ray propagation and age distributions for various diffusion models.) The implications for unstable secondaries are also different in the diffusion model. Secondaries are produced at an average rate

$$Q_S = \beta c \frac{< \rho >}{m_H} \sigma_{P \to S} \mathcal{N}_P, \tag{9.21}$$

where $< \rho >$ is the gas density averaged over the volume in which the secondary nuclei are contained. For stable secondaries and for unstable secondaries with $\gamma \tau_S > t_H$, $< \rho > = h\rho_g/H$, as in (9.19). For unstable secondaries with $\gamma \tau_S < t_H$, however, the equivalent "containment" volume is smaller than the full halo. Physically, this is because the unstable cosmic rays do not live long enough to reach a distance H from the plane. In this case

$$< \rho > = \rho_g h/\ell_S,$$

where ℓ_S is the distance travelled during the lifetime of the unstable secondary.

This is the situation for ^{10}Be, which has $\tau_S \approx 3.9 \times 10^6$ yrs. Because $H > 700$ pc, $t_H > 2 \times 10^7$ yrs. From (9.16), $\ell_S \sim \sqrt{D \gamma \tau_S}$, so

$$Q_S = \beta c \frac{\rho_g h}{m_H \sqrt{D \gamma \tau_S}} \sigma_{P \to S} \mathcal{N}_P. \tag{9.22}$$

The average density of the secondary is $\mathcal{N}_S = Q_S \tau$. When $\ell_S < H$ escape can be neglected, so

$$\frac{1}{\tau} = \frac{1}{\tau_{\rm int}} + \frac{1}{\gamma \tau_S}.$$

The average interaction rate in the volume of the unstable secondary is

$$\frac{1}{\tau_{\rm int}} = \frac{h}{\ell_S}\frac{\rho_g}{m_H}\beta c\,\sigma_s. \tag{9.23}$$

We now need to express the secondary to primary ratio in a form that can be compared with leaky box parameters. We make use of the relation (9.20) already established between $\lambda_{\rm esc}$ and H/D. Manipulating (9.22), (9.23) and the definition of τ leads to

$$\frac{\mathcal{N}_S}{\mathcal{N}_P} = \frac{Q_S\,\tau}{\mathcal{N}_P} = \frac{\sigma_{P\to S}}{\sigma_P}\,\frac{\lambda_{\rm esc}}{\lambda_P\left(\lambda_{\rm esc}/\lambda_S + H/\sqrt{D\,\gamma\,\tau_S}\right)}. \tag{9.24}$$

This should be compared to the corresponding expression in the leaky box model as given in the problem on p. 121. Because the two expressions have a different energy-dependence, they can only be equated at one energy. The two models give the same value for the beryllium isotopes if

$$1 + \tau_{\rm esc}/(\gamma\,\tau_S) = H/\sqrt{D\,\gamma\,\tau_S}. \tag{9.25}$$

The low energy measurements require the leaky box parameter, $\tau_{\rm esc}$, to have a value $\sim 2\times10^7$ yrs, and we have already determined $D/H \sim 1.5\times10^6$ cm/s. Thus at low energy ($\gamma \approx 1$)

$$H \sim 2\,{\rm kpc} \text{ and } D \sim 10^{28}\,{\rm cm^2/s}.$$

With these parameters we find $\ell_S \sim 500$ pc at low energy. In other words, the mildly relativistic, unstable ^{10}Be nuclei are to be found within ~ 500 pc of the galactic plane, a volume in which the average gas density is

$$<\rho>/\rho_g \sim h/\ell_S \sim \frac{1}{5}.$$

In principle, it should be possible to verify the diffusion picture experimentally by its characteristically slower increase of the ratio of unstable to stable beryllium as the energy increases.

Chapter 10

Gamma rays and antiprotons

A key to understanding propagation of cosmic rays is study of the production of secondary particles in collisions of the cosmic ray primaries with gas in the interstellar medium. Secondary nuclei were emphasized in the previous chapter, but they tell us only about the propagation of nuclei with Z $\geq$4. In this chapter I discuss the production of gamma rays (with emphasis on those from π^0 decay) and antiprotons. These are tracers of the dominant proton component. Another important difference is that the gamma rays, being neutral, follow straight lines, in contrast to charged particles which wander along complicated trajectories through the complex interstellar magnetic fields. Photons from decay of neutral pions produced in collisions of protons can therefore be used directly to map regions in which cosmic rays interact with matter. Antiprotons, like nuclei, diffuse in galactic magnetic fields and therefore do not map their origin. They have an interesting kinematic feature, however, that provides an extra diagnostic tool for studying the origin and propagation of the primary cosmic rays. Because of their relatively large mass, the threshold for antiproton production is high (kinetic energy = 5.6 GeV) and the production cross section is strongly energy dependent. As a result, antiprotons of a given energy can only be produced by interactions of primary particles that have much higher energy. Secondary nuclei, on the other hand, have essentially the same energy per nucleon as their parent nuclei.

10.1 Overview

Photons, neutrinos, electrons, positrons and antinucleons in the cosmic radiation are all produced by interactions of cosmic rays in the interstellar medium. (They may also be produced in discrete sources, and the charged particles may be directly accelerated, but this chapter concerns only production in the diffuse interstellar medium.) For each of these stable particles, the contribution from interactions at a point in the instellar medium is given by a convolution of the cosmic ray spectrum with the gas density at that point and with the cross section × decay function for production of the secondary. The secondary spectra also have some kinematic features in common, although there are specific differences due to the different masses and decay chains involved.

10.1.1 Source functions

The number of secondaries produced per cubic centimeter per second per unit energy interval at position **r** (the source function) is given by the last term in (9.1). In terms of the flux of primary cosmic rays, $\phi(E_i) = \mathrm{d}N_i/\mathrm{d}E_i$, the source function can be expressed as

$$q_k(E_k,\mathbf{r}) = \int \frac{\mathrm{d}\sigma_{i\to k}(E_k,E_i)}{\mathrm{d}E_k}\left(\frac{c\,\rho(\mathbf{r})}{m}\right)\left(\frac{4\pi}{c}\,\phi(E_i)\right)\mathrm{d}E_i. \qquad (10.1)$$

In this equation I denote the source of secondaries by small "q" to distinguish it from "Q_i" in (9.1), which is an explicit source term for primaries, for example as injected by a cosmic accelerator. If the secondary of interest is produced as the end product of a decay chain (e.g. $\pi^0 \to \gamma$ or $\pi^+ \to \mu^+ \to \nu_e$), then the differential cross section in (10.1) stands for the appropriate convolution of cross section times decay distribution. For detailed calculations, (10.1) needs to be corrected for the contribution of helium (and heavier nuclei) in the cosmic ray spectrum and for helium gas in the interstellar medium. This leads to a sum over terms with the appropriate cross section for each combination (i.e. proton on hydrogen, proton on helium, alphas on hydrogen and alphas on helium).

The observed flux at Earth is calculated differently depending on whether the secondary is neutral or charged. For photons (or neutrinos) the counting rate per unit area of detector from a given direction is

$$\frac{\mathrm{d}n_\gamma}{\mathrm{d}A\mathrm{d}E_\gamma\mathrm{d}t} = \int \frac{q_\gamma(E_\gamma,\mathbf{r})}{4\pi\,r^2}\mathrm{d}^3r = \int_0^{r_{\max}} \frac{q_\gamma(E_\gamma,\mathbf{r})}{4\pi}\mathrm{d}r\,\mathrm{d}\Omega. \qquad (10.2)$$

Here **r** is the polar vector in a geocentric coordinate system. If the source function is independent of position in the disk of the galaxy (i.e. a uniform distribution of interstellar matter and a uniform distribution of cosmic rays with their energy spectra also independent of position) then the differential flux at Earth is

$$\phi_\gamma(E_\gamma) = \frac{\mathrm{d}n_\gamma}{\mathrm{d}A\,\mathrm{d}E_\gamma\,\mathrm{d}t\,\mathrm{d}\Omega} = \frac{q_\gamma}{4\pi}\,r_{\max}(b,\ell), \qquad (10.3)$$

where b and ℓ are galactic latitude and longitude, and $r_{\max}$ is the limit of the galactic disk as a function of direction.

Photons and neutrinos propagate along straight lines and so have only one pass at an observer. Antiprotons, once they are produced, diffuse just like protons in turbulent interstellar magnetic fields.[1] Thus, for example, in the leaky box model the equilibrium flux of antiprotons is given by an equation like (9.9) with the source function for primary cosmic rays replaced by the source function for antiprotons: $Q_p \to q_{\bar p}$. Neglecting subsequent loss of antiprotons by interactions with the interstellar gas (which is valid for relativistic $\bar p$'s), the equilibrium flux of antiprotons is

$$\phi_{\bar p}(E_{\bar p}) = \frac{c}{4\,\pi}\,\tau_{\mathrm{esc}}(E_{\bar p}) \times q_{\bar p}(E_{\bar p}). \qquad (10.4)$$

Note the important point that the differential flux of antiprotons depends on the escape time at the energy of the antiproton, not at the energy (typically much higher) of the cosmic ray that produced it. The fact that the escape time for the more energetic parents is smaller has already been taken into account by using the observed cosmic ray spectrum to calculate the source function, $q_{\bar p}$. Equations (10.3) and (10.4) are the basis of the more detailed discussions of gamma rays in §10.2 and of antiprotons in §10.3 below.

---

[1] One should not forget, however, that the handedness of the motion of an antiproton through a magnetic field is opposite to that of a proton, which could be significant when the field has large scale order. Webber & Potgieter (1989) have pointed out that differences between solar modulation of protons and antiprotons could result in large differences in fluxes of protons and antiprotons that change during the solar cycle.

Expressions for spectra of secondary electrons and positrons are similar to those for antiprotons, with the important difference that energy losses due to synchrotron radiation in interstellar magnetic fields are important and must be taken into account. This makes interpretation of their spectra somewhat more complicated. (For a discussion and relevant references see Stephens and Golden, 1987).

10.1.2 Kinematics

At sufficiently high energy, all mass scales become negligible compared to the energy. Then both the decay distributions and the production cross sections may be approximated by scaling functions that depend only on the ratio of two energies. In this limit, for a power law spectrum, the source function is proportional to the primary spectrum just as for cascades in the atmosphere. For photons, for example (cf (4.13))

$$q_\gamma(E_\gamma) \;=\; 4\,\pi\,\frac{\rho}{m}\,\left(\sigma_{pp}^{\rm inel}\times\frac{2\,Z_{N\to\pi^0}}{\alpha}\right)\times\phi_N(E_\gamma), \qquad (10.5)$$

where ϕ_N is the spectrum of cosmic ray nucleons with differential spectral index α (cf. (3.6) for nucleons at Earth up to $\sim 10^{15}$ eV). Since the total inelastic cross section varies slowly with energy, it must be evaluated at the appropriate energy, e.g. $\sim$ 10 times the energy of the secondary.

When the production of a secondary is characterized by a mass scale, such as the mass of a decaying parent or a production threshold, then the production spectrum has a characteristic peak that reflects the mass scale. In this case, even if the primary spectrum can be described as a power law at all relevant energies, the production spectrum of the secondary is not a simple power. We have already seen an example of this with low energy neutrino spectra, which peak around 30–35 MeV, which is the typical share of the parent meson mass taken by the neutrino. The simplest example is photons from π^0 decay. In his book, Stecker (1971) gives a detailed treatment of this and related processes, which I use here.

Each photon has $E_\gamma = m_\pi/2 \approx 70$ MeV in the rest frame of the π^0. For decay in flight, the laboratory energy of the photon is given by (4.8). Because the decay is isotropic in the pion rest frame, the distribution of laboratory energies is flat with the limits determined by $\cos\theta^* = \pm 1$, where θ^* is the decay angle in the pion rest frame.

The limits are

$$\frac{m_\pi}{2}\sqrt{\frac{1-\beta}{1+\beta}} \;\le\; E_\gamma \;\le\; \frac{m_\pi}{2}\sqrt{\frac{1+\beta}{1-\beta}}, \qquad (10.6)$$

where β is the velocity of the parent pion. The geometric mean energy of photons from decay in flight of neutral pions is $m_\pi/2 \approx 70$ MeV independent of the energy of the parent pion. Thus the composite distribution of photons from decay of an arbitrary distribution of parent pions is symmetric about 70 MeV when plotted *vs* $\ln(E_\gamma)$. It consists of a weighted sum of boxes, as illustrated in fig. 10.1. A photon with energy less than $m_\pi/2$ must be a backward decay product of a moving parent pion. For $E_\gamma < m_\pi/2$, the lower the energy of the photon, the higher the energy of the parent pion must be.

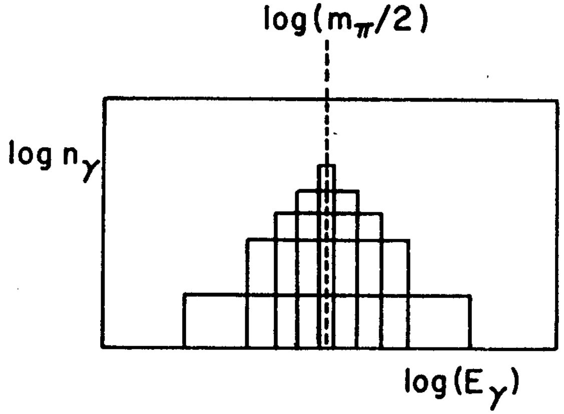

Figure 10.1: Schematic construction of the photon spectrum produced by decay of a spectrum of neutral pions. (After Stecker, 1971.)

> **Problem:** (After Stecker, 1971). Show that the minimum total pion energy (rest mass plus kinetic) needed to produce a photon of energy E_γ is
>
> $$E_\pi(\mathrm{min}) \;=\; E_\gamma \;+\; \frac{m_\pi^2}{4\,E_\gamma} \qquad (10.7)$$
>
> for any value of E_γ (either greater than or less than 70 MeV).

Interactions of protons of a certain energy will produce a symmetric distribution of photons that reflects the shape of the spectrum of π^0's from nucleon interactions of that energy. A weighted sum of these distributions in turn gives the distribution of photons from a spectrum of nucleons, and the result is again symmetric in logarithmic variables. This is illustrated in fig. 10.2*b*. Because each component of the distribution is symmetric about $m_\pi/2$, the distribution of photons from any composite distribution of parent π^0's peaks at $\ln(m_\pi/2)$.

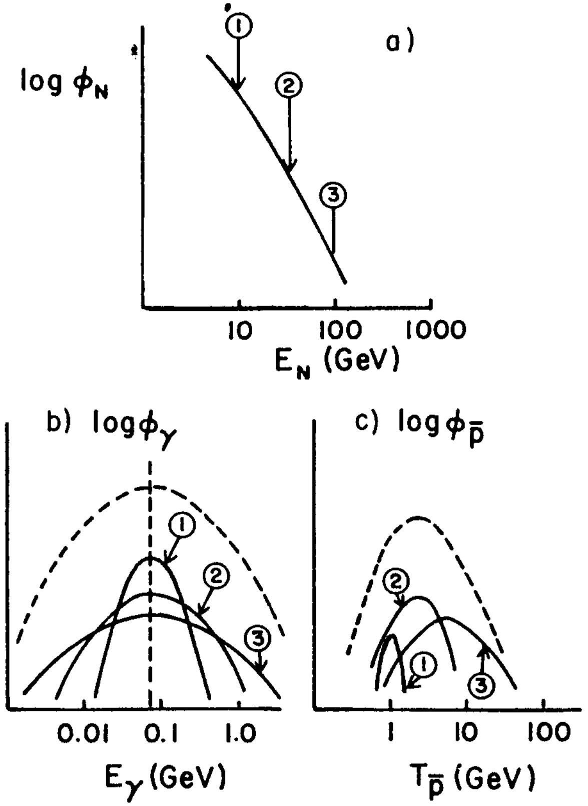

Figure 10.2: Construction of secondary spectra. From each numbered point on the primary spectrum (a), one obtains the distributions of secondaries shown in (b) for photons from π^0-decay and in (c) for antiprotons. The dashed lines show the convolution of all contributions.

To treat antiprotons (or other massive secondaries) we need to consider a Lorentz transformation from a system in which particle production is symmetric back to the laboratory frame. The laboratory energy of the particle of interest is given by (4.8), here written as

$$E = \gamma(E^* + \beta\sqrt{(E^*)^2 - m^2}\cos\theta^*) \qquad (10.8)$$

where E^* is the total energy of the secondary particle in the symmetry system. The laboratory energy of the secondary is bounded by (10.8) with $\cos\theta^* = \pm 1$:

$$\gamma E^* - \sqrt{\gamma^2 - 1}\sqrt{(E^*)^2 - m^2} \leq E \leq \gamma E^* + \sqrt{\gamma^2 - 1}\sqrt{(E^*)^2 - m^2}. \qquad (10.9)$$

For antiprotons, the symmetry system is the center of mass (CM) system of the parent nucleon–nucleon collision. Thus the Lorentz factor in (10.8) and (10.9) is

$$\gamma = \sqrt{s}\,/\,2m. \qquad (10.10)$$

Because of conservation of baryon number in hadronic interactions, the minimum process for production of an antiproton is

$$pp \rightarrow ppp\bar{p}. \qquad (10.11)$$

The center of mass threshold for $\bar{p}$ production is therefore

$$\sqrt{s_{\rm th}} = \sqrt{2mE_{\rm th} + 2m^2} = 4m. \qquad (10.12)$$

Thus $E_{\rm th} = 7m$ is the threshold (total) energy that an incident proton must have in the laboratory system to produce an antiproton. From (10.10) and (10.12), the Lorentz factor at threshold is $\gamma_{\rm th} = 2$.

At threshold, the antiproton is produced at rest in the CM, and $E^* = m$. Then from (10.8) the antiproton has a unique energy in the laboratory frame, $E_{\bar{p}} = 2m$, or a kinetic energy of one proton mass. To get an antiproton with kinetic energy less than 938 MeV requires that it be produced in the backward CM hemisphere of a higher energy collision. Taking into account the kinematic limit for antiproton production in a nucleon–nucleon collision, a good approximation for the minimum kinetic energy of a $\bar{p}$ that can be produced by the interaction of a proton with total laboratory energy E_p is

$$T_{\bar{p}} \approx \frac{m^2}{E_p - 6m} \qquad (10.13)$$

(Gaisser and Levy, 1974). Since the cosmic ray flux decreases with increasing energy, and since the production spectrum of $\bar{p}$'s is strongly peaked around $E^* \approx m$, the spectrum of antiprotons produced by cosmic ray collisions in the interstellar medium will decrease for kinetic actually a more complicated version of that for $\pi^0 \to 2\gamma$, as illustrated in fig. 10.2c. An antiproton produced near rest in the center of mass (i.e. in the peak of the distribution) will have a lab energy

$$E_{\bar{p}} \sim \gamma m = \frac{1}{2}\sqrt{2mE_p + 2m^2}, \tag{10.14}$$

Unlike the case for $\pi^0 \to 2\gamma$, the peak of the secondary distribution moves with energy.

To summarize this section on kinematics, both photons and antiprotons produced in inelastic collisions of cosmic ray nucleons with the interstellar gas have a distinctive kinematic feature in their energy spectra. It is a peak in the spectrum related to the mass scale associated with the production. For photons, the peak is at 70 MeV, and for antiprotons it is around 2 GeV kinetic energy.

10.2 Diffuse gamma rays and neutrinos

The term "gamma ray" in high energy astrophysics refers to all photons with energies above the x-ray region, with the dividing line usually taken to be around 0.1 MeV. This includes continuum radiation, as well as nuclear lines. Our interest here is in diffuse gamma rays with energies above 10 MeV. In the galaxy these are produced primarily by bremsstrahlung from cosmic ray electrons and from decay in flight of π^0's produced by interactions of cosmic ray protons. Inverse Compton scattering on starlight is less important, and synchrotron radiation is much less important for production of diffuse gamma rays in the galaxy. Fichtel and Trombka (1981) review the subject in the light of satellite data not available when Stecker's book was written.

10.2.1 Bremsstrahlung

For electrons producing photons by bremsstrahlung, the cross section that goes into (10.1) is

$$\frac{d\sigma_{e\to\gamma}(E_\gamma, E_e)}{dE_\gamma} = \frac{1}{E_e}\frac{\phi(v)}{N_A X_0}, \tag{10.15}$$

where X_0 is the radiation length and $v \equiv E_\gamma/E_e$. The bremsstrahlung function, $\phi(v)$, is defined and discussed in §15.1.

Problem: Derive (10.15). For a power law differential energy spectrum for the electrons,

$$\phi_e(E_e) \propto E^{-\alpha},$$

show that

$$q_{e\to\gamma} \approx \frac{4\pi\rho}{X_0}\phi_e(E_\gamma)\left(\frac{1}{\alpha+1} + \frac{1.35}{\alpha-1} - \frac{1.35}{\alpha}\right). \tag{10.16}$$

The bremsstrahlung spectrum is proportional to the parent electron spectrum down to energies much less than the energy of 70 MeV at which the photon spectrum from π^0 decay peaks. This is because the only scale in the problem is the electron mass. Therefore, unless the source function for photons from electrons is very much less than that from π^0's, bremsstrahlung will dominate on the low energy side of the peak.

We can use (10.5) and (10.16) to express the ratio of bremsstrahlung photons to π^0 photons for power law spectra at high energy ($E_\gamma \gg 70$ MeV). It is

$$\begin{aligned}\frac{e\to\gamma}{\pi^0\to\gamma} &= \left[\frac{1}{N_A X_0 \sigma_{pp}^{\text{inel}}}\right]\left[\frac{\alpha}{2Z_{N\to\pi^0}}\left(\frac{1}{\alpha+1} + \frac{1.35}{\alpha-1} - \frac{1.35}{\alpha}\right)\right]\left[\frac{\phi_e}{\phi_N}\right] \\ &\approx [0.85]\,[27\times(0.6)]\left[\frac{\phi_e}{\phi_N}\right]. \end{aligned} \tag{10.17}$$

The square brackets group the expression into three distinct factors. The first is the ratio of interaction lengths for the two processes, which is about one. The second factor is the ratio of the spectrum weighted moments of the inclusive cross sections. Bremsstrahlung is more than an order of magnitude more efficient for the spectral index chosen in this example, $\alpha = 2.6$. The ratio of the electron spectrum to the nucleon spectrum in the few GeV energy range is somewhat less than 1%. Thus for $E_\gamma > 1$ GeV, photons from nuclear interactions (*via* π^0 decay) dominate by an order of magnitude. At lower energy, however, we expect the bremstrahlung to dominate. This is a plausible interpretation of the data, as shown in fig. 10.3.

10.2.2 Nuclear interactions

The calculations shown in fig. 10.3 are based on detailed evaluations of the source spectra that take into account the deviations of the primary spectra from power laws (both for electrons and for nucleons) as well as the contributions of nuclei other than hydrogen (both in the interstellar gas and in the cosmic rays). Another complication that enters is the required "demodulation" of the primary spectrum at low energy (below about 10 GeV in practice). It is necessary to correct for the fact that the cosmic ray spectrum observed at the top of the atmosphere is decreased relative to its value in the local interstellar medium by the expanding, magnetized solar wind. In addition, near threshold the production of neutral pions in nucleon interactions does not scale (in the sense defined in (2.7)). A definitive treatment of the source spectrum for π^0 gamma rays in the region around a GeV and below is that of Dermer (1986).

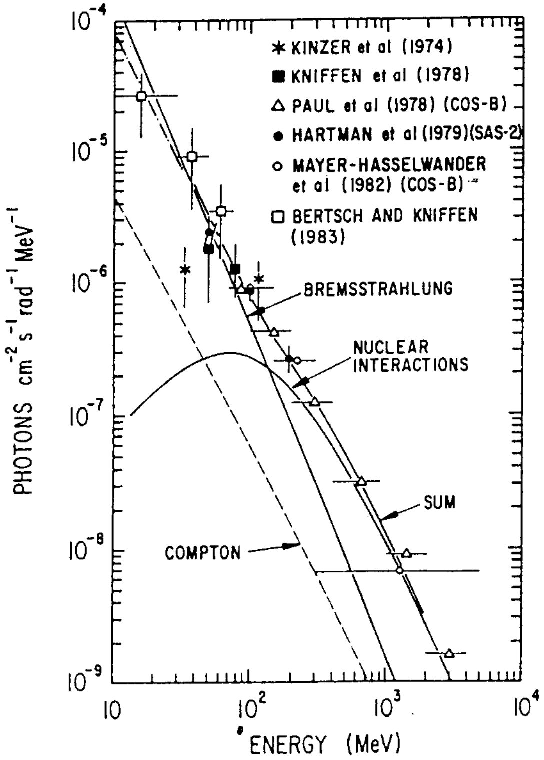

Figure 10.3: Compilation of data and comparison with calculation of gamma rays from the direction near the galactic center. (From Fichtel & Kniffen, 1984.)

A simple estimate of the diffuse galactic gamma flux, based on scaling and power law spectra of cosmic ray nucleons, gives a reasonable estimate above several hundred MeV where the energy dependent complications enumerated above are less important and the contribution from π^0 decay dominates. The largest uncertainties in this energy region come from the astrophysical assumptions about distribution of interstellar matter and cosmic rays in the galaxy. For orientation consider the approximation that these densities are uniform. In this case it is sufficient simply to evaluate (10.3) using the expression (10.5) for the source function:

$$\phi_\gamma(E_\gamma) \;\sim\; \sigma_{pp}^{\rm inel}\,\frac{\rho}{m}\,\frac{2\,Z_{N\pi^0}}{\alpha}\,\phi_N(E_\gamma)\,r_{\max}(b,\ell). \tag{10.18}$$

Here $\rho_{\rm ISM}$ is the density of the interstellar medium and m the proton mass. Numerically, the ratio of the photon flux to the cosmic ray flux in a particular direction is

$$\frac{\phi_\gamma(E_\gamma)}{\phi_N(E_\gamma)} \;\sim\; 3\times10^{-6}\left(\frac{\rho}{m}\right)\left(\frac{r_{\max}(b,\ell)}{1\,\rm kpc}\right). \tag{10.19}$$

These numbers are for differential spectral index $\alpha\approx1.7$ and $\sigma_{pp}^{\rm inel}\approx$ 30 mb (see chapter 5). In the air shower energy range ($\sim$ 100 TeV) the corresponding estimate is about a factor of two larger because of the increase of the cross section (Berezinsky and Kudryavtsev, 1990).

In the direction of the galactic center $r_{\max}\sim20$ kpc in the plane of the galaxy and $\sim$ 5 kpc away from the center. In the disk model $r_{\max}$ decreases rapidly out of the plane of the galaxy, to $\sim$ 0.1 kpc at 90°. In this crude picture, therefore, the flux of $>$ 100 MeV gamma rays in the galactic plane should be several times more intense toward the center than away, and it should be about two orders of magnitude less at directions normal to the plane than in the plane. The half thickness of the disk would be less than a degree ($\tan^{-1}[0.1/10]$), which is less than the angular resolution of the experiments for which results are available.

Neutrinos from decay of charged pions produced in the interstellar medium have fluxes comparable to the gamma rays from π^0-decay (Stecker, 1979). Unfortunately, these are much too low to be seen with present detectors and are well below the atmospheric backgrounds in any case.

10.2.3 Observations

Observations of gamma rays do show the general features of the galaxy expected from the preceding considerations. In fact, the data are sufficient to reflect the major spiral arm features of the galaxy. A comparison between the COS-B data (Mayer-Hasselwander et al., 1982) and the calculation of Fichtel and Kniffen (1984) is shown in fig. 10.4. The diffuse intensity in the galactic center region ($\ell \sim 0 \pm 30°$) is a factor 3 or 4 higher than in directions in the plane away from the center. (The prominent feature at $b \sim 265°$ is the Vela Pulsar.) The widths of the distributions in galactic latitude are larger than expected in the uniform disk model because they reflect the concentration of gas in nearby spiral arms. The calculations shown assume that the cosmic ray density is proportional to the matter density as determined independently of the gamma ray observations. This also means that the ratio of the intensity in the plane to that out of the plane is less that in a simple disk because of the local spiral arm. The correlation between energy density in cosmic rays and kinetic energy of matter (as well as with magnetic pressure) is based on the observation that these three are approximately equal locally, presumably because of coupling among them, and that the total outward pressure of the cosmic ray gas is as great as can be contained by the gravitational attraction of the mass in the galaxy. This general picture is due to Parker (1966).

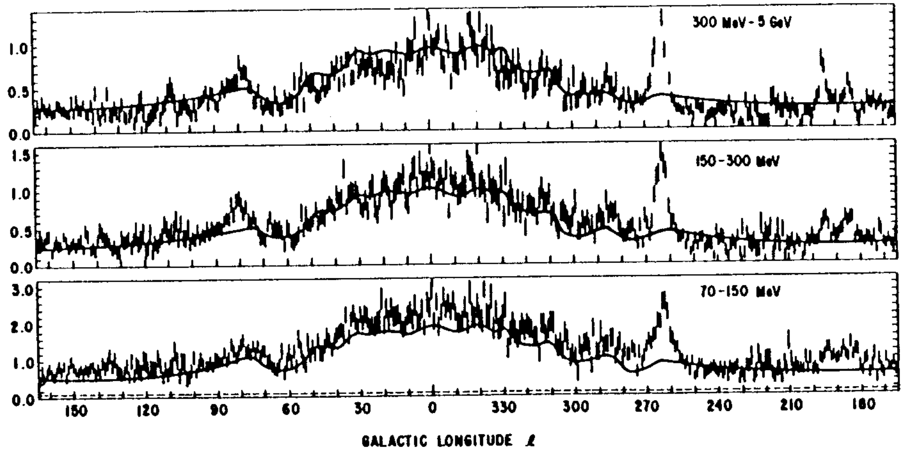

Figure 10.4: Distributions in galactic longitude of diffuse gamma fluxes, averaged over latitude from $-10° \leq b \leq 10°$. Data is that of the COS-B experiment as compared with calculations by Fichtel & Kniffen (1984).

> **Problem:** Compare the magnitude of the flux from the galactic center region calculated in the simple disk model of §10.2.2 with that shown in fig. 10.4 for 300 MeV $\leq E_\gamma \leq$ 5 GeV.

> **Problem:** Assume that an external galaxy at a distance of 1 megaparsec is identical to the Milky Way Galaxy as regards distribution of cosmic rays and diffuse matter. What is the intensity of > 300 MeV gamma rays from such a source? What angular resolution and exposure would be required of a detector to see such an external galaxy as a point source above the local background, assuming that it lies outside the plane of the local galaxy.

Because the flux of gamma rays depends on a convolution of the cosmic ray density with the distribution of interstellar gas, the fact that the gamma radiation is more intense from the center of the galaxy than from the outer galaxy does not necessarily imply that the cosmic ray density falls off in the outer galaxy. As we have seen, this effect is at least partly due to the fact there is less matter in the line of sight looking away from the galactic center. Wolfendale (1988) concludes, however, that the deconvolution of the data does indeed also imply that the cosmic ray density falls off in the outer galaxy. In addition, in this review Wolfendale raises the intriguing question of whether there is any *experimental* evidence whatsoever for association of cosmic rays with supernova remnants. After examining details of the flux of gamma rays from regions associated with supernova remnants he decides that there is some evidence for an excess of cosmic rays in the supposed sites of acceleration. He concludes, however, with an admonition to theorists: "...in addition to examining the subtleties of inclined shocks and nonspherical shocks, spare some time to look at the experimental observations favoring shocks at all in the cosmic ray situation."

10.3 Antiprotons

The subject of antimatter in the cosmic radiation has been of great interest for a long time, even though there is very little direct experimental information on the subject. One obvious reason for this interest is that anticosmic rays would be accelerated in antigalaxies, so observation of primary cosmic antinuclei would signal the existence of antimatter on large scales in the Universe. The experimental upper limits on antinuclei with $Z < -1$ (which are the most likely to be primary) are quite low, with $\overline{\mathrm{He}}/\mathrm{He} < 2 \times 10^{-5}$ (Buffington, Schindler & Pennypacker, 1981). Many indirect arguments also lead to the conclusion that the Universe has a large excess of baryonic over antibaryonic matter (Steigman, 1976). These include the difficulty of separating baryons from antibaryons on large scales before they annihilate in the early Universe, and the high level of diffuse gamma radiation that would emanate from regions where matter and antimatter came into contact. Stecker (1985) and collaborators have vigorously explored possible scenarios under which the Universe could be symmetric despite apparent theoretical and experimental difficulties. From the experimentalist's point of view, however, the existence of antinuclei remains an open question. Ahlen et al. (1982) have argued that, even if distant antigalaxies did exist and did accelerate cosmic rays at the same rate as our galaxy, the ratio of heavy antinuclei to nuclei could still be as low as 10^{-6} at Earth. This is a result of the low density of metagalactic cosmic rays and of the suppression of cosmic rays entering the galaxy against an expanding galactic wind.

10.3.1 Secondary antiprotons and observations

Because antiprotons are expected in the local cosmic radiation as a result of collisions in the interstellar medium, they are not suitable as a probe of the existence of large-scale antimatter.[2] The study of antiprotons is nevertheless extremely interesting because they provide information about the propagation of the proton component of the cosmic rays. Another interesting aspect of antiprotons is the very high energies required for their production. Figure 10.5 shows the yield of antiprotons per proton-proton collision. The source function that is needed to calculate the expected secondary antiproton spectrum from (10.4) is given by the convolution of the primary cosmic ray spectrum with the inclusive cross section for $(p\,p) \to (\bar{p} + \text{anything})$ according to (10.1). This inclusive cross section is parametrized by Taylor et al. (1976), and the convolution leads to a shape like that shown in Fig. 10.2*c*. Further details and references can be found in the review of Stephens and Golden (1987).

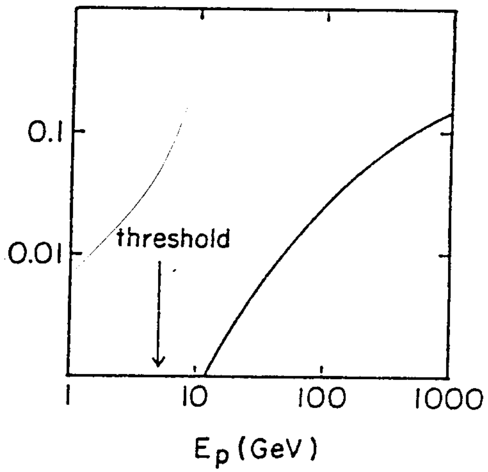

Figure 10.5: Fraction of inelastic pp collisions in which a $\bar{p}$ is produced, as a function of total lab energy of the incident proton.

Spectrometer experiments that measure the antiproton flux also measure protons. The two species are distinguished, for example by measuring the sense of the curvature in a magnetic field. It is therefore usual to give the results as a measurement of the $\bar{p}/p$ ratio. The data are summarized in fig. 10.6. The *lowest* curve in that figure is the flux predicted from (10.4) in the leaky box model, as calculated by Protheroe (1981).[3] The data in the 5–10 GeV range appear to be significantly higher than this prediction (although there are only some 20 antiprotons in this sample: Golden et al., 1979 and Bogomolov et al. 1987). Two independent experiments (Ahlen et al., 1988; Streitmatter et al., 1989) give only upper limits for antiproton kinetic energies below 1 GeV. The shape of the antiproton spectrum, though

---

[2] The history of this subject bears out this point. An early measurement (Buffington et al., 1981) indicated that the antiproton spectrum was not only higher than expected but that it also lacked the falloff at low energy characteristic of a secondary spectrum (see fig. 10.2*c*). The spectral shape appeared to be like that of a primary spectrum. Nevertheless, several scenarios were developed that could account for this apparent over-abundance of very low energy antiprotons without invoking large-scale antimatter – such as evaporation from primordial black holes, collisions in relativistic plasmas, deceleration in an expanding medium and annihilation of dark matter particles (photinos or Higgsinos) in the galactic halo. This history can be traced in the review of Stephens & Golden (1987).

[3] This prediction has remained essentially unchanged since antiproton production was first measured at high energy at the CERN Intersecting Storage Rings in 1972.

very poorly determined, is therefore not inconsistent with the leaky box model prediction.

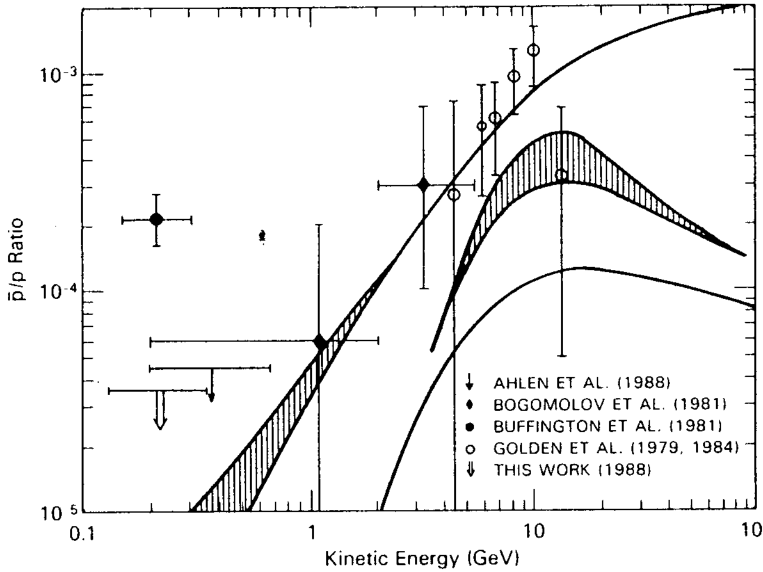

Figure 10.6: Summary of data and calculations of the $\bar{p}/p$ ratio. (From Streitmatter et al., 1989.)

In view of the apparent excess of antiprotons over the simplest expectation, it is necessary to look again at the derivation and see what the implications might be. The relevant leaky box model diffusion equation is (compare (9.7))

$$\left(\frac{1}{\lambda_{\rm esc}} + \frac{1}{\lambda_{\bar{N}}}\right)\phi_{\bar{p}}(E_{\bar{p}}) = \frac{q_{\bar{p}}(E_{\bar{p}})}{4\pi\rho}. \tag{10.20}$$

The two loss terms on the left side of (10.20) are due respectively to escape of antiprotons from the containment region and to loss by interaction. The source term for secondary protons is given by (10.1), and includes both production by interactions of primary cosmic ray nucleons with interstellar gas and feed-down from collisions of higher energy antiprotons:

$$\frac{q_{\bar{p}}}{4\pi\rho} = \frac{2}{m}\int\frac{\mathrm{d}\sigma_{p\to\bar{p}}}{\mathrm{d}E_{\bar{p}}}\phi_N(E_0)\mathrm{d}E_0 + \frac{1}{m}\int\frac{\mathrm{d}\sigma_{\bar{p}\to\bar{N}}}{\mathrm{d}E_{\bar{p}}}\phi_{\bar{p}}(E_0)\mathrm{d}E_0. \tag{10.21}$$

The factor 2 in the $p \to \bar{p}$ term accounts for the production of antineutrons, which decay on a timescale $\ll \tau_{\rm esc}$ to give $\bar{p}$'s. Because of the strong energy dependence of $\bar{p}$ production (fig. 10.5), numerical integration is required to obtain quantitative results, even in the leaky box model. In more realistic models, where density is not homogeneous for example, the situation becomes still more complex. In any case, special care is required to obtain the low energy fluxes correctly, because of the kinematic features of $\bar{p}$ production discussed in §10.1.2, and because of the necessity to include energy loss effects, annihilation and solar modulation.

10.3.2 Models with enhanced $\bar{p}$ flux

Without getting bogged down in these details, it is still possible to see qualitatively how two of the main ideas for explaining an excess of antiprotons work. Both are modifications of the simplest leaky box model. The calculation of the secondary flux of antiprotons is closely related to the calculation of secondary fluxes in the atmosphere as discussed in chapter 3. The essential difference here is that the driving primary flux may be dispersed in the interstellar medium rather than attenuating through a slab. Equations (10.20) and (10.21) may be rewritten as

$$\begin{aligned}\frac{1}{\lambda_{\rm esc}(E_{\bar{p}})}\phi_{\bar{p}}(E_{\bar{p}}) &= \frac{2}{\lambda_N}\int F_{N\bar{p}}(E_{\bar{p}},E_0)\phi_N(E_0)\frac{\mathrm{d}E_0}{E_{\bar{p}}} \\ &\quad -\frac{1}{\lambda_{\bar{N}}}\phi_{\bar{p}}(E_{\bar{p}}) + \frac{1}{\lambda_{\bar{N}}}\int F_{NN}(E_{\bar{p}},E_0)\phi(E_0)\frac{\mathrm{d}E_0}{E_{\bar{p}}},\end{aligned} \tag{10.22}$$

where the F_{ij} are defined in Chapter 3. As for pions, we expect that at high energy the antiproton flux can be approximated (at least over a limited energy range) by a falling power law, with integral spectral index $\gamma_{\bar{p}} \le \gamma_p$. The two terms in the last line of (10.22) can then be approximated by a single attenuation term. Thus,

$$\phi_{\bar{p}}(E_{\bar{p}}) \sim \left(\frac{1}{\lambda_{\rm esc}} + \frac{1}{\Lambda_{\bar{N}}}\right)^{-1}\frac{2}{\lambda_N}\int F_{N\bar{p}}(E_{\bar{p}},E_0)\,\phi_N(E_0)\frac{\mathrm{d}E_0}{E_{\bar{p}}}, \tag{10.23}$$

where

$$\frac{1}{\Lambda_{\bar{N}}} \sim \frac{1 - Z_{NN}(\gamma_{\bar{p}})}{\lambda_{\bar{N}}}. \tag{10.24}$$

Because of annihilation and extra channels for inelastic processes when antiprotons interact with nucleons, the antiproton attenuation will be somewhat different than for nucleons at low energy; hence the approximation sign in (10.24). (Note also that Z_{NN} depends on $\gamma_{\bar{p}}$.)

In the simple leaky box model, $\lambda_{\text{esc}} \ll \Lambda_{\bar N}$, so

$$\begin{aligned}\phi_{\bar p}(E_{\bar p}) \quad &\sim \quad \frac{2\,\lambda_{\text{esc}}(E_{\bar p})}{\lambda_N}\int F_{N\bar p}(E_{\bar p},E_0)\,\phi_N(E_0)\,\frac{\mathrm{d}E_0}{E_{\bar p}} \;\equiv\; \text{SLB}\\ &\rightarrow \quad \frac{\lambda_{\text{esc}}(E_{\bar p})}{\lambda_N}\,Z_{N\bar N}(E_{\bar p})\,\phi_p(E_{\bar p}).\end{aligned} \tag{10.25}$$

This is essentially the result shown as the lowest curve in fig. 10.6 for the simple leaky box (SLB) model. In this model, the escape length, λ_{esc}, is to be evaluated at the energy of the antiproton, even though it is produced by a parent nucleon of significantly higher energy. At high energies ($E_{\bar p} \sim$ 10 to 100 GeV) Z_{NN} approaches a constant scaling limit. In this limit the secondary $\bar p$ flux is almost proportional to the parent energy spectrum, apart from a slow falloff that is a consequence of the decreasing escape length. The energy dependence at lower energy reflects the threshold behavior of antiproton production shown in fig. 10.5.

The middle shaded curve in fig. 10.6 is the predicted antiproton flux in a leaky box model modified to include reacceleration of cosmic rays during propagation in the interstellar medium (Simon et al., 1987). The idea is that, even if the basic acceleration of particles occurs relatively quickly in localized regions of space, some "distributed acceleration" will also occur on long time scales as particles propagate through the galaxy (see Cesarsky, 1987 for a review). This tends to increase the $\bar p/p$ ratio over the SLB result at high energy because the peaked injection spectrum of antiprotons (dashed line in fig. 10.2*c*) is shifted somewhat to higher energy relative to the steep proton spectrum. Protons are of course also reaccelerated, but this is already accounted for by using the *observed* proton spectrum in (10.21) to calculate the production spectrum of antiprotons.

Closed galaxy

In the closed galaxy model (§9.3.3), the flux of primary cosmic rays observed at Earth consists of two parts. A young component, accelerated in the local region of the galaxy, is contained locally for a time characterized by τ_{esc}, which decreases with increasing energy. This component includes the heavy nuclei and their secondaries and is tuned to account for the energy-dependent secondary/primary ratio of fig. 9.1. A fraction f of the primary protons observed locally is an old component, contained indefinitely in the galaxy. Heavies are absent from this component, having been broken up during their long confinement time. Effectively, for the old component $\lambda_{\text{esc}} \rightarrow \infty$. Thus, from (10.23),

$$\phi_{\bar p} \;\sim\; \left[f\,\frac{\Lambda_{\bar N}}{\lambda_N}\,\frac{\lambda_N}{\lambda_{\text{esc}}} \;+\; (1-f)\right] \times \text{SLB}. \tag{10.26}$$

Since $\Lambda_{\bar N}/\lambda_N > 1 \gg \lambda_{\text{esc}}/\lambda_N$, this model can lead to a considerable enhancement of secondary antiprotons. Steigman (1977) first suggested that cosmic ray antiprotons could be used as a test of the closed galaxy model. Protheroe's (1981) quantitative evaluation of the $\bar p/p$ ratio in this model is shown as the highest curve in fig. 10.6.

Shrouded sources

Another approach to the large $\bar p/p$ ratio originates from a modification of the nested leaky box model (§9.3.2) suggested by Cowsik and others (Cowsik & Gaisser, 1981 and Lagage & Cesarsky, 1985). The idea here is that there are some "shrouded" cosmic accelerators surrounded by enough matter so that heavy nuclei are completely broken up on the way out of the source – but not so much matter that all the antiprotons are reabsorbed. Consider a source surrounded by a cloud of gas characterized as a slab of thickness λ_s g/cm^2. A central accelerator that produces a spectrum $S_0(E)$ protons per GeV per second then gives rise to a spectrum of protons outside the cloud of

$$S_p(E) \;=\; e^{-\lambda_s/\Lambda_N}\,S_0(E). \tag{10.27}$$

Among the secondaries produced by collisions of the primary protons on the way out of the source region are antinucleons. Their spectrum outside the cloud is

$$S_{\bar p}(E_{\bar p}) \;\sim\; \frac{\lambda_s}{\lambda_N}\,e^{-\lambda_s/\Lambda_{\bar N}}\int F_{N\bar N}(E_{\bar p},E_0)S_0(E_0)\frac{\mathrm{d}E_0}{E_{\bar p}}. \tag{10.28}$$

> **Problem:** Derive the expression for the secondary spectrum of antiprotons at a depth λ_s in a slab of matter and show that (10.28) results when the attenuation for protons and antiprotons is assumed equal. Show that the efficiency $S_{\bar p}/S_0$ is maximum for $\lambda_s \approx \Lambda_N$.

The shrouded sources will also contribute to the observed spectrum of protons. From (10.27) and (10.28) we can obtain the $\bar p/p$

ratio for the fraction f of cosmic rays from shrouded sources. Then the relation between the antiproton flux in this model and in SLB is given by an equation like (10.26) with the replacement $\Lambda_{\bar{N}} \rightarrow \lambda_s$.

A common feature of both these models is that they enhance the flux of antiprotons by arranging for cosmic ray protons to have a different history from the cosmic ray nuclei that are observed locally. Note, however, that λ_s cannot be increased indefinitely. Because of attenuation, S_0 would have to increase exponentially to keep f constant in (10.29) when $\lambda_s \gg \Lambda_N$. The optimum situation occurs for $\lambda_s \sim \Lambda_{\bar{N}}$. A possibility to avoid the fine tuning implied by this constraint is to have charged particles magnetically confined *indefinitely* to a low density source region small enough so that neutrons and antineutrons can escape before they decay (Dermer & Ramary, 1986).

Constraints and implications

Shrouded sources of antinucleons will also be point sources of gamma rays. They cannot be more powerful than observed point sources (Swanenburg et al., 1981), and this constrains such models (Lagage & Cesarsky, 1985). Indeed, any model that enhances cosmic ray antiprotons by increasing the interaction of primary cosmic rays will tend to increase the fluxes of photons, and possibly also of positrons and light secondary nuclei, depending on the details of the model. The ratio of ^{3}He/He is not as high as would be expected in the simplest shrouded source picture (Webber et al. 1987). It has also been pointed out that, when a recent result, such as (9.8), is used for λ_{esc} the discrepancy between the measurement and prediction of the antiproton flux in the SLB model decreases (Webber & Potgieter, 1989). The ratio of positrons to electrons (Müller & Tang, 1986 and Golden et al., 1987) also shows interesting features which need to be explained. A systematic study of all these light secondaries and their energy dependence is needed. This is currently an active field of research, with new experimental data expected to improve the statistics and range of energies of the measurements, both for antiprotons and for positrons.

Chapter 11

Acceleration

A principle question in cosmic ray physics is whether the major acceleration processes occur on large scales in the Galaxy or near discrete, point sources. On a smaller scale, in the Solar System we know that both occur. Spacecraft experiments have seen evidence of acceleration of particles to suprathermal energies of keV to MeV by interplanetary shock waves, for example at the Earth's bow shock and in other shocks associated with the solar wind. At the same time there is direct evidence that particles are accelerated to GeV energies at the sun in solar flares. In the latter case, in addition to detecting the accelerated particles in interplanetary space and at Earth soon after a flare, observers have also seen evidence of neutral pions as well as neutrons from the Sun (Chupp, 1984). The production of these secondaries occurs when accelerated particles collide with material near the source. Some continuum gamma rays come from bremsstrahlung from primary electrons, but some also come from

$$\begin{array}{lcl} p + \text{gas} \rightarrow & \pi^0 & + \text{anything} \\ & \searrow & \\ & & \gamma + \gamma. \end{array} \qquad (11.1)$$

For galactic cosmic rays, where *in situ* observations with satellites are not possible, the *only* way to trace the cosmic rays is to look for stable, neutral secondaries produced by collisions of the accelerated charged particles. The collisions can occur either in the interstellar gas (as discussed in the previous chapter) or in the immediate vicinity of discrete sources. The charged particles themselves do not point back to their sources because of their diffusion in the galactic magnetic fields. As with solar system cosmic rays, it is likely that both extended and point sources play a role in acceleration of particles in the Galaxy. A major current effort is the operation of experiments to follow up evidence for secondary photons from point sources of very high energy cosmic rays such as the binary stellar systems Her X-1 and Cygnus X-3. The background and implications of these experiments will be discussed later. My purpose in this chapter is to introduce the theory of shock acceleration and its possible role as the source of the bulk of the cosmic rays, which have energies in the region $\sim 1 - 100$ GeV.

11.1 Power

There are two aspects to the question of cosmic ray acceleration: what is the source of power for the accelerator; and what is the actual mechanism. From the discussion of fig. 1.6 we recall that the energy density in cosmic rays locally is $\rho_E \approx 1\ \mathrm{eV/cm^3}$. If we assume this to be typical of the cosmic ray energy density throughout the galactic disk, the power required to supply all the galactic cosmic rays is

$$L_{\mathrm{CR}} = \frac{V_D\,\rho_E}{\tau_R} \sim 5\times 10^{40}\,\frac{\mathrm{erg}}{\mathrm{sec}}, \tag{11.2}$$

where the volume of the galactic disk, V_D is

$$V_D = \pi R^2 d \sim \pi\,(15\ \mathrm{kpc})^2\,(200\ \mathrm{pc}) \sim 4\times 10^{66}\ \mathrm{cm}^3$$

and where τ_R is the residence time of cosmic rays in the volume assumed to contain the sources (i.e. in the disk of the galaxy). The correct estimate of the residence time is $\tau_R \sim 6\times 10^6$ years, from (9.11). The age of the cosmic rays may be greater than this because of time spent outside the disk, but the equilibrium power requirement for sources in a volume, V_D, depends only on the observed cosmic ray energy density and the residence time in that volume. (A large halo simply takes longer to fill up when the sources are first turned on.)

It was emphasized long ago by Ginzburg and Syrovatskii (1964) that the power requirement (11.2) is suggestive of supernovae. For example, for 10 $M_\odot$ ejected from a type II supernova with a velocity $u \sim 5\times 10^8$ cm/s every 30 years,

$$L_{\mathrm{SN}} \sim 3\times 10^{42}\,\mathrm{erg/s}. \tag{11.3}$$

There are large uncertainties in these numbers, but it appears plausible that an efficiency of a few per cent would be enough for supernova blast waves to energize all the galactic cosmic rays. Note that by terrestrial standards this is *very* efficient indeed. Such high efficiencies may be natural in space where there is no need to cool magnets (as at an accelerator laboratory) and where particle acceleration may in fact be a major source of energy dissipation.

11.2 Shock acceleration

The case for supernova explosions as the powerhouse for cosmic rays becomes even stronger with the realization that first order Fermi acceleration at a strong shock naturally produces a spectrum of cosmic rays close to what is observed. The subject of Fermi acceleration at large-scale astrophysical shocks has been extensively reviewed recently (e.g. Axford, 1981; Drury, 1983 and Blandford and Eichler, 1987). Longair (1981) gives a nice derivation of the basic acceleration equation, which is a special case of the general equation (9.1). The derivation I use here is close to that of Bell (1978). My object is to review how the basic mechanism works in the context of acceleration by supernova blast waves and in particular to describe how an upper limit for energy per particle occurs in this context. I will mention other acceleration mechanisms in later chapters, in connection with models of point sources.

11.2.1 Fermi mechanism

The object is to transfer macroscopic kinetic energy of moving magnetized plasma to individual charged particles, thereby increasing the energy per particle to many times its original value and achieving the nonthermal energy distribution characteristic of particle acceleration. Consider a process in which a test particle increases its energy by an amount proportional to its energy with each "encounter" (to be defined later). Then, if $\Delta E = \xi E$ per encounter, after n encounters

$$E_n = E_0\,(1 + \xi)^n, \tag{11.4}$$

where E_0 is the energy at injection into the accelerator. If the probability of escape from the acceleration region is P_{esc} per encounter, then the probability of remaining in the acceleration region after n

encounters is $(1-P_{\rm esc})^n$. The number of encounters needed to reach energy E is, from (11.4),

$$n \;=\; \ln(\frac{E}{E_0})/\ln(1+\xi). \tag{11.5}$$

Thus, the proportion of particles accelerated to energies greater than E is

$$N(\geq E) \;\propto\; \sum_{m=n}^{\infty}(1-P_{\rm esc})^m \;=\; \frac{(1-P_{\rm esc})^n}{P_{\rm esc}}, \tag{11.6}$$

with n given by (11.5). Substitution of (11.5) into (11.6) gives

$$N(>E) \;\propto\; \frac{1}{P_{\rm esc}}\left(\frac{E}{E_0}\right)^{-\gamma}, \tag{11.7}$$

with

$$\gamma \;=\; \ln\left(\frac{1}{1-P_{\rm esc}}\right)\,/\,\ln(1+\xi) \;\approx\; \frac{P_{\rm esc}}{\xi} \;=\; \frac{1}{\xi}\times\frac{T_{\rm cycle}}{T_{\rm esc}}. \tag{11.8}$$

The Fermi mechanism leads to the desired power law spectrum of energies. In the last step of (11.8) I have introduced the characteristic time for the acceleration cycle, $T_{\rm cycle}$, and the characteristic time for escape from the acceleration region, $T_{\rm esc}$. The ratio of these two times is the probability per encounter of escape from the acceleration region. After the acceleration process has been working for a time t, $n_{\rm max} = t/T_{\rm cycle}$ and

$$E \;\leq\; E_0\,(1\;+\;\xi)^{t/T_{\rm cycle}}. \tag{11.9}$$

Two characteristic features of Fermi acceleration are apparent from (11.9). First, higher energy particles take longer to accelerate than low energy particles. Second, if a certain kind of Fermi accelerator has a limited lifetime, $T_{\rm A}$, then it will also be characterized by a maximum energy per particle that it can produce. This would be given by (11.9) with $t = T_A$ if $T_{\rm cycle}$ were independent of energy, which turns out not to be the case (§11.3 below).

11.2.2 1st and 2nd order Fermi acceleration

Diffusion of charged particles in turbulent magnetic fields physically carried along with moving plasma is the mechanism for energy gains and losses. In his original paper, Fermi (1949) considered encounters with moving clouds of plasma, as illustrated in fig. 11.1. A particle with energy E_1 goes into the cloud where it begins to diffuse by "scattering" on the irregularities in the magnetic field. ("Scattering" is in quotes here because the process must be "collisionless" in terms of interactions between particles that would prevent acceleration because of collisional energy loss.) The result of the diffusion inside the gas cloud is that, after a few "scatterings" the *average* motion of the particle coincides with that of the gas cloud. In the rest frame of the moving gas the cosmic ray particle has total energy (rest mass plus kinetic)

$$E_1' \;=\; \gamma\,E_1\,(1\;-\;\beta\cos\theta_1), \tag{11.10}$$

where γ and $\beta \equiv V/c$ are the Lorentz factor and velocity of the cloud and the primes denote quantities measured in a frame moving with the cloud. All the "scatterings" inside the cloud are due to motion in the magnetic field and are therefore elastic. Thus, the energy of the particle in the moving frame just before it escapes is $E_2' = E_1'$. If we transform this energy back to the laboratory frame, we have the energy of the particle after its encounter with the cloud,

$$E_2 \;=\; \gamma\,E_2'\,(1\;+\;\beta\cos\theta_2'). \tag{11.11}$$

For simplicity, (11.10) and (11.11) are written for a particle that is already sufficiently relativistic so that $E \approx pc$. Substituting (11.10) into (11.11) now gives the energy change for the particular encounter characterized by θ_1 and θ_2,

$$\frac{\Delta E}{E_1} \;=\; \frac{1\;-\;\beta\cos\theta_1\;+\;\beta\cos\theta_2'\;-\;\beta^2\cos\theta_1\,\cos\theta_2'}{1\;-\;\beta^2}\;-\;1. \tag{11.12}$$

The other physical situation that we want to consider is illustrated in fig. 11.2. Here a large, plane shock front moves with velocity $-\mathbf{u}_1$. The shocked gas flows away from the shock with a velocity $\mathbf{u}_2$ relative to the shock front, and $|u_2| < |u_1|$. Thus in the laboratory frame the gas behind the shock moves to the left with velocity $\mathbf{V} = -\mathbf{u}_1 + \mathbf{u}_2$. Equation (11.12) applies also to this situation with $\beta \;=\; V/c$ now interpreted as the velocity of the shocked gas ("downstream") relative to the unshocked gas ("upstream").

The crucial difference between the two cases comes when we take the angular averages to obtain the average fractional energy gain per encounter, ξ, for (11.4) – (11.9). The same steps will be followed in each case. In the equations that follow, I indicate scattering from

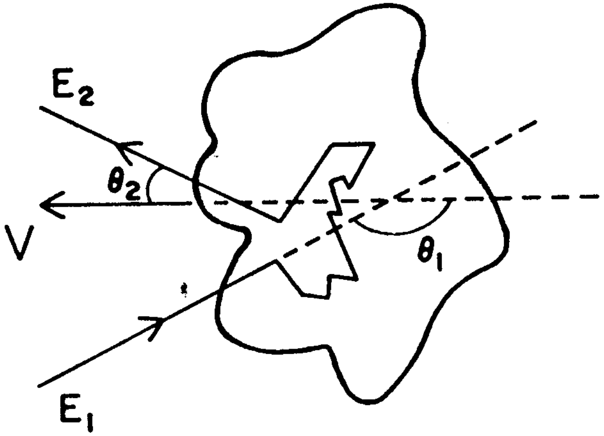

Figure 11.1: Acceleration by a moving, partially ionized gas cloud.

clouds as case (a) and encounters with a plane shock front as (b). For gas clouds

$$\text{(a)}\quad \frac{\mathrm{d}n}{\mathrm{d}\cos\theta_2'} = \text{constant},\quad -1 \le \cos\theta_2' \le 1,$$

so that $\langle\cos\theta_2'\rangle_\mathrm{a} = 0$. For a plane shock

$$\text{(b)}\quad \frac{\mathrm{d}n}{\mathrm{d}\cos\theta_2'} = 2\cos\theta_2',\quad 0 \le \cos\theta_2' \le 1.$$

This distribution is the normalized projection of an isotropic flux onto a plane, and $\langle\cos\theta_2'\rangle_\mathrm{b} = 2/3$. Averaging over $\cos\theta_2'$ for the two cases gives

$$\begin{aligned}\text{(a)}\quad \frac{\langle\Delta E\rangle_2}{E_1} &= \frac{1-\beta\cos\theta_1}{1-\beta^2} - 1\\ &\text{and}\\ \text{(b)}\quad \frac{\langle\Delta E\rangle_2}{E_1} &= \frac{1-\beta\cos\theta_1+\frac{2}{3}\beta-\frac{2}{3}\beta^2\cos\theta_1}{1-\beta^2} - 1.\end{aligned} \tag{11.13}$$

Next we need to average over $\cos\theta_1$. For clouds, the probability of a collision is proportional to the relative velocity between the cloud and the particle,

$$\frac{\mathrm{d}n}{\mathrm{d}\cos\theta_1} = \frac{c - V\cos\theta_1}{2c},\quad -1 \le \cos\theta_1 \le 1,$$

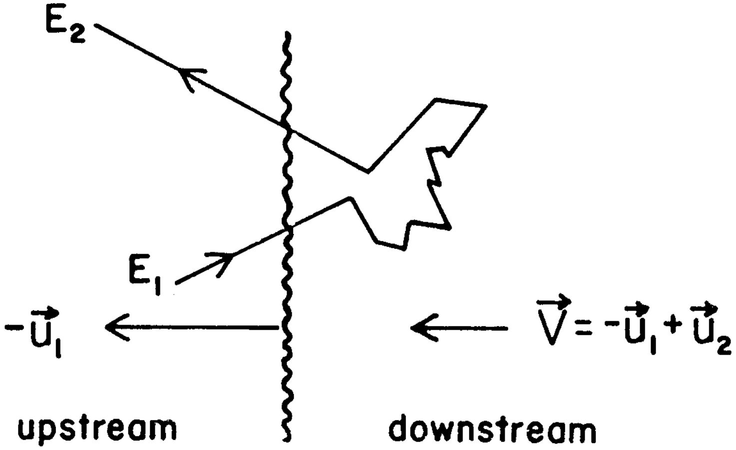

Figure 11.2: Acceleration at a plane shock front.

so that $\langle\cos\theta_1\rangle_\mathrm{a} = -V/3c$. The distribution of $\cos\theta_1$ for the plane shock is again the projection of an isotropic flux onto a plane, but this time with $-1 \le \cos\theta_1 \le 0$, so that $\langle\cos\theta_1\rangle_\mathrm{b} = -2/3$. Thus

$$\begin{aligned}\text{(a)}\quad \xi &= \frac{1+\frac{1}{3}\beta^2}{1-\beta^2} - 1 \sim \frac{4}{3}\beta^2\\ &\text{and}\\ \text{(b)}\quad \xi &= \frac{1+\frac{4}{3}\beta+\frac{4}{9}\beta^2}{1-\beta^2} - 1 \sim \frac{4}{3}\beta = \frac{4}{3}\frac{u_1-u_2}{c}.\end{aligned} \tag{11.14}$$

Here $\beta = V/c$ refers to the relative velocity of the plasma flow, not to the cosmic rays. The approximate forms in (11.14) hold when the shock (or cloud) velocities are nonrelativistic. See Webb (1987) for a treatment of relativistic shocks.

Notice that in both cases an "encounter" is one pair of in and out crossings, in case (a) into and out of the cloud and in case (b) back and forth across the shock. The original Fermi mechanism is called second order because particles can either gain or lose energy in a given encounter, depending on the angles, but after many encounters there is a net gain. (This is often incorrectly expressed by saying that there are more approaching encounters ($\cos\theta_1 < 0$) than overtaking encounters ($\cos\theta_1 > 0$). But note from (11.12) that an approaching encounter with a cloud in which the particle goes out the back side ($\cos\theta_2' < 0$) can result in a loss of energy. Similarly, an overtaking collision can sometimes result in an energy gain.) On the other hand, the geometry of the infinite plane shock is such that an "encounter" always results in an energy gain (because $\cos\theta_2'$ is always positive and $\cos\theta_1$ always negative). The two versions of Fermi acceleration are also characterized by being first and second order in the velocity of the plasma flow for nonrelativistic plasma.

In the original version of Fermi acceleration, the acceleration region is the galactic disk, so $T_{\rm esc} \sim 10^7$ years. The acceleration rate is the rate of collisions between a cosmic ray of velocity c with clouds characterized by a spatial density ρ_c and cross section σ_c. Thus $T_{\rm cycle} \sim 1/(c\,\rho_c\,\sigma_c)$. The integral spectral index then is

$$\gamma \sim \frac{1}{\frac{4}{3}\beta^2\, c\,\rho_c\,\sigma_c\, T_{\rm acc}}. \qquad (11.15)$$

The numerical value of this spectral index is not universal, but depends on details of properties of the clouds, and tends to be very large (Davis, 1956).

For the configuration of the large, plane shock, the rate of encounters is given by the projection of an isotropic cosmic ray flux onto the plane shock front,

$$\int_0^1 \mathrm{d}\cos\theta \int_0^{2\pi} \mathrm{d}\phi \frac{c\rho_{\rm CR}}{4\pi}\cos\theta = \frac{c\rho_{\rm CR}}{4}, \qquad (11.16)$$

where $\rho_{\rm CR}$ is the number density of particles undergoing acceleration. The rate of convection downstream away from the shock front is $\rho_{\rm CR} \times u_2$, so

$$P_{\rm esc} = \frac{\rho_{\rm CR}\, u_2}{c\,\rho_{\rm CR}/4} = \frac{4\,u_2}{c}. \qquad (11.17)$$

Thus for the case of acceleration at a shock,

$$\gamma = \frac{P_{\rm esc}}{\xi} = \frac{3}{u_1/u_2 - 1}. \qquad (11.18)$$

Unlike the model for second order Fermi acceleration, the spectral index here is independent of the absolute magnitude of the velocity of the plasma – it depends only on the ratio of the upstream and downstream velocities. Note that it is also independent of the diffusion coefficient.[1]

---

[1] But see §11.3.9 for a discussion of the upper limit for acceleration at a shock, in which the diffusion constant enters explicitly.

Problem: Show that for a relativistic shock

$$1 - P_{\rm esc} = \left(\frac{1 - u_2/c}{1 + u_2/c}\right)^2,$$

in the approximation that the cosmic rays are isoptropic in the downstream rest frame.

Hint: Work in the rest system of the downstream material in which the shock front moves to the left (see fig. 11.2) with velocity u_2. Consider an imaginary plane about one diffusion scattering length downstream of the shock and calculate the rate at which particles cross this moving plane in the down to upstream direction and *vice versa*. The ratio of these two rates is an estimate of the probability that a downstream particle succeeds in crossing back to the upstream side of the shock.[2]

A shock can form when $u_1 > c_1$, the sound speed in the gas. The Mach number of the flow is $M = u_1/c_1$. The continuity of mass flow across the shock ($\rho_1 u_1 = \rho_2 u_2$), together with the kinetic theory of gases, gives

$$\frac{u_1}{u_2} = \frac{\rho_2}{\rho_1} = \frac{(c_p/c_v + 1)M^2}{(c_p/c_v - 1)M^2 + 2} \qquad (11.19)$$

(Landau and Lifshitz, 1982). For an monatomic gas the ratio of specific heats is $c_p/c_v = \frac{5}{3}$, so

$$\gamma \approx 1 + \frac{4}{M^2} \qquad (11.20)$$

for a strong shock with $M \gg 1$. Not only is the spectral index for first order Fermi acceleration universal, but it has a numerical value close to what is needed to describe the observed cosmic ray spectrum! (Recall from the discussion of §9.2.1 that the differential spectral index required from the accelerator is ~2.1, which corresponds to $\gamma \sim 1.1$ in (11.20).)

Implicit in this derivation is the assumption that the particles being accelerated do not affect the conditions in the acceleration region. This is called the test particle approximation. In fact, the cosmic rays being accelerated can cause streaming instabilities and generate hydromagnetic waves. These waves themselves can be the source of

---

[2] I am grateful to Frank Jones for informing me of this result and giving a hint at how to obtain it.

diffusion in the upstream, unshocked region. With this coupling, the acceleration process is non-linear, and spectra other than the ideal power law with $\gamma = 2$ can occur. In particular, it is possible to have a harder spectrum with the energy of accelerated particles concentrated near the maximum energy of the accelerator. I have also avoided any discussion of the question of how particles are injected into the accelerator. The microscopic realization of spatial diffusion through pitch angle scattering in turbulent magnetic fields is also a very complex question that has been the subject of much work. The reader is referred to the review of Blandford & Eichler (1987) for a discussion of these and related topics.

11.2.3 Magnetic field geometry

As suggested by the preceding paragraph, the subject of particle acceleration is much more complicated than the very simplified analysis I have given here. There are several other plasma processes that can accelerate particles and that have been observed at work in the solar system. One example is acceleration in the electric fields generated when stressed magnetic field lines "reconnect" to relieve the energy built up by turbulence. Another example more closely related to stochastic shock acceleration discussed above is shock drift acceleration (Armstrong, Pesses and Decker, 1985).

It was implicitly assumed in the preceding treatment of diffusive shock acceleration that the magnetic field is parallel to the shock normal. If not, there is an electric field in the rest frame of the shock of magnitude $E = u \times B_1/c$. A particle of charge $Z\,e$ that drifts along the shock front a distance Δy gains energy $Z\,e\,E_y\,\Delta y$. By itself, the shock drift mechanism leads to a gain in energy limited by whatever is the physical realization of Δy. Perhaps this is one reason that this mechanism has not received as much attention in the context of cosmic ray acceleration as stochastic shock acceleration, which has the potential of accelerating some particles by orders of magnitude above the injection energy. Jokipii (1987) argues, however, that the combination of diffusion and drift acceleration in a quasiperpendicular shock can accelerate particles significantly more efficiently than the diffusive mechanism alone in a quasiparallel shock. (The standard terminology here is confusing: a "parallel shock" is one in which the magnetic field is perpendicular to the plane of the shock, while a "perpendicular shock" has the field parallel to the shock plane.)

11.3 Supernova blast waves

The ejected material from a supernova explosion will move out through the interstellar medium driving a shock wave at which acceleration can occur. As long as the characteristic length for diffusion, D/u, is much less than the radius of curvature of the shock, the plane approximation can be used. The time scale during which a supernova blast wave is active may be estimated by calculating the time it takes the expanding shell to sweep through its own mass of the ISM, after which it begins to slow down. For $10M_\odot$ expanding at mean velocity of 5×10^8 cm/sec into a medium of average density 1 proton/cm^3 this charactistic time is $T_A \sim 1000$ years. We thus come to the schematic picture of cosmic ray acceleration shown in fig. 9.2, with some 30 supernovae of typical size 5 pc actively accelerating cosmic rays at any time. As we will see in the discussion of first order Fermi acceleration by large shock waves, escape from the acceleration region is only possible into the shocked gas, i.e. to the inside of the shell. Thus the cosmic rays eventually get injected into the galactic disk after the shock begins to disintegrate, as indicated in the figure.

11.3.1 Maximum energy

The finite lifetime of the supernova blast wave as a strong shock also limits the maximum energy per particle that can be achieved with this mechanism. The acceleration rate is

$$\frac{\mathrm{d}E}{\mathrm{d}t} = \frac{\xi\,E}{T_{\mathrm{cycle}}}, \tag{11.21}$$

with the fractional energy gain per encounter, ξ, given by (11.14). To integrate (11.21) and estimate E_{max}, we need to know the cycle time for one back-and-forth encounter. The following derivation is due to Lagage and Cesarsky (1983) as presented by Drury (1983).

Consider first the upstream region. The particle current with convection is given by

$$\mathbf{J} = -D\nabla N + \mathbf{u}\,N. \tag{11.22}$$

(Compare (9.1), (9.12) and (9.13).) In the upstream region the fluid velocity $\mathbf{u}_1$ is negative relative to the shock front so in equilibrium there is no net current, and

$$D_1\,\frac{\mathrm{d}N}{\mathrm{d}z} = -u_1\,N. \tag{11.23}$$

Then in the upstream region

$$N(z) = \rho_{\rm CR} \exp[-z\,u_1/\,D_1], \qquad (11.24)$$

where $\rho_{\rm CR}$ is the number density of cosmic rays at the shock. The total number of particles per unit area in the upstream region is $\rho_{\rm CR} D_1/u_1$. From (11.16) the rate per unit area at which relativistic cosmic rays cross a plane shock front is $c\,\rho_{\rm CR}/4$. Thus the mean residence time of a particle in the upstream region is

$$(\rho_{\rm CR}\,D_1/\,u_1)\,(c\,\rho_{\rm CR}/\,4)^{-1} = 4\,D_1/(u_1\,c).$$

The downstream region is somewhat more complicated to analyze because it is necessary to average the residence time only over those particles that do not escape. The analysis is straightforward and is shown explicitly by Drury. This form is identical to that in the upstream region. Thus

$$T_{\rm cycle} = \frac{4}{c}\left(\frac{D_1}{u_1} + \frac{D_2}{u_2}\right). \qquad (11.25)$$

To proceed we need an estimate of the diffusion coefficient. Lagage and Cesarsky (1983) argue that the diffusion length, λ_D cannot be smaller than the Larmor radius of the particle, $r_L = pc/(ZeB)$, where Z is the charge of the particle and p its total momentum. The idea is that energetic particles cannot respond to irregularities in the magnetic field smaller than the particle gyroradius. From (9.2) one finds a minimum diffusion coefficient, which gives the maximum possible acceleration rate and hence an upper limit to the energy accessible for an accelerator that works for a limited time, T_A. It is

$$D_{\rm min} = \frac{r_L\,c}{3} \sim \frac{1}{3}\,\frac{E\,c}{Z\,e\,B}, \qquad (11.26)$$

so that $T_{\rm cycle} \geq 20\,E/(3u_1 Z\,e\,B)$ for a strong shock with $u_2 = u_1/4$. Here E is the total energy of the nucleus being accelerated. Inserting $D_1 = D_2 = D_{\rm min}$ into (11.25) and (11.21) leads to an expression for the acceleration rate that is independent of energy because $T_{\rm cycle} \propto E$.

The resulting estimate of the maximum energy is

$$E_{\rm max} \leq \frac{3}{20}\,\frac{u_1}{c}\,Z\,e\,B\,(u_1\,T_A). \qquad (11.27)$$

Lagage and Cesarsky show that most acceleration occurs before the time when the supernova has swept up its own mass, after which the shock begins to weaken. The value of T_A to use in (11.27), therefore, is obtained from

$$\frac{4}{3}\,\pi\,(u_1\,T_A)^3\,\rho_{\rm ISM} = M_{\rm ejecta}. \qquad (11.28)$$

For $10\,M_\odot$ ejected at 5×10^8 cm/s into the nominal ISM with one proton per cubic centimeter, $T_A \sim 1000$ yrs. An estimate of $B_{\rm ISM} \sim 3\mu$ Gauss in (11.27) then gives

$$E_{\rm max} \leq Z \times 3\times10^4\ {\rm GeV}. \qquad (11.29)$$

Problem: Show that the characteristic length for diffusion upstream, $D_{\rm min}/u_1$, for a particle with $E_{\rm max}$ given by (11.29) is smaller than the radius of the supernova blast wave at time T_A. If the opposite were true, the upper limit on the energy would be determined by $D_{\rm min} > R_{\rm SN} u_1$, at which point the shock would no longer appear planar to the upstream particles, which would be lost from the acceleration process.

There are large uncertainties and oversimplifications in the parameters and derivation used to reach the estimate of (11.29). The supernova parameters themselves have uncertainties of factors of 2 to 3, but T_A depends only on the cube root of $M_{\rm ejecta}/\rho_{\rm ISM}$. By assuming the supernova explodes into the low density, hot interstellar medium, Lagage and Cesarsky obtain a somewhat higher maximum energy than in (11.29). On the other hand, the acceleration process in reality is probably not as efficient as implied by the use of the minimum diffusion coefficient. So $E_{\rm max} \sim 100$ TeV is a good round number to use for cosmic ray acceleration by supernova blast waves.

11.3.2 Maximum energy for electrons

The analysis described above to estimate $E_{\rm max}$ for cosmic ray acceleration in a supernova shock goes through also for electrons. Because of the magnetic field, however, it is necessary to check whether synchrotron losses give a more restrictive limit for the maximum energy of electrons. The loss rate for relativistic particles of mass Am and charge Ze in a magnetic field B is (Longair, 1981)

$$\left(-\frac{{\rm d}E}{{\rm d}t}\right)_{\rm synchrotron} \approx 1.6\times10^{-3}\,\frac{\rm erg}{\rm s}\left(\frac{Z}{A}\,\frac{m_e}{m}\right)^4 E^2\,B^2, \qquad (11.30)$$

where all quantities are in cgs units and E is the total energy of the particle. Because of the strong dependence on the small mass ratio, synchrotron losses are negligible for protons and nuclei in all but the most extreme circumstances (e.g. near the surface of a neutron star).

Electrons, however, have $m = m_e$ (and $Z = A$), so the synchrotron loss rate is relatively much more important than for protons. To find the limit placed by synchrotron losses on shock acceleration of electrons, we equate the acceleration rate from (11.27) with the synchrotron loss rate. The limit is

$$E_{\mathrm{max}}^{(\mathrm{synchrotron})} \sim 23 \ \mathrm{TeV} \, \frac{u_1}{c} \frac{1}{\sqrt{B}}. \tag{11.31}$$

For the same supernova parameters used to obtain (11.29) ($B \sim 3\,\mu$G and $u_1 \sim 5 \times 10^8$ cm/s) this gives an upper limit of ~ 220 TeV, nearly a factor of ten higher than the limit from the supernova age in (11.29). Therefore, because of the low magnetic field assumed in this example, the acceleration of electrons is not limited by synchrotron radiation.

On the other hand, it is clear from the result of (11.31) that whenever shock acceleration occurs in a region of high magnetic field, synchrotron losses are likely to limit the acceleration of electrons. Two such examples that involve a neutron star interacting with nearby matter will be discussed in the next chapter.

11.3.3 Composition and spectral shape

The maximum energy in (11.29) is E_{max} per nucleus, and it is proportional to the charge of the nucleus. Thus, if there is a steepening of the spectrum that is due to the end-point of this kind of acceleration mechanism, then the composition should become progressively enriched in heavier nuclei as energy increases through the cutoff region (Peters, 1959). Unfortunately, this is not a unique characteristic of this acceleration mechanism. For example, if there is rigidity-dependent leakage from the galaxy that increases with energy, this also would give an increasingly heavy composition associated with a steepening of the all particle energy per nucleus spectrum.

Chapter 12

Acceleration to > 100 TeV

The simplest set of assumptions for particle acceleration at supernova blast waves gives a very nice account of the origin of the bulk of the cosmic rays, but it leaves open the origin of those with energies greater than ~ 100 TeV. Yet cosmic rays with energies up to 10^{20} eV are observed with air shower experiments. How are they accelerated?

From (11.27) it is clear that the shock mechanism itself can achieve higher energy per particle if the magnetic field is increased or if the time-scale for acceleration is increased. Other acceleration mechanisms may also be active in the galaxy. The very highest energy cosmic rays ($> 10^{19}$ eV) may be of extragalactic origin, but an argument due to Hillas (1984), based on the small, energy-dependent anisotropy of the cosmic rays (see below), suggests that the cosmic rays we see below this energy originate in this galaxy. In this chapter I consider some of the possible scenarios for accelerating the ultra high energy cosmic rays (i.e., those with $E > 100$ TeV).

12.1 Diffuse sources

The first possibility is that the supernova blast wave mechanism itself may actually give higher energies than the estimate of chapter 11. Supernovas probably do not occur in the "average" interstellar medium. The recent Supernova 1987A, for example, exploded into an environment formed by the wind of its progenitor. Völk and Biermann (1988) have pointed out that this could raise the limit of (11.27) by one or two orders of magnitude. Another factor is the magnetic field configuration relative to the supernova, which is assumed to be parallel to the direction of propagation of the shock in the canonical derivation. As noted in §11.2.3, Jokipii (1987) has pointed out that the rate of acceleration may be faster when the field has a component perpendicular to the direction of propagation. He estimates that the combination of diffusive and shock drift acceleration that is possible with a nearly perpendicular shock can increase the upper limit of (11.27) by a factor of ten or more. He assumes the supernova to go off in a uniform magnetic field, so there is an equatorial region in which the supernova shock is quasiperpendicular and two polar regions in which it is quasiparallel.

Strong shocks may also accelerate particles to high energy in other environments. An example is the termination shock of a stellar wind (Cesarsky & Montmerle, 1983), which might accelerate particles an order of magnitude above the limit in (11.29). Another possibility, which might account even for the highest energy cosmic rays with $E \sim 10^{20}$ eV, is the termination shock of a galactic wind. Jokipii and Morfill (1987) argue that a wind driven by the cumulative energy of all galactic supernovas may stream into the intergalactic medium with a velocity $u_W > u_{\rm esc}$, where $u_{\rm esc}$ is the escape velocity from the galaxy (about 300 km/s for a galactic mass of $1.4 \times 10^{11}\,M_\odot$). A standing termination shock would be set up in the wind as a result of the external pressure in the intergalactic medium. As an example, if $u_W = 600$ km/s, $B = 10^{-7}$ Gauss and $T_A = 1.5 \times 10^{10}$ years (the age of the galaxy), (11.27) gives $E_{\max} \sim Z \times 3 \times 10^8$ GeV. This is significantly higher than is possible with individual supernova shocks, primarily because of the long time scale involved. This estimate of $E_{\max}$ could be boosted further by taking into account the likely spiral nature of the field carried out by the galactic wind, which would lead to a quasiperpendicular magnetic field geometry.

12.2 Point sources

At the other extreme, it may be possible to achieve high energy on short time scales in compact acceleration regions with very high magnetic fields. Neutron stars are obvious candidates for compact cosmic accelerators. Energy of rotation of neutron stars is one possible power source. As an illustration, consider a neutron star of mass $1.4\,M_\odot$ rotating initially with period $P = P_{10} \times 10$ ms. With a radius of $\approx 10^6$ cm, it has a moment of inertia of $10^{45}\,{\rm g\,cm^2}$. The initial energy of

rotation is $\approx 2 \times 10^{50}\,{\rm erg}/P_{10}^2$. If all supernovas left behind neutron stars with periods of 10 ms or less, and if a large fraction of this rotational energy went into acceleration of particles, then this would provide another scenario for accelerating the bulk of cosmic rays. To see this, note that 2×10^{50} erg released every 30 years is about a factor 5 larger that the power reuired to supply all the galactic cosmic rays (11.2). The distribution of initial periods of rotation of neutron stars is uncertain, however, and it is possible that many have slow initial rates. In addition, acceleration would take place inside the expanding supernova, so that accelerated particles would find themselves diffusing inside an expanding medium due to scattering from irregularities in the comoving magnetic fields. These "adiabatic" energy losses over a period of some thousands of years as the remnant dispersed into the ISM would make this scenario still more inefficient.

Another possible source of power is the release of gravitational potential energy as mass falls onto the surface of a neutron star in a close binary stellar system. Such systems have characteristic X-ray emission of order 10^{38} erg/s (Joss & Rappaport, 1984). If a comparable amount of energy went into acceleration of particles, then 500 such sources continuously active in the galaxy would satisfy the energy requirement of (11.2). There is no reason to expect such a large number of accreting binaries putting this much power into particle acceleration, so accretion power is also not the most likely source to account for the bulk of the cosmic rays.

12.3 Power required for >100 TeV

Even if they do not supply all the galactic cosmic rays, compact sources such as X-ray binaries or pulsars in young supernovae have one advantage over supernova blast waves: The energy per particle may be many orders of magnitude higher than is possible with shock acceleration by blast waves. This is basically because the magnetic field in the acceleration region around a collapsed object is much higher than the interstellar field, which governs the rate of acceleration outside an expanding supernova shell. This statement will be explained below. At this point we simply note that, because of the steeply falling primary cosmic ray spectrum, the power required for the very high energy cosmic rays is significantly smaller than the total power requirement of (11.2), so even one or two powerful point sources could be important.

To make an estimate like that in (11.2) for the very high energy cosmic rays, we need to know their residence time in the disk of the galaxy. Simple extrapolation of (9.8) would give $\tau_R \approx 1000$ years (the light crossing time) at $E \approx 3 \times 10^{15}$ eV. Apart from the unreliability of an extrapolation by more than 4 orders of magnitude beyond the data, the anisotropy of the cosmic rays at this energy is only of order 0.1%. One would expect it to be larger if cosmic rays of this energy were streaming freely away from the disk of the galaxy. Hillas (1984) has observed a correlation between the anisotropy of the cosmic rays and the energy spectrum that extends from 10^{12} to 10^{19} eV, as shown in fig. 12.1. The plot shows that the amplitude A of the first harmonic of the arrival directions of air showers has the same energy dependence as $E^{2.47} \times dN/dE$. Since one expects $A \propto 1/\tau_R$, this leads to the interpretation of a source spectrum $\propto E^{-2.47}$ (differential) and a residence time that falls off rather slowly up to $\sim 5 \times 10^{15}$ eV and more rapidly at higher energies. If we normalize at 1 TeV by extrapolation of (9.8) from low energy, we get the following estimate of τ_R at high energy:

$$\tau_R \approx 2.5 \times 10^5 \,\mathrm{yrs} \left(\frac{E}{1\,\mathrm{TeV}}\right)^{-0.13} \qquad 1\,\mathrm{TeV} < E < 5\,\mathrm{PeV}$$

and

$$\tau_R \approx 0.8 \times 10^5 \,\mathrm{yrs} \left(\frac{E}{5\,\mathrm{PeV}}\right)^{-0.53} \qquad E > 5\,\mathrm{PeV}. \tag{12.1}$$

A direct calculation of cosmic ray propagation in a realistic galactic field configuration (Honda et al., 1985) gives numbers within a factor two of this in the range 10^{16} to 10^{18} eV. To obtain the energy density in high energy cosmic rays, we use Hillas' summary of the integral spectrum, which can be represented as

$$F(>E) \sim 2 \times 10^{-10} \frac{\mathrm{particles}}{\mathrm{cm^2\,s\,sr}} \times \left(\frac{E}{1000\,\mathrm{TeV}}\right)^{-\gamma}, \tag{12.2}$$

with $\gamma = 1.6$ for $E < 1000$ TeV and $\gamma = 2.0$ for higher energy. Substitution in (11.2) then gives the following estimates for the power required to sustain the high energy cosmic rays:

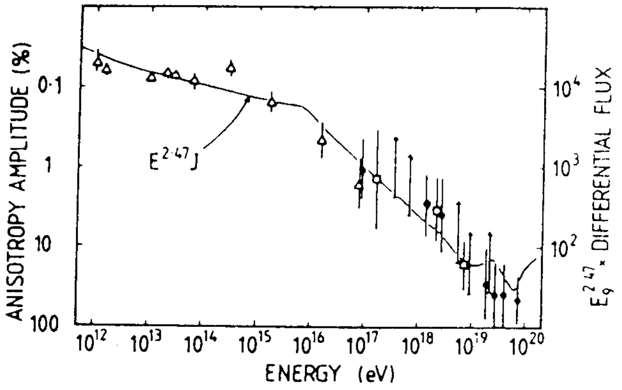

Figure 12.1: Left ordinate: anistropy; right ordinate: $E^{2.47} \times$ cosmic ray spectrum, *vs* energy (from Hillas, 1984). (Reproduced with permission, from the *Annual Review of Nuclear and Particle Science,* Vol. 34, © 1984 by Annual Reviews Inc.)

$$\sim 2 \times 10^{39} \text{ erg/s for } E > 100 \text{ TeV},$$

$$\sim 2 \times 10^{38} \text{ erg/s for } E > 1 \text{ PeV},$$

$$\sim 5 \times 10^{37} \text{ erg/s for } E > 10 \text{ PeV}.$$

These are considerably less than the total power requirement for all the cosmic rays, and comparable to what might be available from just one or a few very energetic sources.

12.4 New supernova remnants

Let us return to consider how a neutron star *inside* the expanding shell of a new Type II supernova remnant might accelerate particles. An accelerator could be powered either by rotational energy of the remnant neutron star or by accretion of matter from the inside of the shell falling back onto the neutron star. In the latter case, the possible acceleration mechanisms would be similar to those in the case of accretion onto a neutron star in a binary system, which will be discussed in the next section. Whatever the source of power, there is likely to be enough material falling back from the expanding shell to provide nuclei for the acceleration process. Since the inner parts of the shell consist of heavy nuclei (iron and its relatives), we might expect a large fraction of heavies among the nuclei accelerated here.

In the case of rotation, the power available is related to the electromagnetic power of an oscillating dipole. A magnetized neutron star rotating in vacuum with angular frequency Ω would lose energy as magnetic dipole radiation at a rate

$$L_d = \tfrac{2}{3} \sin^2(\theta) \frac{\mu^2 \Omega^4}{c^3}, \qquad (12.3)$$

where μ is the magnetic moment of the neutron star and θ is the angle between its magnetic axis and its axis of rotation. For a neutron star with a radius of ≈ 10 km and a surface magnetic field of 10^{12} Gauss, $\mu \approx 10^{30}$ cgs units and $L_d \sim 2 \times 10^{39}$ erg/s$\times(P_{10})^{-4}$.

Problem: Show that if the evolution of a neutron star were determined only by energy loss at the rate given in (12.3), then

$$L_d(t) = L_d(0) \left(1 + \frac{4}{3} \frac{\Omega_0^2 \mu^2}{c^3 I \sin^2 \theta} t\right)^{-2}, \qquad (12.4)$$

in which case the pulsar would have a characteristic lifetime

$$T_d \sim c^3 I / (\Omega_0^2 \mu^2)$$

See Section 4.4 of Katz (1987) for a discussion of pulsar evolution.

The power indicated in (12.3) and (12.4) is not expected to be emitted as magnetic dipole radiation because, even for an isolated pulsar, it is expected that there is sufficient plasma so that the plasma frequency $\omega_p > \Omega$. In this case the electromagnetic wave cannot propagate, but instead will drive a relativistic wind of electrons and positrons (Arons 1981). The energy of rotation may still be available for acceleration of ions, for example through acceleration at a standing shock in the relativistic wind,[1] as shown in fig. 12.2. The supernova blast wave shock discussed in Chapter 11 is in region *(c)*, ahead of the expanding shell. The shock in the pulsar wind, at which acceleration may also occur, is indicated by the small circle around the pulsar, P. The upstream, unshocked region in this case is *inside* the pulsar wind shock, which expands homologously with the supernova.

---

[1] Another possible mechanism for converting rotational energy into accelerated particles could be plasma turbulence in the expanding medium (Berezinsky & Ginzburg, 1987).

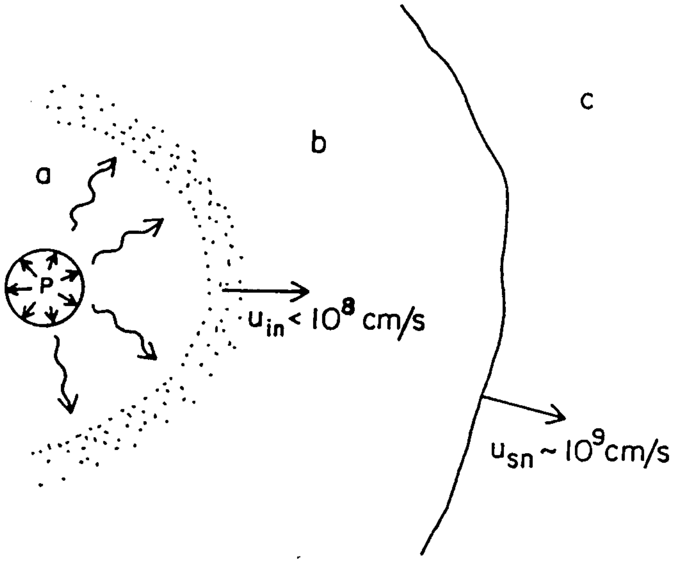

Figure 12.2: A very young supernova remnant: (a) shocked pulsar wind; (b) expanding ejecta; (c) interstellar medium (perhaps modified by wind of progenitor star). Straight and wavy arrows represent, respectively, unshocked and shocked pulsar wind. From Gaisser, Harding & Stanev, 1989.

The location of the pulsar wind shock is obtained, following the original discussion of Rees and Gunn, 1974 (also Pacini and Salvati, 1973), by assuming the energy carried out by the wind is accumulated in the region of the shocked wind (region *(a)* of fig. 12.2). The shock occurs where the ram pressure of the wind balances the accumulated energy density,

$$\frac{L}{4\pi R_s^2 c} \sim \frac{\int L \, dt}{\frac{4}{3}\pi R_a^3}, \qquad (12.5)$$

where $R_a \sim u_{\rm in}\, t$ is the radius of the region *(a)* inside the ejecta. The shell expands homologously, with an outer velocity $\sim 10^9$ cm/s and an inner velocity, $u_{\rm in} < 10^8$ cm/s (see fig. 12.2). At early times ($t < T_d$ from (12.4)) $L \sim$ constant, and (12.5) can be solved to find the shock radius,

$$R_s = \sqrt{u_{\rm in}/(3c)} \times R_a. \qquad (12.6)$$

To estimate the maximum energy for acceleration at the pulsar wind shock, we also need to know the magnetic field in this vicinity. A dipole field falls off like r^{-3} out to the velocity of light cylinder,

$$r_{LC} = c/\Omega. \qquad (12.7)$$

Beyond this radius, the field has a spiral character and falls off like r^{-1}, characteristic of the radiation zone. Thus, for $r > r_{LC}$

$$B \sim B_* \frac{R_*^3}{c^2 R_s} \Omega^2 = B_* \frac{R_*^3}{(u_{\rm in}\, c)^{3/2}\, t} \Omega^2, \tag{12.8}$$

where B_* and R_* are the magnetic field and radius at the neutron star surface. Note that the problem is not spherically symmetric – this estimate applies in a region near the equatorial plane of rotation. For a 10 ms pulsar with a 10^{12} Gauss surface field, this gives an estimate of 10 Gauss at $t = 1$ year for $u_{\rm in} = 5 \times 10^7$ cm/s.

With such a strong magnetic field, the acceleration rate can now be many orders of magnitude faster than for acceleration at the exterior supernova blast shock. In this situation the limiting factor is the size of the acceleration region rather than the age of the supernova. Moreover, because the wind is relativistic, some of the assumptions used in Chapter 11 for the treatment of stochastic, first order Fermi acceleration break down. Acceleration may still occur (Webb, 1987), however. An order of magnitude estimate of the maximum energy can be made by evaluating the characteristic energy, eB_sR_s. (Because of the relativistic flow, $u_1/c \sim 1$.) From (12.6) and (12.8),

$$E_{\rm max} \sim e B_s R_s = \frac{e B_* R_*^3 \Omega^2}{\sqrt{3}\, c^2}. \tag{12.9}$$

For a 10 millisecond pulsar with a 10^{12} Gauss surface field, this is nearly 10^5 TeV. Note that this estimate of $E_{\rm max}$ is independent of the poorly determined $u_{\rm in}$ and also of the age of the supernova, both of which cancel from the product B_sR_s.

Because of the high magnetic field near the pulsar wind shock, synchrotron losses are likely to give a much lower limit for acceleration of electrons. For example, with the parameters used to illustrate (12.8), one has from (11.31) $E^{(s)}_{\rm max} \sim 7$ TeV. For this acceleration model, therefore, observation of air showers generated by photons with $E > 100$ TeV from a new supernova would imply accelerated ions (rather than electrons) as the source of the photons (for example *via* the process 11.1). The conclusion that > 100 TeV photons imply acceleration of protons or nuclei is likely to be more general for new Type II supernovas than the particular acceleration model discussed here because it depends in an important way on the fact that the acceleration occurs in a region of high magnetic field.

12.5 Binary stars as cosmic accelerators

A neutron star in a binary system can be a source of thermal x-rays if it is accreting matter, either from a wind from its companion star or because the companion star overflows the critical "Roche" potential. The physics of X-ray binaries is discussed in the books by Frank, King and Raine (1985) and by Pringle and Wade (1985). The x-radiation is released as the accreting matter is thermalized. Accretion might also power a high energy particle accelerator.

The rate of accretion is limited by the Eddington luminosity, $L_{\rm edd}$. This limit is obtained by equating the outward force per electron due to accretion-induced radiation to the inward gravitational force per proton (since significant charge separation does not occur):

$$\frac{L_{\rm edd}}{4\pi R^2 c}\sigma_T = \frac{GMm_p}{R^2}. \tag{12.10}$$

where σ_T is the Thomson cross section. Because the radial dependence cancels from the equation, the result is rather independent of details. Numerically, $L_{\rm edd} \approx 1.4 \times 10^{38}(M/M_\odot)$ erg/s. Equation (12.10) assumes spherical symmetry of the accretion, so it is not a strict upper limit; nevertheless, many X-ray binaries are observed with luminosities near this characteristic value.

Because of the angular momentum of the binary system, the accretion is far from spherical, at least at large distances. Instead, matter spirals in following nearly Keplerian orbits, losing energy by viscous processes. One scenario is shown in fig. 12.3, which shows a companion star filling its Roche lobe (the equipotential that contains the inner Lagrange point). Matter falls through the inner Lagrange point and flows into the accretion disc. Tidal bulges may occur where matter flows into the accretion disk and at the conjugate location on the disk. Another possibility is that the accreting matter is due to a stellar wind from the companion, which may not fill its Roche lobe.

The X-ray emission from a binary is typically modulated by the orbital period of the system, which is given by Kepler's law,

$$P = 2\pi\sqrt{\frac{a^3}{G(M_1 + M_2)}}, \tag{12.11}$$

where a is the semimajor axis of the system. For given masses, short orbital periods are associated with small separations, which must,

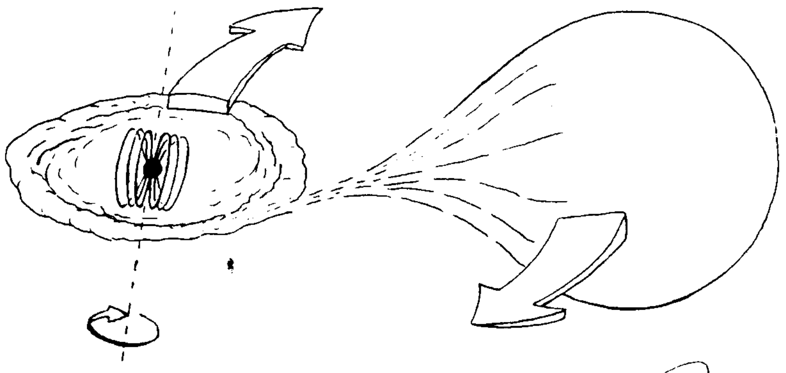

Figure 12.3: Sketch of a neutron star accreting matter from a companion star that overflows its Roche lobe. The sense of orbital rotation is shown by the flat arrows. The neutron star, its magnetosphere and its rotation are also indicated.

however, be large enough so the noncompact partner is no larger than its Roche lobe. The minimum separation and corresponding minimum period are given in table 12.1 as a function of the companion mass M_2 for main sequence hydrogen stars.[2] The compact partner is assumed to be a neutron star with a mass of $M_1 = 1.4\,M_\odot$. Of course, the companion need not necessarily be a main sequence star.

The inner edge of the accretion disk around a neutron star may be determined by its magnetic field rather than by its surface. This occurs when the magnetic pressure above the neutron star surface is great enough to balance the ram pressure of the accreting matter. The distance at which the balance occurs is called the Alfvén radius, R_A, which is the solution of

$$\frac{B^2}{8\pi} = \rho v^2 \approx \sqrt{\frac{2GM}{R_A}}\,\frac{\dot{M}}{4\pi R_A^2}. \qquad (12.12)$$

For a field of dipole moment μ, $B(R) \approx \mu/R^3$. Solving (12.12) gives

$$R_A = \mu^{4/7}(2\dot{M})^{-2/7}(2GM)^{-1/7}. \qquad (12.13)$$

---

[2] Roche lobe parameters for table 12.1 are taken from Pringle & Wade (1985). Radii of zero age main sequence stars are from Patterson (1984) for $M < 1.5 M_\odot$ and from Clayton (1968) for larger mass companions.

Table 12.1: Separation and period for zero age main sequence stars filling the Roche lobe in a binary system.

$M_2/M_\odot$	$a/R_\odot$	$P_{\min}$(hrs)	$R_2/R_\odot$
0.1	0.68	0.82	0.13
0.2	1.04	1.50	0.24
0.3	1.40	2.27	0.35
0.5	1.86	3.29	0.54
0.7	2.28	4.25	0.73
1.0	2.80	5.4	1.00
1.5	3.82	7.8	1.47
1.8	4.0	8.0	1.60
2.8	4.5	8.3	2.00
4.5	5.4	9.5	2.60
7.1	6.5	11	3.40

For a neutron star with a radius of 10 km and a 10^{12} Gauss surface field (so that $\mu \approx 10^{30}$ c.g.s. units) $R_A \approx 1.3 \times 10^8$ cm for $\dot{M} = 10^{18}$ g/s. (This $\dot{M}$ is the rate of mass transfer onto a neutron star with the canonical mass and radius that results in a luminosity $GM\dot{M}/R$ equal to the Eddington limit.) For the same $\dot{M}$, $R_A = R_* \sim 10^6$ cm for $B_* \sim 2 \times 10^8$ Gauss. When $R_A > R_*$ matter flows from the inner edge of the accretion disk up (or down) along the dipole field lines and onto the polar caps of the neutron star.

With this background I next discuss some possible specific mechanisms for acceleration of high energy cosmic rays in binary stars that contain a neutron star.

12.5.1 Shock in accretion flow

For shock acceleration to work, the shock must occur where the ram pressure of the particle flow in the plasma dominates the magnetic pressure; otherwise, the field irregularities necessary for scattering the cosmic ray particles back and forth across the shock are not frozen into the converging flow of plasma into the shock, and the basic mechanism for converting macroscopic energy of fluid flow into energizing relativistic particles is lacking. For an accreting X-ray binary this means diffusive acceleration can only occur in an accretion shock if it is located at $R \gg R_A$. Thus, from (12.12), the conditions for diffusive shock acceleration near the surface of the neutron star exist only in cases where the surface field is low, of order 10^8 Gauss. An accreting neutron star with a stronger magnetic field will have shocks in the accretion flow above the polar caps, but the fields in this region will be too strong for diffusive shock acceleration to work. A shock may also occur in the accretion flow outside the Alfvén radius, but if the shock is far away from the neutron star's surface, then the full energy of accretion is not available.

Kazanas and Ellison (1986) estimate that the maximum energy accessible for acceleration at an accretion shock would be of order 10^7 GeV per particle. In this scenario, the magnetic field in the acceleration region is so high that the energy is limited by synchrotron losses even for ions.

> **Problem:** Show that with $B \sim 10^8$ Gauss, electrons could only achieve $E < 1$ GeV even if the velocity of the unshocked material into the shock approaches the free fall velocity at the surface of a neutron star.

Because the acceleration in this model occurs in a region of strong magnetic field, the accelerated charged particles could not themselves escape from the acceleration region. Kazanas and Ellison point out that neutrons stripped from accelerated nuclei, either by nuclear collisions or by photodisintegration in the ambient photon fields, would escape to large distances.

12.5.2 Disk dynamo

An alternate mechanism for converting accretion power into particle acceleration is to use a difference in rotation velocity between the accretion disk and the neutron star. As originally suggested (Chanmugam and Brecher, 1985) the idea was an adaptation of one suggested by Lovelace (1976) for acceleration of particles by accretion around black holes. The general idea is that in an accreting neutron star with a strong magnetic field the field lines from the neutron star will intersect the accretion disk, giving rise to a $v \times B$ electric field starting at the inner edge of the accretion disk.

To estimate the particle energy accessible with this mechanism, we can take v as the Keplerian velocity at the Alfven radius and B as the neutron star field at that radius. Then

$$E = \frac{e}{c}(v \times B)\,\Delta r, \qquad (12.14)$$

where Δr is the distance over which the e.m.f. acts. Taking $\Delta r \approx R_A$, we find

$$E \approx 3.5 \times 10^{14}\ \mathrm{eV}\, B_{12}^{-3/7} L_{38}^{5/7}, \qquad (12.15)$$

where L_{38} is the luminosity due to accretion in units of 10^{38} erg/s. In this case we see that the maximum achievable energy occurs for the smallest possible B. This occurs when the Alfvén radius is just above the surface of the neutron star; i.e. for $B \approx 10^8$ Gauss at the surface of the neutron star, in which case $E \approx 2 \times 10^{16}$ eV for accretion near the Eddington limit. As before, the weak field case is also the one for which the maximum power is available.

A detailed model of acceleration by a dynamo of this general kind in an accreting x-ray binary has recently been constructed by Cheng & Ruderman (1989). It is related to their model for acceleration of electrons in an isolated pulsar, such as the Crab Pulsar (Cheng, Ho and Ruderman, 1986). It is motivated specifically to account for a shift of some >TeV signals from Her X-1 relative to the known x-ray period. Isolated pulsars do accelerate electrons and could in principle also accelerate ions. For an isolated pulsar, however, a source of ions for injection into the accelerator is problematic.

12.5.3 Pulsar wind shock

If the Alfvén radius calculated from (12.13) is outside the light cylinder (12.7), then a pulsar wind will form as discussed in §12.4, and accretion will be prevented by the ram pressure of the pulsar wind. Figure 12.4 shows an example. Conversely, when $R_A < R_{LC}$ the accretion disk penetrates into the magnetosphere and the pulsar wind is stifled by accretion. The condition for a pulsar wind to dominate is

$$\frac{P_{ms}\dot{M}_{18}^{2/7}}{B_{12}^{4/7}} < 30, \qquad (12.16)$$

where $\dot{M}_{18}$ is the accretion rate in units of 10^{18} g/s and P_{ms} is the period in milliseconds.

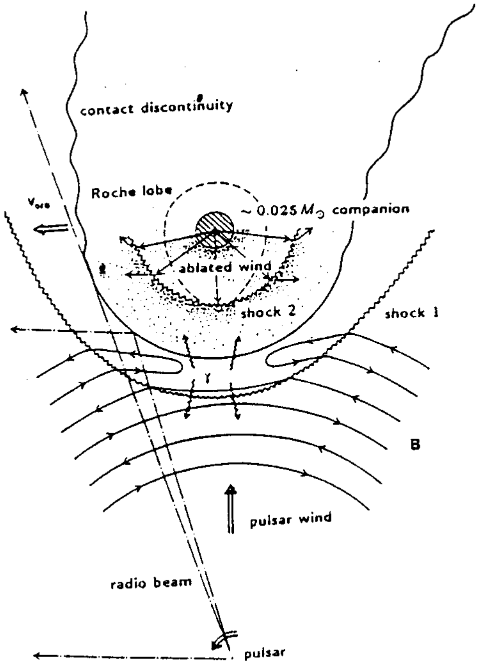

Figure 12.4: A diagram of a colliding wind model for the 1.6 ms eclipsing pulsar 1957 + 20 (from Phinney et al., 1988). (Reprinted with permission from *Nature* Vol. 333 pp. 832. © 1988 MacMillan Magazines Ltd.)

A pulsar wind in a binary system will be shocked due to its interaction with the atmosphere or the wind of the companion star. This interaction region may be a source of x-radiation, as proposed by Bignami, Maraschi & Treves (1977) for Cygnus X-3. By locating the x-ray source near the companion in this way they could explain the nearly sinusoidal shape of the x-ray light curve. In the more conventional scenario, when accretion powers the x-ray emission, the source is near the neutron star and one would expect a sharper eclipse. Cygnus X-3 is obscured by the disk of the galaxy and is not visible in the optical. It is therefore impossible to determine unambiguously by what means it it is powered. The recently discovered 1.6 ms binary pulsar 1957+20 (Fruchter et al., 1988) does appear to be an example of a system driven by a pulsar wind that is in the process of blowing away a very light companion star (Phinney et al., 1988, fig. 12.4). Shocks in the winds in such systems could be sites for acceleration of particles to ultra-high energy (Harding & Gaisser, 1989).

12.5.4 Turbulent reconnection

Many of the candidate sources are observed to be sporadic. This is remniscent of solar flare activity, in which particles are sometimes accelerated to energies of several GeV. The mechanism is thought to be release of energy that has built up as magnetic fields are stressed by turbulent motions of the solar plasma. When magnetic fields "reconnect" in a turbulent magnetohydrodynamic (MHD) plasma, electric fields are generated in which particles can be accelerated (Matthaeus et al., 1984; Sorrell, 1984). Many of the same ingredients are present in x-ray binaries. There are strong magnetic fields that may thread accreting plasma. Differential rotation together with uneven rates of accretion are likely to stress the magnetic fields. If the stress is released through reconnection of tangled field lines impulsive acceleration of charged particles would be likely to occur.

Wang (1986) has proposed that such a mechanism could explain bursts of acceleration to ultra-high energies in accreting x-ray binaries. Another specific suggestion that incorporates acceleration through plasma turbulence driven by accretion is that of Katz & Smith (1987). They suggest that MHD Alfvén waves excited by accretion onto the magnetic polar regions of a neutron star may carry the full energy of accretion outward to where it can effectively be used for acceleration. The energy achievable for protons would be limited by synchrotron radiation in the strong fields needed to make the mechanism work. Energies up to $\approx 10^{16}$ eV might be possible. A prediction is the existence of proton synchrotron radiation at GeV energies and below.

12.5.5 Hercules X-1 and Cygnus X-3

To conclude this section it is instructive to try to apply some of the proposed mechanisms to the two most frequently studied examples of x-ray binaries that appear to accelerate particles to $10^{13} - 10^{15}$ eV. Some of the properties of these two systems are summarized in Table 12.2. We can now check off which of the mechanisms discussed in this section might apply to each system. For Hercules X-1, about which most is known, all but one of the mechanisms have difficulty. So little is known about the Cygnus X-3 system, which is obscured by dust in the disk of the galaxy, that none of the mechanisms is eliminated. The nature of the high energy signals from these and other x-ray binaries is the subject of the next chapter.

Table 12.2: Properties of two X-ray binaries.

	Hercules X-1	Cygnus X-3
Pulsar period	1.24 s	[12.6 ms]
Orbital period	1.7 days	4.8 hours
Companion mass	2.2 $M_\odot$	? (not visible)
Distance	$\sim$ 4 kpc	$\sim$ 10 kpc
B_* (Gauss)	$\sim 5 \times 10^{12}$	?
Possible acceleration mechanisms		
Accretion shock	No (B_* too high)	Possible
Disk dynamo	Problematic (high B_*, so PeV/particle difficult)	Possible
Pulsar wind shock acceleration	No (too slow)	Possible
Turbulent reconnection	Possible	Possible

Chapter 13

Astrophysical beam dumps

It is difficult to distinguish among the various possible scenarios for the origin of cosmic rays because the cosmic ray nuclei themselves do not travel in straight lines, but diffuse through the tangled magnetic fields in the galaxy. The problem is even worse for the ultrahigh energy cosmic rays (those with energies above $\sim$ 100 TeV) because their flux is so low that they cannot be studied in detail with detectors small enough to be carried to the top of the atmosphere. As a consequence, the identity of the primary cannot be determined event by event. The directions of air showers generated by these high energy particles can be measured, but since the cosmic rays do not point back to their sources it is impossible to identify the sources in this way.

As noted in chapter 12, however, some of the possible sources of the ultra-high energy cosmic rays, such as very young supernova remnants and X-ray binaries, are associated with relatively dense concentrations of matter and would therefore be likely point sources of secondary photons and neutrinos. Such a configuration, in which accelerated particles interact with material near their source, is called an astrophysical beam dump. The analogy is to a beam dump at a terrestrial accelerator in which all possible secondaries are produced. Secondary photons and neutrinos from a cosmic accelerator would point back to their sources and would identify them as high energy accelerators. Hence the intense current interest in searches for such signals and their study.

13.1 Nature of the data

Because the field is still developing rapidly, the experimental status of searches for air showers from point sources will be reviewed only very briefly. The main focus will be on illustrating the potential implications for origin of high energy cosmic rays using some reported fluxes from observations of the x-ray binaries Hercules X-1 and Cygnus X-3. Detailed reviews may be found in the papers of Weekes (1988), Nagle et al. (1988), Protheroe (1987) and Watson (1985) and in the comprehensive review of Cygnus X-3 by Bonnet-Bidaud and Chardin (1988). Very young supernovas are also potential astrophysical beam dumps.

13.1.1 X-ray binaries

Typically the observations indicate that x-ray binaries are sporadic, rather than continuous, sources of air showers. In most cases, the signal is established on the basis of a phase or periodicity analysis which shows an excess of events from the direction of the source in phase with the known X-ray period. Examples for Cygnus X-3 are shown in fig. 13.1. No single observation is of very high statistical significance by itself, however. When ~TeV observations (which are made with air Cherenkov telescopes) and ~Pev air shower observations are compared, the energy spectrum appears to be rather flat, with differential spectral index near $-(\gamma+1) = -2$.

The most puzzling feature of the observations of Cygnus X-3 and Hercules X-1 is that, where muon measurements are available, the air showers from these sources seem to have nearly normal muon content, in striking contrast to what is expected for a photon-induced shower. Photon showers should be almost purely electromagnetic and should have at least one order of magnitude fewer muons that background cosmic ray showers. I will return to a discussion of this important point in chapter 16. For the present discussion, however, I assume that the showers from point sources are induced by photons.

Because the sources appear to be sporadic, it is difficult to determine a flux level. For illustration, I use the time-averaged spectrum for Cygnus X-3 given in Watson's 1985 review, though subsequent evidence suggests the signal is weaker than this. The data summarized there for the energy range 1-1000 TeV can be represented by

$$F_\gamma(>E) \sim 4\times10^{-11}\,\mathrm{cm^{-2}s^{-1}}\times E_{\mathrm{TeV}}^{-1}, \tag{13.1}$$

where E_{TeV} is the shower energy in TeV. The limit reported by Dingus et al. (1988) is roughly an order of magnitude lower than this.

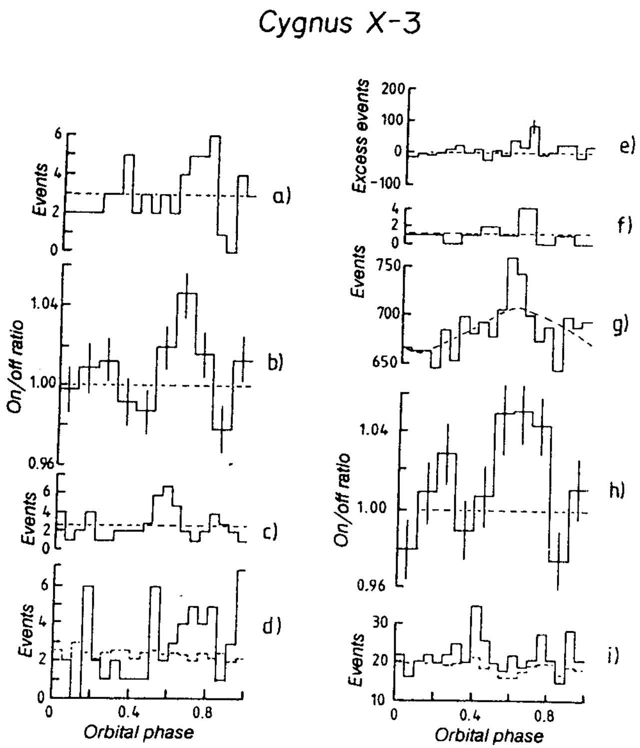

Figure 13.1: Phase distributions reported for ~ PeV air shower observations of Cygnus X-3. The figure is due to Protheroe (1987). See also Nagle et al. (1988) for the references to the data shown. (Reproduced with permission, from the *Annual Review of Nuclear and Particle Science*, Vol. 38, © 1988 by Annual Reviews Inc.)

13.1.2 A very young supernova

Supernova 1987A offers a unique opportunity to look for signals from a new supernova. If it contains a cosmic accelerator, photons and neutrinos could be produced by collisions of the accelerated particles with the surrounding gas while it is sufficiently dense (of order 10 years). As of early 1989, only one suggestion of a signal, in the TeV range, has been reported, although several air shower experiments and air Cherenkov detectors continue to monitor the supernova. Given the distance to SN1987A of ~ 50 kpc, the observed limits correspond to a power in accelerated particles at the source of $< 5\times10^{38}$ erg/s in the TeV range and less than several times 10^{39} erg/s above $\sim$ 100 TeV (see Gaisser et al., 1989 for a summary of the limits). An accelerator in this particular supernova could hardly be this powerful without having altered the behavior of the optical light curve, which was very successfully explained as being powered by the radioactive decay chain of ^{56}Ni synthesized in the explosion (Pinto & Woosley, 1988). Observations of higher sensitivity may be possible in the future.

I will not discuss production of signals in the supernova envelope further here. It is, however, straightforward to apply the formulas derived for signals from X-ray binaries, as discussed below, to the case of production in a supernova envelop – or indeed in any other astrophysical beam dump for which there is some idea about the spectrum of particles and the distribution of gas in which they interact. The calculation is essentially an application of the techniques used in previous chapters to evaluate atmospheric fluxes.

13.2 Possible beam dump configurations

An astrophysical beam dump is similar to a beam dump at an accelerator in that all possible secondaries are produced. A major difference is that the target is likely to be a diffuse astrophysical plasma or gas, so that the decay products of pions and kaons are not suppressed by absorption of the parent mesons. Neutrinos from decay of charged pions will therefore be produced in comparable numbers to photons from π^0 decay, though the photons are much more likely to be reabsorbed in or near the source.

Important aspects of signals from point sources depend on what the beam-target configuration is. In an X-ray binary, the most obvious possibility is that acceleration takes place near the neutron star by one of the mechanisms discussed in §12.4, producing a more or less isotropic beam of particles that impinges on the atmosphere of the companion (Vestrand & Eichler, 1982; Stenger, 1984; Berezinsky et al., 1985; Hillas, 1984). A possible difficulty with this is that the fraction of the orbit during which photons are directed at Earth is likely to be very small, determined by the scale height of the companion star relative to the circumference of the companion's orbit. From a measurement of the duration of the onset of X-ray eclipse (Deeter et al., 1981), this fraction can be estimated as $\sim 10^{-3}$ for Hercules X-1. An accretion disk around the neutron star or an extended gas plume driven off the companion (Hillas, 1984) may make a more favorable target.

In either case, magnetic fields may play an important role in steering charged particles onto (or away from) the target region (Gorham & Learned, 1986). Figure 13.2 shows some examples. Protheroe & Stanev (1987) discuss the consequences of attributing a magnetic field to the companion star which would determine the trajectories of accelerated charged particles through the accretion disk, which acts as target. The dashed lines in fig. 13.2*b* indicate those photons produced on trajectories that lie in the plane of the observer at Earth. The phase of a signal will depend in a complicated way on the energy of the parent particles because the trajectory of a particle through the magnetic field depends on its rigidity. Moreover, if the orientation or strength of the field is variable, the phase of any observed signal would also be expected to vary with time. Since the phases do appear to vary both with time and energy, this is an attractive feature of this general idea.

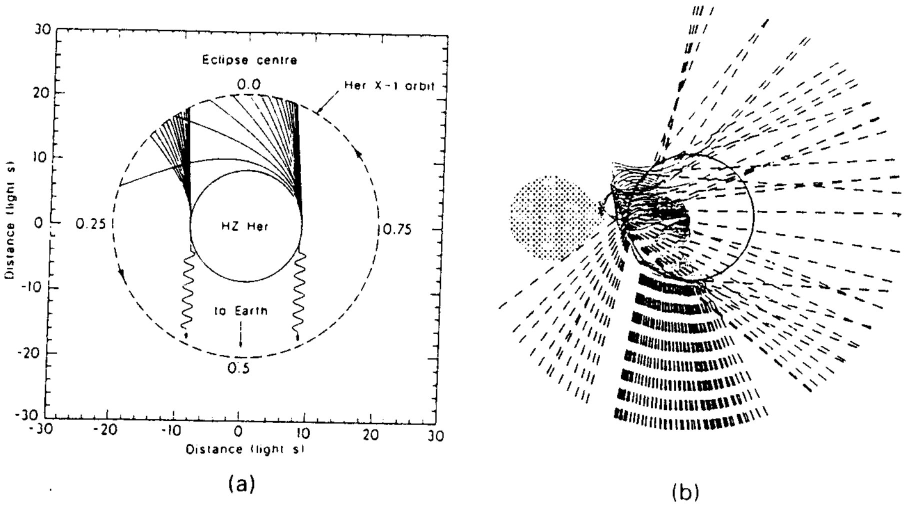

(a) (b)

Figure 13.2: Examples of beam dumps with magnetic steering. (a) A model for Hercules X-1 (Gorham & Learned, 1986); (b) A model of Cygnus X-3 with the accretion disk as target (Protheroe & Stanev, 1987). (Reprinted with permission from *Nature*: (a) Vol. 323 pp. 422. © 1986 MacMillan Magazines Ltd. (b) Vol. 328 pp. 136. © 1987 MacMillan Magazines Ltd.)

13.3 Luminosity at the source

The relation between an observed signal and the power at the source depends on a number of factors, as originally discussed by Hillas (1984). The relation is

$$L_p \approx \int E\,\phi_\gamma(E)\,\mathrm{d}E \times 4\pi d^2 \times \exp[\frac{d}{\ell_3(E)}] \times \frac{1}{\Delta\phi_\gamma} \times \frac{\Delta\Omega}{4\pi} \times \frac{1}{\epsilon_\gamma}, \quad (13.2)$$

where L_p is the power in accelerated charged particles at the source. The first factor after the integral accounts for the distance to the source; the second corrects for attentuation of the signal in the intervening microwave background; the third accounts for the duty cycle of production of photons; the fourth for beaming and the last for efficiency of production of photons by the accelerated particles at the source.

The attentuation of photons in the microwave background *via* the process

$$\gamma + \gamma(3^\circ K) \rightarrow e^+e^-$$

is strongly energy dependent, with a minimum attenuation length of $\approx$7 kpc around 2.5 PeV, as determined by the threshold for e^+e^- production (Gould and Schreder, 1966; Jelley, 1966). Figure 13.3 shows the attenuation length $\ell_3(E)$ plotted vs. E. The rapid rise of the attenuation length below $\sim$200 TeV is due to the fact that below this energy the $\gamma + \gamma(3\ \mathrm{K})$ energy in the CM system is below the threshold for production of an e^+e^- pair. An effective attenuation length, $\ell_3(> E)$, for a particular detector observing a certain spectrum is obtained by a convolution of $\ell_3(E)$ with the spectrum of photons from the source. Because of the strong energy dependence of the process, the power at the source inferred from an observation depends strongly on the shape of the photon spectrum and on the threshold of the detector. In particular, for a detector like the original Kiel air shower array (Samorski & Stamm, 1983), with an effective threshold of ≈ 2 PeV, the intrinsic power inferred depends on how far the photon spectrum extends above the absorption feature. Conversely, a detector at high altitude with closely spaced detectors and consequently a low threshold of ~ 0.1 PeV, has a great advantage for observing a distant source.

The factor $\Delta\phi_\gamma$ is the fraction of the phase during which the alignment of the accelerator beam and the beam dump is such that

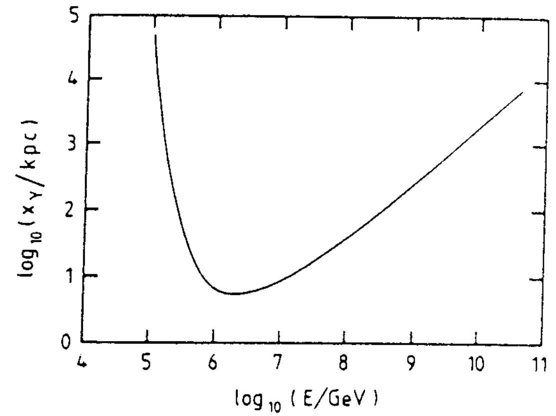

Figure 13.3: Attenuation length of photons in the microwave background radiation. (From Protheroe, 1986. Reprinted with permission of the Royal Astronomical Society.)

photons are produced in the direction of the detector without being reabsorbed. In an ideal experiment with a large signal, it is simply the observed pulse width. In practice, if the signal is confined to a single bin, one can only say that it is smaller than the bin width. The next factor, $\Delta\Omega/4\pi$, represents the amount of beaming and is essentially unknown. One simple generic case would be an isotropic beam continuously illuminating a beam dump of limited extent that is aligned to produce a visible signal once per orbital cycle of the binary system. Another generic configuration would be a uniform, thin shell illuminated by a fan shaped beam with its orientation fixed in the orbiting system. In the first case the observed pulse width is determined by the extent of the beam dump and in the second by the width of the beam. The latter would be the most efficient, with $\Delta\Omega$ cancelling $\Delta\phi_\gamma$. Intermediate cases are of course possible and even likely. Without a conspiracy, however, (such as a pencil beam with geotropic orientation) the ratio $\Delta\Omega/\Delta\phi_\gamma \geq 1$. Observation of a pulsar period $\ll$ orbital period would imply that $\Delta\Omega < 4\pi$. One could, however, have a situation in which the TeV signal shows a pulsar period (e.g. 12.6 ms for Cygnus X-3, Chadwick et al., 1985) but has a different origin from a PeV signal, in which case the conclusion would not apply to the PeV beam.

Finally, the factor $1/\epsilon_\gamma$ corrects for the efficiency with which charged particles with energy $> E$ produce photons above the same energy. For protons producing photons *via* $\pi^0 \to 2\,\gamma$, the production spectrum of photons is given by the first term in (4.14). (The contribution from interactions of charged pions is absent because they are assumed to decay in a diffuse astrophysical environment.) For a thin target configuration (one pass of the parent nucleons through a region of thickness $\Delta X \ll \lambda_N$) the ratio of photons to parent nucleons is

$$\epsilon_\gamma = \frac{\phi_\gamma(E)}{\phi_N(E)} = \frac{\Delta X}{\lambda_N}\,\frac{2Z_{N\pi^0}}{\gamma+1}, \tag{13.3}$$

where γ is the integral spectral index of the source. For a thick target with straight ahead propagation, the electromagnetic cascade must be folded with the nucleonic cascade as in §4.2. Another extreme case that can be treated easily is a plasma in which accelerated protons are confined indefinitely by diffusion in turbulent magnetic fields. In this case protons reinteract, but any produced photons (and neutrons) escape directly. Then $\Delta X/\lambda_N$ in (13.3) is replaced by the factor $(1-Z_{pp})^{-1}$, which is about 1.5 for protons in hydrogen for $\gamma \sim 2$. Since $Z_{p\pi^0} \sim 0.17$ for $\gamma = 2$, $\epsilon(\gamma = 2)$ could be as high as 0.25 for a fully contained parent proton beam.

Let us assume as an example that the flux from Cygnus X-3 is given by (13.1). If we further assume an attentuation factor of three for PeV photons, take $\Delta\phi \approx 0.02$, assume no beaming and take $1/\epsilon_\gamma \approx 10$, we conclude from (13.2) that a particle luminosity of $L_p \sim 2 \times 10^{39}$ erg/s per decade of energy is required at the source. These are similar to the numbers originally used by Hillas (1984), and they imply a luminosity that significantly exceeds the Eddington limit in accelerated particles alone! If there really were a single source this strong, as Hillas remarks, it could supply all the cosmic rays in this energy region. (Recall from §12.3 the power requirement for $E > 100$ TeV is $\sim 2 \times 10^{39}$ erg/s.)

13.4 Production and absorption of neutrinos

In addition to exceeding the Eddington limit, a source this powerful has other serious problems. In a close binary such as Cygnus X-3 must be if its characteristic 4.8 hour period is its orbital period, a high luminosity in accelerated particles will tend to disrupt the system. Unless beaming is invoked, a fraction $\sim R_2^2/4a^2$ of the produced photons and neutrinos will intersect the companion star of radius R_2. Photons will deposit energy near the surface where it will in part be radiated away and in part erode the surface by driving off a wind. Neutrinos with $E >$ TeV are even more disruptive, as they will deposit their energy deep in the stellar interior where it cannot be dissipated in time to prevent the star from expanding in response to this deep deposition of energy (Stecker et al. 1985). The following estimate of neutrino absorption can be made. Referring to table 12.1, if the companion star in Cygnus X-3 is a main sequence dwarf that fills its Roche lobe, $M_2 \sim 0.8\,M_\odot$, $R_2 \sim 5.5 \times 10^{10}$ cm, and $R_2^2/4a^2 \sim 0.03$. The thickness of the companion is of order $M_2/\pi R_2^2 \sim 1.5 \times 10^{11}$ g/cm^2. With σ_ν given by (7.1), the companion star becomes opaque to neutrinos with energy above ~ 2 TeV.

To assess the significance of this, we also need to know the critical energy of pions in the atmosphere of the companion,

$$\epsilon_\pi^* \sim \frac{m_\pi c^2 h^*}{c\tau_\pi}, \tag{13.4}$$

where the scale height of the stellar atmosphere is

$$h^* \sim \frac{k\,T\,R_2^2}{m_H G\,M}.$$

Just as in the Earth's atmosphere, pions will tend to decay if $E < \epsilon_\pi/\cos\theta$ and interact otherwise. For the Sun, for example, $h^* \sim 1.7 \times 10^7$ cm, so $\epsilon_\pi^\odot \sim 3$ TeV. Similarly, for kaons $\epsilon_K^\odot \sim 23$ TeV. The flux of high energy neutrinos produced in the stellar atmosphere will be given by (7.5) evaluated with the critical energies appropriate for the star.

If ϵ^* were much less than the energy threshold for stellar absorption of neutrinos, then only low energy neutrinos, to which the star is transparent, would be produced. On the contrary, because ϵ^* is somewhat larger than the energy for absorption, there will be significant production of neutrinos with energy high enough to be absorbed deep in the companion star. Some examples of neutrino heating have been worked out, one of which is shown in fig. 13.4. This example is unrealistic because the target star is much too big ($R \sim 1.4 \times 10^{11}$) to fit into the Roche lobe when the separation is only $a \sim 1.7 \times 10^{11}$ cm. It nevertheless illustrates two points. First, neutrino absorption deep in the companion may be significantly greater than the stellar luminosity due to nucleosynthesis. Second, the energy deposition is asymmetric because the front of the star shields the back. (The figure shown assumes the rotation of the companion star is phase-locked with the orbital motion so that the same side of the companion star is always facing the accelerator.) More realistic parameters for Cygnus X-3 would be $M_2 \sim 0.8 M_\odot$ and $a/R_2 \sim 3$. In this case, for an isotropic accelerator with 10^{39} erg/s in protons with $\gamma = 1$ and a spectrum that extends from 1 to 10^5 TeV, an estimate (based on (7.5) gives $\sim 10^{36}$ erg/s for the rate at which neutrino energy is absorbed. This is almost three orders of magnitude larger than the luminosity due to nucleosynthesis. At this rate the binding energy of the star would be absorbed in $\sim 10^5$ years.

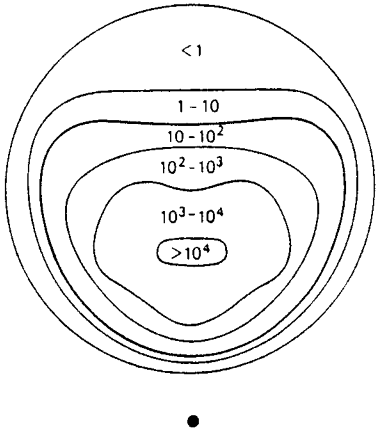

Figure 13.4: Contour map of neutrino absorption (erg cm^{-3} s^{-1}) for a ~ 10^{39} erg/s isotropic accelerator at a distance 1.7×10^{11} cm from a 2.8 $M_\odot$ star (Gaisser et al., 1986). Reprinted with permission from *The Astrophysical Journal*.)

13.5 Ratio of ν to γ

Photons and neutrinos produced and not reabsorbed in the companion star will leave the system and could be detectable if the source is sufficiently strong. If the target is the companion star's atmosphere, as in the discussion of neutrino heating, then an observer at an appropriate angle with respect to the orbital plane would see signals schematically as shown in fig. 13.5 with very narrow photon pulses.

If the target region is located near the neutron star then the phase structure in the signals could instead reflect the structure of the beam dump (e.g. bulges in the accretion disk) or of an accelerated beam, and the photon pulses could be broader. The first case would have a higher neutrino to photon ratio than the second.

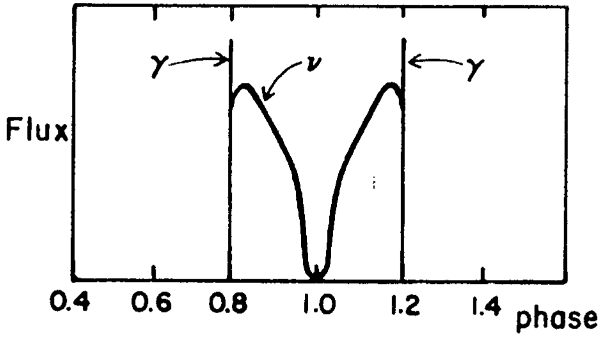

Figure 13.5: Schematic phase diagram of neutrino and photon fluxes produced in the atmosphere of the companion star in an eclipsing binary. (Adapted from Gaisser & Stanev, 1985.)

As a practical matter, one needs to know the ν/γ ratio to be able to estimate the expected high energy neutrino flux from a source for which a signal of high energy photons has been detected. The ratio at production is easy to determine, by modifying the calculations in the Earth's atmosphere (see Chapter 4 for photons and 7 for neutrinos). The spectra of photons and neutrinos at production are

$$\phi_\gamma \sim \frac{\Delta X}{\lambda_N} \frac{K}{E_\gamma^{\gamma+1}} \frac{2\, Z_{N\pi^0}}{\gamma+1}, \tag{13.5}$$

and

$$\phi_{\nu_\mu+\bar{\nu}_\mu} \sim \frac{\Delta X}{\lambda_N} \frac{K}{E_\nu^{\gamma+1}} \frac{Z_{N\pi^+} + Z_{N\pi^-}}{\gamma+1} \left(1 - \frac{m_\mu^2}{m_\pi^2}\right)^\gamma, \tag{13.6}$$

where K is a normalization constant. Table 13.1 is a summary of the relevant parameters. The table also shows the ν/γ ratio at production assuming that all muons decay without energy loss.

> **Problem:** Refer to the discussion of §7.1.3 to show that, if the beam dump is such that high energy muons decay without appreciable energy loss, then (13.6) must be multiplied by a factor 2.2 (2.5) for $\gamma = 1\,(1.7)$. Similarly, show that there will then also be an appreciable high energy flux of $\nu_e + \bar{\nu}_e$ of 0.54 (0.59) times the *total* flux of $\nu_\mu + \bar{\nu}_\mu$.

Table 13.1: Parameters for neutrino and photon production

γ	1.0	1.2	1.4	1.6	1.8
Z_{NN}	0.41	0.37	0.34	0.31	0.29
Z_{pp}	0.36	0.32	0.30	0.28	0.26
$Z_{N\pi^0}$ (includes 6% η)	0.17	0.092	0.066	0.048	0.036
$Z_{N\pi^+} + Z_{N\pi^-}$ (includes $K^\pm$)	0.35	0.19	0.14	0.10	0.075
$(\nu_\mu + \bar{\nu}_\mu)/\gamma$ (at production)	0.98	0.86	0.77	0.66	0.58

In a "leaky source" scenario, i.e. one in which the charged particles are magnetically confined in a tenuous medium from which all neutral particles escape, the ν/γ ratios at production would coincide with the ratio a long distance from the source. This would be the most efficient type of photon source because it minimizes the accelerator power required to produce a given photon signal. For the same reason, however, it produces the lowest neutrino/photon ratio. The opposite extreme would be a completely shrouded source from which *only* neutrinos emerge (Berezinsky et al., 1985)[1].

13.6 High energy ν-astronomy

Ideally, one would like to measure both the neutrinos and the photons from an astrophysical beam dump because the highly penetrating neutrinos give information that complements the photon signal, which is readily absorbed at the source.[2] This is in fact the essential motivation for high energy neutrino astronomy. The difficulty, of course, is the high penetrating power of the neutrinos that makes them of special interest in the first place!

Most neutrinos do not interact in the Earth, let alone in the vicinity of a detector. Therefore, to estimate the neutrino signal expected from a source it is necessary also to fold in the probability that the neutrinos make a detectable interaction. In this situation, as discussed in chapter 8, it is advantageous to look for neutrino-induced muons that originate outside the volume of the detector, thus enlarging the effective detector volume (Markov, 1960). The probability, P_ν, that a ν_μ on a trajectory toward an underground detector produces a muon with enough energy to emerge from the rock and go through the detector was plotted in fig. 8.2. For convenience I repeat P_ν (averaged for ν_μ and $\nu_{\bar{\mu}}$) here in table 13.2.

Table 13.2: Probability for $\nu \to$ detectable μ.

E_ν (GeV)	$P_{\nu\to\mu}$ ($E_\mu > 2$ GeV)
3	4×10^{-12}
10	5×10^{-11}
30	8×10^{-10}
100	8×10^{-9}
300	7×10^{-8}
10^3	4.5×10^{-7}
3×10^3	3×10^{-6}
10^4	1.2×10^{-5}
3×10^4	4×10^{-5}
10^5	1.0×10^{-4}
3×10^5	2.6×10^{-4}
10^6	4.5×10^{-4}
3×10^6	10^{-3}

---

[1] Berezinsky et al. authors point out that a "hidden" neutrino source would have to have a very large visible magnitude due to the thermalized energy deposited in the shell – unless it were located in a region of the galactic disk so that intervening dust obscured it.

[2] Note, however, that both cannot be measured simulataneously at the same site because one has to look up for photons and down for neutrinos.

With the values given in Table 13.2 it is straightforward to convolute the flux of muon neutrinos (see 13.6) with P_ν and obtain the expected neutrino-induced signal of muons. For a power law spectrum of accelerated nucleons that extends from $E_{\min}$ to $E_{\max}$, the normalization constant in (13.5) – (13.6) is given by

$$K = 624 \, \frac{\mathrm{GeV}}{\mathrm{erg}} \times L_p \times \left(\int_{E_{\min}}^{E_{\max}} \frac{\mathrm{d}E}{E^\gamma} \right)^{-1}, \tag{13.7}$$

where L_p is the luminosity of the accelerator (in erg/s). For numerical examples I take $E_{\min} = 1$ GeV and $E_{\max} = 10^8$ GeV. With these assumptions, the neutrino-induced signal can be approximated by

$$\mathrm{Signal} = 8 \times 10^{-8} \,\mathrm{cm}^{-2}\mathrm{s}^{-1} \times \frac{L_p(\mathrm{erg/s})}{4\pi d^2} \, e^{-5(\gamma-1)\ln 5}. \tag{13.8}$$

The numerical values here assume that all muons decay without energy loss. The integration was cut off at $E_\nu = 10^6$ GeV to represent a cutoff of the proton spectrum at 10^8 GeV. The signal calculated from (13.8) must be further reduced by the fraction of time that the potential source is sufficiently below the horizon to avoid the background of atmospheric muons for the particular detector.

At a declination of 41°, Cygnus X-3 itself is not an ideal source for underground detectors in the Northern Hemisphere because it spends little time far below the horizon. It is nevertheless often used for guidance on the question of how big an underground detector must be in order to expect to see a neutrino-induced signal of upward muons. Suppose there is a similar source at $d = 10$ kpc with $L_p = 10^{39}$ erg/s. Assuming a reduction factor of 1/2 for the fraction of time the source is sufficiently below the horizon to suppress the background of atmospheric neutrinos, (13.8) predicts a signal of $\sim 4 \times 10^{-15}$ per cm^{-2} per second. This would give ~ 1 upward, neutrino-induced muon per 1000 m^2 per year, in agreement with estimates in the literature (Kolb et al., 1985, Gaisser & Stanev, 1985).

Clearly, there are large uncertainties associated, not with the calculation itself, but with the underlying assumptions. If there is significant beaming, for example, it may be possible to obtain a photon signal in the range shown in (13.1) with lower L_p, in which case the neutrino signal could be an order of magnitude lower. Alternatively, the source may be variable, as suggested by the later measurement (Dingus et al., 1988) that gives a significantly lower average flux from Cygnus X-3 for the period April 1986-May 1987 than was reported earlier by Samorski & Stamm (1983) – again lowering the expectation for the correlated neutrino signal. On the other hand, it is conceivable that for Cygnus X-3 itself or for some other potential source, the power of the accelerator could be much higher, with more attenuation in the source to reduce the flux of photons. The neutrino flux would be much higher, but one then has to worry about how such a powerful source avoids destroying itself.

Typical experimental limits for a number of potential point sources obtained with the large nucleon decay detectors are at the level of several times 10^{-14} neutrino-induced muons per cm^2s (Svoboda et al., 1987; Oyama et al., 1989). These limits are thus at least a factor of ten higher than the signal expected from a 10^{39} erg/s accelerator at 10 kpc. Evidently, detectors of very much larger effective area are needed.

13.7 Neutron astronomy

Neutrons with energies such that $\gamma = E_n/(mc^2) > d/(c\tau_n)$ can survive the journey from a distant source (survival probability $\exp[-d/(\gamma c\tau)]$). The characteristic decay path for neutrons is $c\tau_n = 1.8$ astronomical units, so it is perhaps not surprising that neutrons are among the solar energetic particles that have been observed (Chupp, 1984). To reach Earth from a galactic source at ~ 10 kpc, however, a neutron must have $E \sim 10^{18}$ eV. Jones (1988) has emphasized the importance of this possibility.

Cassiday et al. (1989) have reported an excess of showers from the direction of Cygnus X-3 based on operation of the Fly's Eye experiment from November 1981 through May 1988. The detector threshold is 5×10^{17} eV, so the events satisfy $\gamma c\tau_n > 5$ kpc and could therefore be due to neutrons. The observation has not been confirmed in the observations with the giant air shower array at Haverah Park (Lawrence, Prosser & Watson, 1989). For the period 1974 to 1987 no excess was seen. The corresponding 95% confidence level upper limit is a factor of 5 lower that the flux implied by the Fly's Eye observation. Despite the uncertainty implied by the conflicting observations, it is still interesting to consider the implications of the possibility that $\sim 10^{18}$ eV neutrons live long enough to travel galactic distances.

Neither of the air shower experiments mentioned above can discriminate between photon-induced cascades and those initiated by neutrons. From a theoretical point of view, however, neutrons have an advantage over photons for transmitting signals of such extremely high energy: they make somewhat less demand on the maximum energy required of the accelerator. A numerical example illustrates this point. In view of the estimates for various acceleration mechanisms in chapter 12, we would like $E_{\max}$ for the accelerator to be as small as possible consistent with the typical event energy of $\sim$ 1000 Pev, say 3×10^{18} eV for protons (1.5×10^{18} eV/nucleon for nuclei). The observed flux is $\sim 2 \times 10^{-17}$ cm^{-2}s^{-1}. With $d \approx 10$ kpc this implies $\sim 3 \times 10^{35}$ erg/s of $\sim$ 1000 TeV photons at the source (assuming isotropic emission). If the signal is induced by neutrons, their luminosity at the source must be a factor of three higher because $\exp[-d/(\gamma c \tau_n)] \sim 0.3$. The efficiency for producing the neutrons is greater than that for photons, however. For $p \to \pi^0 \to 2\gamma$, the partial efficiency for producing a photon above 0.5×10^{18} eV from a spectrum that extends only a factor 6 higher than this is (very crudely) $\sim 10^{-3}$ because the cross section for $p\,p \to \pi^0$ falls rapidly near the kinematic limit. The $p \to n$ cross section is flatter, so the efficiency for neutrons is somewhat higher, $\sim 10^{-2}$. The total energy requirement for primary protons above $\sim$ 1000 PeV would therefore be 3×10^{38} erg/s if the signal is photon-induced and a factor of 3 *lower* if it is due to neutrons.

For a flat primary spectrum (E^{-2} differential) that extends over 9 decades of energy with $E_{\max} \sim 3 \times 10^{18}$ eV, the total power requirement for the accelerator would be a factor of $\sim$ 20 higher than these numbers because of the accelerated particles below the threshold for producing the signal. This factor would be correspondingly larger for a steeper spectrum. The required *total* luminosity is therefore well over 10^{39} erg/s in both cases discussed above. This situation can be improved substantially if Cygnus X-3 is a heavy ion accelerator. The estimate for total luminosity could be reduced below 10^{38} erg/s in the most favorable case that the accelerated nuclei are completely broken down to protons and neutrons, if the neutrons escape from the source region without further interaction. The gain in efficiency for accelerated nuclei (rather than protons) results because nuclear fragmentation takes place at constant energy per nucleon.

Chapter 14

Air showers

An air shower is a cascade of particles generated by the interaction of a single high energy primary cosmic ray nucleus or photon near the top of the atmosphere. The number of particles at first multiplies, then reaches a maximum and attenuates as more and more particles fall below the threshold for further particle production. In some languages an air shower is called a "swarm" (e.g. in Italian, *sciame*) because it consists of a thin disk of relativistic particles, as shown schematically in fig. 14.1.

14.1 Particle content

A cosmic ray induced air shower has three components, electromagnetic, muonic and hadronic. (The classic discussion of this subject is contained in the reviews by Greisen, 1956 and 1960.) The shower consists of a core of high energy hadrons that continually feeds the electromagnetic part of the shower, primarily by photons from decay of neutral pions and eta particles. Each high energy photon generates an electromagnetic subshower of alternate pair production and bremsstrahlung starting at its point of injection. (Electromagnetic cascades are the subject of the next chapter.) Nucleons and other high energy hadrons contribute further to the hadronic cascade. Lower energy charged pions and kaons decay to feed the muonic component. (The competition between decay and interaction depends on energy and depth in the atmosphere, as discussed in chapters 3 and 4.)

At each hadronic interaction, slightly more than a third of the energy goes into the electromagnetic component. Since most hadrons re-interact, most of the primary energy eventually finds its way into the electromagnetic component. In addition, because of the rapid multiplication of electromagnetic cascades, electrons and positrons are the most numerous particles in cosmic ray air showers. Thus most of the shower energy is eventually dissipated by ionization losses of the electrons and positrons. It is correct to think of the atmosphere as a calorimeter to be sampled by the air shower detector. Apart from the small fraction, $F(E_0)$, of energy lost to neutrinos, the primary energy, E_0 is given by the *track length integral*,

$$(1 - F) \times E_0 \sim \alpha \times \int_0^\infty \mathrm{d}X \, N(X), \tag{14.1}$$

where $N(X)$ is the number of charged particles in the shower at depth X (measured along the shower axis) and α is the energy loss per unit path length in the atmosphere.

The number of low energy (1 to 10 GeV) muons increases as the shower develops then reaches a plateau because muons rarely interact catastrophically, but only lose energy relatively slowly by ionization of the medium. In contrast, the number of electrons and positrons declines rapidly after maximum because radiation and pair production subdivide the energy down to the critical energy ($E_c \sim 80$ MeV – see §6.4) after which electrons lose the remaining energy to ionization quickly.

14.2 Types of experiment

If the incident particle has an energy around 100 TeV or more, there are enough particles left at ground level to trigger an array of detectors deployed on a mountain (fig. 1b). (About 1000 TeV is required for a conventional array at sea level.) Lower energy showers (~TeV) can be detected with a telescope of reflectors that collects the atmospheric Cherenkov light produced by the particles high in the atmosphere, near shower maximum (fig. 1*a*). These two energy regions are sometimes referred to as very high energy (VHE, ~ TeV) and ultra-high energy (UHE, > 50 TeV).

14.2.1 Air Cherenkov experiments

In the case of air Cherenkov experiments the direction of the shower is determined by the directionality of the light pool, which is of the order of a degree. (See the review of Weekes(1988) for a discussion of this and other aspects of the air Cherenkov technique.) Since the altitude of shower maximum is of order 10 km, the light pool has an area of the order of 10^5 m^2. In order to be able to see the Cherenkov light, this type of experiment can only work on clear, moonless nights, and so has a duty cycle of less than 10%. For gamma ray astronomy, this must be reduced by another factor of 5 to 10 because any potential source will only be high enough in the sky for a limited time each day.

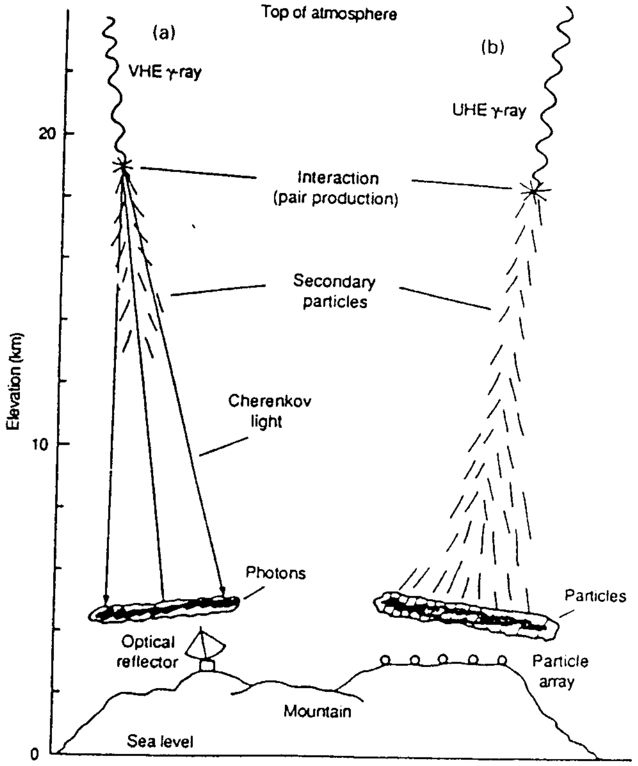

Figure 14.1: Schematic representation of air showers in two energy regions and the corresponding detectors: (*a*), $E \sim 1$ TeV, air Cherenkov telescope; (*b*) $E \sim 1$ PeV, air shower array. (From Lamb & Weekes 1987. © 1987 by AAAS.)

The cosmic ray flux above a TeV is of order 10^{-5} cm^{-2}sr^{-1}s^{-1}, so, with a nominal 10^5 m^2 collecting area, one has a counting rate of about ten showers per second in a bin of 1° angular radius. It is interesting to see what this implies about the flux level required to see a point source above this background. After observing a source for an accumulated time of 30 hours, for example, one would have a million background events and so require a signal of 3000 events to have a 3 sigma effect. This would correspond to a flux from the source of

$$\frac{3000}{10^5\,\mathrm{sec}\times 10^5\,\mathrm{m}^2} \sim 3\times 10^{-11}\,\frac{\mathrm{photons}}{\mathrm{cm}^2\,\mathrm{s}}.$$

If the source has a known period, for example, the orbital period of an X-ray binary, the sensitivity is increased correspondingly.

The energy of a cascade measured with an air Cherenkov detector must be estimated from the pulse heights of the signals in the phototubes that collect light from the reflectors. This is an experimental determination of the track length integral, but it needs to be calibrated. This is done in two complementary ways. One is simply to estimate the acceptance of the telescope (area times solid angle) and then compare the observed trigger rate to the integral cosmic ray spectrum as a function of threshold energy. The threshold energy that reproduces the observed counting rate for the assumed acceptance is the estimate of the energy threshold of the detector. The other method is to compare simulated showers with observed ones. This allows one to do a more detailed analysis (at the expense of complexity). It is possible, for example, to investigate differences between showers induced by hadrons and showers induced by photons to improve the sensitivity of a search for photons from point sources (Weekes et al., 1989).

14.2.2 Classic air shower experiments

When the incident cosmic ray nucleus has sufficient energy to generate a cascade that penetrates to ground level, some of the track length integral (14.1) is lost. Even more problematic is the fact that the classic air shower experiment only samples the shower at one depth, and then not the whole shower front but only the particles that go through the scattered detectors. Thus extensive fitting and interpolation are needed to determine the particle content and the shower energy.

Experimental determination of the primary energy on a shower by shower basis with an air shower array is limited by fluctuations in shower development. Since the shower is only sampled once, a large

range of energies can give the same shower size at the observation level, depending on whether the shower happens to develop late or early. The problem is exacerbated by sampling fluctuations. Figure 14.2 illustrates the point: a detector at sea level (~ 1100 g/cm^2 slant depth for these examples) would measure ~ 5×10^4 particles in the shower that happened to develop early, but three times as many particles in the late developing shower. A measurement of the muon content would give a better measure of primary energy because the muons are generated by decay of pions and kaons high in the atmosphere and attenuate very slowly. At ground level, the muon content is therefore about the same for showers of the same primary energy and primary nucleus independent of the stage of cascade development. The muon measurement is technically more difficult, however, because sampling problems are more severe for muons (which generally have a lower density than electrons and positrons), and the muon counters must be shielded from the more numerous $e^\pm$.

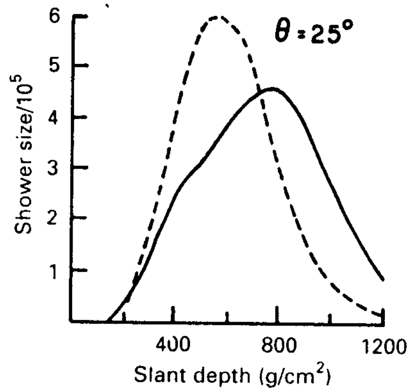

Figure 14.2: Two simulated proton showers of total energy ~ 1000 TeV.

Another reason for measuring the muon component of a shower simultaneously with its electron component is to improve the discrimination against hadron showers in a search for photons from point sources. In a shower initiated by a photon, muons are expected to be rare, less than 5% of the number in a hadron-initiated shower of comparable energy. This is because the probability of photons to produce electron-positron pairs is orders of magnitude greater than any competing process that might lead to production of muons, such as $\mu^+\mu^-$ production or photopion production. The same is true of bremstrahlung of electrons relative to any process such as $e \rightarrow e + \mu^+\mu^-$.

Because of the anomalous content of apparent signals from some point sources referred to in chapter 13, muon detection has become a focus of new and proposed experiments, such as those at Dugway, Utah and Los Alamos and several others. I will consider the question of the muon content of air showers in chapter 16.

The direction of an air shower is determined with an array of particle detectors by fast timing of the shower front. A crude estimate of the kind of resolution that one can expect comes from the following simple considerations. The characteristic lateral scale of the shower, called the Molière unit in electromagnetic cascade theory, is 50-100 m. (This is determined by the amount of multiple scattering in the pathlength needed to lose E_c and is density-dependent.) Comparing this lever arm with the few–nanosecond rise time of the "swarm" gives an estimated pointing accuracy of ~ 0.5°. In practice, it is hard to achieve this resolution, and one degree is generally considered good.

At the higher energies needed to trigger an air shower array, the cosmic ray flux – and presumably also the flux from a potential point source – is several orders of magnitude lower than for air Cherenkov detectors. On the other hand, the array can run 24 hours a day, and it accepts showers from a large solid angle window (~ 1 sr), limited only by the ability of a shower to penetrate through a large slant depth to the array. As an example, suppose there is an array with angular resolution $\delta\psi \sim 1°$, an area of 10^4 m^2 and a nominal threshold of 100 TeV. A source with a declination near the latitude of the array (so that it passes nearly overhead) would be visible ~4 hours per day or 5×10^6 seconds per year. From Eq. 12.2 the flux of primaries above 100 TeV is $\sim 8 \times 10^{-9}$ cm^{-2}s^{-1}sr^{-1}, so the background in the bin of one degree angular radius would be

$$8 \times 10^{-9} \times 10^{-3}\,\mathrm{sr} \times 10^8\,\mathrm{cm}^2 \times 5 \times 10^6\,\mathrm{s} \sim 4000.$$

It would therefore take ~200 events in the same time period to give a 3 sigma signal from the point source, for a minimum detectable flux of $\sim 4 \times 10^{-13}$ cm^{-2}s^{-1}. For a source with an E^{-2} differential spectrum this is essentially equivalent to the sensitivity of an air Cherenkov array – provided the spectrum of the source extends to > 100 TeV.

14.2.3 Signal to noise for point sources

It is also instructive to look at the general expression for signal to noise as a function of the spectral index of a point source and of the parameters of the detector. Consider a point source with an integral power law spectrum $\propto E^{-\gamma_*}$. The ratio is

$$\frac{\mathrm{signal}}{\mathrm{noise}} \propto \frac{E^{-\gamma_*} \times A \times T}{\sqrt{E^{-\gamma} \times A \times T \times \pi \times (\delta\psi)^2}} \propto E^{\gamma/2-\gamma_*} (A\,T)^{1/2} (\delta\psi)^{-1}, \tag{14.2}$$

where γ is the integral spectral index of the background cosmic ray spectrum. Signal to noise only improves with the square root of exposure ($A \times T$), but it improves linearly as the angular resolution is made better (smaller $\delta\psi$). Equation (14.2) can be used to compare the sensitivity of different detectors (and the energy dependence of the sensitivity of a given detector) *provided* the exposure factors and angular resolutions and their energy dependences are known.

14.2.4 Fly's Eye experiment

The concept for a novel air shower experiment that would follow the longitudinal development of individual cascades was suggested by Greisen (1960) and independently by others in the 1960's (see Sokolsky, 1988). The idea is to detect nitrogen fluorescence light excited by the ionization trail of the shower. The experiment was realized by the Fly's Eye detector at Dugway, Utah (Baltrusaitas et al., 1985). The detector consists of two arrays of parabolic mirrors, each mirror viewed by a bank of phototubes in its focal plane. Each array maps the sky with each phototube forming a pixel. (The second "eye" covers only part of the sky.) By timing the atmospheric scintillation light radiated by a shower as it passes overhead, the shower trajectory can be reconstructed. Once the distance and orientation of the line source of scintillation light is known, the signal in each phototube can be converted into a power radiated along the portion of the trajectory in the field of view of that tube. This requires knowing the number of scintillation photons per meter of pathlength and the attentuation of the atmosphere and the detection efficiency at the phototube. The sum of all contributions then gives directly the path lengh integral, and the energy can be determined on a shower by shower basis. Trajectories pointing near the array cannot be analyzed in this way because the isotropically emitted scintillation or flourescence is swamped by direct Cherenkov light. (Fly's Eye can, however, be used as a high energy atmospheric Cherenkov detector for showers with energies > 100 TeV.)

The threshold for the current (1988) version of Fly's Eye is in the range of 10^{17} eV, with a peak response around 10^{18} eV, when folded with the primary spectrum. This is a noteworthy energy for two reasons. As discussed in §13.7 it is the energy above which a neutron can travel a distance approximately equal to the radius of the galactic disk before it decays, so that "neutron astronomy" becomes a possibility (Jones, 1988). Secondly it corresponds to a center of mass energy of $\sqrt{s} \sim 40$ TeV, the design goal of the SSC. Sokolsky (1988) discusses the Fly's Eye and its application to high energy physics and astrophysics.

14.3 Basic features of cascades

I will discuss further details of both photonic and hadronic air showers in later chapters, including results of detailed computer simulations. For orientation I summarize here some simple general considerations.

14.3.1 General form of solution

Recall that the particle content of an air shower (number of particles of each species as a function of E and X) is given by the solution of the coupled cascade equations (3.17) subject to the delta function boundary condition (3.7). If the transfer functions, F_{ji} scale (see (3.12)), then there is no dimensional quantity in the problem and the dimensionless quantity, $E_i N_i(E_i, E_0, X)$ must be a function only of the ratio $\xi_i \equiv E_i/E_0$. Let us call this dimensionless function

$$\mathcal{F}_i(\xi_i, X) \equiv E_i\, N_i(E_i, E_0, X). \tag{14.3}$$

The yield function, $\mathcal{F}_i$, gives the number of particles of type i per logarithmic interval of fractional energy. The yield depends only on the ratio of the particle energy, E_i, to the total energy, E_0, of the air shower. This result holds only to the extent that scaling is valid and only when decay and continuous energy loss can be neglected. It is approximately valid for high energy hadrons and for electrons and photons with $E > E_c$ in air showers.

It is interesting to express the differential flux, $N_i(E_i, X)$ that results from a spectrum of primary particles in terms of $\mathcal{F}$. It is

$$N_i(E_i, X) = \int_0^1 N_0(E_i/\xi_i)\, \mathcal{F}(\xi_i, X)\, d\xi_i, \tag{14.4}$$

where $N_0(E_0)$ is the differential spectrum of primary particles. For a power law spectrum, $N_0(E_0) \propto E^{-(\gamma+1)}$ and

$$N_i(E_i, X) = N_0(E_i) \int_0^1 \xi_i^{\gamma-1}\, \mathcal{F}(\xi_i, X)\, d\xi_i. \tag{14.5}$$

Note the similarity between the role of a whole cascade (represented here by $\mathcal{F}$) and the role of individual interactions in the spectrum weighted moments given by (3.15). The integral in (14.5) is a spectrum weighted moment of a whole cascade. In fact, in the late 40's it was not clear experimentally whether elementary multiple production occurs at all or whether events with more than one created pion required interactions of the projectile with several separate target nucleons inside a nucleus. This is the question of "multiple" *versus* "plural" production discussed by Heitler (1949) and others in the same volume of *Reviews of Modern Physics.*

14.3.2 Toy model

A very simple model due to Heitler (1944) illustrates some general features of air showers. Heitler introduced the model in his book on quantum theory of radiation in the context of a discussion of purely electromagnetic cascades, but its basic structure applies also to air showers initiated by hadrons.

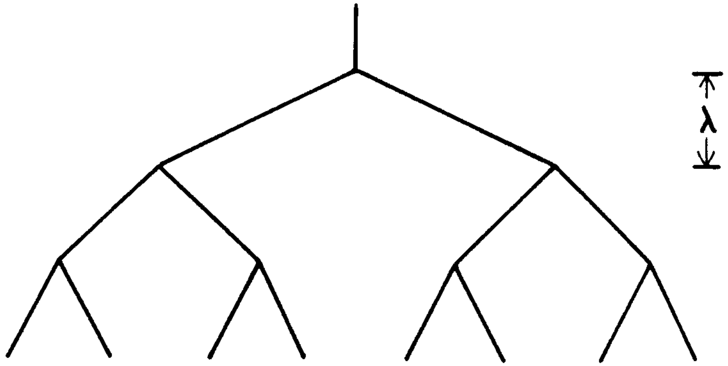

Figure 14.3: Simple branching model of an air shower.

Consider the branching process shown in fig. 14.3. Each line segment can be thought of as a particle or as a packet of energy. At each vertex the energy on a line is split in two. Branching occurs after one collision length, λ, for whatever the splitting process is. After

$n = X/\lambda$ branchings the number of segments is

$$N(X) = 2^{X/\lambda},$$

where X is the slant depth along the shower axis (fig. 3.1). At depth X the energy per "particle" is

$$E(X) = E_0/N(X).$$

The splitting continues until $E(X) = E_c$, a critical energy for the splitting process. After this the "particles" only lose energy, get absorbed or decay (depending again on what the physics is).

The number of particles at shower maximum in this model is

$$N(X_{\max}) = E_0/E_c, \qquad (14.6)$$

and

$$X_{\max} = \lambda \frac{\ln(E_0/E_c)}{\ln 2}. \qquad (14.7)$$

The basic features of (14.6) and (14.7) hold for high energy electromagnetic cascades and also, approximately, for hadronic cascades; namely

$$N_{\max} \propto E_0 \text{ and } X_{\max} \propto \ln(E_0). \qquad (14.8)$$

14.4 Nuclear primaries

One of the main problems of air shower physics is to determine the chemical composition of the primary cosmic ray nuclei in the energy range above 100 TeV. The flux is so low at these high energies that the composition has not been determined with detectors flown at the top of the atmosphere. To use measured properties of air showers for this purpose we first need to know how showers generated by heavy nuclei differ from those initiated by protons or light nuclei.

The simplest model, which is adequate for many purposes, is the superposition model. Here it is assumed that a nucleus of mass A and total energy E_0 is equivalent to A independent nucleons each of energy E_0/A. What is crucial for development of an air shower initiated by a nucleus is the distribution of points of first interaction of each nucleon. By this I mean the point at which each nucleon first interacts inelastically with a target nucleus. This may or may not occur when the nucleon is released from the nucleus. The superposition model assumes that the distribution of first interactions is the same as if the nucleons had entered the atmosphere separately; i.e.,

$$\frac{dP_1}{dX} = \exp[-X/\lambda_N], \qquad (14.9)$$

where, as usual, λ_N is the nucleon interaction length in air.

In the superposition model, (14.6) is unchanged, but (14.7) becomes

$$X_{\max} \propto \lambda \ln[E_0/(A\,E_c)].$$

In other words, showers generated by heavy primaries develop more rapidly on average (i.e., higher in the atmosphere) than proton showers of the same total energy. On the other hand, the effect is only logarithmic, so it is clear, given the nature of air shower experiments, that the best one can hope for is to be able to distinguish among groups of nuclei with quite different masses. In practice, even this has proved difficult. Another important distinguishing feature of showers generated by heavy nuclei is that fluctuations in their longitudinal development are smaller than those of light nuclei. This is simply because each nucleus is a beam of many incident nucleons.

In reality what happens when a heavy nucleus enters the atmosphere is that it interacts very quickly (recall, for example, that $\lambda \sim 2.3$ g/cm^2 for an iron nucleus). In this first collision, however, only a few of the nucleons in the nucleus interact inelastically with an air nucleus to create secondary pions. Several other nucleons and light nuclear fragments may also be released, and there will generally be one heavy fragment. By studying fragmentation histories of nuclei in photographic emulsion and the multiplicities of secondary particles produced in the various fragmentation events, it is possible to build up a more realistic picture of how nuclei break up in the atmosphere and when their constituent nucleons first interact. The procedure is complicated and very approximate, but it serves to give an indication of the reliability of the superposition model. One complication with the analysis is that a subset of the interactions that correspond with interactions on the light nuclei in the emulsion must be selected since the atmosphere consists almost entirely of light nuclei. Another is that there may be a selection bias for events with higher multiplicity. As a consequence, the estimate of the number of nucleons that interact to produce pions may be somewhat overestimated. Figure 14.4 shows the distribution of points of first interaction for the superposition model as compared to that inferred from the data. The distributions become steeper at higher energy because of the increase with energy of the nucleon cross section.

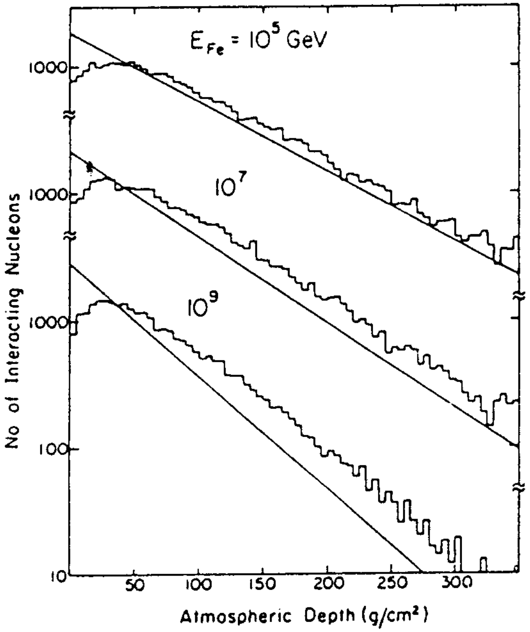

Figure 14.4: Distribution of points of first interaction for nucleons in iron nuclei. Histograms: inferred from data in photographic emulsion. Lines: superposition model. (From T.K. Gaisser, T. Stanev, P. Freier and C.J. Waddington, 1982.)

In the preceding discussion I have assumed that the collective effects of two or more nucleons in a nucleus acting coherently to produce pions can be neglected. Such effects are probably important only at the edge of phase space and should therefore not make an important contribution to shower development. The general idea of reducing a nucleus–nucleus collision to a series of nucleon–nucleon collisions is called the "wounded nucleon" picture. A simplified version can be constructed directly from Eq. 5.1. In collisions between single nucleons and nuclei of mass A, the mean number of wounded nucleons in the target (i.e. the number of nucleon–nucleon collisions) is

$$\langle N\rangle_{pA} = \frac{A\,\sigma_{pp}}{\sigma_{pA}}.$$

For a nuclear projectile of mass A incident on a target nucleus of mass B the generalization is (Bialas, Bleszynski & Czyz, 1976)

$$\langle N\rangle_{AB} = \frac{A\,\sigma_{pB}}{\sigma_{AB}} + \frac{B\,\sigma_{pA}}{\sigma_{AB}}.$$

The first term is the number of wounded nucleons in the projectile and the second the number of wounded nucleons in the target. This simple geometrical result predicts that a somewhat larger fraction of the freed nucleons interact to produce pions than the analysis of emulsion data described above.

> **Problem:** Show that the expression (5.1) for the absorptive proton–nucleus cross section can be developed as a sum of partial cross sections for exactly N wounded nucleons:
>
> $$\sigma_{pA} = \sum_{N=1}^{\infty} \sigma_N,$$
>
> where
>
> $$\sigma_N = \int d^2b \frac{[\sigma\,T(b)]^N}{N!} \exp[-\sigma T(b)],$$
>
> and σ is the nucleon-nucleon cross section. Calculate the mean number of wounded nucleons in this approximation.

14.5 Coincident multiple energetic muons

Before embarking on a more detailed discussion of cascade calculations in the next few chapters, I describe here the case of coincident, multiple muons detected with a large, deep detector. Because the muons must have high energy at production in the atmosphere to penetrate to a deep underground detector, only the highest energy parts of the cascades are relevant. These events therefore illustrate some of the principle questions of air shower physics in a particularly clear way. The questions include the problem of the chemical composition of the primary cosmic rays above 100 TeV, which has not been measured directly because of the extremely low flux at high energy. Interpretation of the results also depends on details of hadronic interactions at high energies, particularly the transverse momentum distribution, which determines the fraction of the muons above threshold that falls within the detector. The amount of charm production may also be important because charmed mesons are a source of prompt muons.

In addition, the problem illustrates, again in a simple way, technical aspects such as event sampling: What is the probability that an event with two or three muons in the detector is a low energy shower with its trajectory through the detector or a large shower whose fringe was detected? There is currently a great deal of experimental activity in this field.

14.5.1 Number of high energy muons

Calculation of the number of muons in an air shower follows the same steps as the calculation of the flux of uncorrelated atmospheric muons in §6.1. One starts with the spectrum of decaying pions, given by (4.2), and a similar expression for kaons. The spectrum of decaying pions in an air shower with zenith angle θ is

$$\mathcal{D}_\pi = \frac{\epsilon_\pi}{E_\pi\, X\, \cos\theta}\,\frac{\mathcal{F}_\pi(\xi_\pi, X)}{E_\pi}, \tag{14.10}$$

where $\mathcal{F}$ is the scaled distribution of (14.3). As long as $E_\mu \gg \epsilon_\pi \sim$ 115 GeV, pion decay can be neglected in computing $\mathcal{F}$. Generally we will be interested in muons with energies in the TeV region and above, so this condition is approximately valid even for the contribution from kaons. The muon production spectrum is given by an integral like (6.2) over the spectrum of decaying pions,

$$\frac{\mathrm{d}N_\mu}{\mathrm{d}E_\mu \mathrm{d}X} = \frac{\epsilon_\pi}{E_0\,\cos\theta}\,\frac{1}{E_0}\int_{\xi_\mu}^{\xi_\mu/r_\pi} \frac{\mathcal{F}_\pi(\xi_\pi, X)}{X\,(1-r_\pi)}\,\frac{\mathrm{d}\xi_\pi}{\xi_\pi^3}, \tag{14.11}$$

where $\xi_\mu = E_\mu/E_0$.

To get the total number of muons produced by the shower, we now integrate (14.11) over X. Since production of high energy muons takes place high in the atmosphere, it is safe to extend the X integration to ∞. This leads to an expression for the differential flux of high energy muons in the shower deep in the atmosphere of

$$\frac{\mathrm{d}N_\mu}{\mathrm{d}E_\mu} = \frac{\epsilon_\pi}{E_0\,\cos\theta}\,\frac{1}{E_0}\,F(\xi_\mu), \tag{14.12}$$

where $F(\xi_\mu)$ is the integral over X of the integral in (14.11). (There is a similar term for the contribution from kaons.)

We will be interested in all muons that have high enough energy when they are produced in the atmosphere to be able to penetrate to the depth of the detector. This minimum energy is given approximately by (6.18) (in which X is the slant depth between the surface and the deep detector and $\xi = \epsilon/\alpha \sim 2.5 \times 10^5$ g/cm^2 of rock). The total number of muons above a minimum energy E_μ is obtained by integrating (14.12) over all muon energies above E_μ up to the primary energy:

$$N_\mu(> E_\mu) = \frac{\epsilon_\pi}{E_\mu\,\cos\theta}\,\xi_\mu \int_{\xi_\mu}^{1} F(z)\mathrm{d}z. \tag{14.13}$$

Equation (14.13) shows that the average number of muons in a shower front at the depth of a detector should depend only on the ratio of the muon threshold energy to the primary energy of the incident proton that initiated the shower, apart from the explicit factor $(E_\mu \cos\theta)^{-1}$.

Elbert (1978) suggested a form for parameterizing the mean number of high energy muons in an air shower. Several different Monte Carlo cascade calculations (Elbert et al., 1983, Gaisser & Stanev, 1985, Forti, 1988) with somewhat different hadronic event generators give results in good agreement with this form and with nearly identical parameters. The formula (Elbert, 1978) is

$$\langle N_\mu \rangle \approx A \times \frac{0.0145\,\mathrm{TeV}}{E_\mu\,\cos\theta}\left(\frac{E_0}{A\,E_\mu}\right)^{0.757}\left(1 - \frac{A\,E_\mu}{E_0}\right)^{5.25}. \tag{14.14}$$

I have used the superposition model for nuclear primaries in writing (14.14) in terms of the total energy and mass of the primary nucleus.

It is instructive to compare (14.14) to the result of Heitler's simple model, which gives $N_\mu(> E) \propto E_0/E$. Here the number of high energy muons increases less quickly with energy. The reason for this is that, as the primary energy increases, the cascade penetrates deeper into the atmosphere before reaching the energy $\sim E_\mu$. But then the atmosphere is more dense and the probability that the parent pions decay rather than interact is smaller. The factor $(1 - A\,E_\mu/E_0)^{5.25}$ reflects the inclusive cross section for pion production, which vanishes near the kinematic limit. This factor only comes into play when the threshold is high enough and the primary energy low enough so that the muons must have a large fraction of the energy of the nucleon interaction in which they were produced.

14.5.2 Muon bundles underground

The result of calculations of muon production in air showers followed by propagation of the high energy muons through the rock is that the mean number of muons at the depth of a detector can be represented by a form like (14.14) with the parameter E_μ given by

$$E_\mu \;=\; 0.53\,\mathrm{TeV} \times (e^{0.4X} \;-\; 1), \tag{14.15}$$

where X in this subsection is the slant depth of the detector in kilometers of water equivalent (km.w.e.). This is essentially (6.18). (Sometimes the notation hg/cm^2 is used. One km.w.e. is 1000 hg/cm^2.) The values of minimum muon energy at the surface needed to penetrate to various underground detectors are given in table 6.1.

It is also possible to parameterize the multiplicity distribution of the muons at the depth of the detector as well as their lateral distribution. These are somewhat more dependent on the model of hadronic interactions. With an interaction model that includes details of multiplicity distributions, transverse momentum distributions and their correlations as measured in proton–antiproton collisions at the CERN collider ($\sqrt{s}$ = 200 → 900 GeV), Forti (1988) has found the multiplicity distribution and lateral distributions at the depth of an underground detector. The multiplicity distribution is (Bilokon et al., 1990)

$$P(N_\mu) \;=\; \left[\begin{array}{c} N_\mu + k - 1 \\ N_\mu \end{array}\right] \left(\frac{< N_\mu > /k}{1 + < N_\mu > /k}\right)^{N_\mu} \left(\frac{1}{1 + < N_\mu > /k}\right)^{k}, \tag{14.16}$$

where the square brackets indicate the binomial coefficient and

$$k \;=\; A^{\frac{2}{3}}\; \exp[1.72 \;+\; 0.33\; \ln(< N_\mu > /A) \;+\; 0.026\; \ln^2(< N_\mu > /A)]. \tag{14.17}$$

This multiplicity distribution is close to a Poisson, but has an excess of events relative to the Poisson distribution at high multiplicity (the "high multiplicity tail").

The lateral distribution is of the form (Bilokon et al., 1990)

$$\frac{1}{N_\mu}\,\frac{\mathrm{d}N_\mu}{\mathrm{d}r} \;=\; C\,\frac{r}{(r \;+\; r_0)^\alpha}, \tag{14.18}$$

where the normalization constant $C = (\alpha - 1)(\alpha - 2)/r_0^{2-\alpha}$ and $\langle r\rangle = 2r_0/(\alpha - 3)$. These parameters give a good description of the lateral distribution of the muons for a range of depths and primary energies when

$$\langle r\rangle \;=\; -0.913\, E_\mu^{-1.745} \;+\; 12.34\, E_\mu^{-0.714}\, (\frac{A\, E_\mu}{E_0})^{0.11} \times \sec\theta, \tag{14.19}$$

and

$$\alpha \;=\; \left(\frac{1.138}{-1.126 + \langle r\rangle} \;+\; 0.848\right) \tag{14.20}$$
$$\times \exp\{2.413 \;-\; 0.113 \ln(E_0/A) \;+\; 0.0050[\ln(E_0/a)]^2\}$$

In these equations, E_μ is in TeV, r in meters and X in km.w.e.

Parameterizations of this kind can be used as the basis of a simplified simulation to estimate rates of coincident multiple muons in underground detectors (Gaisser & Stanev, 1985). The procedure is to select a primary nucleus from an assumed spectrum and calculate the E_μ at the surface needed to give a muon that penetrates to the detector. (Note that the slant depth and hence E_μ depends in general both on the azimuth and zenith angle of the selected shower trajectory.) Then $\langle N_\mu\rangle$ is calculated from (14.14) and N_μ from (14.16). For each of the N_μ muons the perpendicular distance from the core is selected from the distribution (14.18). The cores must be dropped randomly relative to the detector to finish the simulation.

14.5.3 Sensitivity to composition

The dependence on the mass of the primary nucleus is displayed explicitly in (14.14). For low energies, because of the threshold factor, heavy nuclei will be less prolific than protons at producing high energy muons. On the other hand, when $E_0 \gg A\, E_\mu$, the threshold factor is approximately one and

$$N_\mu(> E_\mu) \;\propto\; A^{0.243}.$$

The mean number of muons from showers initiated by protons is compared with the corresponding quantity for showers initiated by iron nuclei in fig. 14.5.

As an example, I show in fig. 14.6 a comparison made by Bologna et al. (1985) between the distribution of muon multiplicities measured with the NUSEX detector and the calculated distributions for several different models of the primary spectrum and composition. Model 1 is essentially the composition measured at low energy (column 4 of table 1.1). All components of the spectrum are assumed to steepen from integral spectral index $\gamma = 1.71$ to $\gamma = 2.0$ at 2×10^6 GeV. Model 2 has a constant composition at low energy with a steepening from $\gamma = 1.71$ to 2.0 at a rigidity $R = 2\times10^6$ GV. Since the total energy per nucleus is

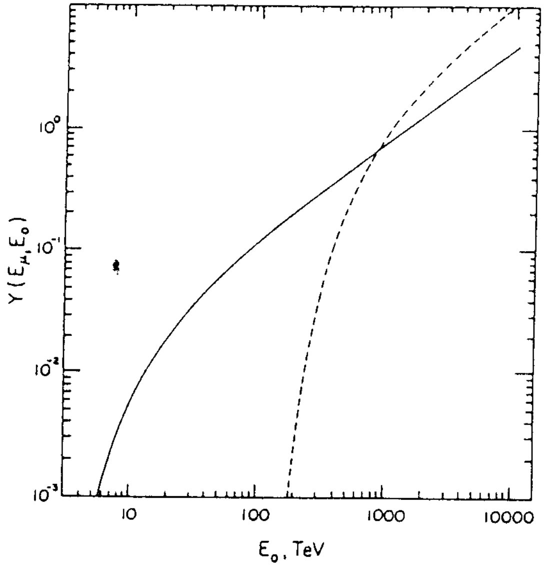

Figure 14.5: Muon yields from primary protons (solid line) and iron nuclei (dashed line) at a slant depth of 4 km.w.e. From Gaisser & Stanev, 1985.

related to rigidity by $E \approx (A/2)\, R$ for nuclei heavier than protons, this spectrum becomes progressively richer in heavy nuclei at high energy (see §16.3 for further discussion of this point). In model 3 the fraction of iron group nuclei (VH) increases linearly with energy from 1 TeV per nucleus until it saturates at 65% above 2000 TeV per nucleus. Model 4 has a still larger fraction of heavy nuclei at high energy. The iron-rich composition was originally suggested by Goodman et al. (1979) to account for the large number of delayed hadrons they observed near air shower cores. Data on gamma families, discussed in §4, have also been interpreted as suggesting heavy composition at high energy (Ren, et al., 1988). An increased fraction of iron group or other heavy nuclei around 10^6 GeV is consistent with the observed flatness of the spectrum of iron nuclei at lower energy. In fact, however, the question of the composition of the primary cosmic rays above 100 TeV is one that is still unsolved and the subject of much debate. Indeed, arguments can be made that the high energy cosmic rays are mostly protons (Fichtel and Linsley, 1986). The subject of composition in this energy region is discussed further in §16.4.

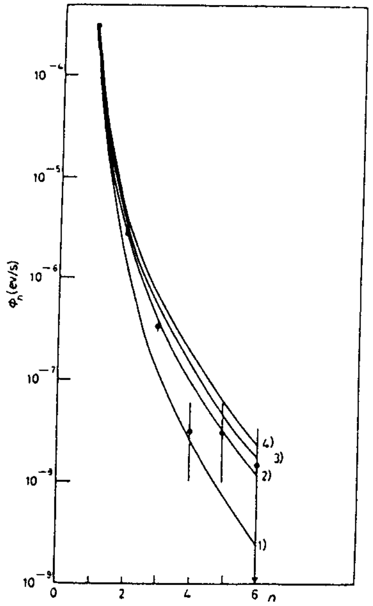

Figure 14.6: Muon multiplicities deep underground measured with the NUSEX detector and compared to four models of primary spectrum/composition (from Bologna et al., 1985). (© Società Italiana di Fisica.)

Despite large differences between some of the models used for the comparison in fig. 14.6, it is difficult to reach a definite conclusion about composition on the basis of these multiple muon measurements. There are two reasons for this. First, the NUSEX detector is rather small, a cube 3.5 meters on a side, so that only a small fraction of the muons in a high multiplicity event is typically seen by the detector. The lateral separation of the muons at the detector depends on the transverse momentum distribution of the parent mesons, as well as on their height of production. What is needed is a good knowledge of the transverse momentum distribution of the energetic secondaries (forward fragmentation region) of hadronic interactions. As discussed in §5.4, this is not directly measured in collider experiments. The second difficulty is that the multiplicity distribution underground involves a convolution of muon production with the energy spectrum as well as with the composition. It is possible to improve the sensitivity of an undergound detector to primary composition by using a larger area, which includes a larger fraction of each event and thus decreases somewhat the dependence on transverse momentum. It is also possible to get some information about the primary energy of each event by measuring the shower at the surface in coincidence with the underground measurement. Both are being done in some current experiments, for example, at Gran Sasso, Homestake and Soudan.

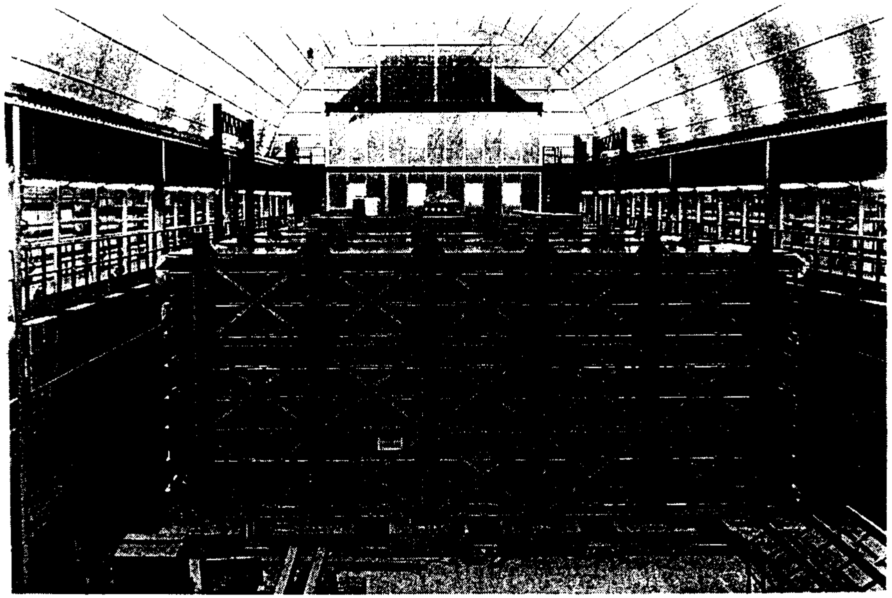

View of three supermodules of the MACRO detector in place inside Hall B of the Gran Sasso Underground Laboratory in Italy. The visible end of the detector is 12 m wide and 5 m high. The experimental hall is 17 m high and 110 m long. (Photo courtesy of Sergio Petrera.)

Chapter 15

Electromagnetic cascades

Electromagnetic cascade theory was developed in the late 30's after the discovery of the positron (1932), in response to the discovery of cascade showers. The classic treatment of the subject is that of Rossi and Greisen (1941), which remains an exceedingly clear and elegant paper to read. The techniques for Monte Carlo simulation of electromagnetic cascades were developed by Butcher & Messel (1960), and many codes exist for implementing electromagnetic cascade calculations.

I shall review this well developed subject here for three reasons. First it is a nice illustration of the type of coupled cascade equations considered earlier in this book. Second, it is useful to summarize the notation of cascade theory and the definition of quantities such as shower age. Finally, the subject of muons in photon-induced air showers has become important in recent years in connection with gamma-ray astronomy at air shower energies. If electromagnetic cascades behave as expected, a measurement of the muon or hadron content of a shower should be a very good way to enhance the signal to noise ratio by rejecting showers with muons. On the other hand, there have been indications that signals from point sources, presumably photon-induced, nevertheless contain many muons. It is necessary to have the standard electromagnetic cascade theory at hand before considering how it is to be modified to include production of muons and other particles.

15.1 Pair production and bremsstrahlung

The basic high energy processes that make up an electromagnetic cascade shower are pair production and bremsstrahlung. Feynman diagrams for these processes are shown in fig. 2.3, and the basic formulas are due to Bethe and Heitler (1934). The shower energy is eventually dissipated by ionization of the medium by all the electrons and positrons in the cascade. (Recall the track length integral of chapter 14.) As long as we consider particles with energies large compared to the critical energy, however, collision losses, and also Compton scattering, can be neglected in calculating the development of the cascade. Since both pair production and bremsstrahlung occur in the field of an atomic nucleus, the processes will be screened by the atomic electrons for impact parameters larger than the radius of the atom. For high energy electrons and photons, atomic screening provides the upper cutoff to the impact parameter for all relevant frequencies in the processes. (See Chapter 15 of Jackson, 1962, for a discussion of screening in the context of his semiclassical treatment of bremsstrahlung.) This is called the "complete screening" limit, and applies for electrons in air at energies above ~ 40 MeV. The high energy approximation with complete screening and neglect of collision losses and Compton scattering is approximation A of electromagnetic cascade theory. In this approximation, which is all we consider here, the transfer functions that appear in the cascade equations scale.

The probability for an electron of energy E to radiate a photon of energy $W = vE$ in traversing $\mathrm{d}t = \mathrm{d}X/X_0$ of atmosphere is $\phi(E,v)\mathrm{d}t\mathrm{d}v$, with

$$\phi(E,v) \to \phi(v) = v + \frac{1-v}{v}\left(\tfrac{4}{3} + 2b\right). \qquad (15.1)$$

The radiation length for electrons in air (called X_0 here) is 37.1 g/cm^2, and

$$b \equiv \left(18 \ln[183/Z^{1/3}]\right)^{-1} \approx 0.0122.$$

The energy loss rate due to bremsstrahlung is therefore

$$\frac{\mathrm{d}E}{\mathrm{d}X} = -\frac{1}{X_0}\int_0^1 (vE)\,\phi(v)\mathrm{d}v = -\frac{1}{X_0}E \times (1+b) \approx -\frac{E}{X_0}, \qquad (15.2)$$

as given in (6.15).

The corresponding expression for pair production is the probability, $\psi(W,u)\mathrm{d}t\mathrm{d}u$ that a photon produces a pair in which the positron, say, has energy $E = uW$. In approximation A,

$$\psi(W,u) \to \psi(u) = \tfrac{2}{3} - \tfrac{1}{2}b + \left(\tfrac{4}{3} + 2b\right)\left(u - \tfrac{1}{2}\right)^2. \qquad (15.3)$$

Unlike the case for bremsstrahlung, which has the characteristic infrared divergence, the pair production probability can be integrated to get the total probability for pair production per unit radiation length. It is

$$1/\lambda_{\mathrm{pair}} = \int_0^1 \psi(u)\,\mathrm{d}u = \tfrac{7}{9} - \tfrac{1}{3}b \approx \tfrac{7}{9}. \qquad (15.4)$$

Since there are N_A/A target nuclei per g/cm^2, the cross section per target nucleus for pair production is

$$\sigma_{\gamma\to e^+e^-} \approx \frac{7}{9}\left(\frac{A}{N_A X_0}\right) \approx 500\,\frac{\mathrm{mb}}{\text{air nucleus}}. \qquad (15.5)$$

The cross section for bremsstrahlung,

$$\frac{1}{\lambda_{\mathrm{brems}}} = \int_0^1 \phi(v)\mathrm{d}v, \qquad (15.6)$$

is logarithmically divergent at $v \to 0$. This infrared divergence requires special care when the distributions (15.1) and (15.3) are used as the basis of a Monte Carlo calculation. Basically, a simulation consists of choosing randomly the distance a photon (or electron) propagates from an exponential distribution with characteristic length λ_{pair} (or λ_{brems}), then splitting the energy randomly according to the distribution (15.3) for pair production, or (15.1) for bremsstrahlung. A cutoff procedure must be introduced for bremsstrahlung to handle the infrared divergence. The procedure must be tailored to the application, but basically it consists of using a cutoff, v_{min}, chosen so that $v_{\mathrm{min}}E_0 \ll E_{\mathrm{th}}$, where E_{th} is the lowest energy of interest in the problem[1] (Butcher & Messel, 1960). At low energies, incomplete screening, energy loss by ionization and Coulomb scattering must also be included.

---

[1] Care must be taken to account correctly for the energy dissipated by particles below threshold.

15.2 Cascade equations

The coupled cascade equations for electromagnetic cascades are, in analogy to (3.17),

$$\frac{\mathrm{d}\gamma}{\mathrm{d}t} = -\frac{\gamma(W,t)}{\lambda_{\text{pair}}} + \int_W^\infty \pi(E',t)\,\frac{\mathrm{d}n_{e\to\gamma}}{\mathrm{d}W\,\mathrm{d}t}\,\mathrm{d}E' \tag{15.7}$$

and

$$\frac{\mathrm{d}\pi}{\mathrm{d}t} = -\frac{\pi(E,t)}{\lambda_{\text{brems}}} + \int_E^\infty \pi(E',t)\,\frac{\mathrm{d}n_{e\to e}}{\mathrm{d}E\,\mathrm{d}t}\,\mathrm{d}E' + 2\int_E^\infty \gamma(W',t)\,\frac{\mathrm{d}n_{\gamma\to e}}{\mathrm{d}E\,\mathrm{d}t}\,\mathrm{d}W', \tag{15.8}$$

where $\gamma(W,t)\mathrm{d}W$ is the number of photons in $\mathrm{d}W$ at depth t and $\pi(E,t)\mathrm{d}E$ is the number of $e^\pm$ in $\mathrm{d}E$ at depth t. For energies large compared to the critical energy, collisional losses and Coulomb scattering can be neglected and the scaling functions (15.1) and (15.3) can be used. This is *Approximation A*. With the identifications,

$$E'\frac{\mathrm{d}n_{e\to\gamma}}{\mathrm{d}W\,\mathrm{d}t} = \phi(\frac{W}{E'}),$$

$$W'\frac{\mathrm{d}n_{\gamma\to e}}{\mathrm{d}E\mathrm{d}t} = \psi(\frac{W}{W'}) \tag{15.9}$$

and

$$E'\frac{\mathrm{d}n_{e\to e}}{\mathrm{d}E\mathrm{d}t} = \phi(1-\frac{E}{E'}),$$

the cascade equations (15.7) and (15.8) can be written in scaling form:

$$\frac{\mathrm{d}\gamma}{\mathrm{d}t} = -\frac{\gamma}{\lambda_{\text{pair}}} + \int_0^1 \pi(\frac{W}{v},t)\phi(v)\frac{\mathrm{d}v}{v} \tag{15.10}$$

and

$$\frac{\mathrm{d}\pi}{\mathrm{d}t} = -\frac{\pi}{\lambda_{\text{brems}}} + \int_0^1 \pi(\frac{E}{1-v},t)\phi(v)\frac{\mathrm{d}v}{1-v} + 2\int_0^1 \gamma(\frac{E}{u},t)\psi(u)\frac{\mathrm{d}u}{u}. \tag{15.11}$$

The first two terms in (15.11) must be combined, with the help of (15.6), to remove the infrared divergence at $v \to 0$.

15.2.1 Power law solutions

For incident power law spectra, the solutions of (15.7) and (15.8) have the form

$$\gamma(W,t) = f_\gamma(t)W^{-(s+1)} \quad\text{and}\quad \pi(E,t) = f_\pi(t)E^{-(s+1)}.$$

Substituting these forms into (15.7) and (15.8) and changing to scaled energy variables gives

$$f'_\gamma(t) = -f_\gamma(t)/\lambda_{\text{pair}} + f_\pi(t)\int_0^1 v^s\phi(v)\mathrm{d}v \tag{15.12}$$

and

$$f'_\pi(t) = -f_\pi(t)\int_0^1 [1-(1-v)^s]\phi(v)\mathrm{d}v + f_\gamma(t)2\int_0^1 u^s\psi(u)\mathrm{d}u. \tag{15.13}$$

Note how the infrared divergence cancels in the first term of (15.13).

The integrals in (15.12) and (15.13) are spectrum weighted moments for electromagnetic processes. (The integrals have $x^{\gamma-1}$ in (3.15) replaced by v^s because the inclusive cross section for hadrons, $F_{ij}(x) \propto x\mathrm{d}n/\mathrm{d}x$, is replaced by $\phi(v) \propto \mathrm{d}n/\mathrm{d}v$, etc.) Table 15.1 gives some values for the integrals and shows the conventional notation of electromagnetic cascade theory (Rossi & Greisen, 1941). In terms of these definitions, (15.12) and (15.13) may be rewritten as

$$\left[\frac{\mathrm{d}}{\mathrm{d}t} + \sigma_0\right] f_\gamma(t) - C(s)\,f_\pi(t) = 0 \tag{15.14}$$

and

$$\left[\frac{\mathrm{d}}{\mathrm{d}t} + A(s)\right] f_\pi(t) - B(s)\,f_\gamma(t) = 0. \tag{15.15}$$

Both $f_\pi(t)$ and $f_\gamma(t)$ satisfy the same second order differential equation,

$$f'' + (A+\sigma_0)f' + (A\sigma_0 - BC)\,f = 0, \tag{15.16}$$

which has *elementary solutions* of the form $f \propto \exp(\lambda t)$, where $\lambda(s)$ satisfies the quadratic equation obtained by substitution of the exponential form into (15.16),

$$\lambda^2 + (A+\sigma_0)\,\lambda + (A\sigma_0 - BC) = 0. \tag{15.17}$$

The roots of (15.17) are

$$2\lambda_1(s) = -[A(s)+\sigma_0] + \{[A(s)-\sigma_0]^2 + 4B(s)C(s)\}^{\frac{1}{2}} \tag{15.18}$$

Table 15.1: Definitions used in cascade theory.

Quantity	Conventional notation	s=1.0	s=1.7
$1/\lambda_{\text{pair}}$	$\sigma_0 \approx 7/9$	0.774	0.774
$\int_0^1 [1-(1-v)^s]\phi(v)\,\mathrm{d}v$	$A(s)$	1.0135	1.412
$2\int_0^1 u^s \psi(u)\,\mathrm{d}u$	$B(s)\ (= Z_{\gamma\to e})$	0.7733	0.5842
$\int_0^1 v^s \phi(v)\,\mathrm{d}v$	$C(s)\ (= Z_{e\to\gamma})$	1.0135	0.5666
Root of Eq. 15.17	$\lambda_1(s)$	0.0	-0.435
Root of Eq. 15.17	$\lambda_2(s)$	-1.7868	-1.751

and

$$2\lambda_2(s) \;=\; -[A(s)+\sigma_0] - \{[A(s)-\sigma_0]^2 + 4B(s)C(s)\}^{\frac{1}{2}}. \qquad (15.19)$$

The solutions, $f_\gamma(t)$ and $f_\pi(t)$, are linear combinations of the elementary solutions $\exp[\lambda_1 t]$ and $\exp[\lambda_2 t]$ appropriate for the boundary conditions at injection.

Problem: Show that, for a spectrum of injected photons, $\gamma(W,0) = f_\gamma(0)W^{-(s+1)}$,

$$f_\pi(t) \;=\; \frac{Bf_\gamma(0)}{\lambda_1-\lambda_2}\left\{e^{\lambda_1 t} - e^{\lambda_2 t}\right\} \qquad (15.20)$$

and

$$f_\gamma(t) \;=\; \frac{f_\gamma(0)}{\lambda_1-\lambda_2}\left\{(A+\lambda_1)e^{\lambda_1 t} - (A+\lambda_2)e^{\lambda_2 t}\right\}. \qquad (15.21)$$

For a spectrum of injected photons with integral spectral index γ and no injected electrons, the differential spectrum of photons plus electrons and positrons at depth t is

$$\frac{\mathrm{d}N_{\gamma+e^\pm}}{\mathrm{d}E} \;=\; \frac{f_\gamma(0)}{\lambda_1-\lambda_2}\,E^{-(\gamma+1)}\left\{(A+B+\lambda_1)\,e^{\lambda_1 t} - (A+B+\lambda_2)\,e^{\lambda_2 t}\right\}. \qquad (15.22)$$

For depths greater than one radiation length, only the first term is important. With the numerical values from table 15.1 for $\gamma = s = 1.7$,

$$\frac{\mathrm{d}N_{\gamma+e^\pm}}{\mathrm{d}E} \;\sim\; 1.18\,f_\gamma(0)\,E^{-2.7}\,e^{-X/85}, \qquad (15.23)$$

where the depth in (15.23) is expressed in g/cm^2. This is the expression used in chapter 4 to calculate the electromagnetic flux as measured by emulsion chambers.

15.2.2 Electromagnetic air showers

To calculate the number of photons and electrons in an air shower induced by a single electron or photon incident at $t = 0$ requires solution of the same equations ((15.10) and (15.11)) subject to δ-function boundary conditions. The obvious approach is a Monte Carlo computer code. There are several well-developed codes in existence which can be used to generate electromagnetic cascades in complex detectors. (One example is the EGS system, Nelson et al., 1985.) Because of the vast amount of detail it contains and the millions of particles that need to be followed, a code like this consumes a large amount of computer time and becomes impractical when the incident energy is very high. Electromagnetic Monte Carlo codes tailored to air showers may run significantly faster (e.g. Stanev & Vankov, 1979) because many details necessary for the most general code can be simplified. It is not necessary in an air shower, for example, to allow for abrupt changes in materials between adjacent layers, as in a calorimeter, nor is it necessary to take account of the finite geometry of the medium. Even codes specialized for electromagnetic air showers, however, are sufficiently time consuming that straightforward application of them for calculation of very high energy cascades becomes impractical. It is then necessary to resort to parametrizations.

The reference point for virtually all parametrizations of air showers (hadronic as well as electromagnetic) is the work on electromagnetic cascades summarized in the review by Rossi & Greisen (1941). Since the details are available in their paper and in Rossi's book (1952), I will outline the results here as briefly as possible consistent with motivating the forms of the parametrizations and summarizing their essential features.

The starting point is the observation that the Mellin transforms of (15.10) and (15.11) satisfy the same equations, (15.14) and (15.15), as the factors $f(t)$ in the solutions for power law boundary conditions.

> **Problem:** From the definition of the Mellin transform of a function $F(W)$ as
>
> $$\mathcal{M}_F(s) \equiv \int_0^\infty W^s F(W) \mathrm{d}W,$$
>
> show by substitution into (15.10) and (15.11) that the Mellin transforms of $\gamma(W,t)$ and $\pi(E,t)$ satisfy (15.14) and (15.15). Show that the boundary conditions are $f_\gamma(0) = (W_0)^s$ and $f_\pi(0) = 0$ for a single incident photon of energy W_0 and $f_\gamma(0) = 0$, $F_\pi(0) = (E_0)^s$ for a single incident electron of energy E_0.

The air shower solutions are then obtained by inverting the Mellin transforms,

$$\gamma(W,t) = \frac{1}{2\pi i}\int_{-i\infty+s_0}^{i\infty+s_0} W^{-(s+1)} f_\gamma(s,t)\mathrm{d}s, \tag{15.24}$$

for photons, with a similar expression for electrons. Solutions subject to δ-function boundary conditions are thus convolutions of the elementary solutions for power law boundary conditions.

It is only in the inversion of the Mellin transforms that approximations are required to obtain analytic solutions. The approximation consists of evaluating (15.24) by the saddle point method. To simplify the formulas and to motivate the standard parametrizations it is also useful to make some numerical approximations to the Mellin transform functions. The function $\lambda_1(s)$ is positive for $s < 1$ and negative for $s > 1$. An approximation that is good to better than 2% for $0.5 \leq s \leq 2$ is

$$\lambda_1(s) = \tfrac{1}{2}(s - 1 - 3\ln s). \tag{15.25}$$

The other root of (15.17) is always negative and larger in magnitude than $\lambda_1(s)$, so that only the term with λ_1 is important for $t \gg 1$.

As specific examples, I consider the solutions for electrons plus positrons for a single incident photon of energy W_0 and for a single incident electron of $E_0 = W_0$. From (15.20) the Mellin transform for an incident photon is

$$f_\pi^{(\gamma)}(s,t) \approx \frac{B(s)}{\lambda_1(s)-\lambda_2(s)}(W_0)^s \exp[\lambda_1(s)t]. \tag{15.26}$$

The corresponding expression for an incident electron is

$$f_\pi^{(e^\pm)}(s,t) \approx \frac{\sigma_0+\lambda_1(s)}{\lambda_1(s)-\lambda_2(s)}(E_0)^s \exp[\lambda_1(s)t]. \tag{15.27}$$

The inverse transform of $f_\pi^{(\gamma)}(s,t)$, for example, gives

$$\begin{aligned}\pi^{(\gamma)}(E,t)\mathrm{d}E &= \frac{\mathrm{d}E}{E}\frac{1}{2\pi i}\int_{-i\infty+s_0}^{i\infty+s_0}\left\{\frac{B(s)}{\sqrt{s}[\lambda_1(s)-\lambda_2(s)]}\right\} \\ &\qquad \times\sqrt{s}\left(\frac{W_0}{E}\right)^s \exp[\lambda_1(s)t]\mathrm{d}s,\end{aligned} \tag{15.28}$$

which can be rewritten as

$$\begin{aligned}\pi^{(\gamma)}(E,t)\mathrm{d}E &= \frac{\mathrm{d}E}{E}\frac{1}{2\pi i}\int_{-i\infty+s_0}^{i\infty+s_0}\left\{\frac{B(s)}{\sqrt{s}[\lambda_1(s)-\lambda_2(s)]}\right\} \\ &\qquad \times\exp[\lambda_1(s) + sy + \tfrac{1}{2}\ln s]\mathrm{d}s.\end{aligned} \tag{15.29}$$

Here $y \equiv \ln(E_0/E)$ (a quantity called "lethargy" in the context of radiation shielding). The factors in curly brackets have been arranged to cancel a $1/\sqrt{s}$ behavior of $\lambda_1(s) - \lambda_2(s)$ at small s. The rapidly varying part of the s-dependence in the integrand is thus all in the argument of the exponent.

The saddle point approximation for the integral in (15.29) consists of expanding the argument of the exponent to second order in a Taylor series about $\bar{s}$, where $\bar{s}$ is the solution of

$$\frac{\mathrm{d}}{\mathrm{d}s}[\lambda_1(s)t + sy + \tfrac{1}{2}\ln s] = 0.$$

The slowly varying part of the integrand in curly brackets is approximated by its value at $s = \bar{s}$. This leaves a Gaussian integral which can be evaluated by integrating along the contour through the saddle point at $\bar{s}$.

The same procedure can be carried out to find the corresponding approximation for electrons generated by an incident electron and for photons in showers of either type. Integral spectra also have the same form. (From (15.28) it is apparent that integral spectra differ from the corresponding differential spectra by an extra factor of $1/s$ in the integrand.) In general, the integral to be approximated is of the form

$$I(t,\bar{s}) = \frac{1}{2\pi i}\int_{-i\infty+\bar{s}}^{i\infty+\bar{s}} \mathrm{d}s\ \{F(s)\}\exp[\lambda_1(s) + sy - n\ln s]. \tag{15.30}$$

The condition for the location of the extremum is

$$\lambda_1'(\bar{s})\,t + y - \frac{n}{\bar{s}} = 0. \qquad (15.31)$$

Expanding the argument of the integrand about $\bar{s}$ gives

$$\begin{aligned} I(t,\bar{s}) &\approx F(\bar{s}) \exp[\lambda_1(\bar{s})t + \bar{s}y - n\ln\bar{s}] \\ &\quad \times \frac{1}{2\pi i}\int_{-i\infty+\bar{s}}^{i\infty+\bar{s}} \mathrm{d}s \exp[(\lambda_1''(s)t + n/\bar{s}^2)\frac{(s-\bar{s})^2}{2}] \\ &\approx \frac{F(\bar{s})}{\sqrt{\lambda_1''(s)t + n/\bar{s}^2}} \, \frac{\exp[\lambda_1(\bar{s})t + \bar{s}y - n\ln\bar{s}]}{\sqrt{2\pi}}. \end{aligned} \qquad (15.32)$$

The depth of maximum, T, occurs approximately when the argument of the exponential is a maximum,

$$\left\{\frac{\mathrm{d}}{\mathrm{d}s}[\lambda_1(s)t + sy - n\ln s]\right\}\frac{\mathrm{d}s}{\mathrm{d}t} + \lambda_1(s) = \lambda_1(s) = 0. \qquad (15.33)$$

(In this equation and below the bar over s is understood.) The factor in square brackets vanishes by (15.31), and $\lambda_1(s) = 0$ for $s = 1$. It therefore follows from (15.31) that $T = -(y-n)/\lambda_1'(1)$. With the approximation (15.25), $\lambda_1'(1) \approx -1$ and

$$T \approx \ln\frac{E_0}{E} - n. \qquad (15.34)$$

Here T is explicitly a function of E and is shallower for higher E as expected in a cascade. Values of n and $F(s)$ are listed in table 15.2 for the differential spectra. For each case the corresponding integral expression is the same except that

$$n(\text{integral}) = n(\text{differential}) + 1.$$

Note that maximum is reached one-half radiation length sooner for showers initiated by electrons than for photon-initiated showers.

The parameter s, related to t and y by (15.31), is called the *age parameter*. Since $I(t) \propto \exp[\lambda_1(s)\,t]$, the number of shower particles in a given energy range increases with depth for $s < 1$ (i.e. when $\lambda_1(s)$ is positive), reaches a maximum when $s = 1$, and declines for $s > 1$ (when $\lambda_1(s)$ is negative). In the approximation (15.25)

$$s = \frac{2n + 3t}{t + 2y}, \qquad (15.35)$$

Table 15.2: Quantities in the Rossi & Greisen approximations.

	n	$F(s)$
$e^+ + e^-$ from γ	$-\frac{1}{2}$	$\frac{B(s)}{\sqrt{s}[\lambda_1(s)-\lambda_2(s)]}$
$e^+ + e^-$ from $e^\pm$	0	$\frac{\sigma_0+\lambda_1(s)}{\lambda_1(s)-\lambda_2(s)}$
γ from γ	0	$-\frac{\sigma_0+\lambda_2(s)}{\lambda_1(s)-\lambda_2(s)}$
γ from $e^\pm$	$+\frac{1}{2}$	$\frac{\sqrt{s}\,C(s)}{\lambda_1(s)-\lambda_2(s)}$

and

$$\lambda_1''(s) \sim 1.5/s^2. \qquad (15.36)$$

From (15.32) one can see that in general the energy spectrum of particles in a shower will be of the form

$$\frac{\mathrm{d}N}{\mathrm{d}E} = \frac{1}{E_0}\left(\frac{E_0}{E}\right)^{s+1} \exp[\lambda_1(s)\,t] \times (\text{function of s}). \qquad (15.37)$$

Since s depends only logarithmically on $y = \ln(E_0/E)$, the energy dependence is approximately a power. The spectrum steepens as age increases—physically, high energy particles become rare as the shower develops. At maximum $s = 1$, and the spectrum is $\sim E^{-2}$. (Note that because s does depend on y, these statements apply only for limited ranges of energy.)

Approximations like (15.32) are used with s as a parameter. For each value of s one finds the corresponding t from (15.31). The value of $I(t(s),s)$ is then plotted at this value of t. With the help of (15.25) and (15.35), the exponent in (15.32) can be written in the following conventional form:

$$\exp[\lambda_1(s)t + sy - n\ln s] = \exp[n(1-\ln s) + t(1-\tfrac{3}{2}\ln s)]. \qquad (15.38)$$

Explicitly, for example for the integral spectra,

$$\Pi^{(e^\pm)}(> E, t) \approx \frac{1}{(\sqrt{2\pi})^{1/2}}\,\frac{\sigma_0 + \lambda_1(s)}{\lambda_1(s) - \lambda_2(s)}\,\frac{e}{\sqrt{1.5t+1}} \exp[t(1-\tfrac{3}{2}\ln s)] \qquad (15.39)$$

and

$$\Pi^{(\gamma)}(> E,t) \approx \frac{1}{(\sqrt{2\pi})^{1/2}} \frac{B(s)}{\sqrt{s}[\lambda_1(s) - \lambda_2(s)]} \frac{\sqrt{s}\, e^{\frac{1}{2}}}{\sqrt{1.5t + 0.5}} \exp[t(1-\tfrac{3}{2}\ln s)] \qquad (15.40)$$

At maximum $T = \ln(E_0/E) - n$, and $s = 1$, so[2]

$$\Pi^{(e^\pm)}(> E,t) \approx \frac{0.14}{\sqrt{\ln(E_0/E) - 0.33}} \frac{E_0}{E} \qquad (15.41)$$

and

$$\Pi^{(\gamma)}(> E,t) \approx \frac{0.14}{\sqrt{\ln(E_0/E) - 0.25}} \frac{E_0}{E}. \qquad (15.42)$$

Note the similarity of the formulas for depth of maximum, (15.34), and size at maximum, (15.41) and (15.42), here as compared with those obtained from the simple branching model, (14.6) and (14.7).

15.2.3 Approximations for total number of particles

What is measured by a scintillator that samples an air shower front is the signal produced by all the electrons and positrons incident on the scintillator plus the signal produced by photons that convert in the scintillator.[3] One would therefore like a formula for the total number of electrons and positrons down to, say, 1 MeV. Energy loss and Coulomb scattering must be taken into account, and Approximation A is no longer adequate. The conventional form used for the total number of electrons in a photon-initiated shower is (Greisen, 1956)

$$N(t) \sim \frac{0.31}{(\beta_0)^{1/2}} \exp[t(1 - \tfrac{3}{2}\ln s)], \qquad (15.43)$$

where $\beta_0 = \ln(W_0/E_c)$ and s, t and $y = \beta_0$ are related by (15.35) with $n = 0$. This simple expression is similar in form to the Approximation A solutions but has a depth of maximum at $T = \ln(E_0/E_c)$.

A ((15.39)–(15.40)) evaluated at $E = E_c$ by a slowly increasing function of s. When more accurate results are required it may be desirable to use these approximations, which distinguish between electron and photon-initiated showers.

15.3 Fluctuations

For a given primary energy, fluctuations in the size of a shower measured at a particular depth in the atmosphere arise both from fluctuations in starting point and from fluctuations in the way the shower develops. An incident photon interacts with probability $\mathrm{d}P/P = -\sigma_0 \mathrm{d}t$, so $P(t_1) = \sigma_0 \exp[-\sigma_0 t_1]$ is the distribution of starting points for photon-induced showers. For this distribution

$$\delta t = \sqrt{< t^2 > - < t >^2} = \frac{1}{\sigma_0} = \tfrac{9}{7}. \qquad (15.44)$$

Since $N(t) \propto \exp[\lambda_1(s)t]$, a measure of the corresponding fluctuation in $\ln N$ is

$$\delta \ln N \sim \lambda_1(s)\delta t \sim \tfrac{9}{14}(s - 1 - 3\ln s). \qquad (15.45)$$

Fluctuations in shower size are thus proportional to N and are smallest near shower maximum. For a 10^{15} eV γ-initiated shower at sea level, for example, $s \sim 1.4$ and $\delta N \sim 0.4\,N$. When development fluctuations are included the overall fluctuations are somewhat larger. Fluctuations in proton-initiated showers may be larger, at least at energies low enough so $\lambda_N > X_0$. In summary, fluctuations in a sample of showers of the same energy observed at the same slant depth are approximately log-normal, reflecting the multiplicative character of the cascade process. This is clearly a general property of the branching process that will also hold for hadron-initiated showers.

Moliere unit, r_1, the natural unit of lateral spread due to Coulomb scattering. For multiple Coulomb scattering (Nishimura, 1967)

$$< \delta\theta^2 > = \left(\frac{E_s}{E}\right)^2 \delta t,$$

where $E_s = m_e c^2 (4\pi/\alpha)^{1/2} \approx 21$ MeV. The Moliere unit, which characterizes the spread of low energy particles in a shower is

$$r_1 = \frac{E_s}{E_c} X_0 \approx 9.3 \text{ g/cm}^2, \tag{15.46}$$

which is 78 m at sea level. For higher energy particles the characteristic spread, $R_E \sim r_1 \, E_c/E$, is smaller.

For calculations of showers in three dimensions it is necessary to solve equations for $\pi(E, x, y, \theta_x, \theta_y, t)$. Approximate solutions obtained by Kamata & Nishimura (1958) and by Greisen (1956) are compared in the article in *Handbuch der Physik* by Nishimura (1967). Greisen's form of the lateral distribution of electrons is known as the NKG formula,

$$x\, f(x) \propto x^{s-1} (1 + x)^{s-4.5}, \tag{15.47}$$

valid for $1.0 \leq s \leq 1.4$. In the NKG formula, $x = r/r_1$, and the particle density at a perpendicular distance r from the shower core is

$$\rho_N(r,t) = \frac{N_e(t)}{r_1^2} f(x),$$

where $N_e(t)$ is the total number of particles in the shower at t radiation lengths. The normalization is defined so that

$$2\pi \int_0^\infty x f(x)\, \mathrm{d}x = 1.$$

The correlation between shower age and shape of the lateral distribution implied by (15.47) has been used to correlate a fitted value of s for a shower with its stage of development. This is problematic since real showers have hadronic cores that continually feed the electromagnetic component through $\pi^0 \to 2\gamma$. In addition, Monte Carlo simulations of electromagnetic cascades in air find steeper lateral distributions than the NKG distribution (Hillas & Lapikens, 1977; Fenyves et al., 1988). Nevertheless, the general form of the NKG function, or modifications of it, have proved useful in fitting observed showers.

Chapter 16

Cosmic ray showers

Because of their hadronic cores, atmospheric cascades generated by incident cosmic ray nuclei develop differently from purely electromagnetic cascades. Interactions of high energy hadrons replenish the electromagnetic component *via* π^0 production as the showers develop. As a consequence, both the longitudinal development and lateral structure are more complex than for photon-induced showers. The differences are subtle, however, and it is practically impossible to distinguish between the two kinds of showers by looking at the electromagnetic component alone.

This chapter begins with the subject of low energy muons in cosmic ray showers because the muons are related to primary energy in a somewhat simpler fashion than the more numerous electrons and positrons. Primary energy is not directly measured with conventional surface arrays however, because they only sample each shower at one depth. It is therefore necessary to see how measurements of the density of electrons and positrons at a fixed observation level can be related to primary energy. This leads to a discussion of the model-dependence of the interpretation of air shower measurements. A major goal is to determine the primary cosmic ray spectrum from air shower measurements in a way that depends as little as possible on uncertainties in the physics that governs cascade development. At the end of the chapter, I return to a discussion of muons in photon-induced showers.

16.1 Muons in air showers

Muons in air showers are typically measured with detectors buried under a meter or more of earth or concrete to absorb the electromagnetic component. A depth of 2 meters of concrete with specific density of 2.5, for example, is 19 radiation lengths thick but only stops muons if they have energy less than about a GeV. Muons in the GeV energy range are therefore typical of those sampled in air shower experiments. (See fig. 16.1 for an example of a muon detector.) Such low energy muons are predominantly from decay of charged pions and kaons of comparable energy. Since virtually all these low energy pions and kaons decay rather than interact, the height of origin of the muons traces the height of production of the parent particles.

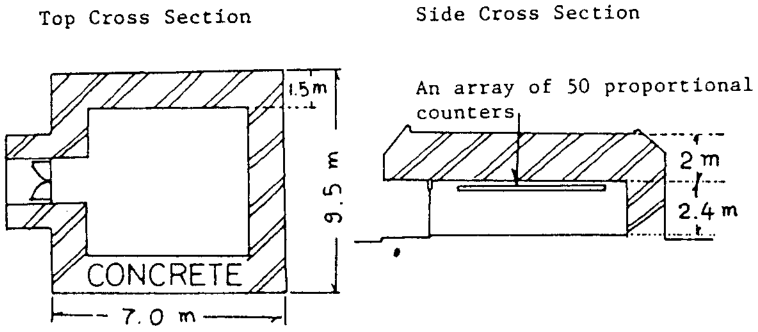

Figure 16.1: Sketch of a muon detector in the Akeno air shower experiment. (Kamata et al., 1987.) See also fig. 16.3.

Because the muons do not multiply, but only lose energy slowly by ionization as they traverse the atmosphere, the muon content of a shower builds up to a maximum then attenuates very slowly. This is quite different from the electron component, which attenuates relatively rapidly after maximum. The contrast is shown in fig. 16.2. One consequence is that a measurement of the muon content should be a better measure of the primary energy because the flat shower profile

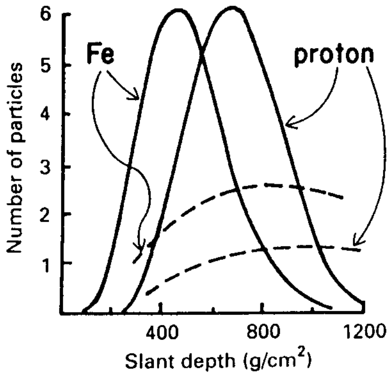

Figure 16.2: Schematic shower profiles for small air showers. Solid lines show $e^{\pm}$; dashed lines show muons. ($E_0 \sim 10^7$ GeV. N_μ is multiplied by 20 relative to N_e on an arbitrary linear scale.)

the heavy primary. Finally, because muons originate from decay of hadrons, a measurement of the muons should be a good tag for enhancing the signal to background ratio in photon-induced showers. This is because showers initiated by photons should produce very few hadrons.

Several problems arise in trying to apply these simple ideas. One is that, as a result of the fact that the muons do not multiply, there are fewer muons than electrons and positrons in typical showers. For every ~GeV muon from a charged pion, there is roughly one ~GeV photon (because $\pi^0/\pi^\pm \sim 1/2$ and $\pi^0 \rightarrow 2\gamma$). But each ~ GeV photon gives ~10 $e^\pm$ above the critical energy (see fig. 14.3). Very crudely therefore, we expect $N_\mu/N_e \sim 0.1$. In addition to the fact that the number of muons is relatively small, their detection is not as easy as for the electromagnetic component because of the required shielding. Thus muons tend to be poorly sampled. As a result, the advantage of smaller fluctuations in development tends to be offset by fluctuations due to sampling. Another complication is that, with a conventional air shower array, showers are classified by size at a given depth rather than by primary energy.

teractions. The number of hadronic interactions in a cascade initiated by a primary nucleon with energy E_0 can be represented as

$$\frac{\mathrm{d}n_{\mathrm{int}}}{\mathrm{d}z} \sim \delta(1-z) + \frac{1}{z} + 0.77\frac{(1-z)^3}{z^{1.78}}, \tag{16.1}$$

where $z = E/E_0$ is the energy of the interaction scaled to the primary energy. The first two terms are nucleon interactions and the last is due to interactions of mesons. The scaling form for the cascade follows from the assumption of constant cross sections and scaling of the inclusive cross sections, as discussed in chapter 14.

> **Problem:** Show that the expression for the nucleon interactions in (16.1) follows from the assumption that the inclusive cross section for $p + p \to N +$ anything is $F_{NN}(x) = x$, together with neglect of production of pairs of nucleons and antinucleons.

A check on energy conservation is useful to verify that formula (16.1), though rudimentary, is at least reasonable. Let $K_\pi^{(\gamma)}$ and $K_N^{(\gamma)}$ represent the fraction of the interaction energy that goes into the electromagnetic component in collisions of $\pi^\pm$ and nucleons respectively. Then the total energy dumped into the electromagnetic component in all interactions is

$$\frac{E_{\mathrm{tot}}}{E_0} = \sum_i K_i \int_0^1 z\frac{\mathrm{d}n_i}{\mathrm{d}z}\mathrm{d}z = 2\,K_N^{(\gamma)} + 2.41\,K_\pi^{(\gamma)}, \tag{16.2}$$

where the sum is over two kinds of interactions, $i = N$ and $i = \pi^\pm$. Roughly, we expect half the energy of nucleon interactions to go into pions, of which approximately 1/3 is in neutral pions, so $K_N^{(\gamma)} \approx 1/6$. For pion-induced interactions, the corresponding number should be somewhat less than 1/3. (If all outgoing particles were pions that shared equally in the energy, the number would be exactly 1/3; however, there is a tendency for the fastest produced pion to carry the charge of the pion that initiates the collision.) Energy conservation is satisfied by (16.2) if $K_N^{(\gamma)} \approx 1/6$ and $K_\pi^{(\gamma)} \approx 0.28$.

To get a crude estimate from (16.2) of the number of low energy muons in a shower, let us assume that all charged pions with $E_\pi < \epsilon_\pi$ decay and all higher energy charged pions interact. The spectrum of low energy charged pions produced in the shower is then

$$\frac{\mathrm{d}N_\pi}{\mathrm{d}E_\pi} \sim \sum_i \int_{\epsilon_\pi}^{E_0} \frac{F_{i\pi^\pm}(x_\pi)}{E_\pi}\,\frac{\mathrm{d}n_i}{\mathrm{d}z}\,\frac{\mathrm{d}E}{E_0}, \tag{16.3}$$

where $x_\pi = E_\pi/E$ and $F_{i\pi}$ is the inclusive cross section for $i \to \pi$ as defined in (3.4). Changing variables gives

$$\frac{\mathrm{d}N_\pi}{\mathrm{d}E_\pi} \sim \frac{1}{E_\pi}\sum_i \int_{\epsilon_\pi/E_0}^{1} F_{i\pi^\pm}\left(\frac{E_\pi}{zE_0}\right)\frac{\mathrm{d}n_i}{\mathrm{d}z}\,\mathrm{d}z. \tag{16.4}$$

For $E_\pi < \epsilon_\pi$ the integral can be approximated by evaluating the inclusive cross section at small value of its argument where it is nearly constant. Furthermore, for $E_0 \gg \epsilon_\pi \approx 115$ GeV, the integral is dominated by its most divergent term, so

$$\frac{\mathrm{d}N_\pi}{\mathrm{d}E_\pi} \sim \frac{1}{E_\pi}F_{\pi\pi}(0)\left(\frac{E_0}{\epsilon_\pi}\right)^{0.78}. \tag{16.5}$$

The estimate for the total number of muons with $E_\mu > 1$ GeV in a nucleon-initiated shower, assuming one muon per pion, is obtained by integrating (16.5) up to $E_\pi \sim \epsilon_\pi$:

$$N_\mu(>1\,\mathrm{GeV}) \sim F_{\pi\pi}(0)\,\ln\epsilon_\pi(\mathrm{GeV})\left(\frac{E_0}{\epsilon_\pi}\right)^{0.78}. \tag{16.6}$$

If Feynman scaling were valid, then $F_{\pi\pi}(0)$ would be a constant independent of energy. Recall that

$$F_{i\pi} = E_\pi\frac{\mathrm{d}n_\pi}{\mathrm{d}E_\pi} = \frac{\mathrm{d}n_\pi}{\mathrm{d}\ln E_\pi} \sim \frac{\mathrm{d}n_\pi}{\mathrm{d}y} \sim \frac{\mathrm{d}n_\pi}{\mathrm{d}\eta}.$$

Thus fig. 5.4 shows the energy dependence of the data for $F_{N\pi}$, which should be similar to $F_{\pi\pi}$ in the central region. One source of model dependence is therefore explicit in (16.6); namely, what value to use for $F_{\pi\pi}$. The general form for the total number of low energy muons in an air shower is

$$N_\mu(>1\,\mathrm{GeV}) = A\,B\left(\frac{E_0}{A\epsilon_\pi}\right)^{p_\mu}, \tag{16.7}$$

where A is the mass number of a primary nucleus of total energy E_0 and B is a constant (note the similarity to (14.14) for $\geq$ TeV muons in air showers). The exponent p_μ also depends on the model used for the cascade calculation. The simulations described by (16.1) assumed scaling starting from low energy data with $F_{\pi\pi}(0) \approx 1.5$. A more detailed numerical integration of the cascade equations, such as (3.1), (3.18), etc., subject to the air shower boundary conditions has been made with a code developed by Elbert. The results (Elbert & Gaisser, 1979) are numerically similar to (16.6) and can be described by (16.7) with $B = 2.8$ and $p_\mu = 0.86$.

Because the primary energy is not measured directly in an air shower experiment, it is difficult to compare (16.7) with data. This problem will be discussed in some detail in the next section. For now, I simply quote the result of the Akeno group (Nagano et al., 1984), which can be expressed as

$$N_\mu(>1\ \mathrm{GeV}) \;\approx\; 11 \left(\frac{E_0}{\epsilon_\pi}\right)^{0.83}. \tag{16.8}$$

This result is tabulated in the last column of Table 16.1. It is more than twice as large as the calculations. Since $N_\mu \propto A^{(1-p_\mu)}$, the discrepancy between the numerical integration and the Akeno result can be reduced if the primaries contain a large fraction of heavy nuclei. Even with $A = 56$, however, (16.7) gives only 6.3×10^5 muons at 10^{17} eV, and a more realistic mixed composition gives only a modest increase in N_μ.

Table 16.1: $N_\mu(>1$ GeV) in showers of various energies.

E_0 (eV)	Eq. 16.6	Numerical integration	Akeno
10^{15}	8.4×10^3	6.9×10^3	
10^{16}	5.1×10^4	5.0×10^4	1.4×10^5
10^{17}	3.1×10^5	3.6×10^5	9.4×10^5
10^{18}	1.8×10^6	2.6×10^6	6.3×10^6

Problem: Show that the composition listed in Table 1.1 (sometimes called the "low energy composition") gives an enhancement by a factor of 1.26 over pure protons if $p_\mu = 0.86$ and 1.48 if $p_\mu = 0.78$.

The prediction can be further increased by taking account of the increase with energy of $F_{\pi\pi}(0)$ and the increased inelasticity into pions appropriate for a nuclear target. For air, the total inelasticity is $K_N \sim 0.60$ (i.e. $\sim 40\%$ of the energy is carried off by the leading nucleon), so the dominant pion production term in (16.1) should be increased correspondingly. As discussed in §5.6, the inelasticity may increase to a value as large as 0.8 to 0.9 for proton-nucleus collisions at 10^{17} eV, which could increase the muons content of showers even more.

Whether such modifications of simple scaling of hadronic interactions are sufficient to explain the relatively large number of low energy muons in air showers, or whether a primary composition much richer in very heavy nuclei than the "low energy" composition is required, remain questions of current interest.

16.1.2 Lateral distributions of muons

In his review, Greisen (1960) gave a parameterization of the lateral distribution of ≥ 1 GeV muons in nearly vertical showers, based on earlier experiments near sea level, that is still the standard for the field. He expressed the density of muons as

$$\rho_\mu(\mathrm{m}^{-2}) \;=\; 18 \left(\frac{N_e}{10^6}\right)^{3/4} r^{-0.75} \left(1 + \frac{r}{320\,\mathrm{m}}\right)^{-2.5}.$$

This equation expresses two experimental observations. The first is that

$$N_\mu(>1\ \mathrm{GeV}) \;\approx\; 0.95 \times 10^5 \left(\frac{N_e}{10^6}\right)^{3/4}, \tag{16.9}$$

where N_e is the total number of charged particles in the shower front, most of which are electrons and positrons. The second is that the lateral distribution of muons is approximately independent of shower size and given by

$$\rho_\mu(\mathrm{m}^{-2}) \;=\; \frac{\Gamma(2.5)}{2\pi\Gamma(1.5)\Gamma(1.5)} \left(\frac{1}{320}\right)^{1.25} N_\mu r^{-0.75} \left(1 + \frac{r}{320}\right)^{-2.5}. \tag{16.10}$$

The Greisen formula is based on experimental observations and therefore relates N_μ to N_e rather than to E_0. This is because the total number of charged particles is related rather directly to measured quantities, unlike the primary energy. Because small showers are sampled after maximum, one has, at a fixed observation depth,

$$N_e \;\propto\; [N_e(\max)]^{(1+\epsilon)} \;\propto\; (E_0/E_c)^{(1+\epsilon)},$$

where ϵ is a small quantity that depends somewhat on shower size and on the altitude of the experiment. This is due to the fact that shower maximum is closer to the observation level for more energetic showers, and it accounts for the fact that $N_\mu \propto N_e^{0.75}$ whereas $N_\mu \propto E_0^{p_\mu}$ with $p_\mu \sim 0.83$.

16.2 Relation of N_e to E_0

Broadly speaking, there are two classes of problems to be dealt with in finding the relation between shower size and primary energy. One is that there are large fluctuations in N_e for a fixed E_0 and *vice versa*. These arise both from the different kinds of primary nuclei likely to be present and from fluctuations in shower development. The result of the fluctuations in N_e for fixed E_0 in the presence of a steep spectrum is that the ratio of mean energy for showers of the same observed size, $< E_0 > /N_e$, is smaller than the ratio $E_0/ < N_e >$, where $< N_e >$ is the mean size of a sample of showers all of which have the same energy. The other problem is that shower development depends on the model of hadronic interactions, which is not entirely determined by accelerator experiments.

16.2.1 Lateral distribution of charged particles

A conventional air shower experiment only samples the shower front with an array of small detectors, as illustrated for the Akeno experiment in fig. 16.3. The total number of particles in a shower therefore has to be obtained by fitting the individual densities sampled at each detector to an assumed lateral distribution function, which can be integrated to assign N_e. It has been traditional to use a form like the NKG lateral distribution (15.47) with s left as a free parameter to be determined for each shower. The procedure involves many experimental complications (such as locating the shower core, accounting for the zenith angle of the shower and relating the signal in a particular scintillator to a number of particles incident on the detector) that I will not attempt to describe here. A complete analysis may be found in the paper of Nagano et al. (1984).

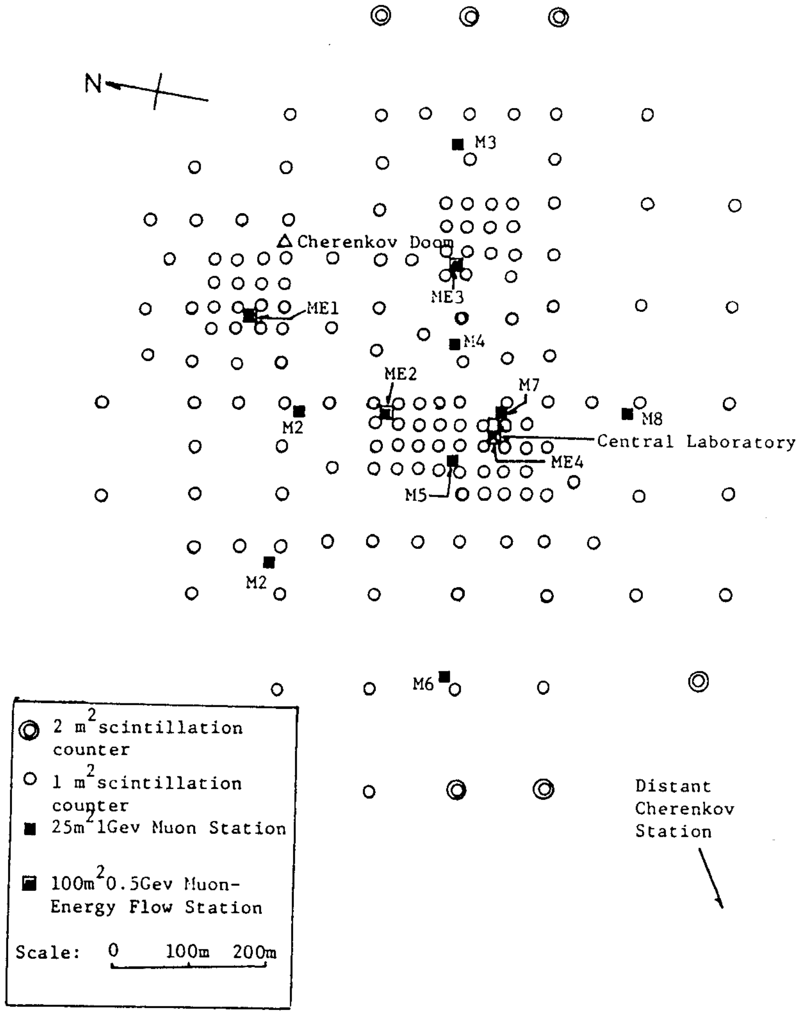

Figure 16.3: Arrangement of the Akeno EAS array. (Kamata et al., 1978). The detectors labelled M1, M2, . . . are muon stations, as shown in fig. 16.1.

The scale for the NKG lateral distribution function is the Molière unit, which at the depth of the Akeno array of 920 g/cm^2, for example, is $r_1 \approx 92$ m. It is found that cosmic ray showers are not described well over the whole distance range by the NKG function with a single age parameter. Rather, the lateral distribution tends to be steeper ("younger") near the core and flatter ("older") at large distances from the core. Photons very near the core are from new cascades generated locally by π^0's produced along the core, whereas photons at large core distances are from more fully developed electromagnetic cascades initiated higher up. In addition, at very large distances muons (which have a flatter lateral distribution than electrons and positrons) dominate. The standard modified NKG form is

$$f(x) = C_1(s)\, x^{(s-2)} (1+x)^{(s-4.5)} (1 + C_2\, x^d), \qquad (16.11)$$

where $x = r/r_1$, and the normalization constant is[1]

$$C_1(s) = \frac{N_e}{2\pi r_1^2} [B(s, 4.5-2s) + C_2\, B(s+d, 4.5-d-2s)]^{-1}.$$

For showers of size $N_e \approx 10^6$ at sea level, Greisen (1960) uses $s = 1.25$, $d = 1$, and $C_2 = 0.088$. Nagano et al. (1984) at 920 g/cm^2 use $d = 1.3$ and $C_2 = 0.2$ with s fitted for each shower.

A comparison of Greisen's average forms for muon density (16.10) and for total density of charged particles is shown in fig. 16.4. The density of electrons and positrons is comparable to the density of muons around 500 m. Showers that fluctuate in such a way that there is more energy in the electromagnetic component at the expense of the muons (or *vice versa*) would therefore tend to have minimum fluctuations around this energy. In general, it is possible to find a core distance for a particular array at which fluctuations in measured density are minimal. This distance may be different for different arrays, depending on array spacing, altitude, etc. Hillas et al. (1971) established with simulations that, for the Haverah Park array, a good distance is 500 m. (Since this was approximately the detector spacing, it is also a distance at which the density is usually measured well.) For a variety of models, they found the relation between $\rho(500)$ and E_0. This density was related experimentally to ρ_μ and hence to N_μ by the Akeno group (Nagano et al. 1984) and is the basis of the result in (16.8).

16.2.2 Method of constant intensity cuts

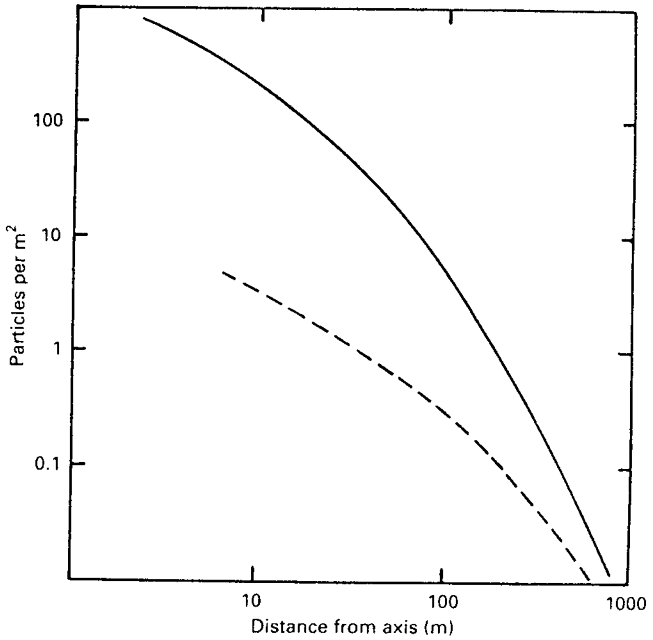

Figure 16.4: Lateral distribution of all charged particles (solid line) and muons for showers of size ~ 10^6.

Since a shower initiated by a cosmic ray proton or nucleus is basically a branching process which just has a richer variety of elementary processes than a purely electromagnetic cascade (including the possibility of subdividing the energy among many particles at a single interaction), we expect some general properties to be similar. In particular, the fluctuations in shower size should be approximately a normal distribution in the logarithm of the size (see fig. 16.5), and the fluctuations should be least near shower maximum. Thus, if it were possible to extract from the data the size at maximum that corresponds to a given observed counting rate, it would then be possible to convert (on average) N_e to $N_e(\max)$. Since the number of particles at maximum comes close to being a calorimetric measure of primary energy, this procedure allows one to convert a measured size spectrum to a primary energy spectrum in a way that minimizes model dependence. Again I refer to the Akeno experiment for illustration. The basic idea of the method is to compare the average size of showers in various zenith angle bins that fall at the same rate. Since showers at large zenith angle have penetrated a large slant depth to reach the detector, the size that corresponds to a given intensity (showers per m^2 sr s) will be smaller for larger zenith angle. A plot of size vs slant depth for each intensity then maps out the average development curve for the primary energy that corresponds to that intensity. Because

---

[1] $B(m,n) = \Gamma(m)\Gamma(n)/\Gamma(m+n)$ is the beta-function.

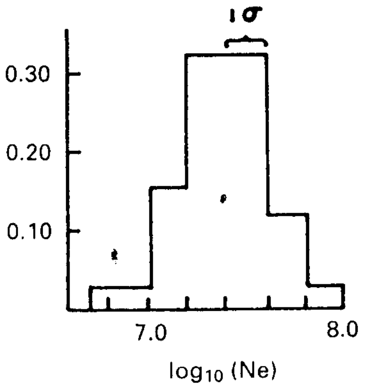

Figure 16.5: Distribution of measured shower size for nearly vertical showers with $N_\mu \sim 8 \times 10^5$ as measured by Nagano et al. (1984). The distribution is approximately log-normal with $\sigma \sim 0.2$.

most showers are well past maximum at 920 g/cm^2, it is necessary to use a very high altitude experiment to extend the development curves high enough to see shower maximum. A compilation of the measurements from Chacaltaya (altitude 5200 m.a.s.l or 550 g/cm^2 vertical depth) and elsewhere is shown in fig. 16.6. Because of the evident uncertainties in absolute normalization, only the ratio $N(\max)/N(920)$ is taken from these curves. The intensities measured with the large Akeno array (fig. 16.3) are used to construct the energy spectrum. But first we need the relation between primary energy and size at maximum.

16.2.3 Relation between size at maximum and E_0

As for electromagnetic cascades, we expect the size at maximum to be proportional to primary energy and therefore independent of the mass of the primary nucleus. At this point it is necessary to resort to simulations to make the final step. It is possible to characterize the results of simulations of proton-initiated showers by

$$S_1(E, X - X_1) \;=\; S_0 \frac{E}{\epsilon}\, e^p \left(\frac{X - X_1}{X_{\max} - \lambda}\right)^p \exp\left[-(X - X_1)/\lambda\right]. \quad (16.12)$$

Here $X - X_1$ is the atmospheric slant depth (g/cm^2) measured from the point of first effective interaction, X_1, and $p + 1 = X_{\max}/\lambda$.

$$X_{\max} \;=\; X_0' \ln(E/\epsilon) \quad (16.13)$$

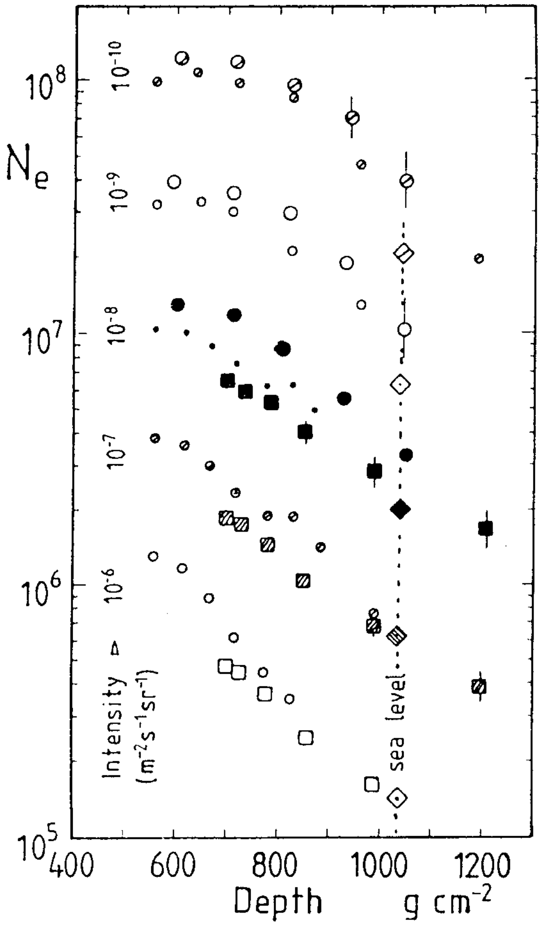

Figure 16.6: Constant intensity development curves (size vs. depth from top of atmosphere) summarized by Hillas (1983). Large circles show the Chacaltaya data from Kakimoto et al. (1981). Small circles are earlier data from Chacaltaya.

is the depth of maximum of the average of many showers. The average size at depth X is the convolution of S_1 with the starting point distribution, $\exp[-X_1/\lambda]$:

$$\bar{S}(E, X) \;=\; S_0 \frac{E}{\epsilon} \frac{p}{p+1}\, e^p \left(\frac{X}{X_{\max} - \lambda}\right)^{p+1} \exp(-X/\lambda). \quad (16.14)$$

This scheme was manufactured to simulate some fluctuations in longitudinal development of showers simply by varying the starting point for the S_1 function (Gaisser, 1979). The subshower function, S_1, has a maximum of $S_0 E/\epsilon$ at $X - X_1 = X_{\max} - \lambda$. Because the average shower curve is composed of many individual showers, $\bar{S}(X_{\max})$ is somewhat smaller (by about 5%) than the maximum value of S_1. Values of the parameters in Eqs. 16.12-16 are given in Table 16.2. The relation between shower maximum and primary energy is

$$E \;=\; w \times N_e(\max). \tag{16.15}$$

The more realistic model, which takes account of nuclear target effects and the violation of scaling in the central region, has $w \approx 1.6$ GeV at 4×10^6 GeV and $w \approx 1.5$ GeV at 10^8 GeV. Hillas (1983) suggests $w \approx 1.4$ GeV. For nearly vertical showers at 920 g/cm², Nagano et. (1984) use this kind of constant intensity cut analysis to estimate

$$E_0 \;\sim\; 3.9 \times 10^6 \, GeV \left(\frac{N_e}{10^6}\right)^{0.9}. \tag{16.16}$$

Table 16.2: Parameters for longitudinal development curves.

Parameter	Simple scaling	Realistic model
S_0	0.045	$0.045 \times \{1 + 0.0217 \ln(E/100\,\mathrm{TeV})\}$
X_0'	36 g/cm²	34.5
λ	70 g/cm²	energy-dependent
ϵ	0.074 GeV	0.074 GeV
w	1.7 GeV	1.4–1.6 GeV

16.3 Primary spectrum 10^{15}–10^{18} eV

The primary spectra obtained by the Akeno group by the two different methods – converting N_μ to E_0 and converting N_e to E_0 – give consistent results, as shown in fig. 16.7, which is reproduced from their

paper. The filled circles are the best Akeno results.[2] The labelled lines represent other treatments of the data of this and of the Chacaltaya experiment. The differences serve to illustrate the difficulty of establishing an energy spectrum from air shower measurements and the degree of uncertainty in the normalization of that spectrum. Hillas (1983) discusses these uncertainties in some detail.

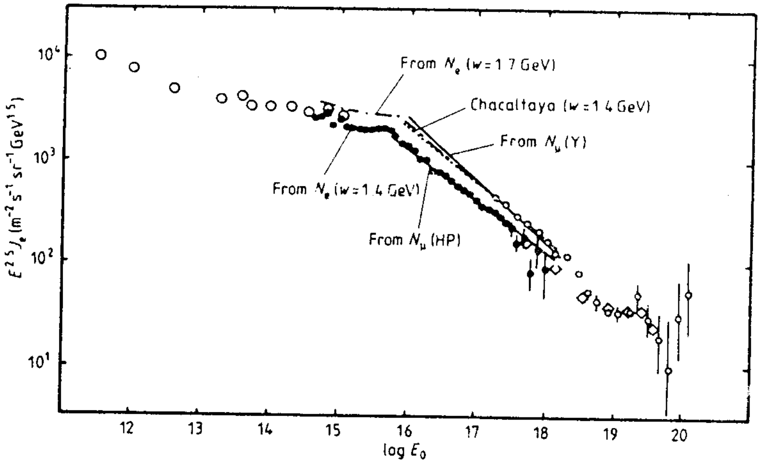

Figure 16.7: Primary spectrum as determined by Nagano et al. (1984).

The prominent feature in the spectrum around 5×10^{15} eV is often referred to as the "knee". The spectrum steepens rather suddenly from integral spectral index $\gamma \approx 1.7$ below the knee to $\gamma \approx 2$ above. An attractive possibility, hallowed by long tradition, is that the steepening of the spectrum is a rigidity dependent effect (Peters, 1959). Such a steepening could be a consequence of the breakdown of an acceleration mechanism at high energy or to an increased rate of escape from the galaxy at high energy. The latter interpretation corresponds to an increase in the exponent δ (9.8) that characterizes the residence time in the galactic disc, as discussed also in §12.3. In

---

[2] In fig. 16.7, open circles show direct measurements (Grigorov et al., 1970). The results shown above 10^{18} are from Yakutsk and Haverah Park. These high energy results, together with more recent results from the Fly's Eye experiment, are discussed by Watson (1985), by Baltrusaitas et al. (1985) and by Sokolsky (1989). At issue is whether there is evidence of interaction of the highest energy cosmic rays with the cosmic background radiation.

either case, if the steepening depends on rigidity, in the same way for all nuclei, then protons would steepen first (when classified by energy per nucleus), then helium, then CNO, etc. In this scenario, the relative fraction of heavy nuclei would increase with energy.

Hillas (1983, 1984) points out, however, that the break appears to be rather too sharp for this explanation to work easily. Perhaps there is a new component that dominates above 100 to 1000 TeV, as suggested by Fichtel & Linsley(1986) and others. This could tie in with the ideas discussed in chapters 12 and 13 for different kinds of sources and acceleration processes at ultrahigh energies. Clearly, a knowledge of the composition in this energy region is crucial for discriminating among the possibilities.

16.4 Primary composition 10^{15}–10^{18} eV

The problem of determining the composition of the primary cosmic rays from air shower measurements is obviously difficult because the primaries are not observed directly. One approach is to measure the depth of maximum as a function of shower energy.

To see how the depth of maximum reflects composition, consider (16.13) in the superposition approximation for incident nuclei. A model with approximate scaling for hadronic interactions will lead to

$$X_{\rm max} \;=\; X_0' \sum_i W_i \ln\left(\frac{E_0}{A_i \epsilon}\right). \qquad (16.17)$$

One problem is immediately apparent from this equation. The weights, W_i, depend on the experiment and may not correspond to the true weights of the nuclei in the primary energy spectrum. For example, if the depth of maximum dependence on energy is determined indirectly by an array that triggers on N_e, then light nuclei will be preferentially weighted because they penetrate more deeply.

The logarithmic derivative of the mean depth of maximum is the *elongation rate* (Linsley; 1977; Linsley & Watson, 1981). If the W_i are independent of energy (unbiased trigger and energy-independent composition) then the elongation rate is just $X_0' \sim 80$ g/cm^2 per decade of energy. In some circumstances it is possible to measure the elongation rate even when the absolute magnitude of the depth of maximum cannot be obtained, for example by observing the thickness of the shower front as a function of shower size. Clearly, a direct measurement of $X_{\rm max}$, as with Fly's Eye, for example, is preferable.

If the inelasticity increases in hadronic interactions at high energy, the effect would be similar to increasing the fraction of heavy nuclei. This is because increasing the inelasticity effectively increases the number of pieces into which the interaction energy is subdivided. Suppose this effective number is n_0 at some threshold energy below which the inelasticity is $K \sim 0.6$. Then at higher energy, $n_{\rm eff} \sim (K(E)/0.6) \times n_0$. For proton primaries, we can write

$$X_{\rm max} \;\sim\; X_0' \ln\left(\frac{E_0}{K(E)\epsilon}\right) + \text{constant}. \qquad (16.18)$$

If $K(E) \propto E_0^p$ over some energy range, then the elongation rate will change from X_0' to $(1-p)\times X_0'$. Increasing the interaction cross section has a similar effect to increasing the inelasticity because it is another way of obtaining a more rapid degradation of the primary energy. In the QCD-motivated model of hadronic interactions described in §5.4, neither of these should produce a very sudden change, though both must be included to get a quantitative prediction for the depth of maximum and other shower properties.

Let us assume that the dependence on the model of hadronic interactions is under control and investigate the sensitivity of depth of maximum to primary composition. Let us also assume that the weights in (16.17) are the true weights. Then

$$X_{\rm max} \;=\; X_0' \left(\ln\frac{E_0}{\epsilon} - <\ln A>\right). \qquad (16.19)$$

With the parameters of the "realistic model" in table 16.2 together with the weights from table 1.1 for the "low energy" composition, $<\ln A> \approx 1.5$, and the depth of maximum for a given primary energy is decreased by ≈ 50 g/cm^2 relative to the case of pure protons. This is comparable to the uncertainty in the measurements of $X_{\rm max}$, as indicated in fig. 16.8. The data in this figure are from the rapporteur talk of Sokolsky at the Moscow cosmic ray conference (1987).

Fluctuations in depth of maximum also carry information about primary composition. For example, it is unlikely that all nuclei in the 10^{18} eV range are very heavy nuclei like iron. If all showers were generated by iron nuclei, the distribution would be narrower than what is observed (Walker & Watson, 1982; Cassiday et al. 1990). On the other hand, the fact that a few showers observed with Fly's Eye in this energy appear to have maxima as shallow as ~ 600 g/cm^2 suggests that some very heavy nuclei must be present.

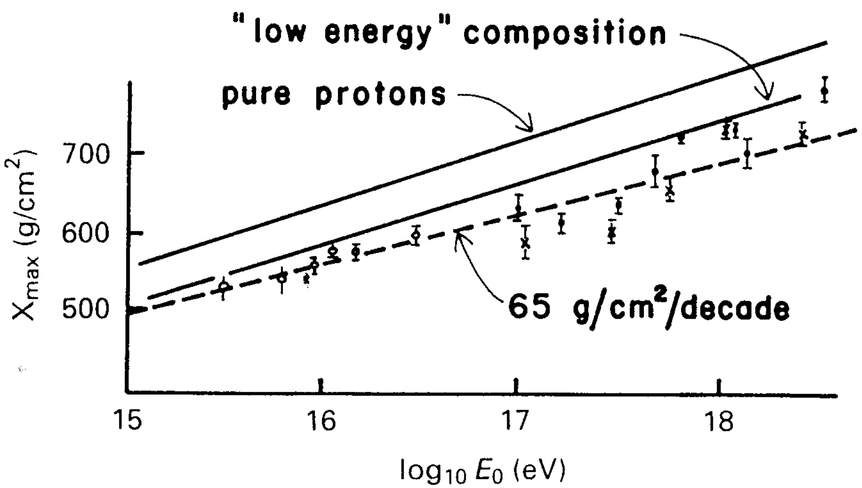

Figure 16.8: Summary of data on the elongation rate (Sokolsky, 1987). The solid lines are from Eq. 16.19.

Because of the indirect nature of the observations and the uncertainties in the models needed to interpret the data, establishing the primary composition in the air shower energy range is a painstaking process. Success depends on a global treatment of as many aspects of air showers as can be measured to find a self-consistent set of assumptions that best fits the observations.

16.5 Muons in electromagnetic cascades

An attraction of gamma ray astronomy (as compared to studying air showers in order to extract primary composition and gross features of hadronic interactions such as inelasticity and cross section) is its simplicity – at least in principle. Only the most elementary aspect of the air shower technique is crucial, the assignment of direction. Given an excess of events from a point source, the crudest measure of shower energy would suffice to study the implications for cosmic ray acceleration in astrophysical beam dumps. In view of typical galactic distances and natural limitations such as the Eddington luminosity, as discussed in chapter 13, potential sources are necessarily relatively faint. To reduce the background of ordinary cosmic ray showers, several large air shower experiments emphasize measurement of the muon content of the shower. Ironically, early indications are that the signal seems to have the same muon content as the background. Understanding the muon content of photon showers becomes therefore even more important.

16.5.1 Conventional expectation

The dominant process for producing low energy muons in an electromagnetic cascade is through photoproduction,

$$\gamma + \text{nucleus} \rightarrow \text{hadrons}.$$

When photoproduction occurs, the interaction is essentially like a pion-nucleus interaction. Muons originate from decay of the produced pions and kaons and their progeny in the resulting hadronic subshowers. The cross section for this photoproduction has been measured up to $\sim$ 20 GeV for the incident photons. Above the resonance region the cross section is about 100 μbarns per nucleon, and it appears to be rising slowly above $\sim$ 10 GeV. The corresponding cross section on an air nucleus is thus of order 1.4 mb. Comparison with (15.5) leads to the expectation that the relative probability of photoproduction as compared to pair production when a photon interacts with an air nucleus is $R = \sigma_{\gamma\to\text{hadrons}}/\sigma_{\gamma\to e^+e^-} \approx 2.8 \times 10^{-3}$.

Other potential sources of muons are smaller than this. Any pair production process in which an $e^\pm$ pair is replaced by a $\mu^\pm$ pair is suppressed by a factor of order $m_e^2/m_\mu^2 \sim 2 \times 10^{-5}$. Hadroproduction by electrons also contributes less than photoproduction because the process has to occur through exchange of a virtual photon, and the energies of the produced hadrons are low. They therefore do not contribute a large number of muons.

Before describing the results of some quantitative calculations of muons in electromagnetic cascades, I go back to Heitler's branching model and make a simple estimate of what to expect. As noted in the first section of this chapter, the numbers of $\sim$GeV muons and photons in a hadronic shower are about equal to each other. Also, $N_\mu/N_e \sim 0.1$ because each GeV photon produces of order 10 $e^\pm$ above the critical energy. This is obviously a crude argument, but it gives about the correct result for showers with $N_e \sim 10^6$ (see (16.9)). I use a related argument to estimate the number of muons in a shower initiated by a photon. If we think of a shower as an inverted branching structure (fig. 14.3), then the number of splittings to reach the GeV level is of order $n \sim \ln(E_0/1\text{ GeV}) \sim 15$ for $N_e \sim 10^6$. Once a photoproduction event occurs in an electromagnetic cascade, all further sub-branches in that segment of the tree are in the same proportions as in a cascade with a hadronic core; i.e. about equally divided between hadronic and electromagnetic. Thus, if $nR \ll 1$, the probability that a twig at the GeV level is hadronic is $R \times \ln E_0/2$. The crude estimate for the number of ~GeV muons in an electromagnetic cascade is therefore

$$N_\mu^{(\gamma)} \sim \frac{1}{2} R \ln E_0 \times N(\mathrm{GeV}),$$

where $N(\mathrm{GeV})$ is the number of branches in a shower at the GeV level. For a hadronic shower, $N_\mu^{(p)} \sim N(\mathrm{GeV})/2$, so

$$N_\mu^{(\gamma)} \sim R \ln E_0 \times N_\mu^{(p)}. \tag{16.20}$$

This result, which is derived assuming an energy-independent cross section for photoproduction, is essentially correct for the average number of muons in an electromagnetic cascade. It was obtained long ago by Karakula & Wdowczyk (1963), who did the calculation by convoluting the photoproduction cross section with the formulas in approximation A for the number of photons in an electromagnetic cascade. Similar results were found later with Monte Carlo methods (Stanev, et al., 1985: Edwards et al., 1985). One set of Monte Carlo results is shown in fig. 16.9.

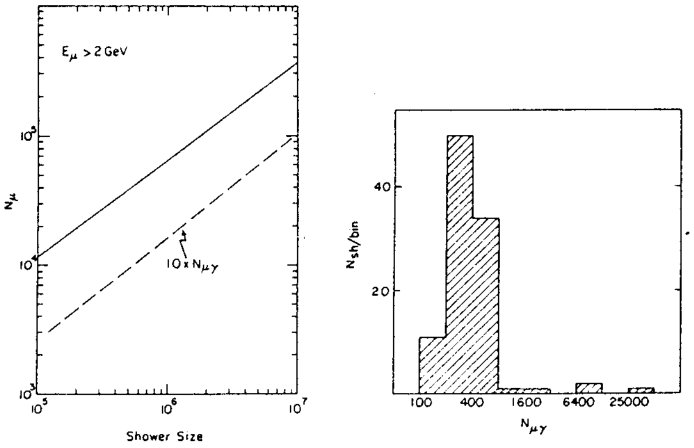

(a) (b)

Figure 16.9: (*a*): N_μ *vs* N_e for proton showers (solid line) and photon showers (dashed line) from Stanev et al. (1985). (*b*): Distribution of photon-induced showers classified by N_μ.

Fluctuations in the number of muons in photon-induced showers are rather different from ordinary cosmic ray showers. If the first interaction of the incident photon happens to be hadronic (probability $R \sim 0.003$ for conventional photoproduction), then the shower is indistinguishable from a hadronic shower. The histogram in fig. 16.9*b* contains one or two such photon showers with approximately the muon content of a hadronic shower.

16.5.2 Enhancing the muon content

There are some surprising indications (Samorski & Stamm, 1983; Dingus et al. 1988) that there may be signals from point sources that are *not* muon poor compared to hadronic showers. It is therefore important to ask how the muon content of photon-induced showers might be increased. Drees et al. (1988, 1989) argue that the type of QCD-motivated minijet model of multiparticle production referred to in §5.4 would lead to an effective threshold in the photoproduction cross section in the 100–1000 TeV range of energy. Above this threshold the photoproduction cross section may increase by as much as an order of magnitude. Instead of one shower in about 300, one would then have one in about 30 with $N_\mu^{(\gamma)} \approx N_\mu^{(p)}$. Stanev (1989) has emphasized, however, that in any model with a threshold above which $\sigma_{\gamma\to\mathrm{hadrons}}$ increases, the effect will be to increase the relative importance of the hadron-like peak at large N_μ in a sample of photon-induced showers. One cannot simply multiply (16.20) by a factor of 10, because it was derived assuming a constant photoproduction cross section. The bremsstrahlung process (15.1) rapidly degrades the energy of secondary photons in a cascade below the effective threshold for enhanced photoproduction. Thus, even a factor of 10 increase in the photoproduction cross section at high energy may not be enough to explain signals with high muon content.

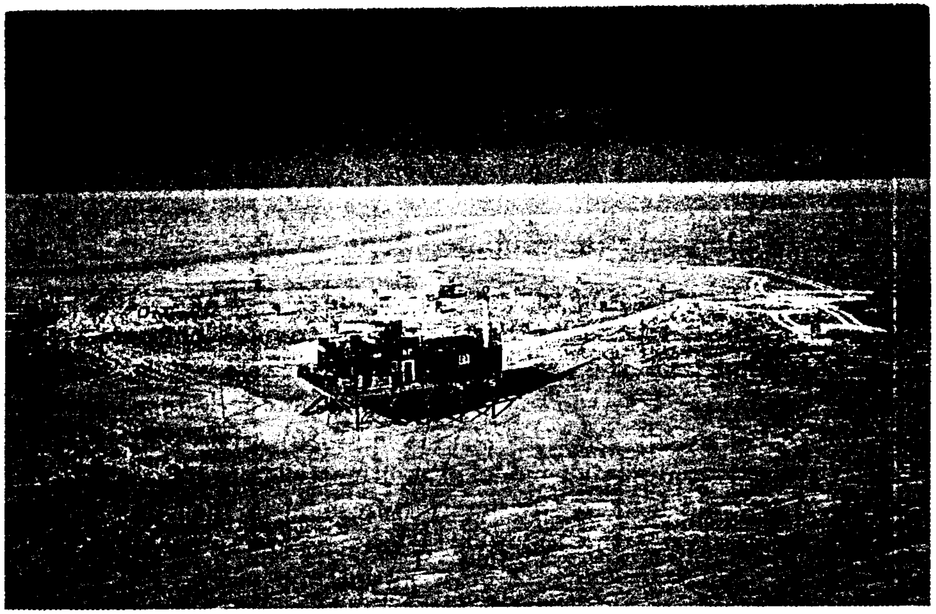

View of the South Pole Air Shower Experiment (Smith et al., 1989). At the time of this photograph (beginning of 1990) the array comprised 14 stations on a 30 meter hexagonal grid, with an additional outer guard ring of 8 detectors. It is located a few hundred meters from the geographic South Pole. The building in the foreground is the clean air facility, unrelated to SPASE. (Photo courtesy of Jay Perrett.)

Chapter 17

Simulation techniques

In this chapter I describe some techniques for simulation of air showers and two further examples of their application. One application – the calculation of coincident, energetic muons as observed with deep underground detectors – has already been discussed in chapter 14. The examples to be discussed here are: (1) calculation of the acceptance of an air shower array; and (2) inference of the proton cross section from measurements of fluctuations in air showers. Both depend on the use of Monte Carlo simulations of shower development.

17.1 Monte Carlo showers

The problem is to develop the inverted cascade tree (shown schematically in fig. 14.3) in Monte Carlo fashion. The location of each vertex and the number and properties of the lines emanating from it must be chosen randomly from appropriate distributions. Vertices can represent either decay or interaction of a particle. The length of a line is determined by the distance a particle travels before it decays or interacts – whichever occurs first. A crucial element is the model used for hadronic interactions, which affects the cascade development by determining the way in which the energy of the incoming particle at a vertex is subdivided among a number of different kinds of secondary particles. For some applications, such as multiple muons deep underground, the transverse structure of the cascade, as determined by the transverse momentum of the produced particles, is also of paramount importance.

17.1.1 UNICAS—a cascade algorithm

Several simulation programs in use are descended from J.A. Wrotniak's SHOWERSIM package (1986). The core of this set of programs is UNICAS, a subroutine that generates a shower due to the interaction of a single nucleon or photon starting at slant height H_1. The flow chart for a generalized version that includes photoproduction of hadrons is shown in fig. 17.1. (The new element here (Stanev & Vankov, 1989) is the connection, denoted by the heavy arrow, between the electromagnetic and the hadronic part of the cascade.) The modular design of SHOWERSIM allows individual subprograms to be replaced with other versions. Some of the important subroutines and their purpose are listed in Table 17.1.

Table 17.1: Major subprograms called by UNICAS (Wrotniak, 1986).

Subprogram	Function
FPNI(L,E)	selects interaction length for particle of type L, energy E
INTER(L,E,...)	generates hadronic interaction of particles L, E
DECAY(L,E,...)	generates decay of particles L, E
BREMS, PAIR	bremsstrahlung, pair production
RECORD (READY)	records information

The basic idea of the program is to follow along one series of branches of the inverted tree shown in fig. 14.3 until a twig is reached that is either below the smallest energy or the lowest altitude of interest for the problem at hand. The particles remaining to be dealt with are kept in an array (WAITAR). The index I in the flow chart is the number of particles waiting to be treated. It fluctuates up and

down during the simulation, and the shower is finished when I=0. As the program deals with each hadron, a pathlength from the point of creation to the point of next interaction is chosen randomly from the distribution appropriate for the particle. This then defines the point (H'_i in the flow chart) at which the particle is to interact. For an unstable particle (e.g. $\pi^\pm$) the height at which the particle will decay (H_{decay}) is also chosen from the appropriate distribution and compared with H'_i. Decay or interaction is chosen depending on which occurs first.

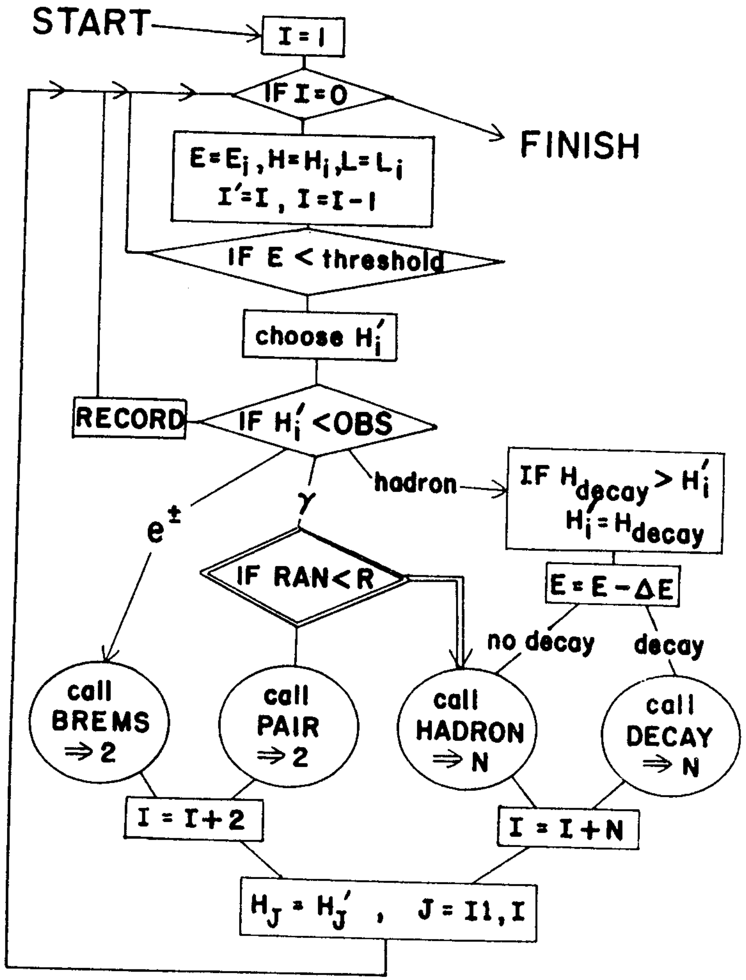

Figure 17.1: Schematic flow chart for a version of UNICAS.

17.1.2 Nuclear fragmentation

It is straightforward to incorporate UNICAS into a program that generates showers initiated by primary nuclei of mass A. One strategy is to formulate the model for nucleus–nucleus interactions, however complex it may be, as an algorithm that generates the height at which each nucleon in the projectile nucleus first interacts inelastically with a nucleus in the atmosphere. An inelastic collision is one in which secondary pions or other particles are produced. Collisions in which a nucleon is merely a spectator ejected quasi-elastically from a parent nucleus do not count here. Such a spectator nucleon will, however, have acquired transverse momentum because of the Fermi momentum it had inside the projectile nucleus. Depending on the application, UNICAS may therefore have to be generalized to allow for an initial transverse momentum.

The superposition model is trivial to incorporate – one simply calls UNICAS A times with independently chosen points of first interaction as if the nucleons in the incident nucleus were free. Each nucleon has energy E_0/A. A more realistic model, based on data from emulsions in the energy range of several GeV/nucleon, was described briefly in §14.4. This model is implemented as a library of events that contains a large number of fragmentation histories.

17.1.3 Splitting algorithm for hadronic interactions

The core of an air shower simulation is the generation of individual hadronic interactions. For detailed analysis and interpretation of experiments it is of course desirable to use a model that includes all details relevant for the application at hand, that correctly reproduces all aspects of interactions as measured at accelerators, and that makes reasonable predictions for extrapolation beyond the range of energies explored at accelerators. The goal is to make a code that embodies all relevant aspects of an appropriate physical model. In general, it is not practical simply to use an event generator designed for analysis of accelerator experiments in the context of a cosmic ray cascade. For one thing, there may be significant overhead associated with setting up the generator on the assumption that many interactions will be generated at a fixed energy with the same beam and target particles. This is not suitable for an air shower, where the energy and particles involved are different for each interaction. In addition, for a cascade simulation, energy flow in the fragmentation region is of primary importance, whereas collider experiments emphasize the central region.

The many interaction algorithms in use can be divided into two broad classes, which might be called "energy priority" and "multiplicity priority." In the first case, particles are chosen according to some algorithm until the energy is exhausted, and one must ensure that the resulting multiplicity distribution is in agreement with data. In the second case, the number of particles to be produced is chosen from the desired multiplicity distribution, and energy conservation is then imposed. In either case, it is essential to control especially carefully the momentum distributions of fast secondaries, which dominate cascade development.

For many purposes it is useful to have a fast and simple event generator that approximately reproduces the main features of hadronic interactions, and that can be tuned to explore the effects on shower development of different physical assumptions. One example is the splitting algorithm of Hillas (1981), which accomplishes these goals in an elegant way, closely related to the underlying physics. The original statement of Hillas' splitting algorithm for a nucleon projectile on a target nucleon is:

> (1) Split the total available energy randomly into two parts, A and B
> (2) Assign A as the energy of the leading nucleon;
> (3) Further subdivide the remaining energy B randomly into $J = 2^N$ parts, with $N = 2$;
> (4) Split each of the $J = 4$ pieces of energy randomly into two parts, A' and B';
> (5) Assign A' as the energy of a pion;
> (6) Subdivide B' again and assign one piece as another pion;
> (7) Continue in this way until the energy remaining is less than some preassigned threshold value. The energy threshold can depend on the problem at hand, but must be at least as large as m_π.

Two advantages are obvious immediately: first, energy is automatically conserved to the accuracy required for the problem; second, no time is wasted calculating particles below the threshold for the problem of interest. For a calculation of deep underground multiple muons, for example, the threshold could be set as high as the minimum energy of a muon that can reach the depth of the detector; i.e. in the TeV range.

To understand how Hillas' splitting algorithm can be adapted to describe interactions even better than in its original statement, it is useful to consider the analytic representations of the distributions obtained from the original version. The distribution of the leading nucleon is flat; i.e.

$$F_{NN}(x) = x\frac{\mathrm{d}n}{\mathrm{d}x} = x. \tag{17.1}$$

This distribution can be modified simply by choosing the first A according to whatever best fits the proton–nucleus data.

To derive the analytic form of the distribution of pions in the model, consider the picture shown in fig. 17.2. In this figure x_n represents the fraction of energy remaining after n splittings, and Δ_n is the fraction of energy to be assigned to a pion at the nth splitting. It is clear from the diagram that $x_n + \Delta_n = x_{n-1}$ and that $\mathrm{d}P_n/\mathrm{d}\Delta_n = \mathrm{d}P_n/\mathrm{d}x_n$, where P_n is a probability distribution normalized to one. The joint probability for finding x_n and x_{n-1} is

$$\frac{\mathrm{d}P}{\mathrm{d}x_n\mathrm{d}x_{n-1}} = \frac{1}{x_{n-1}}\frac{\mathrm{d}P_{n-1}}{\mathrm{d}x_{n-1}}\theta(x_{n-1}-x_n),$$

where θ is the step function. Thus

$$\frac{\mathrm{d}P_n}{\mathrm{d}x_n} = \int_{x_n}^{1}\frac{\mathrm{d}P_{n-1}}{\mathrm{d}x_{n-1}}\frac{\mathrm{d}x_{n-1}}{x_{n-1}}.$$

Since $\mathrm{d}P_1/\mathrm{d}x = 1$,

$$\frac{\mathrm{d}P_n}{\mathrm{d}x} = \frac{(-\ln x)^{n-1}}{(n-1)!} \tag{17.2}$$

is the normalized probability distribution for the fraction of energy assigned at the nth splitting.

The number of initial splittings of the energy remaining after the leading nucleon is chosen is N, so there are 2^N pieces of energy to be split into pions. The inclusive distribution of pions is thus 2^N times the sum over all possible splittings that can produce a pion with momentum fraction x_π:

$$\frac{\mathrm{d}n_\pi}{\mathrm{d}x_\pi} = 2^N\sum_{n=N+2}^{\infty}\frac{\mathrm{d}P_n}{\mathrm{d}x_\pi} = 2^N\sum_{n=N+2}^{\infty}\frac{(-\ln x_\pi)^{n-1}}{(n-1)!}. \tag{17.3}$$

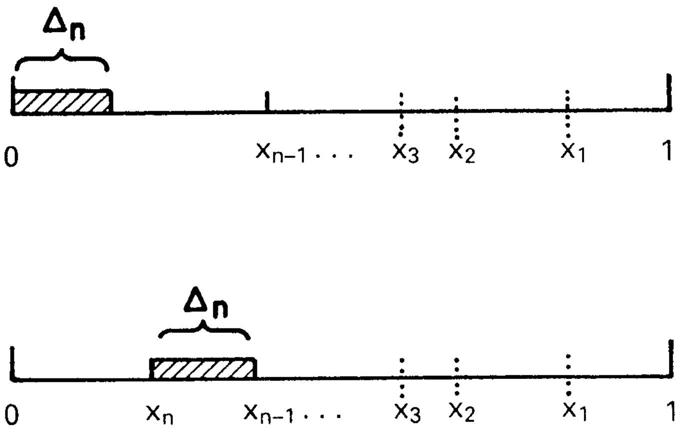

Figure 17.2: Diagram of Hilas' splitting algorithm.

Problem: Show that the leading term in the expansion of (17.3) near $x_\pi \sim 1$ is

$$\frac{dn_\pi}{dx_\pi} = 2^N\frac{(1-x)^{N+1}}{(N+1)!}.$$

Also check that the average total energy carried by pions is half the available energy, as required by energy conservation.

The series in (17.3) can be summed to show that

$$F_{N\pi} = x_\pi\frac{\mathrm{d}n_\pi}{\mathrm{d}x_\pi} = x_\pi 2^N\left\{\frac{1}{x_\pi} - \sum_{n=0}^{N}\frac{(\ln\frac{1}{x})^n}{n!}\right\}. \tag{17.4}$$

The distribution $\mathrm{d}n_\pi/\mathrm{d}x_\pi$ has the $1/x$ singularity that is characteristic of bremsstrahlung.

Problem: Show from (17.4) that

$$< n_\pi > \approx 2^N\left\{\ln\frac{1}{x_{\min}} - (N+1)\right\}.$$

Since $x_{\min} \propto 1/\sqrt{s}$, the average multiplicity in this version of the model obeys $< n_\pi > \propto \ln(s)$. Show also that the height of the rapidity plateau in the central region is proportional to 2^N.

The model can be fine-tuned in many ways. Segments of energy can be assigned as pions of different charge; some pieces can be assigned as kaons; the number of initial splittings, J, can itself be chosen from a distribution, so that it varies from event to event (J need not be an integral power of 2). The model as originally formulated manifests Feynman scaling. This feature will be maintained as any of the preceding modifications are made, provided they are made in a way that is independent of energy. Violation of Feynman scaling can also be incorporated in the algorithm. For example, the growth of the central plateau can be reproduced by making the mean number of initial splittings increase with energy.

17.2 Acceptance of an air shower array

To convert an air shower observation into a statement about the primary energy spectrum or about the spectrum of showers from a point source, one needs to know the acceptance of the array. This is crucial to be able to convert an observed rate to a measured flux:

$$\mathrm{Flux}\,(\mathrm{cm}^{-2}\,\mathrm{s}^{-1}\,\mathrm{sr}^{-1}) = \frac{\mathrm{Rate}}{A(E)\times T\times\Delta\Omega}. \tag{17.5}$$

Here $A(E)$ is the energy-dependent effective area of the array, T the on-time and $\Delta\Omega$ the solid angle. For a given triggering condition, the effective area increases with energy. Small showers that happen to penetrate very deeply and to land in favorable locations can sometimes trigger the array. At the other extreme, very large showers can trigger the array even when their cores land some distance outside the physical perimeter of the array. To calculate the acceptance it is therefore crucial to take account of fluctuations in shower development. On the other hand, it is desirable for convenience to do so in a way that avoids full Monte Carlo simulations of many showers. This section describes a method which accomplishes these goals in a straightforward way. It is sufficiently simple, for example, to be used as a standard way of comparing the acceptance of different air shower arrays. It is reliable in regions that do not depend on the extreme tails of the fluctuation distributions.

To implement the method, I use results of shower simulations obtained by Fenyves et al. (1988). They used a version of the Hillas algorithm to represent an interaction model with a rising central plateau.

They performed a series of air shower simulations to determine the longitudinal and lateral structure of showers generated by nuclei with energies from 10^{14} to 10^{16} eV. They also simulated purely electromagnetic cascades. They have represented the results with parametric forms that are modified versions of the Greisen formulas (15.43) and (15.47) for longitudinal and lateral structure of air showers. It is possible to use these parameterizations to determine the acceptance of an air shower array, including effects of fluctuations in shower development in an approximate way. Other parametric representations of shower development could be substituted into the procedure.[1]

To see how this simplified acceptance calculation works, consider the longitudinal development formulas (16.12) and (16.14). The relation between the function S_1, which represents the development of a single shower, and the function $\bar{S}$, which is the average of many showers, is

$$S_1(X) = \frac{p+1}{p}\,\frac{X_{\max}-\lambda}{X}\,\bar{S}(X) \approx \frac{X_{\max}-\lambda}{X}\,\bar{S}(X). \tag{17.6}$$

The basic idea makes use of the fact that shower development is in fact close enough to the simple equations (16.12) and (16.14) so that the relation (17.6) can be used. The average longitudinal development curves given by Fenyves et al. can be reproduced by injecting individual showers with a starting point distribution given by

$$\frac{dP}{dX_1} = e^{-X_1/\Lambda}. \tag{17.7}$$

The profile used for single showers is given by (17.6), but with the form of Feynves et al. for $\bar{S}(X)$. (It is a modified form of the Greisen parameterization, (15.43).) The average longitudinal development of photon-induced cascades is reproduced if

$$\Lambda \approx 1.5X_0, \tag{17.8}$$

where X_0 is the radiation length in air. The showers generated by protons require

$$\Lambda \approx 2.5X_0. \tag{17.9}$$

---

[1] The lateral structure functions given by Fenyves et al., are significantly narrower than the distribution for all particles shown in fig. 16.4. This is at least in part a consequence of the fact that Fenyves et al., are computing only $e^{\pm}$. For large arrays, and especially when the trigger rate due to showers outside the array perimeter are important, a broader lateral distribution may be needed.

The effective area can be calculated in a completely straightforward way at this point:

(1) Select the shower starting point randomly according to the exponential distribution (17.7) with Λ given by (17.8) or (17.9) for a photon or nucleon-induced shower.
(2) Select the intersection of the trajectory with the ground randomly from a uniform distribution over an area large enough to include all possible distances at which a shower of this energy can trigger the array.
(3) Randomly choose an azimuthal angle.
(4) For each shower calculate the density at each detector from the parameterization of the lateral structure.
(5) Take account of counting fluctuations. This can be done either by using a Poisson distribution with mean given by the density times the detector area or by using a distribution of signal about the mean that has been measured experimentally. (Remember to project the detector locations onto a plane normal to the particular shower trajectory. However, the projected signal itself remains approximately constant for a scintillator because the smaller projected area of the detector is compensated by the longer track length through the scintillator.)
(6) Check to see whether this particular shower has triggered the array.

The effective area for a set of showers of the same primary energy and particle type and for the same zenith angle is given by the projected trial area normal to the shower trajectory multiplied by the number of showers that triggered the array. The procedure needs to be repeated for a grid of primary energies and zenith angles. It can also be repeated for different kinds of nuclei.

An important point is that one can finesse the problem of determining in detail the actual physical triggering condition for a detector.[2] This is done by adjusting the nominal trigger condition (e.g. the number of $e^{\pm}$ above 5 MeV) to reproduce the observed counting rate of the detector. (This will work when the primary spectrum can be assumed known from other measurements, for example, when the object is to calculate the acceptance for photons from point sources.) The observable features that can be reproduced, in addition to the overall triggering rate, are the angular distribution of triggers and the relative rates of events that trigger more than the minimum number of detectors. Since this is an overconstrained fit, it is in fact a test of the assumptions used for the simulation. (It may, for example, be possible to compare simulated and measured angular distributions to make inferences about the primary composition.)

An example of an application of this method is shown in fig. 17.3, which shows the effective area of the array separately for photons and protons for particular trigger settings of the South Pole Air Shower Array (SPASE – Smith et al., 1988; Gaisser et al., 1989). The response of the array, which is the effective area times an incident spectrum, is shown for two assumed photon spectra in fig. 17.4. Note that an array does not have a single threshold energy, but an efficiency for shower detection that increases with energy. The response curves in fig. 17.4 were used to place upper limits on showers from SN1987A.

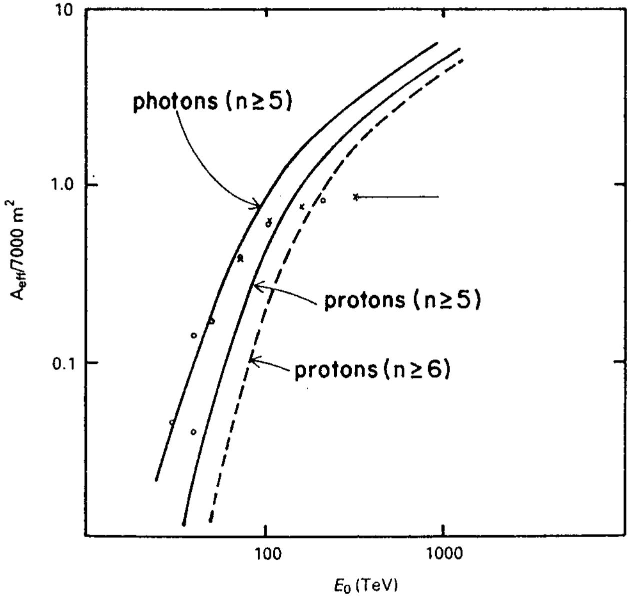

Figure 17.3: Effective area for a particular trigger setting of SPASE in units of the physical area of the array (~ 7000 m^2).

---

[2] The threshold for a detector will depend on the pulse height and rise time of the signal generated, which is generally related in a complex way to the number, type and location of the particles incident on the detector.

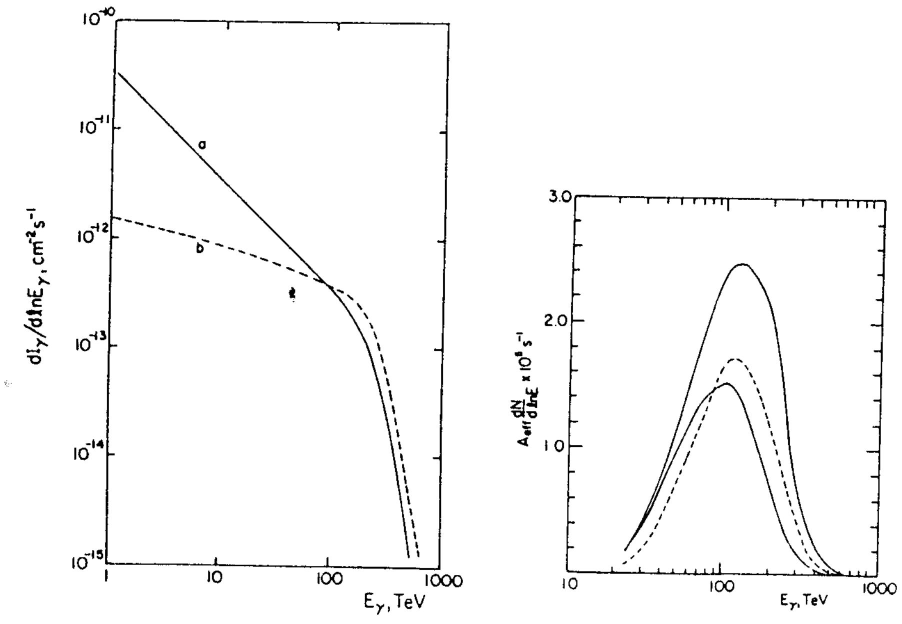

(a) (b)

Figure 17.4: Response of SPASE (b) for two assumed photon spectra (a). Dashed and solid curves in the two graphs correspond to each other. The upper solid curve in (b) is for all triggers; the lower curves are for showers that land inside the perimeter of the array.

17.3 Cross section at air shower energies

Independent air shower simulations (Ellsworth et al., 1982; Hara et al., 1983) lead to the result that fluctuations in longitudinal shower development deep in the atmosphere can be represented by an exponential attenuation with attenuation length

$$\Lambda \sim 1.6 \times \lambda_N, \tag{17.10}$$

where λ_N is the nucleon interaction length. This result is for models with approximate scaling in the fragmentation region, and it is the basis for two different determinations of the cross section from air shower experiments. (Note the similarity of (17.10) to (17.9). Both are expressing the same physics of fluctuations in longitudinal development of air showers.) A summary of results for the inelastic cross section for nucleons interacting with air nuclei ($A \approx 14.5$) is shown in fig. 17.5.

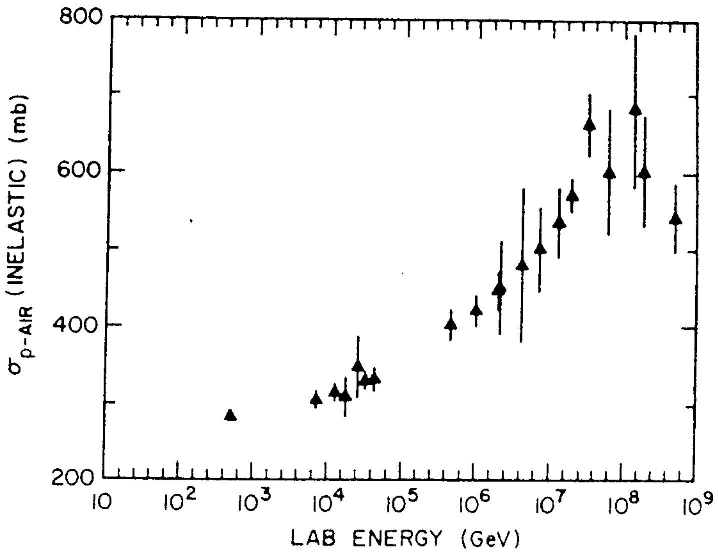

Figure 17.5: A summary of measurements of the inelastic proton-air cross section from cosmic ray experiments. The points above 10^6 GeV are from conventional air shower experiments (Hara et al., 1983), except for the point at the highest energy from the Fly's Eye (Baltrusaitas et al., 1984).

In the Akeno experiment, the cross section is measured by studying the zenith angle dependence of showers with the same values of N_μ and N_e. Classifying showers by N_μ is approximately equivalent to binning them by energy, whereas, showers of the same energy with the same N_e are at the same stage of development relative to ground level. (Recall the discussions of figures 14.2 and 16.2.) Thus by fitting the angular dependence of a given group of showers to

$$\exp\left[-\frac{X\sec\theta}{\Lambda}\right],$$

one estimates λ_N from (17.10), and hence $\sigma^{\text{inel}}_{\text{p-air}}$.

The Fly's Eye method to determine the cross section is in principle more direct, because the experiment can measure the depth of maximum directly on a shower by shower basis. The deep tail of the depth of maximum distribution is assumed to reflect the proton cross section, again according to the relationship in (17.10). In practice, this method also has its complexities because the depth of maximum distribution has a significant instrumental component which must be understood and deconvoluted. Further discussion of the Fly's Eye measurement of cross section is contained in the book by Sokolsky (1988).

Both methods have the fundamental limitation that they must assume that there are sufficient protons in the primary spectrum to allow a measurement of the proton interaction length. If the primaries are all nuclei with $Z > 1$, no analysis, however sophisticated, can extract the proton cross section! On the other hand, the full depth of maximum distribution, which can be explored by Fly's Eye, carries information about composition as well cross section, so that both can be inferred from the data by fitting the whole distribution. This work is in progress (Cassiday et al., 1990).

References

Section headings in the References correspond to the chapters of the book.

1. Cosmic rays

Burnett, T.H., et al. (1983). *Phys. Rev. Letters* **51**, 1010.

Evenson, P.A. (1988). *Proc. Conf. on Interplanetary Particle Environment* (JPL Pub. 88-28, ed. Joan Feynman and Stephan Gabriel) pp. 149-161.

Grigorov, N.L., et al. (1970). *Yad. Fiz.* **11**, 1058.

Grunsfeld, John M., et al. (1988). *Ap. J.* **327**, L31.

Ormes, J. & Freier, P. (1978). Ap. J. **222**, 471.

Simpson, J.A. (1983). *Ann. Revs. Nucl & Part. Sci.* **33**, 323.

General bibliography on cosmic rays and related astrophysics.

Ginzburg, V.L. & Syrovatskii, S.I. (1964). *The Origin of Cosmic Rays.* Pergamon Press. Classic monograph.

Hayakawa, S. (1969). *Cosmic Ray Physics.* Wiley-Interscience. Standard reference text.

Hillas, A.M. (1972). *Cosmic Rays.* Pergamon Press. Reprint volume of classic papers with extensive introduction.

Longair, M.S (1981) *High Energy Astrophysics.* Cambridge University Press.

Pomerantz, M.A. (1971). *Cosmic Rays.* Van Nostrand.

Rossi, B. (1952). *High-Energy Particles.* A storehouse of relevant information and techniques from the era when cosmic rays and particle physics were a single subject.

Waddington, C.J. (ed.), (1989). *Cosmic Abundances of Matter*, American Institute of Physics Conference Proceedings No. 183.

2. Particle physics

Arnison, G. et al. (1984). *Physics Letters* **136B**, 294.

Bagnaia, P. et al. (1984). *Physics Letters* **144B**, 283.

Cabibbo, N., Corbo, G. & Maiani, L. (1979). *Nuclear Physics* **B155**, 93.

Feynman, R.P. (1969). *Phys. Rev. Letters* **23**, 1415.

Yen, E. (1974). *Phys. Rev.* **D10**, 836.

General bibliography on particle physics.

Halzen, Francis & Martin, Alan D. (1984). *Quarks & Leptons: An Introductory Course in Modern Particle Physics*. John Wiley & Sons.

Perkins, Donald (1986). *Elementary Particle Physics* (3rd ed.). Addison-Wesley.

3. Cascade equations

Frazer, W.R. et al. (1972). *Phys. Rev.* **D5**, 1653.

Garraffo, Z., Pignotti, A., & Zgrablich, G. (1973). *Nucl. Physics* **B53**, 419.

Heitler, W. & Janossy, L. (1949). *Proc. Phys. Soc. (London) Sect. A* **62**, 374, 669.

Rossi, B. & Greisen, K. (1941). *Revs. Mod. Phys.* **13**, 240.

4. Hadrons & photons

Aubert, J.J. et al. (1974). *Phys. Rev. Letters* **33**, 1404.

Augustin, J.-E. et al., *Phys. Rev. Letters* **33**, 1406.

Bayburina, S.G. et al. (1981). *Nucl. Phys.* **B191**, 1.

Burnett, T.H. et al. (1983). *Phys. Rev. Letters* **51**, 1010.

Burnett, T.H. et al. (1987). *Phys. Rev.* **D35**, 824.

Ellsworth, R.W. et al. (1981). *Phys. Rev.* **D23**, 771.

Gaisser, T.K. & Halzen, F. (1976). *Phys. Rev.* **D14**, 3153.

Gaisser, T.K. & Yodh, G.B. (1980). *Ann Rev. Nucl. Part. Sci.* **30**, 475.

Glashow, S., Iliopoulos, J. & Maiani, L. (1970). *Phys. Rev.* **D2**, 1285.

Hayashi, T. et al. (1972). *Prog. Theor. Phys.* **47**, 280 and 1998.

Lattes, C.M.G., Occhialini, G.P.S. & Powell, C.F. (1947). *Nature* **160**, 453.

Lattes, C.M.G. et al. (1971). *Suppl. Prog. Theor. Phys.* **47**, 1.

Lattes, C.M.G., Fujimoto, Y. & Hasegawa, S. (1980). *Physics Reports* **65**, 151.

Navia, C.E. et al. (1989). *Phys. Rev.* **D40**, 2898.

Niu, K., Mikumo, E. & Maeda, Y. (1971). *Prog. Theor. Phys.* **46**, 1644.

Pfotzer, G. (1936). *Z. Phys.* **102**, 23.

Powell, C.F., Fowler, P.H. & Perkins, D.H. (1959). *The Study of Elementary Particles by the Photographic Method*. Pergamon, London.

Ren, J.R. et al. (1987). *Nuovo Cimento* **10C**, 43.

Ren, J.R. et al. (1988). *Phys. Rev.* **D38**, 1404, 1417 and 1426.

Shibuya, E. (1987). Rapporteur talk, 20th Int. Cosmic Ray Conf. (Moscow).

Stanev, T. & Yodh, G. B. (1988). In *Hadronic Multiparticle Production* (ed. P. Carruthers) World Scientific, Singapore, p. 289.

5. Accelerator data

Albajar, C. et al. (1988). *Nucl. Phys.* **B309**, 405.

Alner, G.J. et al. (1986). *Z. Phys. C* **33**.

Anisovich, V.V. et al. (1985). *Quark Model and High Energy Collisions*. World Scientific, Singapore.

Baltrusaitis, R.M. et al. (1984). *Phys. Rev. Letters* **52**, 1380.

Barton, D.S. et al. (1983). *Phys. Rev.* **D27**, 2580.

Block, M.M. & Cahn, R.N. (1985). *Revs. Mod. Phys.* **57**, 563.

Bozzo, P. et al. (1984). *Physics Letters* **147B**, 392.

Braune, K. et al. (1983). *Z. Phys.* **C17**, 105.

Brenner, A.E. et al. (1982). *Phys. Rev.* **D26**, 1497.

Cline, D., Halzen, F. & Luthe, J. (1973). *Phys. Rev. Letters* **31**, 491.

Denisov, S.P. et al. (1973). *Nucl. Phys.* **B61**, 62.

Durand, L. & Pi, H. (1987). *Phys. Rev. Letters* **58**, 303.

Durand, L. & Pi, H. (1989). *Phys. Rev.* **D40**, 1436..

Eichten, E., et al. (1984). *Revs. Mod. Phys.* **56**, 579 (and E**58**, 1065 (1986).

Ellsworth, R.W. et al. (1982). *Phys. Rev.* **D26**, 336.

Flaminio, V. et al. (1983). CERN-HERA Report 83-01, π^+ *and* π^- *Induced Reactions* and 83-02, K^+ *and* K^- *Induced Reactions.*

Flaminio, V. et al. (1984). CERN-HERA Report 84-01, *p and* $\bar{p}$ *Induced Reactions.*

Fowler, G.N., et al. (1987). *Phys. Rev.* **D35**, 870.

Gaisser, T.K. & Stanev, T. (1989). *Phys. Lett.* **219**, 375.

Gaisser, T.K., Sukhatme, U.P. & Yodh, G.B. (1987). *Phys. Rev.* **D36**, 1350.

Glauber, R.J. & Matthiae, G. (1970). *Nucl. Phys.* **B21**, 135.

Hara, T. et al. (1983). *Phys. Rev. Letters* **50**, 2058. See also *Proc. Int. Symposium on Cosmic Rays and Particle Physics* (Tokyo, 1984, ed. A Shsawa and T. Yuda) Institute for Cosmic Ray Research, University of Tokyo, p. 756.

Kopeliovich, B.Z., Nikolaev, N.N. & Potachnikova, I.K. (1989). *Phys. Rev.* **D39** 769.

Pal, Y. & Peters, B. (1964). *Mat. Fys. Medd. Dan. Vid. Selsk.* **33**, no. 15.

Sokolsky, Pierre (1988). *Introduction to Ultrahigh Energy Cosmic Ray Physics*, Addison-Wesley Publishing Company.

Westfall, G.D. et al. (1979). *Phys. Rev.* **C19**, 1309.

Yodh, G.B. et al. (1983). *Phys. Rev.* **D27**, 1183.

Yodh, G.B., Pal, Y. & Trefil, J.S. (1972). *Phys Rev. Letters* **28**, 1005. Also *Phys. Rev.* **D8**, 3233 (1973).

6. Muons

Adarkar, H. et al. (1990). *Proc. 21st Int. Cosmic Ray Conf.* (Adelaide), **9**, 310.

Allkofer, O.C. & Grieder, P.K.F. (1984). "Cosmic Rays on Earth," *Physics Data.* Fachinformationszentrum, Karlsruhe, Nr. 25-1.

Andreyev, Yu. M. et al. (1990). *Ibid.*, 301.

Barrett, P.H. et al. (1952). *Revs. Mod. Phys.* **24**, 133.

Berger, Ch. et al. (1989). *Phys. Rev.* **D40**, 2163.

Cassiday, G.L., Keuffel, J.W. & Thompson, J.A. (1973). *Phys. Rev.* **D7**, 2022.

Crouch, M.F., et al. (1978). *Phys. Rev.* **D18**, 2239.

Crouch, M.F. (1987). *Proc. 20th Int. Cosmic Ray Conf.* (Moscow) **6**, 165.

Elbert, J.W., et al. (1975). *Phys. Rev.* **D12**, 660.

Frazer, W.R. et al. (1972). see §3.

Gaisser, T.K. (1974). *J. Geophys. Res.* **79**, 2281.

Krishnaswamy, M.R. et al. (1977). *Proc. 15th Int. Cosmic Ray Conf.* (Plovdiv) **6**, 85.

Krishnaswamy, M.R. et al. (1982). *Pramāṇa* **19**, 525.

Rosental, I.L. (1968). *Sov. Phys. Uspekhi* **11**, 49.

7. Neutrinos

Auriemma, G. et al. (1988). *Phys. Rev.* **D37**, 665.

Ayres, D. et al. (1984). *Phys. Rev.* **D29**, 902.

Ayres, D. et al. (1986). In *Proceedings of the Summer Study on the Physics of the Superconducting Super Collider*, Ed. R. Donaldson and J. Marx (Division of Particles and Fields of the APS, New York.

Bahcall, J.N. (1989). *Neutrino Astrophysics.* Cambridge University Press.

Barr, G., Gaisser, T.K. & Stanev, T. (1989). *Phys. Rev.* **D39**, 3532.

Barr, S. Gaisser, T.K., Tilav, S. & Lipari, P. (1988). *Phys. Letters* **214**, 147.

Boehm, F. & Vogel, P. (1987). *Massive Neutrinos.* Cambridge University Press.

Carlson, E.D. (1986). *Phys. Rev.* **D34**, 1454.

Gaisser, T.K., Stanev, T. & Barr, G. (1988). *Phys. Rev.* **D38**, 85.

Greisen, K. (1960). *Ann. Revs. Nuclear Science* **10**, 63.

Hayakawa, S. (1969). See §1.

Hirata, K.S. et al. (1988). *Phys. Letters B* **205**, 416.

Kuo, T.K. & Pantaleone, J. (1989). *Revs. Mod. Phys.* **61**, 937.

Langacker, P. et al. (1983). *Massive Neutrinos in Astrophysics and Particle Physics*, (Proc. 6th Moriond Workshop, ed. O. Fackler & J. Tran Thanh Van, Editions Frontières) p. 101.

LoSecco, J.M. et al. (1985). *Phys. Rev. Letters* **54**, 2299.

Lee, H. & Bludman, S.A. (1988). *Phys. Rev.* **D37**, 122.

Mikheyev, S.P. & Smirnov, A. Yu. (1985). *Sov. J. Nucl. Phys.* **42**, 1441.

Reines, F. (1960). *Ann. Revs. Nuclear Science* **10**, 1.

Volkova, L.V. (1980). *Yad. Fiz.* **31** 1510.

Wolfenstein, L. (1978). *Phys. Rev.* **D17**, 2369.

8. Neutrino-induced muons

Boliev, M.M. et al. (1981). *Proc. 17th Int. Cosmic Ray Conf.* (Paris) **7**, 106.

Crouch, M.F. et al. (1978). See §6.

Krishnaswamy, M.R. et al. (1982). See §6.

Gaisser, T.K. & Stanev, T. (1985). In *Sixth Workshop on Grand Unification* (ed. S. Rudaz & T.F. Walsh) p. 236. See also *Phys. Rev.* **D30**, 985-990 (1984).

Gaisser, T.K. & Grillo, A.F. (1987). *Phys. Rev.* **36**, 2752.

Okun, L.B. (1982). *Leptons and Quarks* (North Holland, Amsterdam) p. 149.

Oyama, Y., et al. (1989). *Phys. Rev.* **D39**, 1481.

Reno, M.H. & Quigg, C. (1988). *Phys. Rev.* **D37**, 657.

Svoboda, R. et al. (1987). *Ap. J.* **315**, 420.

9. Propagation

Blandford, R. & Eichler, D. (1987). *Physics Reports* **154**, 1.

Cesarsky, C.J. (1980). *Ann. Rev. Astron. Astrophys.* **18**, 289.

Cesarsky, C.J. (1987). Rapporteur talk in *Proc. 20th Int. Cosmic Ray Conf.* (Moscow), **8**, 87.

Cowsik, R. & Wilson, L. (1973). *Proc. 13th Int. Cosmic Ray Conf.* (Denver) vol. 1, p. 500.

Esposito, J.A. et al. (1990). *Ap. J.* (in the press).

Garcia-Munoz, M., Mason, G.M. & Simpson, J.A. (1977). *Ap. J.* **217**, 859.

Ginzburg, V.L., Khazan, Ya. M. & Ptuskin, V.S. (1980). *Astrophysics and Space Science* **68**, 295.

Gordon, M.A. & Burton, W.B. (1976). *Ap. J.* **208**, 346.

Grunsfeld, J. et al. (1988). See §1.

Gupta, M. & Webber, W.R. (1989). *Ap. J.* **340**, 1124 (1989).

Shapiro, M.M. & Silberberg, M. (1970). *Ann. Rev. Nucl. Sci.* **20**, 323.

Silberberg, R., Tsao, C.H. & Letaw, J. (1983). In *Composition and Origin of Cosmic Rays* (ed. M.M. Shapiro, D. Reidel), p. 321.

Simpson, J.A. (1983). See §1.

Spitzer, L., Jr. (1978). *Physical Processes in the Interstellar Medium* (John Wiley & Sons, New York).

10. Gamma rays and antiprotons

Ahlen, S.P. et al. (1982). *Ap. J.* **260**, 20.

Ahlen, S.P. et al. (1988). *Phys. Rev. Letters* **61**, 145.

Berezinsky, V.S. & Kudryavtsev, V.A. (1989). *Ap. J.* **349**, 620.

Bogomolov, E.A. (1987). *Proc. 20th Int. Cosmic Ray Conf.* (Moscow) **2**, 72.

Buffington, A., Schindler, S.M. & Pennypacker, C.R. (1981). *Ap. J.* **248**, 1179.

Cesarsky, C.J. (1987). See §9.

Cowsik, R. & Gaisser, T.K. (1981). *Proc. 17th Int. Cosmic Ray Conf.* (Paris) **2**, 218.

Dermer, C.D. (1986). *Astron. Astrophys.* **157**, 223.

Dermer, C.D. & Ramaty, R. (1986). In *Accretion Processes in Astrophysics*, eds. J. Audouze & J. Tran Thanh Van (Editions Frontieères, pp. 85-98.

Fichtel, C.E. & Kniffen, D.A., (1984). *Astron. Astrophys.* **134**, 13.

Fichtel, C.E. & Trombka, J.I. (1981). *Gamma Ray Astrophysics, New Insight into the Universe* (NASA Scientific and Technical Information Branch) NASA SP-453.

Gaisser, T.K. & Levy, E.H. (1974). *Phys. Rev.* **D10**, 1731.

Golden, R.L. et al. (1979). *Phys. Rev. Letters* **43**, 1196. See also *Ap. J.* **24**, 75 (1984).

Golden, R.L. et al. (1987). *Astron. Astrophys.* **188**, 145.

Protheroe, R.J. (1981). *Ap. J.* **251**, 387.

Stephens, S.A. & Golden, R.L. (1987). *Space Science Revs.* **46**, 31.

Simon, M. et al. (1987). *Ap. J.* **320**, 699.

Stecker, F.W. (1971). *Cosmic Gamma Rays* (NASA Scientific and Technical Information Office) NASA SP-249.

Stecker, F.W. (1985). *Nucl. Phys.* **B252**, 25.

Stecker, F.W., (1979).*Ap. J.* **228**, 919.

Stecker, F.W. & Wolfendale, A.W. (1984). *Nature* **309**, 37. See also F.W. Stecker, R.J. Protheroe & D. Kazanas, *Astrophysics and Space Science* **96**, 171 (1983).

Steigman, G. (1976). *Ann. Revs. Astron. Astrophys.* **14**, 339.

Steigman, G. (1977). *Ap. J.* **217**, L131.

Streitmatter, R.E. et al. (1989). *Advances in Space Science* **9**, 65.

Swanenburg, B.N., et al. (1981). *Ap. J.* **245**, L69.

Taylor, F.E. et al. (1976). *Phys. Rev.* **D14**, 1217.

Webber, W.R., Golden, R.L. & Mewaldt, R.A. (1987). *Ap. J.* **312**, 178.

Webber, W.R. & Potgieter, W.S. (1989). *Ap. J.* **344**, 779.

Wolfendale, A.W., (1988). In *Cosmic Gamma Rays, Neutrinos and Related Astrophysics* (NATO ASI Series, ed. M.M. Shapiro & J.P. Wefel) pp. 513-522.

11. Acceleration

Armstrong, T.P., Pesses, M.E. & Decker, R.B. (1985). In *Collisionless Shocks in the Heliosphere* (ed. B. Tsurutani and R.G. Stone), Geophysical Monograph #35, Am. Geophys. Union, p. 271.

Axford, W.I. (1981). *Proc. 17th Int. Cosmic Ray Conf.* (Paris), **12**, 155. See also Axford's rapporteur talk in *Proc. 20th Int. Cosmic Ray Conf.* (Moscow), **8**, 120 (1987).

Bell, A.R. (1978). *Mon. Not. R. Astr. Soc.* **182**, 147 and 443.

Blandford, R. & Eichler, D. (1987). See §9.

Chupp, E.L. (1984). *Ann. Rev. Astron. Astrophys.* **22**, 359.

Davis, L. (1956). *Phys. Rev.* **101**, 351.

Drury, L. O'C. (1983). *Rep. Prog. Phys.* **46**, 973.

Fermi, E. (1949). *Phys. Rev.* **75**, 1169.

Ginzburg, V.L. & Syrovatskii, S.I. (1964). See §1.

Jokipii, J.R., (1987) "Mechanism of Particle Energy Gain at Shocks: The Role of Magnetic Field Geometry," Proc. 6th Int. Solar Wind Conf. (Estes Park, Colorado, August 1977) NCAR TN-306, vol 2, p. 481. See also Ap. J. **313**, 842 (1987) and **255**, 716 (1982).

Lagage, P.O. & Cesarsky, C.J. (1983). *Astron. Astrophys.* **118**, 223 and **125**, 249.

Landau, L.D. & Lifshitz, E.M. (1982). *Fluid Mechanics* (Pergamon Press, Oxford), pp. 315, 331.

Longair, M.S. (1981). See §1.

Peters, B. (1959). *Nuovo Cimento (Suppl.)* **14**, 436. See also *Proc. 6th Int. Cosmic Ray Conf.* (Moscow) **3**, 157 (1960).

Webb, G.M. (1987). *Ap. J.* **319**, 215.

12. Acceleration to >100 TeV

Arons, J. (1981). In *IAU Symposium 94, Origin of Cosmic Rays*, ed. G. Setti, G. Spada & A.W. Wolfendale (D. Reidel), p. 175.

Berezinsky, V.S. & Ginzburg, V.L. (1987). *Nature* **329**, 807.

Bignami, G.F., Maraschi, L. & Treves, A. (1977). *Astron. Astrophys.* **55**, 155.

Cesarsky, C.J. & Montmerle, T. (1983).*Space Sci. Revs.* **36**, 173.

Chanmugam, G. & Brecher, K. (1985). *Nature* **313**, 767.

Cheng, K.S., Ho, C. & Ruderman, M. (1986). *Ap. J.* **300**, 500 and 522.

Cheng, K.S. & Ruderman, M.A. (1989). *Ap. J.* **337**, L77.

Clayton, D.D. (1968). *Principles of Stellar Evolution and Nucleosynthesis* (McGraw-Hill Book Company, New York).

Frank, J., King, A.R. & Raine, D.J., (1985). *Accretion Power in Astrophysics* (Cambridge University Press).

Fruchter, A.S., Stinebring, D.R. & Taylor, J.H. (1988). *Nature* **333**, 237.

Gaisser, T.K., Harding, A. & Stanev, T., (1989). *Ap. J.* **345**, 423. See also *Nature* **329**, 314, (1987).

Harding, A.K. & Gaisser, T.K. (1989). *Ap. J.* (to be published).

Hillas, A.M. (1984). *Ann. Revs. Astron. Astrophys.* **22**, 425.

Honda, M. et al. (1985). *Proc. 19th Int. Cosmic Ray Conf.* (La Jolla) **2**, 272, 276.

Jokipii, J.R. (1987). See §11.

Jokipii, J.R. & Morfill, G.E., (1987). *Ap.J.* **312**, 170 (and **290**, L1, 1985).

Joss, P.C. & Rappaport, S.A. (1984). *Ann. Rev. Astron. Astrophys.* **22**, 537.

Katz, J.I. (1987). *High Energy Astrophysics* (Addison-Wesley Frontiers in Physics series).

Katz, J.I. & Smith, I.A. (1988). *Ap. J.* **326**, 733.

Kazanas, D. & Ellison, D.C., (1986). *Nature* **319**, 380.

Lagage, P.O. & Cesarsky, C.J. (1983). See §11.

Lovelace, R.V.E. (1976). *Nature* **262**, 649.

Matthaeus, W.H., Ambrosiano, J.J. & Goldstein, M.L. (1984). *Phys. Rev. Letters* **53**, 1449.

Pacini, F. & Salvati, M. (1973). *Ap. J.* **186**, 249.

Patterson, J. (1984). *Ap. J.* (Supplement Series) **54**, 443.

Phinney, E.S. et al. (1988). *Nature* **333**, 832.

Pringle, J.E. & Wade, R.A. (1985). *Interacting Binary Stars* (Cambridge University Press).

Rees, M.J. & Gunn, J.E. (1974). *Mon. Not. R. Astron. Soc.* **167**, 1.

Sorrell, W.H. (1984). In *Cosmic Radiation in Contemporary Astrophysics* (ed. M.M. Shapiro) D. Reidel, NATO ASI series.

Völk, H.J. & Biermann, P.L., (1988). *Ap. J.* **333**, L65.

Wang, Y.-M. (1986). Astrophysics and Space Science **121**, 193.

Webb (1987). See §11.

13. Astrophysical beam dumps

Bonnet-Bidaud, J.-M. & Chardin, G. (1988). *Physics Reports* **170**, 325.

Berezinsky, V.S., Castagnoli, C. & Galeotti, P., *Nuovo Cimento* **8C**, 185.

Cassiday, G.L., et al. (1989). *Phys. Rev. Letters* **62**, 383.

Chadwick, P.M. et al. (1985). *Nature* **318**, 642.

Chupp, E.L. (1984). See §11.

Deeter, J.E., et al. (1981). *Ap. J.* **247**, 1003.

Dingus, B.L., et al. (1988). *Phys. Rev. Letters* **60**, 1785.

Gaisser, T.K. & Stanev, T.S. (1985). *Phys. Rev. Letters* **54**, 2265.

Gaisser, T.K. et al. (1986). *Ap. J.* **309**, 674.

Gaisser, T.K. et al. (1989). *Phys. Rev. Letters* **62**, 1425.

Gorham, P.W. & Learned, J.G. (1986). *Nature* **323**, 422.

Gould, R.J. & Schreder, G. (1966). *Phys. Rev. Letters* **16**, 252.

Hillas, A.M. (1984). *Nature* **312**, 50. See also Proc. 19th Int. Cosmic Ray Conf. (La Jolla) vol 9, pp. 407-414 (1985).

Jelley, J.V. (1966). *Phys. Rev. Letters* **16**, 479.

Jones, L.W. (1988). In *Proc. 5th Int. Symposium on Very High Energy Cosmic Ray Interactions* (ed. Maria Giler, Univ. Lodz, Poland) p. 358.

Kolb, E.W., Turner, M.S. & Walker, T.P. (1985). *Phys. Rev.* **D32**, 1145.

Lawrence, M.A., Prosser, D.C. & Watson, A.A. (1989). *Phys. Rev. Letters* **63**, 1121.

Markov, M.A. (1960). In *Proc. 1960 Int. Conf. on High Energy Physics at Rochester* (10th, ed. Sudarshan, E.C.G., Tinlog, J.H. & Melissinos, A.C.) p. 597.

Nagle, D.E., Gaisser, T.K. & Protheroe, R.J. (1988). *Ann Rev. Nucl. Part. Sci.* **38**, 609.

Oyama,Y., et al. (1989). See §8.

Pinto, P.A. & Woosley, S.E. (1988). *Nature* **333**, 534.

Protheroe, R.J. (1986). *Mon. Not. R. Astron. Soc.* **221**, 769.

Protheroe, R.J. (1987). Rapporteur paper in *Proc. 20th Int. Cosmic Ray Conf.* (Moscow), **8**, 21.

Protheroe, R.J. & Stanev, T.S. (1987). *Nature* **328**, 136.

Samorski, M & Stamm, W. (1983). *Ap. J.* **268**, L17.See also Proc. 18th Int. Cosmic Ray Conf. (Bangalore) Vol. 11, p. 244 (1983).

Stecker, F.W., Harding, A.K. & Barnard, J.J. (1985). *Nature* **316**, 418.

Stenger, V.S. (1984). *Ap. J.* **284**, 810.

Svoboda, R. et al. (1987). See §8.

Vestrand, W.T. & Eichler, D. (1982). *Ap. J.* **261**, 251. See also D. Eichler & W.T. Vestrand, Nature **307**, 613 (1984).

Watson, A.A. (1985). Rapporteur paper in *Proc. 19th Int. Cosmic Ray Conf.* (La Jolla) vol. 9, p. 111.

Weekes, T.C., (1988). *Physics Reports* **160**, 1.

14. Air showers

Baltrusaitas, R.M. et al. (1985). *Nucl. Instruments and Methods in Physics Research* **A240**, 410.

Bialas, A., Bleszynski, M. & Czyz, W. (1976). *Nuclear Physics* **B111**, 461.

Bilokon, H. et al., (1990). *Proc. 21st Int. Cosmic Ray Conf.* (Adelaide) **9**, 366.

Bologna, G. et al. (1985). *Nuovo Cimento* **8C**, 76.

Elbert, J.W. (1978). In *Proc. DUMAND Summer Workshop* (ed. A. Roberts) vol. 2, p. 101.

Elbert, J.W., Gaisser, T.K. & Stanev, T. (1983). *Phys. Rev.* **D27**, 1448.

Fichtel, C.E. & Linsley, J. (1986). *Ap. J.* **300**, 474.

Forti, C. (1988). Thesis: University of Rome, "La Sapienza".

Gaisser, T.K. & Stanev, T. (1985). *Nuclear Instruments and Methods in Physics Research* **A 235**, 183.

Gaisser, T.K., Stanev, T.S., Freier, P. & Waddington, C.J. (1982). *Phys. Rev.* **D25**, 2341.

Goodman, J.A. et al. (1979). *Phys. Rev. Letters* **35**, 854.

Greisen, K. (1956). *Prog. Cosmic Ray Physics* **3**, 1.

Greisen, K. (1960). *Ann. Revs. Nuclear Science* **10**, 63.

Heitler, W. (1944). *Quantum Theory of Radiation* (Oxford University Press) 2nd edition.

Heitler, W. (1949). *Revs. Mod. Phys.* **21**, 113.

Lamb, R.C. & Weekes, T.C. (1987). *Science* **238**, 1528.

Ren, J.R. (1988). See §4.

Sokolsky, P. (1988). See §5.

Weekes, T.C. (1988). See §13.

Weekes, T.C. et al. (1989) *Ap. J.* **342**, 379.

15. Electromagnetic Cascades

Bethe, H.A. & Heitler, W. (1934). *Proc. Roy. Soc.* **146**, 83.

Bloomer, S.D., Linsley, J. & Watson, A.A. (1988). *J. Phys. G* **14**, 645.

Butcher, J.C. & Messel, H. (1960). *Nuclear Physics* **20**, 15.

Fenyves, E.J. et al. (1988). *Phys. Rev.* **D37**, 649.

Greisen, K. (1956). See §14.

Hillas, A.M. & Lapikens, J. (1977). *Proc. 15th Int. Cosmic Ray Conf.* (Plovdiv) **8**, 460.

Jackson, J.D. (1962). *Classical Electrodynamics* (John Wiley & Sons, Inc., New York).

Kamata, K. & Nishimura, J. (1958). *Prog. Theor. Phys.* (Kyoto) Suppl. **6**, 93.

Nelson, W.R., Hirayama, H. & Rogers, D.W.O. (1985). SLAC-Report-265 (unpublished).

Nishimura, J. (1967). *Handbuch der Physik* **XLVI/2**, 1.

Rossi, B. & Greisen, K. (1941). See §3.

Rossi, B. (1952). See §1.

Stanev, T. & Vankov, Ch. (1979). *Computer Physics Communications* **16**, 363.

16. Cosmic ray showers

Baltrusaitas, R.M. et al. (1985). *Phys. Rev. Letters* **54**, 1875.

Cassiday, G.L. et al. (1990) *Proc. 21st Int. Cosmic Ray Conf.* (Adelaide) **3**, 154.

Dingus, B.L. et al. (1988). *Phys. Rev. Letters* **61**, 1906.

Drees, M., & Halzen, F. (1988). *Phys. Rev. Letters* **61**, 275.

Drees, M., Halzen, F. & Hikasa, K. (1989). *Phys. Rev.* **D39**, 1310.

Edwards, P.G., Protheroe, R.J. & Rawinski, E. (1985). *J. Phys.* **G11**, L101.

Elbert, J.W. & Gaisser, T.K. (1979). *Proc. 16th Int. Cosmic Ray Conf.* (Kyoto) **8**, 42.

Gaisser, T.K. (1979). *Proc. Air Shower Workshop* (Salt Lake City, ed. T.K. Gaisser) p. 57. See also *Proc. 21st Int. Cosmic Ray Conf.* (Adelaide, paper HE7.4–4, 1990).

Greisen, K. (1960). See §14.

Grigorov, N.L. et al. (1970). See §1.

Hillas, A.M. et al. (1971). *Proc. 12th Int. Cosmic Ray Conf.* (Hobart) **3**, 1001 and 1007.

Hillas, A.M. (1983). *Proc. Cosmic Ray Workshop* (University of Utah, ed. T.K. Gaisser), p. 16.

Hillas, A.M. (1984). See §12.

Kakimoto, F. et al. (1981). *Proc. 17th Int. Cosmic Ray Conf.* (Paris) **11**, 254.

Kamata, K. (1978). In *Cosmic Rays and Particle Physics—1978* (ed. T.K. Gaisser, A.I.P. Conf. Proc. No. 49) p. 443.

Karakula, S. & Wdowczyk, S. (1963). *Acta Physica Polonica* **24**, 231.

Linsley, J. (1977). *Proc. 15th Int. Cosmic Ray Conf.* (Plovdiv) **12** 89.

Linsley, J. & Watson A.A. (1981). *Phys. Rev. Letters* **46**, 459.

Nagano, M. (1984). *J. Phys.* **G10**, 1295.

Peters, B. (1959). See §11.

Samorski, M. & Stamm, W. (1983). *Proc. 18th Int. Cosmic Ray Conf.* (Bangalore) *11*, 244.

Sokolsky, P. (1987). *Proc. 20th Int. Cosmic Ray Conf.* **8**, 318.

Stanev, T. (1989). *Proc. Cosmic Ray Cascade Simulation Workshop* (Salt Lake City, March 2-3, 1989) p. 279.

Stanev, T., Gaisser, T.K. & Halzen, F. (1985). *Phys. Rev.* **D32**, 1244.

Walker, R. & Watson, A.A. (1982). *J. Phys.* **G8**, 1131.

Watson, A.A. (1985). See §13.

17. Simulation techniques

Baltrusaitas, R.M. et al. (1984). See §5.

Cassiday, G.L. et al. (1990). See §16.

Ellsworth, R.W. et al. (1982). See §5.

Fenyves, E.J. et al. (1988). *Phys. Rev.* **D37**, 649.

Gaisser, T.K. et al. (1989). See §13.

Hara, T. et al. (1983). See §5.

Hillas, A.M. (1981). *Proc. 17th Int. Cosmic Ray Conf.* **8**, 193.

Smith, N.J.T. et al. (1989). *Nuclear Instruments and Methods in Physics Research* **A27**, 622.

Sokolsky, P. (1988). See §5.

Wrotniak, J.A. (1984). *SHOWERSIM/84*, University of Maryland Report PP. 85-191 (unpublished).

Index